Intranasal and systemic delivery of therapeutics to the rodent central nervous system: biodistribution and pharmacodynamic insights from normal and transgenic animal models

By
Geetika Nehra

A dissertation submitted in partial fulfillment
of the requirements for the degree of

Doctor of Philosophy
(Pharmaceutical Sciences)

at the

UNIVERSITY OF WISCONSIN-MADISON
2019

Date of final oral examination: 16 August 2019

This dissertation is approved by the following Final Oral Committee members:

Robert G. Thorne, Adjunct Associate Professor, Pharmaceutics (University of Minnesota Twin cities) & Denali Fellow, Denali Therapeutics
Marina E. Emborg, Professor, Medical Physics
Charles T. Lauhon, Associate Professor, Pharmaceutical Sciences
Lingjun Li, Professor, Pharmaceutical Sciences & Chemistry
Luigi Puglielli, Professor, Medicine (Geriatrics)
Michael R. Taylor, Assistant Professor, Pharmaceutical Sciences

Dedicated to my family, mentors and friends for their unconditional faith in my abilities

ACKNOWLEDGEMENTS

"If you take a cat apart to see how it works, the first thing you have on your hands is a non-working cat."

-Douglas Adams (1952 - 2011)

Author of Hitchhiker's Guide to the Galaxy

The process of developing a textbook figure involves months of experimental analysis, negative results and countless replication (technical as well as biological) that pave their way to that one consistent, recurrent finding within reason (i.e. standard error of mean, 95% confidence interval, R-values, limits of detection, correlation coefficients, etc) that carries the possibility of further analysis. Graduate school made me embrace these crushing experiences as 'persistent data' and, in the words of my advisor, Prof. Robert Thorne, taught me to 'not lose sight of the forest by getting lost in the trees'. It wouldn't have been possible to grow scientifically and complete this dissertation without his constant support, and encouragement among all kinds of delays and deadlines to push forward to this date.

I am equally grateful and indebted to Prof. Marina Emborg for her routine checks on my progress and for introducing me to the PD Think Tank; Prof. Luigi Puglielli and his lab (Dr. Samantha Shapiro, Dr. Yajing Peng, Dr. Mark Farrugia, Inca Dietrich) for guiding me though protein extractions and western blots, Prof. Michael Taylor and his lab (Dr. Kevin Lanham, Annette Dean, Fangzhou Mu) for helping me optimize the mouse MMP-9 activity assays using NanoDrop® spectrophotometer (who knew BCA assays do not respond well to enzymes), Prof. Lingjun Li and her lab (especially Dr. Jill Johnson) for their invaluable feedback on my presentations and figures at several instances, and Prof. Charles Lauhon for being my scientific foster parent during the last twelve months of high-throughput research.

On high-throughput researchers, I cannot imagine a better scientific journey without star-mentors (and achievers), Dr. Daniel Wolak, Dr. Jeffery Lochhead, Dr. Michelle Pizzo and Dr. Niyanta Kumar, who made

science a fulfilling experience for me. Equally crucial to my growth was the presence of my classmates, Brynna Wilken-Resman and Montira Tangsangasaksri, the voice(s) of reason and two highly-effective soundboards for graduate school experiences. Further, I cannot comprehend the completion of chronic study projects without two wonderful undergraduate students, Tongzhen Xie and Khoua Vang, who diligently sacrificed their summer breaks and weekends to work with mice (and me) at the animal vivarium, sometimes from 7 am through 7 pm, for more than 9 months. Their persistence will surely reflect in amazing ways as they take on new roles in graduate/medical school this year.

A large proportion of the scientific work in this thesis would not have existed without our collaborators. Prof. Michael Gould, Dr. Jill Haag and Prof. Steven Howard partnered with us to contrast different routes of administration routes for effective brain delivery of chemotherapeutic small molecules in rodents; Dr. Shannon Andrews and Ms. Joan Rettig at the Cancer Pharmacology Lab (UW Carbone Cancer Center) provided the HPLCS instrumentation and analytical support; Dr. John Feltenberger and his colleagues at the Medicinal Chemistry Center, UW-Madison School of Pharmacy synthesized unstable metabolites perillyl alcohol for this study; Prof. Torben Moos, Prof. Maj Thomsen and Prof. Svend Birkenlund (Aalborg University, Denmark) collaborated with us to investigate species differences in Fc receptor distribution with their expertise on *in-vitro* immunofluorescence and gene-expression analysis; Prof. Arash Bashirullah and Prof. Michael Taylor trained and guided us through laser scanning confocal microscopy for the *in vivo* immunofluorescence analysis of brain sections that became a large portion of this thesis; Prof. Tim Bugni provided unlimited access to the Synergy-H1 plate reader; and Prof. Jeffery Johnson's lab (Dr. Delinda Johnson, Dr. Rolando Xavier Aviles-Reyes) provided the training on ultracentrifugation for the chronic study. I would also like to whole-heartedly thank Mr. Josh Cutler, Ms. Sharon Vetter, Dr. Leesa Pennell (Biolegend), Ms. Patricia Esser and the entire Biomedical Research Model Services team for ensuring that our lab had a seamless supply of 6E10, MMP-9, healthy littermates and beta-amyloid ELISA kits as needed.

In the end, I would like to acknowledge my father Sanjiv Nehra and my sister Kajal Nehra for supporting me and my career choices with utmost love, trust and encouragement, not knowing where these decisions may lead us as a unit. I have also been fortunate to have a large (100+) family in India and an even larger group of friends anticipating the verdict on this dissertation. Among them, special thanks are due to Soumya Gupta, Neha Agrawal, Akshita Dhankar, Deepa Deepta Acharya, Tanushree Rawat, Tej Kumar, Ravi Suman, Paras Pratap Singh, Shaurya Chanana, Janna & Bryan Vice, the Dunkin family (Elisa, Erik, Theo and Jayber Dunkin), Dr. Shreya Goel, Dr. Gulpreet Kaur, Prashansa Shrivastav, and Prof. Kirti Yenkie for being my agency for troubleshooting, data recovery, and work-life balance since 2015.

ABSTRACT

Intranasal delivery can lead to rapid central nervous system (CNS) drug exposure through complex pathways associated with the cranial nerves originating in the nasal mucosae. However, certain factors such as variability in CNS exposure, limited long-term pharmacokinetic parameters, strain differences, and understudied CNS receptor distribution have limited the use of this strategy in clinical studies. In this thesis, we investigated these factors by comparing the distribution of therapeutic molecules in the CNS following intranasal or systemic delivery. We first evaluated these routes for the distribution of perillyl alcohol (POH) in the rodent CNS. Our results highlighted that intranasal POH delivery led to higher POH levels but similar metabolite levels in the cerebrospinal fluid (CSF) when compared with systemic dosing; these findings may partly explain how intranasally applied POH leads to brain tumor reduction and/or sensitivity in ongoing clinical studies. We next compared intranasal and systemic delivery of radiolabeled immunoglobulin G (IgG) to the CNS in wild-type mice and transgenic mice representing Alzheimer's disease pathology (APP/PS1). IgG levels were consistently higher in the olfactory bulbs for intranasal experiments across strains compared to brain values following systemic IgG delivery. Additionally, these levels were similar to reported values for a ~2-fold higher intranasal dose in rats. Enhancing nasal permeability with matrix metalloproteinase-9 (MMP-9) led to a ~2-fold higher brain IgG exposure for wild-type and APP/PS1 mice; however, IgG levels for wild-type mice with MMP-9 pretreatment were comparable to those for APP/PS1 mice without MMP-9 administration. Chronic, repeated intranasal delivery of an anti-amyloid IgG (6E10) with MMP-9 pretreatment in APP/PS1 mice led to a reduction in fibrillar amyloid but an increase in soluble oligomeric levels. Finally, we investigated the distribution of two IgG receptors (FcRn and FcγRIIb) across multiple brain-derived cell lines, animal strains, and species to identify potential CNS sites for IgG interactions and cellular uptake. Our results indicated that astrocytes and macrophages have higher FcRn and FcγRIIb immunoreactivity at brain-CSF interfaces compared to the brain parenchyma. This work offers new perspectives on how animal models, endogenous interactions, and dose-response relationships can influence CNS drug distribution following intranasal delivery.

TABLE OF CONTENTS

LIST OF FIGURES

CHAPTER 1: Targeted central nervous system delivery of perillyl alcohol following intranasal administration in rats

CHAPTER 2: Evaluating intranasal antibody delivery to the murine central nervous system: delivery, distribution and effects on amyloid pathology in APPswe/PS1dE9 mice

CHAPTER 3: Passive immunotherapies for central nervous system disorders: current delivery challenges and new approaches

CHAPTER 4: Evident astrocytic and macrophageal FcRn and FcγRIIb immunoreactivity at the rodent brain-cerebrospinal fluid interfaces

EPILOGUE

LIST OF TABLES

CHAPTER 2: Evaluating intranasal antibody delivery to the murine central nervous system: delivery, distribution and effects on amyloid pathology in APPswe/PS1dE9 mice

CHAPTER 4: Evident astrocytic and macrophageal FcRn and FcγRIIb immunoreactivity at the rodent brain-cerebrospinal fluid interfaces

PROLOGUE

Since the 1980s, an ever increasing number of preclinical studies have extensively explored the potential of the intranasal route of administration as a non-invasive strategy to directly deliver a wide range of molecules into the central nervous system (CNS) (Costantino et al., 2007; Dhuria *et al.*, 2010; Illum *et al.*, 2012; Kumar et al., 2016; Kumar *et al.*, 2018; Lochhead *et al.*, 2012; Lochhead *et al.*, 2014, Thorne *et al.*, 1995; Thorne *et al.*, 2004; Thorne *et al.*, 2008, Sakane *et al.*, 1994). These studies have solidified the idea that nasal mucosa architecture and physiology (Harkema *et al.*, 1990) allow for size-dependent, controlled permeability of substances through complex paracellular and transcellular paths that lead to absorption into the nasal vasculature (systemic exposure) and/or transport along cranial nerve-associated pathways (i.e. olfactory and trigeminal nerves) for CNS exposure. These so-called direct pathways for targeting the brain are especially beneficial for large macromolecules as they obviate the need to cross the physiological barriers that protect the brain from the systemic circulation, e.g. the blood-brain barrier (Abbott *et al*., 2010; Abbott *et al*., 2013; Engelhardt *et al*., 2009) and blood-cerebrospinal fluid (CSF) barriers (BCSFB) (Engelhardt *et al*., 2009). While a low basal level of serum-to-cerebrospinal fluid (CSF) transfer for endogenous large molecules such as immunoglobulin G (IgG) has been suggested to occur through fenestrated vessels in CNS circumventricular organs lacking a BBB and through the choroid plexus forming the inner BCSFB (Griffin & Giffels, 1982; Hochwald, 1970; Rappaport & Pettigrew, 1 979; Shrestha *et al*., 2014; Saunders *et al.*, 2018; Wurster & Haas, 1994), increasing evidence suggests IgG molecules internalized by brain endothelial cells comprising the BBB mostly become restricted within lysosomal compartments or recycled back to the plasma (St. Amour *et al*., 2013, Villasenor *et al*., 2016); a much smaller fraction of circulating IgG may undergo transcytosis across brain endothelial cells but, even then, a portion of these molecules likely become impeded at the basal lamina surrounding endothelial cells (Aihara *et al*., 1994), effectively preventing further exposure to the brain parenchyma.

As we continue to improve our understanding about the mechanisms governing nose-to-brain transport, several factors remain insufficiently explored and thus limit the translation of the intranasal route toward

becoming a well-characterized, validated treatment approach for clinical studies: variability in CNS exposure, species and strain differences, poorly characterized receptor distribution profiles, lack of long-term pharmacokinetic parameters, and a limited number of dose-response studies, among other factors. Given the resurgent interest in intranasal delivery over the past decade (Cattepoel *et al.*, 2011; Chauhan *et al.*, 2011; Chauhan *et al.*, 2015; Cooper *et al.*, 2013; Davydova *al.*, 2019; Eisenreid *et al.*, 2017; Gorbatov *et al.*, 2010; Kolobov *et al.*, 2012; Kolobov *et al.*, 2013; Kuznetsova *et al.*, 2013; Mayo *et al.*, 2016; Nellan *et al.*, 2018; Romanova *et al.*, 2010; Romanova *et al.*, 2012; Rosso *et al.*, 2013; Shakova *et al.*, 2013; Vetrile *et al.*, 2013; Vetrile *et al.*, 2016; Xiao *et al.*, 2013), my goal in this thesis work was to address some of the above-mentioned factors through carefully executed *in vivo* experiments designed to contrast intranasal and systemic delivery of large and small molecules in rodents.

Chapter 1 outlines a brief proof-of-concept study to assess the differences in intranasal and intravascular dosing of perillyl alcohol (POH), a small molecule (~ 152 Da) that is currently in clinical trials as an experimental chemotherapeutic (Chen *et al.*, 2015) and radiosensitizing agent (Rajesh *et al.*, 2003). Intranasal clinical studies involving POH are currently ongoing (clinicaltrials.gov) but it has not been clear whether POH achieves CNS exposure through the direct olfactory and trigeminal nerve associated pathways or, alternatively, through extensive metabolism at the nasal mucosa, absorption into the bloodstream, and subsequent entry into the CNS by simply crossing the BBB and BCSFBs owing to its small size and relatively lipophilic nature (Merkus *et al.*, 2003). It is important to understand these mechanisms in detail for POH because a more complete picture will likely influence drug development decisions surrounding its future use in the clinic (e.g. can intravascular dosing be considered instead of developing an intranasal formulation?). We investigated one aspect of POH nose-to-brain delivery by contrasting CSF exposure following nasal versus intravascular administration of equal-doses of POH in wild-type Sprague-Dawley rats. Despite a molecular profile favoring BBB permeability, we observed higher levels of both POH and its metabolite perillic acid in the cerebrospinal fluid (CSF) following intranasal administration; comparison of the CSF-to-plasma ratio further revealed a significantly higher value for POH but not perillic acid with

intranasal as compared to intravascular dosing. Our results demonstrate that intranasal delivery of POH can indeed lead to enhanced CSF exposure for the parent molecule (POH) while the perillic acid metabolite may undergo bidirectional blood-to-CSF transport likely due to high levels of dehydrogenase enzymes at the BBB and BCSFBs. This new information for intranasal dosing of POH may prove useful for optimizing intranasal dosing strategies for ongoing clinical studies.

Chapter 2 shifts the focus to CNS drug disposition in mice following intranasal or intraperitoneal administration of IgG (150 kDa), a large macromolecule with immense promise for future CNS drug development but also major questions surrounding how to deliver it effectively to the brain and spinal cord. Here, we employed a previously described and validated nasal permeation enhancer, matrix metalloproteinase-9 (MMP-9), to allow for improved IgG distribution profiles via olfactory and trigeminal nerve associated pathways following intranasal administration (Lochhead *et al.*, 2015; Kumar *et al.*, 2018). Matrix metalloproteinase-9 is an endogenous protein involved in the degradation of extracellular matrix components (Yabluchanskiy *et al.*, 2013) and modulation of tight junction proteins like claudin-1 (Hackel *et al.*, 2012), both of which form transport barriers to large molecules within the olfactory mucosa (Wolburg *et al.*, 2008); low levels of MMP-9 are naturally secreted within the rat nasal epithelia in the healthy state to allow for constant regeneration of the epithelial layer, a process known as re-epithelialization, because nasal epithelial cells turnover throughout life (Gueye *et al.* 2011). Nasal permeation enhancement with MMP-9 has the potential to revive therapies that have had poor efficacy outcomes in the past due to limited blood absorption or brain access owing to restrictive nasal epithelial permeability; however, the use and effectiveness of MMP-9 as a nasal permeation enhancer has thus far only been evaluated in rats with no information yet available for its effects on murine nasal mucosa. Increasingly easy access to a wide variety of transgenic mouse models of CNS disease coupled with the currently limited availability of validated transgenic rat models has gradually resulted in a species-shift from rats to mice in studies designed to assess effects on pathology following intranasal antibody administration (Cattepoel et al., 2011; Chauhan et al., 2011; Xiao et al., 2013; Mayo et al., 2016). Since pharmacokinetic information on brain IgG disposition in

the CNS has not been provided for specific anatomical regions (e.g. cortical versus sub-cortical) or physiological compartments (perivascular spaces vs parenchymal tissue) in prior mouse studies, we aimed to provide such information with new studies examining intranasal delivery of IgG with and without MMP-9 in wild-type mice as well as in a commonly used mouse transgenic model of Alzheimer's disease (AD). We first characterized acute IgG distribution across different anatomical and physiological compartments in two different murine models (wild-type C57BL/6J mice and AD-model APPswe/PS1dE9 mice) following intranasal dosing (with MMP-9 or saline pretreatment) and compared brain delivery using complementary radiometric and fluorescence-based methods previously described by our laboratory (Kumar *et al.*, 2018). Our results indicate subtle differences in IgG distribution following intranasal administration in wild-type and transgenic mice that are described in this thesis. We next went on to examine the chronic effects of repeated intranasal/systemic dosing of an anti-amyloid IgG (6E10) on olfaction (sense of smell) and neuropathology in awake APPswe/PS1dE9 AD-model mice in order to evaluate the potential of an intranasal anti-amyloid antibody strategy in the chronic treatment of AD. Our chronic survival/efficacy studies indicate no significant behavioral differences but improved target engagement profiles following intranasal MMP-9 pretreatment; biochemical analysis of *postmortem* brains highlight no differences in monomeric Aβ levels but a significant reduction in soluble oligomers of higher molecular weight (~100 kDa) and cored plaques following intranasal 6E10 with MMP-9 pretreatment. These results support the application of intranasal MMP-9 pretreatment in conjunction with nasal IgG formulations in mice and transgenic AD mouse models and suggest the potential of an intranasal anti-amyloid antibody approach for AD. This chapter also highlights and discusses the challenges in conducting such studies in awake mice due to higher inter-animal variability as well as the obviously smaller nasal cavity volumes present in mice as compared to rats.

Chapter 3, in line with the above, reviews advances in clinical studies for passive immunotherapies (i.e. antibody-based therapies) via systemic administration and summarizes the prospects and challenges of using central routes of administration, including intranasal delivery (Kumar *et al.*, 2018; partly written by

coauthor Geetika Nehra and reproduced with permission). IgG-based antibodies have great potential as treatments for several neuropathological conditions due to their abundance in the serum (Kindt et al., 2007), an unusually long systemic half-life (Vieira & Rajewsky, 1988; Spiegelberg & Fishkin, 1972), amenable interactions with endogenous Fc receptors (Woof & Burton, 2004), and the capability to be directed against almost any potential biological target. Given the massive socio-economic burden of CNS disorders, new ideas for developing disease-modifying IgG-based strategies that can effectively overcome the barriers of the CNS to result in sufficient brain exposure for meaningful effects have gained significant attention in the past decade (Dannon et al., 2019; Hammarlund-Udenaes et al. 2014). This chapter also discusses heterogeneity in the CNS interfaces across different brain regions, pathological conditions and disease stages and how such heterogeneity may affect brain distribution and target engagement profiles for passive immunotherapies.

The last component of original research presented in this thesis (**Chapter 4)** describes the endogenous distribution of two key receptors for the Fc domain of IgG in the rodent central nervous system. As already discussed in the preceding chapters, many different antibody-based therapeutic strategies are under active investigation for a wide variety of different CNS disorders. Testing of these different antibody-based approaches in rodents is a key element of all such drug development. A vast array of different antibodies have so far been utilized for this type of work: IgG fusion proteins (Pardridge & Boado, 2012), polymerosomes (Tian *et al*., 2015), IgGs with altered glycosylation (Mimura *et al*., 2018; Podulso *et al*., 1994) or receptor affinity (Cooper *et al*., 2013; Booth *et al*., 2018; Borrok *et al*., 2017), single-domain antibodies (Abulrob *et al*., 2004; Pizzo *et al*., 2018), IgGs with dual variable domains (Hazatian *et al*., 2018), and bispecific antibodies (Stanimirovic *et al*., 2014; Webster *et al*., 2016), among others. To date, a number of prior rodent studies have suggested antibody biodistribution within the CNS (Pizzo *et al*., 2018) or certain aspects of antibody-mediated CNS uptake and spread (Croll *et al*., 1998) may be due in part to IgG-Fc receptor (IgG-FcR) interactions. However, published studies detailing the sites of these interactions in the rodent brain and spinal cord are surprisingly limited; much of what we currently know about rodent

FcR protein distribution within the CNS and at CNS barrier sites and interfaces comes from indirect estimates based on in situ hybridization maps of RNA (Allen Institute for Brain Science, 2004), inferences from pharmacokinetic studies in knockout animals (Abuqayyas & Balthasar, 2013), and IgG immunoreactivity analyses with obvious limitations (Aihara *et al*., 1994; Goldsmith, 2002; Shreshtha *et al*., 2014). This chapter describes experiments where we examined the expression profiles of endogenous IgG Fc receptors in rats and mice; these receptors can reversibly interact with and influence the transport of IgG between different physiological compartments within the CNS (e.g. cerebrospinal fluid, perivascular fluid, and interstitial fluid) so their characterization is quite important for better understanding of IgG biodistribution. Using immunofluorescence and gene expression analysis, we demonstrated the presence of two Fc receptors (FcRn and FcγRIIb) at key interfaces in the rat and mouse CNS. Differences in expression patterns were examined and tested across multiple cell cultures, species and disease-models in one of the most rigorous studies yet conducted on FcRs in the CNS. Our results indicate astrocyte and macrophage immunoreactivity for FcRn and FcγRIIb at brain-cerebrospinal fluid (CSF) interfaces relevant for central drug delivery strategies (e.g. olfactory nerve layer, leptomeninges, glia limitans, perivascular spaces, ventricles, and choroid plexus). Immunolabeling was also observed for neocortical neurons and astrocytes in white matter tracts but, interestingly, minimal staining was observed for endothelial cells across species and in pathology. These results provide critical new insights into the possible roles that non-endothelial (astrocytic and macrophageal) Fc receptors may play in regulating IgG biodistribution and IgG activities within the rodent CNS.

Finally, the **Epilogue** reviews key findings of this thesis and outlines unexplored questions remaining for each of the studies covered in the above chapters. An overarching theme is how species differences may affect intranasal drug delivery to the central nervous system. To conclude, this thesis presents new, highly detailed information that bears on the CNS biodistribution of multiple therapeutically relevant molecules following their intranasal delivery in rodents. These findings may prove to have significant relevance for future applications utilizing these molecules as clinical therapeutics in the treatment of brain cancer,

Alzheimer's disease, and other neurological disorders.

References

Abbott NJ (2013). Blood-brain barrier structure and function and the challenges for CNS drug delivery. *J Inherit Metab Dis* **36**, 437–449.

Abbott NJ, Patabendige AA, Dolman DE, Yusof, SR & Begley DJ (2010). Structure and function of the blood-brain barrier. *Neurobiol Dis* **37**, 13–25.

Abulrob A, Guiseppin S, Andrade MF, McDermid A, Moreno M & Stanimirovic D (2004). Interactions of EGFR and caveolin-1 in human glioblastoma cells: evidence that tyrosine phosphorylation regulates EGFR association with caveolae. *Oncogene* **23**, 6967-6979.

Abuqayyas L & Balthasar JP (2013). Investigation of the role of FcgammaR and FcRn in mAb distribution to the brain. *Mol Pharm* **10**, 1505–1513.

Aihara N, Tanno H, Hall JJ, Pitts LH & Noble LJ (1994). Immunocytochemical localization of immunoglobulins in the rat brain: Relationship to the blood-brain barrier. *J Compar Neurol* **342**, 481-496.

Allen Institute for Brain Science. Allen Mouse Brain Atlas (2004) brain-map.org/api/index.html (accessed on Aug 4, 2019)

Booth BJ, Ramakrishnan B, Narayan K, Wollacott AM, Babcock GJ, Shriver Z & Vishwanathan K (2018). Extending human IgG half-life using structure-guided design. *mAbs*. **10**, 1098–1110.

Borrok MJ, Mody N, Lu X, Kuhn ML, Wu H, Dall'Acqua WF & Tsui P (2017). An "Fc-Silenced" IgG1 Format with Extended Half-Life Designed for Improved Stability. *J Pharm Sci* **106**, 1008–1017.

Cattepoel S, Hanenberg M, Kulic L & Nitsch RM (2011). Chronic intranasal treatment with an anti-Aβ (30-42) scFv antibody ameliorates amyloid pathology in a transgenic mouse model of Alzheimer's disease. *PLoS One* 2011 **6(4)**: e18296.

Chauhan MB & Chauhan NB (2015). Brain Uptake of Neurotherapeutics after Intranasal versus Intraperitoneal Delivery in Mice. *J Neurol Neurosurg* **2(1). pii**: 009.

Chauhan NB, Davis F & Xiao C (2011). Wheat germ agglutinin enhanced cerebral uptake of anti-Aβ antibody after intranasal administration in 5XFAD mice. *Vaccine* **29(44)**: 7631-7637.

Chen T, da Fonseca C & Schönthal A (2016). Perillyl Alcohol and Its Drug-Conjugated Derivatives as Potential Novel Methods of Treating Brain Metastases. *Int J Mol Sci* **17**, 1463.

ClinicalTrials.gov (2019). clinicaltrials.gov (accessed August 4, 2019)

Cooper PR, Ciambrone GJ, Kliwinski CM, Maze E, Johnson L, Li Q, Feng Y & Hornby PJ (2013). Efflux of monoclonal antibodies from rat brain by neonatal Fc receptor, FcRn. *Brain Res* **1534**: 13-21.

Costantino HR, Illum L, Brandt G, Johnson PH & Quay SC (2007). Intranasal delivery: physicochemical and therapeutic aspects. *Int J Pharm* **337**, 1–24.

Croll SD, Chesnutt CR, Rudge JS, Acheson A, Ryan TE, Siuciak JA, DiStefano PS, Wiegand SJ & Lindsay RM (1998). Co-infusion with a TrkB-Fc receptor body carrier enhances BDNF distribution in the adult rat brain. *Exp Neurol* **152(1)**: 20-33.

Davydova TV, Gruden MA, Kudrin VS, Narkevich VB, Vetrile LA, Zakharova IA & Sewell RDE (2019). Effect of Antibodies to Glutamate on Age-Related Memory Changes in C57BL/6 Mice. *Bull Exp Biol Med*. **166(3)**: 326-329.

Dhuria SV, Hanson LR & Frey WH 2nd (2010). Intranasal delivery to the central nervous system: mechanisms and experimental considerations. *J Pharm Sci* **99(4)**: 1654-1673.

Eisenried A1, Meidahl ACN, Klukinov M, Tzabazis AZ, Sabbadini RA, Clark JD & Yeomans DC (2017). Nervous system delivery of antilysophosphatidic acid antibody by nasal application attenuates mechanical allodynia after traumatic brain injury in rats. *Pain* **158(11):** 2181-2188.

Engelhardt B & Sorokin L (2009). Blood-brain and the blood-cerebrospinal fluid barriers: function and dysfunction. *Semin Immunopathol* **31(4)**: 497-511.

Goldsmith SK (2002). Haloperidol reduces IgG immunoreactivity in the rat brain. *Int J Neuropsychopharmacol* **5**, 309-313.

Gorbatov VY, Trekova NA, Fomina VG & Davydova TV (2010). Antiamnestic effects of antibodies to glutamate in experimental Alzheimer's disease. *Bull Exp Biol Med* **150(1)**: 23-25.

Griffin DE & Giffels J (1982). Study of protein characteristics that influence entry into the cerebrospinal fluid of normal mice and mice with encephalitis. *J Clin Investig* **70**, 289–295.

Gueye Y, Ferhat L, Sbai O, Bianco J, Ould-Yahoui A, Bernard A, Charrat E, Chauvin JP, Risso JJ, Féron F, Rivera S, & Khrestchatisky M (2011). Trafficking and secretion of matrix metalloproteinase-2 in olfactory ensheathing glial cells: A role in cell migration? *Glia* **59(5)**: 750-770.

Hackel D1, Krug SM, Sauer RS, Mousa SA, Böcker A, Pflücke D, Wrede EJ, Kistner K, Hoffmann T, Niedermirtl B, Sommer C, Bloch L, Huber O, Blasig IE, Amasheh S, Reeh PW, Fromm M, Brack A, Rittner HL (2012). Transient opening of the perineurial barrier for analgesic drug delivery. *Proc Natl Acad Sci U S A* **109(29)**: E2018-27.

Hammarlund-Udenaes M (2014). Pharmacokinetic Concepts in Brain Drug Delivery, in Drug Delivery to the Brain Physiological Concepts, Methodologies and Approaches. Hammarlund-Udenaes M, de Lange E & Thorne RG (Eds.). 127-161. Springer.

Harkema JR, Carey SA & Wagner JG (2006). The nose revisited: a brief review of the comparative structure, function, and toxicological pathology of the nasal epithelium. *Toxicol Pathol* **34(3)**: 252-269.
Hochwald GM (1970). Influx of serum proteins and their concentration in spinal fluid along the neuraxis. *J Neurol Sci* 10, 269–278.

Illum L (2012). Nasal drug delivery - recent developments and future prospects. *J Control Release* **161(2)**: 254-263.

Karaoglu Hanzatian D, Schwartz A, Gizatullin F, Erickson J, Deng K, Villanueva R, Stedman C, Harris C, Ghayur T & Goodearl A (2018). Brain uptake of multivalent and multi-specific DVD-Ig proteins after systemic administration. *MAbs* **10(5)**:765-777.

Kindt TJ, Goldsby RA & Osborne BA (2007). *Kuby Immunology*. 6th edition. W. H. Freeman and Co.

Kolobov VV, Davydova TV, Zakharova IA, Gorbatov VIu & Fomina VG (2012). [Repressional effects of the glutamate antibodies on expression of Dffb gene in the brain of rats with experimental Alzheimer's disease]. [Article in Russian] *Mol Biol (Mosk)* **46(5)**: 757-765.

Kolobov VV, Zakharova IA, Fomina VG, Gorbatov VY, Davydova TV (2013). Effect of antibodies to glutamate on caspase-3 activity in brain structures of rats with experimental Alzheimer's disease. *Bull Exp Biol Med* **154(4)**: 425-427.

Kumar NN, Gautam M, Lochhead JJ, Wolak DJ, Ithapu V, Singh V & Thorne RG (2016). Relative vascular permeability and vascularity across different regions of the rat nasal mucosa: implications for nasal physiology and drug delivery. *Sci Rep* **6**:31732.

Kumar NN, Lochhead JJ, Pizzo ME, Nehra G, Boroumand S, Greene G & Thorne RG (2018). Delivery of immunoglobulin G antibodies to the rat nervous system following intranasal administration: Distribution, dose-response, and mechanisms of delivery. *J Control Release* **286**: 467-484.

Kumar NN, Pizzo ME, Nehra G, Wilken-Resman B, Boroumand S & Thorne RG (2018). Passive Immunotherapies for Central Nervous System Disorders: Current Delivery Challenges and New Approaches. *Bioconjug Chem* **29(12)**: 2937-3966.

Kuznetsova LV, Karpova MN, Vetrile LA & Klishina NY (2013). Effects of antibodies to glutamate on focal penicillin-induced epileptic activity. *Bull Exp Biol Med* **155(5)**: 609-611.

Lochhead JJ & Thorne RG (2012). Intranasal delivery of biologics to the central nervous system. *Adv Drug Deliv Rev* **64(7)**: 614-628.

Lochhead JJ & Thorne RG (2014). Intranasal Drug Delivery to the Brain, in Drug Delivery to the Brain Physiological Concepts, Methodologies and Approaches. Hammarlund-Udenaes M, de Lange E & Thorne RG (Eds.). 401-431. Springer

Mayo L, Cunha AP, Madi A, Beynon V, Yang Z, Alvarez JI, Prat A, Sobel RA, Kobzik L, Lassmann H, Quintana FJ & Weiner HL (2016). IL-10-dependent Tr1 cells attenuate astrocyte activation and ameliorate chronic central nervous system inflammation. *Brain* **139(Pt 7)**: 1939-1957.

Merkus P, Guchelaar HJ, Bosch DA & Merkus FWHM (2003). Direct access of drugs to the human brain after intranasal drug administration? *Neurology* **60**, 1669–1671.

Mimura Y, Katoh T, Saldova R, O'Flaherty R, Izumi T, Mimura-Kimura Y, Utsunomiya T, Mizukami Y, Yamamoto K, Matsumoto T & Rudd PM (2018). Glycosylation engineering of therapeutic IgG antibodies: challenges for the safety, functionality and efficacy. *Protein Cell* **9**, 47–62.

Nellan A, McCully CML, Cruz Garcia R, Jayaprakash N, Widemann BC, Lee DW & Warren KE (2018). Improved CNS exposure to tocilizumab after cerebrospinal fluid compared to intravenous administration in rhesus macaques. *Blood* **132(6)**: 662-666.

Pardridge WM & Boado R J (2012). Reengineering biopharmaceuticals for targeted delivery across the blood-brain barrier. *Methods Enzymol* **503**, 269-292.

Pizzo ME, Wolak DJ, Kumar NN, Brunette E, Brunnquell CL, Hannocks MJ, Abbott NJ, Meyerand ME, Sorokin L, Stanimirovic DB & Thorne RG (2018). Intrathecal antibody distribution in the rat brain: surface diffusion, perivascular transport and osmotic enhancement of delivery. *J Physiol* **596**, 445–475.

Podulso JF & Curran GL (1994). Glycation increases the permeability of proteins across the blood-nerve and blood-brain barriers. *Brain Res Mol Brain Res* **23**, 157-162.

Rajesh D, Stenzel RA & Howard SP (2003). Perillyl alcohol as a radio-/chemosensitizer in malignant glioma. *J Biol Chem* **278(38)**: 35968-35978.

Rapoport SI & Pettigrew KD (1979). A heterogenous, pore-vesicle membrane model for protein transfer from blood to cerebrospinal fluid at the choroid plexus. *Microvasc Res* **18(1)**: 105-119.

Romanova GA, Kvashennikova YN, Shakova FM & Davydova TV (2012). Effect of antibodies to glutamate on the content of neurotransmitter amino acids in brain structures of rats with ischemic damage to the prefrontal cortex. *Bull Exp Biol Med* **153(1):** 13-15.

Romanova GA, Shakova FM, Gorbatov VY, Kvashennikova YN & Davydova TV (2010). Effect of antibodies to glutamate on retention of conditioned passive avoidance response in rats with ischemic injury of the prefrontal cortex. *Bull Exp Biol Med* **149(3)**: 289-92.

Rosso P, Moreno S, Fracassi A, Rocco ML & Aloe L (2015). Nerve growth factor and autophagy: effect of nasal anti-NGF-antibodies administration on Ambra1 and Beclin-1 expression in rat brain. *Growth Factors*. **33(5-6)**: 401-409.

Sakane T *et al* (1995). Direct drug transport from the rat nasal cavity to the cerebrospinal fluid: the relation to the molecular weight of drugs. *J Pharm Pharmacol* **47**, 379-381.

Saunders NR, Dziegielewska KM, Møllgård K & Habgood MD (2018). Physiology and molecular biology of barrier mechanisms in the fetal and neonatal brain. *J Physiol* **596(23)**: 5723-5756.

Shakova FM, Kodt P, Kudrin VS, Davydova TV & Romanova GA (2013). [The saving role of glutamate antibodies with the acute ischemic damage of the rat brain prefrontal cortex]. *Patol Fiziol Eksp Ter* **3**: 19-22.

Shrestha B, Paul D & Patcher JS (2014). Alterations in tight junction protein and IgG permeability accompany leukocyte extravasation across the choroid plexus during neuroinflammation. *J Neuropathol Exp Neurol* **3**, 1047-1061

Spiegelberg HL & Fishkin BG (1972). The catabolism of human G immunoglobulins of different heavy chain subclasses. *Clin Exp Immunol* **10**, 599–607.
St-Amour I *et al* (2013). Brain bioavailability of human intravenous immunoglobulin and its transport through the murine blood-brain barrier. *J Cereb Blood Flow Metab* **33**, 1983-1992.

Stanimirovic DB, Kemmerich K, Haqqani AS & Farrington GK (2015). Engineering and pharmacology of blood-brain barrier-permeable bispecific antibodies. *Expert Opin Drug Discov* **10**, 141-155.

Thorne RG, Emory CR, Ala TA & Frey WH (1995). Quantitative analysis of the olfactory pathway for drug delivery to the brain. *Brain Res* **692**, 278-282.

Thorne RG, Hanson LR, Ross TM, Tung D & Frey WH 2nd (2008). Delivery of interferon-beta to the monkey nervous system following intranasal administration. *Neuroscience* **152(3)**: 785-797.

Thorne RG, Pronk GJ, Padmanabhan V & Frey WH 2nd (2004). Delivery of insulin-like growth factor-I to the rat brain and spinal cord along olfactory and trigeminal pathways following intranasal administration. *Neuroscience* **127(2)**: 481-496.

Tian X, Nyerg S, S Sharp P, Madsen J, Daneshpur N, Armes SP, Berwick J, Azzouz M, Shaw P, Abbott NJ & Battaglia G (2015). LRP-1-mediated intracellular antibody delivery to the Central Nervous System. *Sci Rep* **5**, 11990.

Vetrile LA, Zakharova IA, Kudrin VS & Klodt PM (2013). Effects of antiglutamate antibodies on the development of stress response and neurotransmitter content in the hippocampus and hypothalamus of rats with different behavioral activity. 2013 *Bull Exp Biol Med* **155(3)**: 318-323.

Vetrile LA, Zakharova IA, Kudrin VS & Klodt PM (2016). [Effect of intranasally administered glutamate antibodies on the content of excitatory and inhibitory amino acids in the rat`s hippocampus and hypothalamus at the combined stress exposure] [Article in Russian]. *Patol Fiziol Eksp Ter* **(1)**: 4-10.

Vieira P & Rajewsky K (1998). The half-lives of serum immunoglobulins in adult mice. *Eur J Immunol* **18**, 313-316.
Villaseñor R, Ozmen L, Messaddeq N, Gruninger F, Loetscher H, Keller A, Betsholtz C, Freskgard PO & Collin L (2016). Trafficking of Endogenous Immunoglobulins by Endothelial Cells at the Blood-Brain Barrier. *Sci Reports* **6**, 25658.

Webster CI, Caram-Salas N, Haqqani AS, Thorn G, Brown L, Rennie K, Yogi A, Costain W, Brunette E & Stanimirovic DB (2016). Brain penetration, target engagement, and disposition of the blood-brain barrier-crossing bispecific antibody antagonist of metabotropic glutamate receptor type 1. *FASEB J* **30**, 1927-1940.

Wolburg H, Wolburg-Buchholz K, Sam H, Horvát S, Deli MA & Mack AF (2008). Epithelial and endothelial barriers in the olfactory region of the nasal cavity of the rat. *Histochem Cell Biol* **130(1)**: 127-140.
Wurster U & Haas J (1994). Passage of intravenous immunoglobulin and interaction with the CNS *J Neurol Neurosurg Psych* **57**, 21–25.

Xiao C, Davis FJ, Chauhan BC, Viola KL, Lacor PN, Velasco PT, Klein WL & Chauhan NB (2013). Brain transit and ameliorative effects of intranasally delivered anti-amyloid-β oligomer antibody in 5XFAD mice. *J Alzheimers Dis* **35(4)**: 777-788.

Yabluchanskiy A, Ma Y, Iyer RP, Hall ME & Lindsey ML (2013). Matrix metalloproteinase-9: Many shades of function in cardiovascular disease. *Physiology (Bethesda).* **28(6)**: 391-403.

CHAPTER 1

Targeted central nervous system delivery of perillyl alcohol following intranasal administration in rats

Geetika Nehra[1], Shannon Andrews[2], Michael N. Gould[3], Jill D. Haag[3], Steven P. Howard[4], Robert G. Thorne[1,5,6]

[1]Pharmaceutical Sciences Division, School of Pharmacy, University of Wisconsin-Madison, Madison, Wisconsin, USA; [2]Cancer Pharmacology Lab, University of Wisconsin Carbone Cancer Center, Madison, Wisconsin, USA; [3]Department of Oncology, McArdle Laboratory for Cancer Research, University of Wisconsin-Madison School of Medicine & Public Health, Madison, Wisconsin, USA; [4]Department of Human Oncology, University of Wisconsin-Madison School of Medicine & Public Health, Madison, Wisconsin, USA;[5]Denali Therapeutics, South San Francisco, California, USA; [6]Department of Pharmaceutics, College of Pharmacy, University of Minnesota Twin Cities, Minneapolis, Minnesota, USA

*Represents section implemented and authored by Geetika Nehra

In preparation for first submission to the *Scientific Reports* journal

Abstract

Perillyl alcohol (POH) is a lipophilic, small (~152 Da) molecule that has been extensively investigated in preclinical models and early-stage clinical trials with primary brain cancer patients for tumor reduction following intranasal (IN) administration. Mounting evidence recommends IN dosing for large macromolecules to access the central nervous system (CNS) through direct olfactory and trigeminal nerve pathways; however, it remains unclear whether POH benefits from these pathways since the nasal mucosa is rich in biotransformation enzymes and a highly permeable vasculature. It is also debated whether POH reaches the CNS compartments by crossing or bypassing the blood-brain and blood-cerebrospinal fluid (CSF) barriers and if there is a need for direct CNS delivery. Here, we investigated these questions by contrasting CNS distribution of POH following equal-dose intra-arterial (IA) and IN administration in wild-type Sprague-Dawley rats. Blood and CSF samples were collected over 70 minutes following the first IN dose or IA bolus dose, and samples were later assayed for POH and perillic acid (PA), major metabolite for POH, via high-performance liquid chromatography (HPLC) experiments. Our results indicate that POH and PA levels are nearly 10-fold higher in the CSF following IN administration. CSF-to-plasma ratio was 10-fold higher for POH following IN administration while PA levels had similar CSF-to-plasma ratios for both routes of administration. These results demonstrate that intranasal administration leads to maximal POH entry into the CSF while bidirectional blood-to-CSF movement limits maximal CSF exposure for PA. Thus, our findings provide novel insights into the CNS disposition of POH following intranasal delivery.

Introduction

The intranasal (IN) route of administration has long been appreciated as an option for local and systemic delivery of certain small molecules, peptides, and protein drugs (Costantino *et al*., 2007; Lochhead & Thorne, 2014). In particular, the nasal route possesses distinct advantages when local effects are needed (e.g. as with decongestants, antibiotics, and mucolytics) or when non-invasive access to the systemic circulation is required for fast drug onset and/or to avoid extensive hepatic first-pass elimination (e.g. as

with the application of the opioid antagonist naloxone following opioid overdose). Many current and past examples exist for the clinical use of both small molecules (e.g. zolmitriptan, sumatriptan, butorphanol tartrate, fentanyl, nicotine, and estradiol) and low molecular weight peptide drugs (e.g. calcitonin, desmopressin, buserelin, oxytocin) administered by the intranasal route (Illum, 2012). Since paraceullar permeability of substances across the nasal epithelia appears to be inversely proportional to molecular weight, systemic bioavailability for intranasally delivered small hydrophilic molecules generally greatly exceeds that of larger peptides (Costantino *et al*., 2007) intranasally applied smaller molecules may also be much more efficiently absorbed into the extensive nasal vasculature within the lamina propria after crossing the nasal epithelia (Kumar *et al*., 2016). Many studies over the past two decades have suggested that a fraction of small and large molecules escaping absorption into the nasal vasculature many potentially access the brain and/or CSF directly through olfactory or trigeminal nerve-associated pathways originating within the nasal mucosa (Lochhead & Thorne, 2012; Lochhead *et al*., 2015; Thorne *et al*., 1995; Thorne *et al*., 2004; Thorne *et al*., 2008). However, whether small molecules can directly access the brain and/or CSF from the nasal passages independent of the bloodstream (i.e. after crossing the blood-brain barrier and/or blood-CSF barriers) has often been questioned (Merkus *et al*., 2003), in part due to the high efficiency of nasal vascular absorption.

Initial preclinical studies to develop perillyl alcohol (POH), a 152 Da plant-derived monocyclic terpene, as a chemotherapeutic agent began with hepatic (Mills *et al*., 1995) and mammary (Haag *et al*., 1994) tumor-bearing rodents through oral administration and a significant reduction in tumor growth was observed. Efforts to intranasally administer perillyl alcohol (POH), however, were initially informed through toxicity findings in multiple phase I clinical trials. These studies involved oral POH dosing in patients with peripheral tumors that led to incidences of dose-limiting gastrointestinal toxicity and low patient compliance (Belanger *et al*., 1998; Hudes *et al*., 2000; Meadows *et al*., 2002; Ripple *et al*., 2000). Ever since, IN POH has been used in clinical trials to sensitize the lesion area after standard procedures (surgical excision, radiotherapy or chemotherapy) (Da Fonseca *et al*., 2006; Da Fonseca *et al*., 2008a; Da Fonseca *et*

al., 2008b). Primary brain cancer patients with tumors in the deep brain regions are reported to have a significantly higher survival rate upon chronic IN POH treatment with non-existent side-effects compared to tumors in the lobar regions (Da Fonseca *et al*., 2009; Da Fonseca *et al*., 2011; Da Fonseca *et al*., 2013). Further, molecular dynamic simulations suggest that long-term POH exposure alters the plasma membrane potential of glioma cells that leads to this delayed tumor progression (Da Fonseca *et al*., 2016). POH has also been intranasally co-administered with well-characterized chemotherapeutic agents (e.g. bortezomib, temozolomide) in rodents; these reports indicate that POH co-delivery prolongs survival outcomes and elevates brain levels for the co-administered chemotherapeutic agents in rodents (Wang *et al*., 2019). Yet, limited information is available for the CNS disposition of POH following intranasal delivery; given that systemic access for POH would interface with specialized barriers of the CNS (Ghersi-Egea *et al*., 1995; Saunders *et al.*, 2018).

Efforts to characterize and quantify POH and its two major metabolites, perillic acid (PA) and dihydroperillaldehyde (DHPA), began in the early 1990s as a part of oral dosing studies in rats (Haag *et al*., 1994) and beagle dogs (Phillips *et al*., 1995). However, POH remained undetectable in some of these studies (Phillips *et al*., 1995). Subsequent attempts to improve assay sensitivity were made using GC-MS analysis (Zhang *et al*., 1999). In these rodent studies, 10-fold lower doses of intravenous POH injection led to detectable and therapeutically relevant POH concentrations (< 100 mM) in the peripheral tissues. Further, high-performance liquid chromatography (HPLC) analysis indicated that lipophilic POH emulsions were stable in the rat plasma with long half-lives (Hua *et al*., 2008). Hence, rapid biotransformation of POH to DHPA and PA was suggested to be a result of exposure to tissue-specific physiological compartments. Recent studies have observed efficacy following chronic intranasal delivery of POH in brain tumor-bearing xenograft mouse models (Cho *et al*., 2012); however, these studies do not provide the pharmacokinetic parameters that had help in appreciating whether POH exposure to the CNS was specific to intranasal POH delivery studies. It is also unclear whether intranasally applied POH gains access to the CSF via systemic circulation or through direct olfactory and trigeminal nerve associated pathways originating in the nasal

mucosa (Lochhead & Thorne, 2012; Lochhead & Thorne, 2014). Therefore, the goal of our study was to provide this quantitative comparison through pharmacokinetic profiles for POH and its metabolite(s) following intranasal and systemic (intra-arterial; IA) POH administration. Our report aims to provide novel insights for intranasal POH delivery to the CNS that may be relevant for investigating POH-drug conjugates, chemically modified POH analogs (Chen *et al*., 2016), and even the physiological effects of POH on central and peripheral organs (Salazar *et al*., 2014) in preclinical and clinical studies.

Materials and Methods

Stock solutions, standards and quality controls

S-(-)-Perillyl alcohol (POH; purity 96.0%; Catalog #218391) was obtained from Millipore-Sigma (St. Louis, MO, USA). Perillic acid (PA) was synthesized by Dr. Gould and colleagues as described previously (Crowell *et al*., 1992; Madrid *et al*., 1991). HPLC grade acetonitrile (Catalog #A998-4) and methanol (Catalog #A452-4) were procured from Fisher Scientific (Hampton, NH, USA). Commercially available Sprague-Dawley rat plasma (Catalog #50642312; Fisher Scientific, Hampton, NH, USA) and artificial cerebrospinal fluid (ACSF; 124 mM NaCl, 3 mM KCl, 26 mM $NaHCO_3$, 1.25 mM NaH_2PO_4, 1.3 mM $MgCl_2$, 1.5 mM $CaCl_2$ and 10 mM D-glucose equilibrated with 95% O_2/ 5% CO_2; 300 ± 5 mOsm/kg osmolality determined using a freezing-point osmometer. Model 3250 Osmometer (Advanced Instruments, Norwood, MA, USA)) were used for assay calibration and validation. POH and PA were dissolved in methanol at a stock concentration of 10 µg/mL and 1000 µg/mL respectively and stored as one-time-use aliquots at -20°C. POH standards were prepared in plasma and/or artificial CSF by serially diluting stock solutions to 1.0, 0.75, 0.5, 0.4, 0.3, 0.2 and 0.1 µg/mL final concentrations. PA standards were prepared in a similar manner as mentioned above at 5.0, 4.0, 3.0, 2.0, 1.0, 0.75, 0.5, and 0.25 µg/mL final concentrations. Quality controls were prepared at 0.8, 0.45 and 0.25 µg/mL final concentrations for POH and 4.5, 2.5, and 0.65 µg/mL final concentrations for PA respectively.

Sample preparation for chromatography

HPLC assay design was based on a previously described pharmacokinetic study by Hua and colleagues (Hua *et al*., 2008) with slight modifications. Briefly, a 50 µL volume of samples/standards/quality controls were supplemented with 100 µL acetonitrile and vortexed vigorously for 3 min (POH) or 1 min (PA). Samples were then centrifuged (14000g, 4°C, 10 min for POH; 14000g, room temperature, 5 min for PA). Following centrifugation, 20 µL of supernatant was injected into the HPLC system. For PA analysis, 120 µL of supernatant was carefully transferred to a clean tube and dehydrated under a stream of nitrogen. Pellets were then resuspended in 100 µL diluted mobile phase (50% mobile phase, 50% acetonitrile, 10 mM $NaHCO_3$) and 80 µL of this resuspension was injected into the HPLC system.

Chromatography parameters

The chromatography setup comprised of Shimadzu Prominence HPLC system modules, a degasser, an auto-sampler, a UV detector (wavelengths set to 210 nm and 217 nm for POH and PA detection respectively) and a column oven (Shimadzu Scientific Instruments Inc., Columbia MD, USA). Separation was performed using a Zorbax Eclipse XDB-C18 column (4.6 x 150 mm, 5 µm; Agilent Technologies, Santa Clara, CA, USA) and a Zorbax C18 guard (8 x 4 mm, 5 µm; Agilent Technologies, Santa Clara, CA, USA). Mobile phase composition for both analytes was isocratic, comprising of water - acetonitrile mixture (60:40, v/v, pre-mixed, 1.0 mL/min) for POH analysis and 0.05M ammonium acetate (pH 5) - acetonitrile mixture (64:36, v/v, pre-mixed, 2.0 mL/min) for PA analysis. Both phases were passed through 0.45 µm filters (Millipore-Sigma, St. Louis, MO, USA) before use.

POH formulation*

POH formulation used for this study was adapted from the nasal formulation recipe used in an ongoing clinical trial that examines the safety and efficacy of perillyl alcohol in recurrent grade IV glioma patients (NCT02704858). This study is conducted at the University of Wisconsin Hospital and Clinics by Dr Howard and colleagues. Briefly, intranasal POH formulation consisted of 10% v/v (9.4% w/w) POH, 55%

v/v glycerin USP (Catalog #G1016, Spectrum Chemicals, New Brunswick, NJ, USA) and 35% v/v dehydrated alcohol (Catalog #ET107, Spectrum Chemicals, New Brunswick, NJ, USA). Dose for our experiments was determined by the allometric scaling method (West *et al*., 2005) to scale the smallest daily dose received by a human subject in the clinical trial for rats i.e. 4.745 mg (~23 mg/kg). Formulations were refrigerated as 54 µL one-time-use aliquots at 4°C. Formulation volume for intranasal administration (i.e. 54 µL) was considered safe based on similar volumes being used for intranasal study paradigms in rats (Lochhead *et al*., 2015; Kumar *et al.*, 2016; Kumar *et al.*, 2018).

Setup for intracisternal sampling of cerebrospinal fluid (CSF)*

A dedicated CSF withdrawal system was used for POH experiments (see Fig. 2). This system comprised of the following components - 20 cm long polyethylene tubing (PE-10; inner diameter: 0.61 mm, outer diameter: 0.28 mm; Plastics One Inc., Roanoke, VA, USA); 100 µL Hamilton syringe (inner diameter: 1.475 mm; Harvard Apparatus, Holliston, MA, USA) and a two-port shut-off valve assembly (PEEK; inner diameter: 0.5 mm; Idex Health and Science, Oak Harbor, WA, USA). Tubing was firmly secured at both ends of the valve assembly using NanoTight^{TM} sleeves (FEP; inner diameter: 0.69 mm; Idex Health and Science, Oak Harbor, WA, USA) flanking on either side of valve fittings. Valve fitting that faced the cisternal space was connected to a different set of tubing assembly i.e. 1 cm PE-10 tubing sealed to a 1.27 mm long polyether ether ketone tubing (PEEK; 33 GA; Plastics One Inc., Roanoke, VA, USA). These tubing parts were joined and sealed using molten wax and cyanoacrylate.

Animal preparation*

180-200 g Sprague Dawley rats were anesthetized under urethane (1.5 g/kg, i.p.) until surgical plane was reached. Atropine sulfate (0.1 mg/kg, i.m.; Med-Pharmex, Pomona, CA, USA) was given every 2 hours to avoid fluid accumulation in the lungs. Animals were maintained at physiological temperatures using a homeothermic monitoring system (Harvard Apparatus, Holliston, MA, USA) throughout the experiment.

Tracheotomy (prior to IN POH administration only) *

Glycerin increased the viscosity of POH formulation compared to ethylene glycol (Ethylene glycol: 0.0162 N s/m^2, Glycerin: 0.95 N s/m^2) resulting in breathing issues and low survival rate of animals at experimental endpoint. Hence, animals subjected to intranasal POH administration underwent a brief tracheotomy procedure prior to cisternal puncture. Briefly, an incision was made parallel to rings of hyaline cartilage and proximal to the thyroid gland in the anterior aspect of trachea; a short piece (5 cm) of PE-205 tubing (outer diameter: 2mm; Plastics One, Roanoke, VA, USA) was then inserted into this opening. Tubing was secured by 2-3 surgical knots with a general purpose thread, followed by sealing the skin at the neck using cyanoacrylate. In our experience, tracheotomy prior to intranasal administration increased the survival rate in rodents. Tracheotomy was not performed for intra-arterial POH dosing experiments.

Intracisternal cannulation*

Intracisternal cannulation was the first procedure conducted on animals undergoing intra-arterial POH dosing. Cannulation was performed after the tracheotomy procedure for intranasal POH administration experiments. Cisternal cannulation procedure was adapted from a recently reported setup for intrathecal delivery in rats at our laboratory (Pizzo *et al*., 2018). Briefly, lidocaine hydrochloride (2%; 0.5 mL, s.c.) was applied as a local anesthetic at the scalp prior to positioning the animals in a stereotaxic frame (Stoelting, Wood Dale, IL, USA). A 5 cm midline incision was then made from the base of the neck up to 2 cm anterior to the bregma. Skin was laterally secured with straight hemostats and muscle layers were sequentially pulled back using vannas scissors (Harvard Apparatus) and cotton tip applicators. Once the atlanto-occipital layer was exposed, gentle incisions were made by alternating between a goniotomy knife and forceps (Fine Science Tools, Foster City, CA, USA) to avoid dural puncture. When the cisterna magna was visible beneath the intact dura, a small dural hole was made using a dental needle at an angle of 60 degrees from the vertical. PEEK tubing was then inserted with the help of a microelectrode holder and stereotaxic frame's manipulator arm. Excess CSF flowing out from the hole was absorbed using cotton tip applicators and tubing was sealed to the cranial opening with cyanoacrylate; sealed setup was then dried

until cured. This procedure was followed by abdominal aortic cannulation for both treatment groups.

Abdominal aortic cannulation*

Once the cyanoacrylate was cured, animals were carefully flipped with back facing the heating blanket such that the tubing stayed in place. An incision was made below the xiphoid process into the abdomen along the midline. The skin was held apart using hemostats, and intestines and cecum were moved laterally to have a clear view of the aorta. Using cotton tip applicators and curved sharp forceps (Fine Science Tools, Foster City, CA, USA), the aorta was separated from the vena cava by breaking the fascia between the two vessels. The separation was widened using forceps (Fine Science Tools) and a 6 inches long pieces of general-purpose thread was tied at the bottom of this opening to cut off lower body blood supply. Another piece of thread (~12 in) was loosely held in place at the top of this opening and the opening was clamped just below the thread. Hemostats were clamped onto both thread strings to hold the aorta taught before making a horizontal nick into the vessel. The cut was enlarged for a 20 GA 1.25 in cannula attached to a 3-way stop cock to allow smooth entry. The cannula was then secured held by multiple knots of the larger thread around the stop cock.

Intranasal administration*

54 µL of POH formation aliquots were administered intranasally using 200 µL gel loading pipette tips. Briefly, 17 mm of a gel loading pipette tip was inserted into one naris at an angle of 45° from the midline and 45°from the horizontal plane. Once 5 mm inside the nasal cavity, an obstruction can be felt by the walls of the nasal septum if going in at this angle. At this point, the tip was aligned parallel to the nasal septum bone and was inserted 12 mm further inside ventrally at an angle of 45° from the horizontal plane. This length (17 mm) ensured that the formulation was ejected close to the nasal passages without causing any tissue damage. Within the first 5 min, 2 x 27 µL of the aliquoted volume of IN POH formulation was administered to each naris.

Intra-arterial administration*

54 µL of POH formation was diluted with 445 µL of physiological saline (150 mM NaCl, 0.9%, pH 7.4) and injected into the 3-way stop-cock connected to the abdominal aorta. This was followed by another round of 500 µL saline to flush the entire formulation through the setup.

Blood and CSF withdrawal*

CSF was withdrawn at 0-12 min, 14-26 min, 28-40 min, 40-54 min and 56-70 min at 5 µL/min. After each withdrawal, there was a 2 min gap for ejecting CSF samples from the tubing into clean microcentrifuge tubes on ice and re-inserting the ports back into the sampling setup. Meanwhile, 300 µL blood samples were collected every 14 min in microcentrifuge tubes containing 3 µL sodium heparin (1000 USP units, NDC 25021-400-0, Sagent Pharmaceuticals, Schaumburg, IL, USA) to prevent coagulation. These tubes were kept on ice and later centrifuged (3,000 rpm, 4°C, 5 min) to separate plasma. Plasma and CSF samples were further spun (12,000 rpm, 4°C, 5 min) to remove blood contamination. Animals were euthanized by injecting 1 mL KCl (1M, Sagent Pharmaceuticals, Schaumburg, IL, USA) into the pericardium. Samples were stored (-80°C) until ready to assay. Prior to HPLC analysis, samples for all times intervals per animal were thawed and pooled to obtain enough starting sample volumes for triplicate HPLC assays with discernible peaks.

Statistical analysis*

For each HPLC assay, lower limits of detection and quantification (LLOD, LLOQ) were determined prior to sample analysis using artificial CSF (aCSF) and/or commercially available rat plasma. As the purpose of this study was to investigate POH concentrations, we depicted values below LLOQ in certain instances (see Fig. 1c) for comparison. Values below LLOD were reported as zero and were excluded in most cases. Raw values of concentrations across both treatment groups were compared using Mann-Whitney rank sum test to check for statistical significance.

Results

23.73 mg/kg POH was administered to 9 adult female Sprague-Dawley rats via IN (n = 5) or IA (n = 4) routes. The amount of POH administered was based on (a) the lowest dose of POH administered in previous preclinical studies (Hua *et al*., 2008; Cho *et al*., 2012) i.e. 21 mg/kg and (b) the allometrically-scaled dose (West *et al*., 2005) of IN POH formulation used in an ongoing clinical trial examining the safety and efficacy of POH in recurrent grade IV glioma patients. Doses were equivalent to the smallest daily dose received by a human subject in the clinical trial. These values were very similar to previously administered POH doses in healthy rats (Zhang *et al*. 1999) and mice (Salazar *et al*., 2014). Fig. 1 graphically illustrates POH and PA concentrations in the cerebrospinal fluid (CSF) and plasma across both treatment groups. $POH_{(CSF, IN)}$ and $POH_{(Plasma, IN)}$ denote POH levels in the CSF and plasma upon IN administration respectively while $POH_{(CSF, IA)}$ and $POH_{(Plasma, IA)}$ denote POH levels in the CSF and plasma upon IA administration respectively. Likewise, $PA_{(CSF, IN)}$ and $PA_{(Plasma, IN)}$ denote PA levels in the CSF and plasma upon IN administration respectively while $PA_{(CSF, IA)}$ and $PA_{(Plasma, IA)}$ denote PA levels in the CSF and plasma upon IA administration respectively. We also compared CSF-to-plasma ratios (CSF/Plasma) for all combinations of analytes and routes of administration to evaluate whether a given route provides brain-targeting advantage for a given analyte. Here, $CSF/Plasma_{(POH, IN)}$ and $CSF/Plasma_{(PA, IN)}$ indicates CSF-to-plasma ratio for POH and PA upon IN POH administration respectively while $CSF/Plasma_{(POH, IA)}$ and $CSF/Plasma_{(PA, IA)}$ indicate the same for IA POH administration.

Intranasal POH enters systemic circulation

Upon IN dosing, $POH_{(CSF, IN)}$ was below the lower limit of quantification (LLOQ) in 1 out of 5 rats while $POH_{(Plasma, IN)}$ were well above LLOQ for all animals. Based on these values, mean $POH_{(CSF, IN)}$ was estimated to be 1.39 ± 0.42 µM while mean $POH_{(Plasma, IN)}$ was 5-fold higher at 7.57 ± 1.77 µM suggesting that IN POH largely accesses systemic blood circulation.

Intra-arterial POH administration led to minimal CSF access

Upon IA dosing, all $POH_{(CSF, IA)}$ values were below LLOQ while $POH_{(Plasma, IA)}$ values were above LLOQ for the 4 animals. For comparison, we estimated mean $POH_{(CSF, IA)}$ to be 0.16 ± 0.03 μM which is 9-fold lower than mean $POH_{(CSF, IN)}$. Meanwhile, mean $POH_{(Plasma, IA)}$ was 4-fold higher than mean $POH_{(Plasma, IN)}$ at 33.09 ± 15.78 μM. These comparisons argue in support of IN POH selectively accessing the CSF via olfactory and trigeminal pathways (Lochhead & Thorne, 2012). The same formulation is restricted outside the CNS upon IA administration.

Intranasal route-specific POH to PA biotransformation

$PA_{(CSF, IN)}$ and $PA_{(Plasma, IN)}$ levels were well above LLOQ for all 5 rat CSF samples with mean $PA_{(CSF, IN)}$ at 5.88 ± 1.14 μM, approximately 4-fold higher than mean $POH_{(CSF, IN)}$. Likewise, mean $PA_{(Plasma, IN)}$ was 4-fold higher than $POH_{(Plasma, IN)}$ at 23.92 ± 0.24 μM. These values indicate that a large fraction of $POH_{(CSF, IN)}$ is converted into $PA_{(CSF, IN)}$ within 70 min. Upon IA administration, $PA_{(CSF, IA)}$ was below LLOQ for 1 out of 4 while ell above LLOQ for all 4 animals while $PA_{(Plasma, IA)}$ was well above LLOQ for all 4 animals. Here, mean $PA_{(Plasma, IA)}$ was 1.88 ± 0.60 μM compared to mean $POH_{(Plasma, IA)}$ at 33.09 ± 15.78 μM suggesting a lower extent of POH to PA conversion in the plasma upon IA dosing. Mean $PA_{(CSF, IA)}$ was 0.51 ± 0.10 μM.

High POH concentrations in the CSF following intranasal delivery

$CSF/Plasma_{(POH, IN)}$ was estimated to be 0.21 ± 0.02 while $CSF/Plasma_{(POH, IA)}$ reduced to zero. If values below LLOQ were included for comparison, $CSF/Plasma_{(POH, IA)}$ would be 0.02 ± 0.01. These values demonstrate that the intranasal route provides direct CNS access for POH. On the contrary, $CSF/Plasma_{(PA, IN)}$ and $CSF/Plasma_{(PA, IA)}$ were closely similar at 0.24 ± 0.02 and 0.23 ± 0.03 respectively. Based on these values, it can be inferred that PA is not selectively reaching the CNS via either route.

Discussion

Previous reports have elaborated on the transport mechanisms by which intranasally applied macromolecules access the CNS (Kumar *et al*., 2016; Kumar *et al*., 2018; Lochhead & Thorne, 2012; Lochhead & Thorne, 2014; Thorne *et al*., 2001; Thorne *et al*., 2004). Briefly, intranasally applied substances move across the nasal epithelium via intracellular, paracellular and extracellular pathways to reach the underlying connective tissue called the lamina propria (Kumar *et al*., 2016; Kumar *et al*., 2018; Lochhead & Thorne, 2012; Lochhead & Thorne, 2014; Thorne *et al*., 2001; Thorne *et al*., 2004). Here, these molecules can (a) access the permeable blood vessels and enter systemic circulation, (b) access the lymphatic vessels and drain into the deep cervical lymph nodes, or (c) enter the perivascular spaces around nasal blood vessels or perineural channels associated with the olfactory and trigeminal nerves and enter the CSF or reach the CNS at the level of the olfactory bulbs and brainstem respectively (Kumar *et al*., 2016; Kumar *et al*., 2018; Lochhead & Thorne, 2012; Lochhead & Thorne, 2014; Thorne *et al*., 2001; Thorne *et al*., 2004). Within the CNS, molecules can undergo widespread distribution via convection or dispersion inside perivascular spaces around cerebral blood vessels and eventually enter the extracellular spaces at the post-capillary venule level before passively diffusing into the brain parenchyma (Kumar *et al*., 2018; Lochhead *et al*., 2015; Pizzo *et al*., 2018). This pathway is often restricted for intravenous or intra-arterial drug delivery due to the presence of specialized blood-brain barrier (BBB) (Abbott *et al*., 2010; Abbott, 2013) and blood-CSF barrier (BCSFB) (Liddlelow, 2015) where tight-junction proteins prevent macromolecules (> 500 Da) (Pajouhesh & Lenz, 2005) in the blood from entering the CNS. In this study, we report that the intranasal route can be effective in rapid, brain-targeted delivery of POH (152 Da) to the CNS.

Incidentally, POH belongs to a subset of non-polar small molecules (< 400 Da) that can passively diffuse through the lipid bilayers of intact brain capillary endothelial cells to enter the CNS (Pajouhesh & Lenz, 2005). First, the lipophilicity or partition coefficient (log P) values for POH are between 1.9 - 2.5 (Wishart *et al*., 2018), well within the acceptable range of 1.5-2.7 for BBB-permeable molecules (Pajouhesh & Lenz, 2005). Second, POH has a polar surface area of approximately 20.23 Å (Wishart *et al*., 2018) which is

lower than the 60-90 $Å^2$ limit for binding to receptors proteins at the BBB prior to transcytosis (Pajouhesh & Lenz, 2005). Third, POH has a favorable profile for structural flexibility with 1 hydrogen donor atom (< 5 preferred), one acceptor hydrogen atom (< 10 preferred) and two rotatable bonds (< 5 preferred) (Mikitsch & Chacko, 2014). In conclusion, POH can potentially diffuse through the BBB based on these well-characterized parameters. However, POH has a high binding affinity for albumin (K_d = 0.19 M) that results in a fairly low unbound drug fraction within an albumin-rich fluid compartment (e.g. plasma, CSF with f_u ~ 0.2 - 0.4) (Song *et al*., 2004) limiting its ability to diffuse across the BBB.

Here, we administered equal amounts of POH via IN and IA routes to ascertain if the BBB-permeable profile would allow for similar POH exposure levels in both cases. Our POH formulation is identical to the intranasal formulation prescribed in an ongoing clinical trial examining the safety and efficacy of POH in recurrent grade IV glioma patients (NCT02704858). We applied this formulation proximal to the nasal olfactory mucosa to increase the likelihood of CNS delivery as this region has relatively lower vascular permeability and mucociliary clearance (Kumar *et al*., 2016; Lochhead & Thorne, 2012). The same formulation was injected intra-arterially to reduce variability associated with excipients. Samples were collected and pooled prior to HPLC analysis to allow for larger injection volumes and discernible chromatogram peaks. Samples were also processed to precipitate residual proteins (e.g. albumin) and ensure that the levels account for total (bound and unbound) POH concentrations.

Upon IN administration, mean $POH_{(Plasma, IN)}$ was approximately 5-fold higher than mean $POH_{(CSF, IN)}$ indicating that IN POH mostly enters systemic circulation. Upon IA POH administration, mean $POH_{(CSF, IA)}$ was below LLOQ while mean $POH_{(Plasma, IA)}$ was nearly 4-fold higher than $POH_{(Plasma, IN)}$ suggesting that plasma-borne POH minimally diffuses across the lipid bilayers of brain endothelial cells despite a BBB-permeable profile. Mean $POH_{(CSF, IN)}$ were substantially higher (~10-fold) than mean $POH_{(CSF, IA)}$ highlighting a selective access to olfactory and trigeminal pathways upon IN administration. For the

metabolite, mean $PA_{(CSF, IN)}$, mean $PA_{(Plasma, IN)}$ and mean $PA_{(CSF, IA)}$ were higher than mean $POH_{(CSF, IN)}$, mean $POH_{(Plasma, IN)}$ and mean $POH_{(CSF, IA)}$ respectively. Interestingly, a similar trend for POH and PA levels was also observed in a recent independent study at 60 min (Wang *et al*., 2019). These findings potentially imply that enzymes along brain-CSF interfaces, olfactory pathways, and trigeminal pathways are rapidly converting POH to PA. Previous reports indicate that POH can be altered to PA by multiple cytochrome P450 enzymes (Miyazawa *et al*., 2002; Shimada *et al*., 2002) or sequentially by alcohol and aldehyde dehydrogenases (Boon *et al*., 2000). Interestingly, these enzymes are present in the nasal mucosa with a higher expression in the olfactory epithelium than the respiratory epithelium (Bogdanffy *et al*., 1987; Bogdanffy *et al*., 1990; Kajiya *et al*., 2001; Kurosaki *et al*., 2004; Thornton-Manning *et al*., 1997). Additionally, significant levels of alcohol dehydrogenases have also been detected across arteries and veins - largely associated with the smooth muscle layer (tunica media), followed by the endothelial cell layer (tunica intima) and the lowest expression associated with the outer collagenous membrane surrounding blood vessels (tunica adventitia) (Allali-Hassani *et al*., 1997). High mRNA expression levels of alcohol and aldehyde dehydrogenases have also been detected at brain-CSF interfaces (leptomeninges, choroid plexus, ependyma (Galter *et al*., 2003; Martinez *et al*., 2001) and within the brain parenchyma (Zimatkin *et al*., 1989). Recent immunohistochemical analysis also suggests that these sites are enriched with monocarboxylate transporters (MCT-1 and MCT-2) (Pierre *et al.*, 2000), however these molecules have not been investigated with POH or PA so far. These reports support the rationale that IN POH is consistently exposed to multiple sites rich in biotransformation enzymes that may be responsible for PA formation. In this regard, mean $PA_{(Plasma, IA)}$ were ~13-fold lower than mean $POH_{(Plasma, IA)}$ suggests that the extent of dehydrogenation is markedly less around the luminal surface of endothelial cells. While we do observe a statistically significant difference for all parameters across both treatment groups, we do realize that the study involves a very small population and the necessity of validating these results in a larger sample size of healthy as well as tumor-bearing rodent models. Nevertheless, this report provides novel findings that support the rationale behind IN POH administration for improved CNS access, an unanswered question that may further the translation of POH in clinical trials.

References

Abbott NJ, Patabendige AA, Dolman DE, Yusof, SR & Begley DJ (2010). Structure and function of the blood-brain barrier. *Neurobiol Dis* **37**, 13–25.

Abbott NJ (2013). Blood-brain barrier structure and function and the challenges for CNS drug delivery. *J Inherit Metab Dis* **36**, 437–449.

Allali-Hassani A, Martinez SE, Peralba JM, Vaglenova J, Vidal F, Richart C, Farres J & Pares X (1998). Alcohol dehydrogenase of human and rat blood vessels: Role in ethanol metabolism. *FEBS Lett* **405**, 26–30.

Belanger JT (1998). Perillyl Alcohol: Applications in Oncology. *Altern Medicine Rev* **3**, 448–457.

Bogdanffy MS, Randall HW & Morgan KT (1987). Biochemical quantitation & histochemical localization of carboxylesterase in the nasal passages of the Fischer-344 rat & B6C3F1 mouse. *Toxicol Appl Pharmacol* **88**, 183-194.

Bogdanffy MS (1990). Biotransformation enzymes in the rodent nasal mucosa: the value of a histochemical approach. *Environ Heal Perspect* **85**, 177–186.

Boon PJM., van der Boon D & Mulder GJ (2000). Cytotoxicity and biotransformation of the anticancer drug perillyl alcohol in PC12 Cells and in the rat. *Toxicol Appl Pharmacol* **167**, 55–62.

Chen T, da Fonseca C & Schönthal A (2016). Perillyl Alcohol and Its Drug-Conjugated Derivatives as Potential Novel Methods of Treating Brain Metastases. *Int J Mol Sci* **17**, 1463.

Cho HY, Wang W, Jhaveri N, Torres S, Tseng J, Leong MN, Lee DJ, Goldkorn A, Xu T, Petasis NA, Louie SG, Schonthal AH, Hofman FM & Chen TC (2012). Perillyl alcohol for the treatment of temozolomide-resistant gliomas. *Mol Cancer Ther* **11**, 2462–2472.

Costantino HR, Illum L, Brandt G, Johnson PH & Quay SC (2007). Intranasal delivery: physicochemical and therapeutic aspects. *Int J Pharm* **337**, 1–24.

Crowell PL, Lin S, Vedejs E & Gould MN (2012). Identification of metabolites of the antitumor agent d-limonene capable of inhibiting protein isoprenylation and cell growth. *Cancer Chemother Pharmacol* **31**, 205–212.

da Fonseca CO, Masini M, Futuro D, Caetano R, Gattass CR & Quirico-Santos T (2006). Anaplastic oligodendroglioma responding favorably to intranasal delivery of perillyl alcohol: a case report and literature review. *Surg Neurol* **66**, 611–615.

da Fonseca CO, Linden R Futuro D, Gattass CR & Quirico-Santos T (2008). Ras pathway activation in gliomas: a strategic target for intranasal administration of perillyl alcohol. *Arch Immunol Ther Exp* **56**, 267–276.

da Fonseca CO, Schwartsmann G, Fischer J, Nagel J, Futuro D, Quirico-Santos T & Gattass CR (2008) Preliminary results from a phase I/II study of perillyl alcohol intranasal administration in adults with recurrent malignant gliomas. *Surg Neurol* **70**, 259–266.

da Fonseca CO, Silva JT, Lins IR, Simao M, Arnobio A, Futuro D & Quirico-Santos T (2009). Correlation of tumor topography and peritumoral edema of recurrent malignant gliomas with therapeutic response to intranasal administration of perillyl alcohol. *Invest New Drugs* **27**, 557–564.

da Fonseca CO, Simao M, Lins IR, Caetano RO, Futuro D & Quirico-Santos T (2011). Efficacy of monoterpene perillyl alcohol upon survival rate of patients with recurrent glioblastoma. *J Cancer Res Clin Oncol* **137**, 287–293.

da Fonseca CO, Teixeira RM, Silva JC, DE Saldanha, da Gama Fischer J, Meirelles OC, LAndeiro JA, Quirico-Santos T (2013). Long-term outcome in patients with recurrent malignant glioma treated with perillyl alcohol inhalation. *Anticancer Res* **33**, 5625–5631.

da Fonseca CO, Khandelia H, Salazar MD, Schonthal AH, Meireles OC, Quirico-Santos T (2016). Perillyl alcohol: Dynamic interactions with the lipid bilayer and implications for long-term inhalational chemotherapy for gliomas. *Surg Neurol Int* **7,** 1.

Galter D, Carmine A, Buervenich S, Duester G & Olson L (2013). Distribution of class I, III and IV alcohol dehydrogenase mRNAs in the adult rat, mouse and human brain. *Eur J Biochem* **270**, 1316–1326.

Ghersi-Egea JF, Leininger-Muller B, Cecchelli R & Fenstermacher JD (1995). Blood-brain interfaces: relevance to cerebral drug metabolism. *Toxicol Lett* **82**, 645–653.

Haag JD & Gould MN (1994). Mammary carcinoma regression induced by perillyl alcohol, a hydroxylated analog of limonene. *Cancer Chemother Pharmacol* **34**, 477–483.

Hua HY, Zhao YX, Liu L, Ye QX & Ge SW (2008). High-performance liquid chromatographic and pharmacokinetic analyses of an intravenous submicron emulsion of perillyl alcohol in rats. *J Pharm Biomed Analysis* 48, 1201–1205.

Hudes GR, Szarka CE, Adams A, Ranganathan S, McCauley RA, Weiner LM, Langer CJ, Litwin S, Yeslow G, Halberr T, Qian M, Gallo JM (2000). Phase I pharmacokinetic trial of perillyl alcohol (NSC 641066) in patients with refractory solid malignancies. *Clin Cancer Res* **6,** 3071–3080.

Illum L (2012). Nasal drug delivery - recent developments and future prospects. *J Control Release* **161**, 254–263

Kajiya K, Inaki K, Tanaka M, Haga T, Kataoka H & Touhara K (2001). Molecular bases of odor discrimination: Reconstitution of olfactory receptors that recognize overlapping sets of odorants. *J Neurosci* **21, 6018–6025.**

Kumar NN, Gautam M, Lochhead JJ, Wolak DJ, Ithapu V, Singh V & Thorne RG (2016). Relative vascular permeability and vascularity across different regions of the rat nasal mucosa: implications for nasal physiology and drug delivery. *Sci Rep* **6**, 31732.

Kumar NN, Lochhead JJ, Pizzo ME, Nehra G, Boroumand S, Greene G & Thorne RG (2018). Delivery of immunoglobulin G antibodies to the rat nervous system following intranasal administration: distribution, dose response and mechanisms of delivery. *J Control Release* **286**, 467–484.

Kurosaki M, Terao M, Barzago MM, Bastone A, Bernardinello D, Salmona M & Garattini E (2004). The aldehyde oxidase gene cluster in mice and rats. Aldehyde oxidase homologue 3, a novel member of the molybdoflavoenzyme family with selective expression in the olfactory mucosa. *J Biol Chem* **279**, 50482–50498.

Liddelow SA (2015). Development of the choroid plexus and blood-CSF barrier. *Front Neurosci* **9**, 32.

Lochhead JJ & Thorne RG (2012). Intranasal delivery of biologics to the central nervous system. *Adv Drug Deliv Rev* **64**, 614–628.

Lochhead JJ & Thorne RG (2014). Intranasal drug delivery to the brain. In Drug Delivery to the Brain, vol. 10, Hammarlund-Udenaes M, de Lange ECM & Thorne RG. American Association of Pharmaceutical Scientists. Springer, New York.

Lochhead JJ, Wolak DJ, Pizzo ME & Thorne RG (2015). Rapid transport within cerebral perivascular spaces underlies widespread tracer distribution in the brain after intranasal administration. *J Cereb Blood Flow Metab* **35**, 371–381.

Madrid Y, Langer LF, Brem H & Langer R (1991). New directions in the delivery of drugs and other substances to the central nervous system. *Adv Pharmacol* **22**, 299–324.

Martinez SE, Vaglenova J, Sabria J, Martinez MC, Farres J & Pares X (2001). Distribution of alcohol dehydrogenase mRNA in the rat central nervous system. *Eur J Biochem* **268**, 5045–5056.

Meadows SM, Mulkerin D, Berlin J, Bailey H, Kolesar, Warren D & Thomas JP (2002). Phase II Trial of Perillyl Alcohol in Patients with Metastatic Colorectal Cancer. *Int J Gastrointest Cancer* **32**, 125–128.

Merkus P, Guchelaar HJ, Bosch DA & Merkus FWHM (2003). Direct access of drugs to the human brain after intranasal drug administration? *Neurology* **60**, 1669–1671.

Mills JJ, Chari RS, Boyer IJ, Gould MN & Jirtle RL (1995). Induction of apoptosis in liver tumors by the monoterpene perillyl alcohol. *Cancer Res* **55**, 979–983.

Mikitsh JL & Chacko AM (2014). Pathways for small molecule delivery to the central nervous system across the blood-brain barrier. *Perspect Med Chem* **6**, 11–24.

Miyazawa M, Shindo M. & Shimada T (2002). Metabolism of (+)- and (-)-limonenes to respective carveols and perillyl alcohols by CYP2C9 and CYP2C19 in human liver microsomes. *Drug Metab Dispos* **30**, 602–607.

Pajouhesh H & Lenz GR (2005). Medicinal chemical properties of successful CNS drugs. *NeuroRx* **2**.

Phillips LRR., Malspeis L & Supko JG (1995). Pharmacokinetics of active drug metabolites after oral administration of perillyl alcohol, an investigational antineoplastic agent, to the dog. *Drug Metab Dispos* **23**, 676–680.

Pierre K1, Pellerin L, Debernardi R, Riederer BM & Magistretti PJ (2000). Cell-specific localization of monocarboxylate transporters, MCT1 and MCT2, in the adult mouse brain revealed by double immunohistochemical labeling and confocal microscopy. *Neuroscience* **100(3)**: 617-627.

Pizzo ME, Wolak DJ, Kumar NN, Brunette E, Brunnquell CL, Hannocks MJ, Abbott NJ, Meyerand Me, Sorokin L, Satnimirovic DB & Thorne RG (2018). Intrathecal antibody distribution in the rat brain: surface diffusion, perivascular transport and osmotic enhancement of delivery. *J Physiol* **596**, 445–475.

Ripple GH, Gould Mn, Arzoomanian RZ, Alberti D, Feierabend C, Simon K, Binger K, Tutsch KD, Pomplun M, Wahamaki A, Marnocha R, Wilding G & Bailey HH (2000). Phase I clinical and pharmacokinetic study of perillyl alcohol administered four times a day. *Clin Cancer Res* **6**, 390–6 (2000).

Salazar MDA, da Silva RF, da Fonseca CO, Lagrota-Candido, J & Quirico-Santos T (2014). Intranasal administration of perillyl alcohol activates peripheral and bronchus-associated immune system *in vivo*. *Arch Immunol Ther Exp* **62**, 59–66.

Saunders NR, Dziegielewska KM, Møllgård K & Habgood MD (2018). Physiology and molecular biology of barrier mechanisms in the fetal and neonatal brain. *J Physiol* **596(23)**: 5723-5756.

Shimada T, Shindo M & Miyazawa M (2012). Species differences in the metabolism of (+)- and (-)-limonenes and their metabolites, carveols and carvones, by cytochrome P450 enzymes in liver microsomes of mice, rats, guinea pigs, rabbits, dogs, monkeys, and humans. *Drug Metab Pharmacokinet* **17**, 507–515.

Song MS, Wang D, & Row KH (2004). Protein binding study of isoflavones by high-performance frontal analysis. *Chromatographia* **26**, 136–138.

Thorne RG, Emory CR., Ala TA. & II, WHF (1995). Quantitative analysis of the olfactory pathway for drug delivery to the brain. *Brain Res* **692**, 278–282.

Thorne RG & Frey WH (2001). Delivery of neurotrophic factors to the central nervous system: pharmacokinetic considerations. *Clin Pharmacokinet* **40**, 907–946.

Thorne R, Pronk G, Padmanabhan V & Frey, WH (2004). Delivery of insulin-like growth factor-I to the rat brain and spinal cord along olfactory and trigeminal pathways following intranasal administration. *Neuroscience* **127**, 481–496.

Thorne, RG, Lakkaraju A, Rodriguez-Boulan E & Nicholson C (2008). *In vivo* diffusion of lactoferrin in brain extracellular space is regulated by interactions with heparan sulfate. *Proc Natl Acad Sci U S A* **105**, 8416–8421.

Thornton-Manning JR, Nikula KJ, Hotchkiss JA, Avila KJ, Rohrbacher KD, Ding X & Dahl AR (1997). Nasal cytochrome P450 2A: identification, regional localization, and metabolic activity toward hexamethylphosphoramide, a known nasal carcinogen. *Toxicol Appl Pharmacol* **142,** 22–30.

Wang W, Swenson S, Cho HY, Hofman FM, Schonthal AH & Chen TC (2019). Efficient brain targeting and therapeutic intracranial activity of bortezomib through intranasal co-delivery with NEO100 in rodent glioblastoma models. *J Neurosurg* 1–9.

West GB & Brown JH (2005). The origin of allometric scaling laws in biology from genomes to ecosystems: towards a quantitative unifying theory of biological structure and organization. *J Exp Biol* **208**, 1575–1592.

Wishart DS, Feunang YD, Marcu A, Guo AC, Liang K, Vazquez-Fresno R, Sajed T, Johnson D, Li C, Karu N, Sayeeda Z, Lo E, Assempour N, Berjanskii M, Sanghal S, Arndt D, Liang Y, Badran H, Grant J, Serra-Cayuela A, Liu Y, Mandal R, Neveu V, Pon A, Knox C, Wilson M, Manach C & Scalbert A (2018). HMDB 4.0: the human metabolome database for 2018. *Nucleic Acids Res* **46**, D608–D617.

Zhang ZH, Chen TC, Chan KK, Budd T & Ganapathi R (1999). Gas chromatographic-mass spectrometric analysis of perillyl alcohol and metabolites in plasma. *J Chromatogr B* **728**, 85–95.

Zimatkin S, Lindrost OK & And KOL (1989). A histochemical study of the distribution of aldehyde dehydrogenase activity in brain structures of rats with genetically different alcohol-related behaviour. *Alcohol* **6**, 321–325.

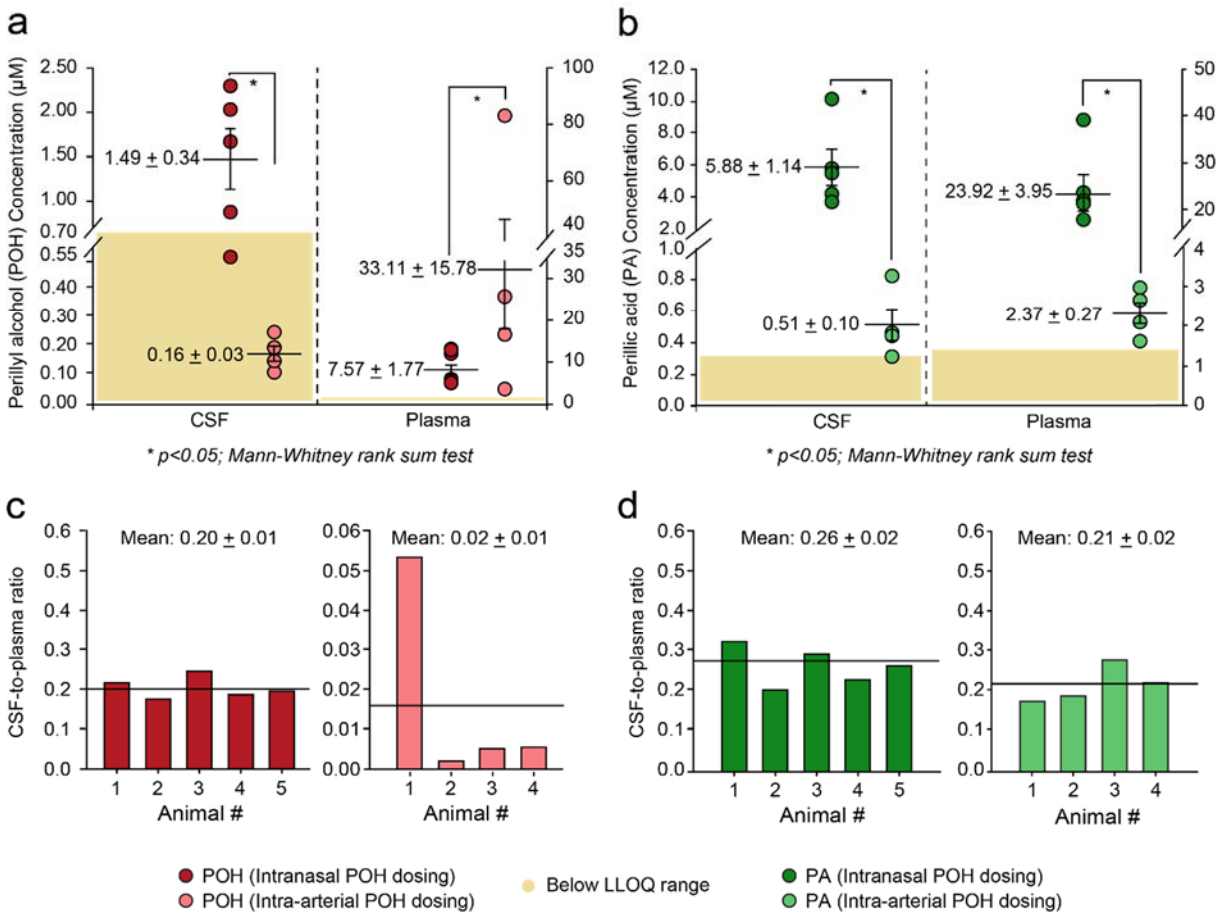

Figure 1. Distribution of perillyl alcohol (POH) and perillic acid (PA) in the cerebrospinal fluid (CSF) and blood plasma following equal-dose intranasal and intra-arterial POH administration. (a) Concentration of POH in the CSF and blood plasma following intranasal (red) and intra-arterial (pink) POH administration. (b) Concentration of PA in the CSF and blood plasma following intranasal (dark green) and intra-arterial (light green) POH administration. (c) CSF-to-plasma ratio for POH after intranasal (red) and intra-arterial (pink) POH administration. (d) CSF-to-plasma for PA after intranasal (dark green) and intra-arterial (light green) POH administration.

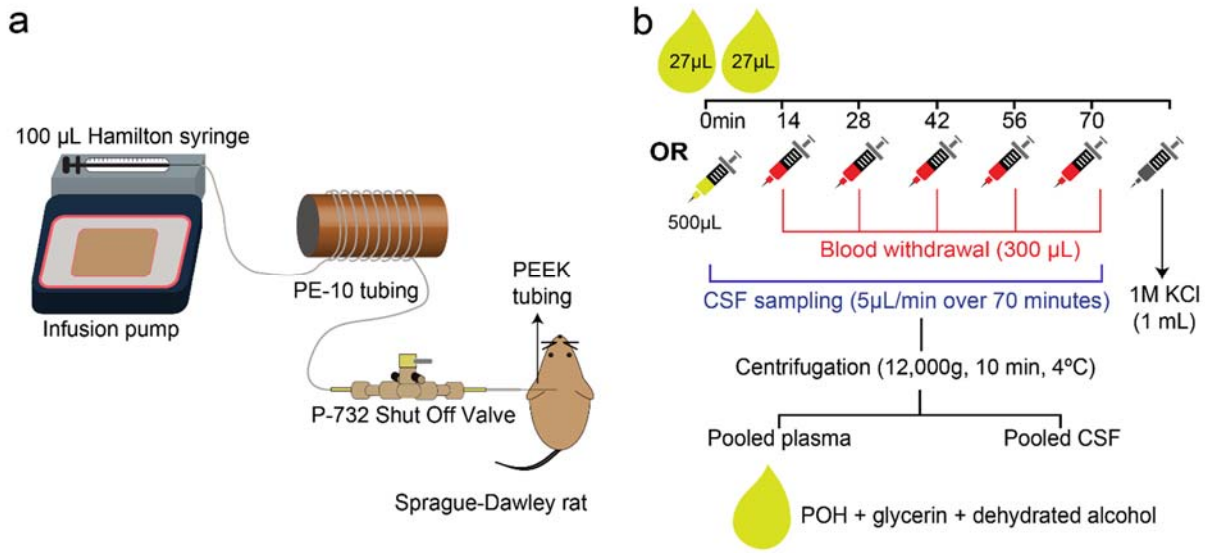

Figure 2. Experimental setup. (a) Surgical setup for intracisternal withdrawal of cerebrospinal fluid. (b) Dosing paradigm for intranasal and intra-arterial POH administration experiments.

CHAPTER 2

Evaluating intranasal antibody delivery to the murine central nervous system: delivery, distribution, and effects on pathology in APPswe/PS1dE9 mice

Geetika Nehra[1], Tongzhen Xie[1], Khoua Vang[1], Niyanta N. Kumar[1], Michelle E. Pizzo[1], Brynna Wilken-Resman[1], Robert G. Thorne[1-3]

[1]Pharmaceutical Sciences Division, School of Pharmacy, University of Wisconsin-Madison, Madison, Wisconsin, USA; [2]Denali Therapeutics, South San Francisco, California, USA; [3]Department of Pharmaceutics, College of Pharmacy, University of Minnesota Twin Cities, Minneapolis, Minnesota, USA

In preparation for first submission to the *Journal of Controlled Release*

Abstract

Intranasal route of administration has been extensively studied as a non-invasive strategy to deliver a wide range of therapeutic molecules to the central nervous system (CNS). Of note, the use of nasal permeation enhancers like matrix metalloproteinase-9 (MMP-9) has now allowed for enhanced antibody delivery to the rat brain for preclinical studies and offers the potential to revive antibodies that have had poor efficacy outcomes in the past due to low levels of CNS exposure in the past. However, this strategy has not been investigated for the murine central nervous system (CNS). In this study, we characterized intranasal IgG delivery with and without the use of MMP-9 using radiolabeled or fluorescently labeled non-targeted IgG molecules in adult wild-type C57BL6/J and double transgenic APPswe/PS1dE9 mice. Our findings reveal significantly higher [^{125}I]-IgG concentrations at the olfactory bulbs following intranasal delivery, compared to intraperitoneal equal-dose experiments. A non-significant increase in ^{125}I-IgG concentrations was observed for multiple brain regions in the C57BL/6J mice; these values were even higher for APPSwe/PS1dE9 mice. Intranasal MMP-9 pre-treatment significantly enhanced [^{125}I]-IgG concentrations at the olfactory bulbs and for major cerebral arteries and associated perivascular spaces (PVS). [^{125}I]-IgG concentrations in C57BL/6J mice receiving MMP-9 pretreatment were comparable to APPswe/PS1dE9 mice values without any nasal permeation enhancement. Next, we evaluated the safety and efficacy following chronic (weekly) intranasal MMP-9 exposure followed by intranasal administration of 6E10 (mouse IgG1 targeting Aβ_{40} and Aβ_{42} N-terminal residues). Intranasal 6E10 administration with or without MMP-9 pre-treatment led to no behavioral differences in latency or olfaction periods in mice over 14 weeks. Further, intranasal MMP-9 pretreatment led to a significantly improved pharmacodynamic efficacy profile for 6E10 in the form of reduced cortical fibrillar plaques and increased levels for the 96-100kDa bands (putatively soluble amyloid precursor protein). Finally, no significant differences were detected for ELISA levels of total Aβ_{40} and Aβ_{42} levels, indicating that higher-order oligomers were selectively engaged by 6E10. These results support the application of MMP-9 prior to intranasal IgG delivery for improving efficacy outcomes in a transgenic Alzheimer's disease mouse model.

Introduction

Intranasal route of administration has been increasingly recognized as a potential non-invasive strategy to deliver a wide range of therapeutics into the central nervous system (CNS) (Dhuria *et al.*, 2010; Illum *et al.*, 2012; Kumar *et al.*, 2018; Lochhead *et al.*, 2012; Lochhead *et al.*, 2014). Aside from ease of self-administration, rapid-onset of effects and evasion of first-pass hepatic elimination (Lochhead *et al.*, 2012; Lochhead *et al.*, 2014), intranasal delivery allows for direct CNS access via olfactory and trigeminal pathways as observed in rats (Kumar *et al.*, 2018; Thorne *et al.*, 2004) and monkeys (Thorne *et al.*, 2008) that lead to subsequent brain-wide distribution through dispersion within the perivascular spaces of cerebral blood vessels (Lochhead *et al.*, 2015; Asgari *et al.* 2016; Pizzo *et al.*, 2018). As a result, intranasal route offers therapeutics molecules a pathway to bypassing the blood-brain barrier (BBB) (Abbott *et al.* 2010) and blood-cerebrospinal fluid barriers (Engelhardt *et al.* 2009) that may lead to improved CNS exposure.

For large molecules such as antibodies, the intranasal route offers an alternative to boost the target engagement capacity in the CNS. Recent findings have shown that systemically applied IgG is largely confined within the endothelial cells, leading to failures in achieving desired efficacy endpoints in clinical trials (Hammarlund-Udenaes *et al.*, 2014; Kumar *et al.*, 2018). Acknowledging restricted brain-access, coupled with an evolved understanding of the intranasal delivery mechanisms, have led to a resurgent interest in the intranasal route for delivering targeted antibodies to the CNS (Cattepoel *et al.*, 2011; Chauhan *et al.*, 2011; Chauhan *et al.*, 2015; Cooper *et al.*, 2013; Davydova *al.*, 2019; Eisenried *et al.*, 2017; Gorbatov *et al.*, 2010; Kolobov *et al.*, 2012; Kolobov *et al.*, 2013; Kuznetsova *et al.*, 2013; Mayo *et al.*, 2016; Nellan *et al.*, 2018; Romanova *et al.*, 2010; Romanova *et al.*, 2012; Rosso *et al.*, 2013; Shakova *et al.*, 2013; Vetrile *et al.*, 2013; Vetrile *et al.*, 2016; Xiao *et al.*, 2013) over the last decade. Majority of these studies have been conducted in healthy rats or rats with acute injuries (Cooper *et al.*, 2013; Eisenried *et al.*, 2017; Gorbatov *et al.*, 2010; Kolobov *et al.*, 2012; Kolobov *et al.*, 2013; Kuznetsova *et al.*, 2013; Romanova *et al.*, 2010; Romanova *et al.*, 2012; Rosso *et al.*, 2013; Shakova *et al.*, 2013; Vetrile *et al.*, 2013; Vetrile *et al.*, 2016), however transgenic rat models for CNS disorders are yet to be extensively available through commercial

vendors. Meanwhile, easy availability of transgenic mouse models for Alzheimer's disease (Cattepoel *et al.*, 2011; Chauhan *et al.*, 2011; Xiao *et al.*, 2013) and multiple sclerosis (Mayo *et al.*, 2016) has led to a species-shift in intranasal studies to assess effects on pathology following intranasal antibody administration. Only one study (Chauhan *et al.*, 2015), so far, provides pharmacokinetics information on brain IgG concentrations following intranasal [^{125}I]-IgG administration for the wild-type C57BL6/J mouse, however these studies do not provide region-specific [^{125}I]-IgG concentrations (cortical versus sub-cortical, PVS vs parenchyma). We previously addressed these gaps for the rat (Kumar *et al.* 2018) and now provide similar insights for brain IgG biodistribution in the wild-type C57BL6 and double-transgenic APPswe/PS1dE9 (APP/PS1) mice following 30 min of intranasal administration.

We were also interested in characterizing antibody distribution following the use of nasal permeation enhancers for the pathogenic murine CNS using complementary radiometric and fluorescence-based methods. Matrix metalloproteinase-9 (MMP-9) is involved in the alteration of extracellular matrix proteins (Yabluchanskiy *et al.*, 2013) and modulation of tight junction proteins like claudin-1 (Hackel *et al.*, 2012) and has been demonstrated to be active in the olfactory mucosa (Wolburg *et al.*, 2008) to potentially allow for constant regeneration of the olfactory epithelial layer, as observed with MMP-2 (Gueye *et al.* 2011). We have recently demonstrated that intranasal pre-treatment with matrix metalloproteinase-9 (MMP-9) improves IgG distribution and perivascular access in a dose-dependent manner within 30 min of intranasal administration in rats (Lochhead *et al.*, 2015; Kumar *et al.*, 2018). Finally, we investigated the effects of chronic intranasal MMP-9 pretreatment in the olfactory behavior and pathology outcomes for chronic intranasal antibody administration, providing novel insights for intranasal antibody delivery to the murine CNS.

Materials and Methods

Ethics Approval

All animal experiments were conducted at the University of Wisconsin-Madison as per the *NIH Guide for the Care and Use of Laboratory Animals* (8^{th} edition, 2011) and were approved by the Institutional Animal Care and Use Committee regulations at the University of Wisconsin-Madison. Mice were housed under 12 h light/ 12 h dark cycle, climate-controlled conditions with *ad libitum* access to food and water. All experiments were terminal and efforts were made to ensure minimal pain and distress during anesthesia and cannulations.

Experimental design and statistical analysis

Our experimental approach to evaluate the effects of acute and chronic intranasal MMP-9 pretreatment in mice were derived from different aspects of several recent reports (Kumar *et al.* 2018; Lochhead *et al.*, 2015; Pizzo *et al.*, 2018; Hanson *et al.*, 2013; Witt *et al.*, 2009; Cattepoel *et al.*, 2011). The study can be divided into four research objectives - (i) quantitative estimation of IgG distribution in the CNS following acute (30 min) IgG administration, (ii) complementary qualitative assessment using low resolution autoradiography and *ex vivo* fluorescence imaging, (iii) behavioral assessment of olfactory differences following chronic (weekly) dosing, and (iv) *postmortem* examination of pathology using biochemical methods. For quantitative estimation of IgG distribution in the CNS, we employed [^{125}I]-labeled mouse IgG and optimized labeling and dissection methods mentioned in previous reports (Thorne *et al.*, 2004; Thorne *et al.*, 2008; Kumar *et al.*, 2018) for murine experiments. Equal-dose intraperitoneal and intranasal administrations were conducted to ascertain the maximum possible brain exposure using either routes. Low resolution autoradiography and *ex vivo* fluorescence images of brain section from intranasally administered radiolabeled IgG experiments highlighted the extent of IgG entry into the CNS. Behavioral assessment of olfaction allowed us to comment upon the tolerability of each excipient (MMP-9, physiological saline, 6E10) in a chronic paradigm. Finally, *postmortem* analysis was conducted to assess the biochemical (e.g. monomers, oligomers) and anatomical (olfactory bulbs, cortex, hippocampus etc) extent of target

engagement. All values were analyzed using SigmaPlot software (version 14.0, Systat Software) and depicted as mean ± standard error of mean (SEM). Significant differences between two groups was assessed using the *t-test* (for normal distribution) or Mann-Whitney rank sum test (for non-normal distribution). For three groups, significant differences were assessed using a one-way ANOVA and *post hoc* Dunn's t-test (for normal distribution) or a Kruskal-Wallis one-way ANOVA and *post hoc* Dunn's t-test. Values within 2 standard deviations of mean was considered to minimize variability in intranasal dosing and intracardiac perfusion. A threshold p values less than 0.05 was considered significant.

Animal preparation, transcardial puncture and euthanasia

Adult female C57BL/6 mice (18 - 28 g; 3 to 8-month-old; Strain #000644, Jackson Laboratory; Strain #044, Envigo/Harlan), and adult female APP/PS1 mice (n = 4; 25 - 35 g; 6 to 9-month-old; Strain #000644; MMRRC at Jackson Laboratory) were anesthetized with urethane (1.2 g/kg, i.p.) until surgical plane was reached. Animals were maintained at physiological body temperature (37°C) using a homeothermic monitoring system (Harvard Apparatus) until the start of transcardial perfusion. Here, an abdominal incision was made using sharp scissors and followed up with blunt scissors to widen the opening towards the thoracic cavity without organ injury. Skin and muscles were retracted, diaphragm was incised and connective tissue around the pericardium was separated using forceps (Fine Science Tools) A 26 GA 1.5 in needle (AgTech Inc.) connected to the peristaltic pump tubing was inserted into the left ventricle and the right atrium was snipped shortly after the start of saline perfusion.

Intranasally and intraperitoneally administered radiolabeled substances

Radioactive substances were held securely behind lead-impregnated acrylic shielding in a laminar fume hood and stored at 4°C in lead pigs. Experiments and labeling were performed after wearing appropriate personnel protective equipment (PPE) and lab area was routinely tested through wipe tests, charcoal breathing monitors, post-labeling thyroid scans and dosimetry. Non-targeted unlabeled ChromPure mouse IgG (Catalog #015-000-003; Jackson Immunoresearch) was radiolabeled with 1 mCi $Na^{125}I$ via the

Chizzonite indirect iodination method (Fraker *et al.*, 1978, Kumar *et al.*, 2018). Amicon ultrafiltration units (Catalog #UFC200324; Millipore-Sigma) were used to calculate average filtration recovery (approximately 74%). Unlabeled ChromPure mouse IgG was supplemented to ~1-2 mg/mL [^{125}I]-IgG solution for a minimum of 15-45 % or 2-8 µg of [^{125}I]-IgG in a 20 µg dose. Purity of [^{125}I]-IgG was estimated to be 97-99% by precipitating in 10% trichloroacetic acid.

Intranasally and intraperitoneally administered fluorescently labeled substances

Lyophilized non-targeted Alexa Fluor® 594 labeled ChromPure mouse IgG (AF594-IgG; Catalog #015-580-003; Jackson Immunoresearch) was reconstituted in 550 µL distilled water to obtain a 2 mg/mL solution. 500 µL of this reconstituted solution was passed through a 0.5 mL Amicon filter unit (Catalog #UFC501096; Millipore-Sigma) and centrifuged at 14,000g (30 min, 4°C) followed by a recovery spin (1000g x 2 min, 4°C). Final concentrations were 16-21 mg/mL that were used for same-day fluorescence experiments.

Intranasally and intraperitoneally administered unlabeled substances

Matrix metalloproteinase-9 (MMP-9): Lyophilized recombinant mouse MMP-9 (909-MM-010; R&D Systems, Minneapolis, MN, USA) was activated in-house as per the manufacturer's protocol. Briefly, MMP-9 was diluted to 0.1 mg/mL in the assay buffer (50 mM Tris, 10 mM CaCl2, 150 mM NaCl, 0.05% Brij-35 (w/v), pH 7.5) and incubated with p-aminophenylmercuric acetate (APMA) (Catalog #A-9563M; Millipore-Sigma) for 120 min at 37°C. Activated MMP-9 was filtered using Zeba™ spin desalting columns (Catalog #89882, Thermo Fisher Scientific) at 1000g x 2 min (4°C) and stored as 2 µL aliquots at -80°C until needed. Concentrated MMP-9 was diluted to 100 nM in saline (Catalog #00409-7101-02; Hospira/Pfizer) and maintained on ice on the day of experiment.

6E10: Ultra-LEAF™ purified anti-A*β*, 1-16 antibody (6E10; Catalog #803024; Biolegend) was stored at -

80°C until needed. On the day of chronic dosing experiments, 6E10 was concentrated using Amicon filtration units (Catalog #UFC501096; Millipore-Sigma) as per the manufacturer's protocol and diluted to 2.5 mg/mL by serial absorbance measurements at 260 nm (A260) using NanoDrop™ 2000 spectrophotometer (Thermo Fisher Scientific, Carlsbad, CA, USA) and maintained on ice until the dosing step. Diluted 6E10 was administered directly to intranasally treated animals while 8 µL of this solution was further diluted to 100 µL for intraperitoneal treatments.

Saline: Physiological saline (8 µL) was used as an excipient in control experiments.

Acute intranasal and intraperitoneal administration

Experiments were based on paradigms described in past reports (Thorne *et al.*, 2004; Lochhead *et al.*, 2015; Kumar *et al.*, 2018) with slight modifications. Briefly, animals were positioned with ventral side facing up and non-invasively administered 8 µL of saline or MMP-9 (4 drops of 2 µL each to alternate nares over 6 min with a gap of 2 min between two drops) followed by 8 µL of [^{125}I]-IgG or AF594-IgG solutions in the same manner. For radioactivity experiments, 2.5 mg/mL or 20 µg of [^{125}I]-IgG solutions were applied to nasal openings. For fluorescence-based experiments, ~16 mg/mL or ~0.1 mg AF594-IgG was applied following saline or MMP-9 pretreatment. Intraperitoneal administrations were performed at a final volume of 100 uL of [^{125}I]-IgG (20 µg, 0.2 mg/mL) using 28 GA 0.5 in BD U-100 Insulin Syringes (Thermo Fisher Scientific).

Chronic intranasal and intraperitoneal administration

Chronic experiments were performed similar to previous report (Hanson *et al.*, 2013) with modifications in volumes (2 µL drops). Treatment groups comprised of (i) intranasal saline (16 µL) administration, (ii) intranasal saline (8 µL) followed by intranasal 6E10 (20 µg, 8 µL) administration, (iii) intranasal MMP-9 (100 nM, 8 µL) followed by intranasal saline (8µL) administration, (iv) intranasal MMP-9 (100 nM, 8 µL) followed by intranasal 6E10 (20 µg, 8µL) administration, and (v) intraperitoneal 6E10 (20 µg, 100 µL)

injections. Animals were placed in individual disposable cages with water and enrichment (Catalog #M-BTM-C8E; Innovive) in a laminar hood for the dosing period. Animal were restrained by one investigator for 30s with the head parallel to the hood floor and the first dose (2 μL) was intranasally administration by another investigator. Animals were then unrestrained inside respective cages for 90s and restrained for 30 s for the next dose. These steps were repeated 8 times to intranasally administer a total volume of 16 μL. Intraperitoneal administrations were performed with one round of 30 s restrain and an injection of 6E10 (20 μg, 0.2 mg/mL) using 28 GA 0.5 in BD U-100 Insulin Syringes. At the end of each dosing cycle, animals were rewarded with sweetened multi-grain cereals (Froot Loops^{TM}; Kellogg Company) for 15 min before returning to clean housing cages. Dosing cycle were initiated in 4-month-old mice on a weekly basis for 14 weeks.

Olfactory behavioral testing & analysis

Olfactory testing paradigm was based on a previous study (Witt *et al.*, 2009). Briefly, 3-month-old animals were serially acclimated in 3 clean cages (18 in x 10 in x 8 in, 3 min per cage) followed by transferring into a test cage (same dimensions as above) containing a 0.2 μm Whatman paper (Z746215, Millipore-Sigma, St. Louis, MO, USA) with 0.5 mL of 0.5% cinnamon oil. Animal activity in the test cage was recorded using a Canon VIXIA HF11 camcorder (Ebling Library, University of Wisconsin-Madison). At the end of each dosing cycle, animals were rewarded with Froot Loops^{TM} for 15 min before returning to clean housing cages. This paradigm was performed one week prior to the start of chronic dosing (week 0) on a biweekly basis until the end of dosing period (week 14). Olfaction testing was performed one day prior to the next dosing cycle. Recordings were analyzed for (i) sniff time, and (ii) latency in olfactory, depicted as mean $\pm$ standard error (SEM).

Retro-orbital blood sampling

Blood (~50μL) was sampled at 10 min following acute intranasal or intraperitoneal [^{125}I]-IgG administration by the retro-orbital blood draw technique (Research Animal Resource Center, University of

Wisconsin-Madison). Blood collection was performed as a terminal procedure using 50 mm plastic hematocrit capillary tubes (Catalog #22-757-131; Thermo Fisher Scientific).

Euthanasia, perfusion-fixation, and tissue processing

Animals undergoing acute intranasal and intraperitoneal [^{125}I]-IgG administration experiments were intracardially exsanguinated by perfusion with 50 mL of 0.01M phosphate buffered saline at pH 7.4 (0.01M PBS) followed by 250 mL of 2.5% glutaraldehyde (Thermo Fisher Scientific) and 2% paraformaldehyde (Alfa Aesar) in 0.1 M phosphate buffer at pH 7.4 (2% PFA, pH 7.4), 30 min after administration. Animals subjected to acute intranasal AF594-IgG administration were exsanguinated by perfusion with 50 mL of 0.01M PBS followed by 250 mL of 4% PFA. Brain were extracted from the skull post-fixed for 30 min in 50 mL of fixative perfusate prior to organ dissection. Animals that underwent chronic intranasal administration were exsanguinated by perfusion with 50 mL of 0.01M PBS. Brains were extracted from the skull on a petri dish cooled on ice and sagittally dissected into two hemibrains using a mouse brain matrix (Harvard Apparatus). One hemibrain was post-fixed in 50 mL of 4% PFA (pH 7.4) overnight at 4°C while the other hemibrain was snap-frozen in dry-ice in a 2 mL Eppendorf tube (Thermo Fisher Scientific) and stored at -80°C until needed.

Microdissection of anteroventral and posteroventral cerebral vasculature

Post-fixed brains were placed on a petri dish and non-perfused areas due to intracardiac perfusion-fixation were noted. Cerebral vasculature was stained with India Ink for easier visibility under a zoom stereomicroscope (Olympus SZ61). Incisions were made using vannas scissors (Harvard Apparatus) at the left and right posterior communicating arteries and vessels were separately peeled off using blunt forceps (Harvard Apparatus) as described previously (Kumar *et al.*, 2018).

Microdissection of brain, spinal cord, and trigeminal nerves

Brain devoid of ventral cerebral arteries was sectioned into serial 1mm coronal brain section using coronal

mouse brain matrix (Harvard Apparatus) as suggested in past reports (Kumar *et al.*, 2018) (see Figure 1). Briefly, the olfactory bulb, midbrain, pons, medulla, cerebellum and cervical spinal cord (following dissection of 1 mm cervical region to prevent tracheal contamination) were dissected based on anatomical indicators (Franklin & Paxinos, 2008; Thorne, 2014). Anterior olfactory nucleus, olfactory tubercle, frontal cortex, motor cortex, primary somatosensory cortex, hippocampus and occipital cortex were dissected using a scalpel with #11 blade (Royal Tek), ant the amygdala was micropunched (Palkovitz, 1983) using a 15 GA stainless steel sample corer (Catalog #18035-01, Fine Science Tools) the help of the mouse brain atlas (Franklin & Paxinos, 2008) under the stereomicroscope (Olympus SZ61). Ophthalmic (V1) and maxillary (V2) branches of the trigeminal nerve innervating the nasal mucosa were horizontally cut between the anterior lacerated foramen and the pontomedullary nerve endings and peeled from the skull. Dissected tissues were placed in a checkered petri dish (see Figure 1) with traces of PBS to prevent tissue dehydration prior to placing the samples in tubes and subsequent measurements.

Radioactivity measurements

5 mL tubes were capped and pre-measured on a microbalance (XP26, Mettler Toledo) to tare the balance for the tube weight. Tissue samples were placed in these tubes immediately after the tare step and measured for net sample weight. For blood containing capillary tubes, capillary tubes were placed inside the 5 mL tubes for the pre-weighing step. Samples were placed in odd-numbered slots in a gamma-counting rack and radioactivity counts per min (CPM) were measured using a Packard Cobra II auto Gamma counter (Perkin Elmer). Tissue or blood [^{125}I]-IgG concentrations were determined using these values, specific activity of [^{125}I]-IgG solution on the day of experiment and tissue weight. Autoradiography was performed on 300 µm thick brain sections. Hemibrains were sectioned sagittally and coronally using a vibratome (Leica VT100S) and placed on Fisherbrand^{TM} microscope glass slides (Catalog #1255015, Thermo Fisher Scientific) mounted on a cardboard (8 in x 11 in). The cardboard was exposed to a pre-erased storage phosphor screen (GE Healthcare, Life Sciences) in the dark and placed inside a light-protected exposure (GE Healthcare, Life Sciences) cassette for 7 weeks. Screen was scanned on a Typhoon phosphor-imager (GE Healthcare,

Life Sciences) at 25 µm.

Tissue sectioning and long-term storage

Whole brains from acute fluorescence experiments and hemibrains from chronic experiments were post-fixed in 4% PFA overnight and sectioned at 100 µm on the vibratome (Leica VT100S) and refrigerated as free-floating sections in 0.01M PBS (pH 7.4) for one week. Sections were later transferred into a cryoprotectant solution (30% ethylene glycol, 30% glycerol, 30% sucrose, 0.1 M phosphate buffer (0.1M Na_2HPO_4, 0.1M NaH_2PO_4), 0.05% sodium azide) and placed at -20°C or -80°C for long-term storage.

Thioflavin-S staining

Selected free-floating brain sections were washed in 0.01 M PBS (pH 7.4) for 5 min and incubated in 0.125 mg/mL Thioflavin-S (Millipore-Sigma) in 50% ethanol (Thermo Fisher Scientific) for 60 min. This was followed by two washes in 50% ethanol, two washes in Milli-Q water (10 min per wash) and a 60-min incubation in 0.1M PBS (pH 7.4). Sections were then mounted on glass slides, air-dried overnight, coverslipped with Prolong Diamond Antifade Mountant (Catalog #P36965; Thermo Fisher Scientific), and cured overnight in the dark prior to storing at -20°C until needed.

Ex vivo fluorescence microscopy

Brain sections were imaged on an Olympus MVX10 microscope (Orca-flash 2.8 CMOS camera, Hamamatsu; Lumen Dynamics X-Cite 120Q illuminator, Chroma U-M49002XL filter set).

Fibrillar amyloid quantification

Quantification of Thioflavin-S positive amyloid aggregates was performed using Fiji (Schindelin *et al.*, 2012) based on a previously described strategy (Pizzo *et al.*, 2018). Briefly, brain section areas (mm^2) were calculated by threshold adjustment and outline selection using the wand tool. Outlined were adjusted to exclude non-cortical regions (striatum, brainstem, thalamus etc). Thresholds were adjusted to ensure

minimal background autofluorescence (~33000) for sections across all animals for a given bregma level. Coronal sections were analyzed for Thioflavin-S counts per unit area per under the following categories (based on Franklin & Paxinos, 2008) – (i) 4.2 mm to 3.2 mm (± 0.5 mm; three sections per animal; olfactory bulbs or OB), (ii) 3.1 mm to 2.1 mm (± 0.5 mm; three sections per animal), (iii) 2.0 mm to bregma (± 0.5 mm; three sections per animal; lateral ventricle or LV). (iv) 0.1 mm to - 4.0 mm (± 0.5 mm; three sections per animal), and (v) -5.0 mm to -8.0 mm (± 0.5 mm; three sections per animal; cerebellum or CBM). For category (ii), outlines were trimmed above and below the rhinal fissue to measure dorsal (frontal cortex or FC) and ventral counts respectively (anterior olfactory nucleus or AON); for category (iv), outlines were trimmed above and below the corpus callosum to measure lateral (cortical or CTX) and medial (hippocampal or HIPP) counts respectively. Intensity values above the threshold were counted with the 'Analyzed Particle' plugin with no changes to singularity. All plugins and commands were implemented using the macros files prepared for Pizzo *et al.*, 2018.

Brain homogenization, protein extraction and estimation

Brain homogenization and protein extraction procedures were curated from several past reports (Lesne *et al.*, 2006; Liu *et al.* 2015; Peng *et al.*, 2014; Shankar *et al.*, 2008; Biolegend LEGEND MAX™ ELISA technical datasheet). Briefly, snap-frozen hemibrains were thawed on a petridish pre-cooled on ice (0-4 °C). Cerebellum and brainstem were dissected out from the hemibrain and the remaining tissue was weighed (Mettler Toledo) and immediately added to 5 volumes of lysis buffer (i.e. 100 µg brain tissue in 500 µL buffer) in a pre-cooled 2 mL low-retention microcentrifuge tube (Thermo Fisher Scientific). Lysis buffer (pH 7.6) comprised of 50 mM Tris-HCl, 150 mM NaCl, 1 mM AEBSF, 5 mM EDTA and cOmplete protease inhibitor tablets (1 tablet per 10 mL buffer; Roche/Millipore-Sigma). Samples were homogenized using a motorized Kimble pellet pestle (Thermo Fisher Scientific) at 8 strokes/min. Homogenate was further disintegrated several times with a 1 mL pipette over 1 min until even consistency was achieved. Tubes were nutated on a rocker overnight at 4°C to enhance cell lysis. Next, homogenates were centrifuged at 16,000g (4°C, 90 min) and supernatant was extracted and stored at -20°C as soluble protein fraction (50-100 µL

aliquots). Pellets were washed with 250 µL lysis buffer three times, centrifuged at 16,000g (4°C, 30 min) and supernatants were discarded to remove residual soluble protein content. Pellets were then transferred into a fresh 2 mL low-binding microcentrifuge tube containing lysis buffer with 0.6 % sodium dodecyl sulphate (SDS) at room temperature. Samples were resuspended in the new solution (8 strokes/min, 2 min) followed by nutating on a rocker for 3-4 h at room temperature. Resuspended homogenate was then centrifuged at 16,000g (4°C, 90 min). Pellets were discarded and supernatants were collected and stored at -20°C as detergent-soluble fraction (50-100 µL aliquots). Protein concentration was measured by bicinchoninic acid method (Pierce).

Monomeric Aβ estimation via enzyme-linked immunosorbent assay (ELISA)

Aβ40, and Aβ42 protein levels in the extracted soluble and detergent-soluble protein fractions were measured using LEGEND MAX™ β-Amyloid ELISA kits (formerly BetaMark™ β-Amyloid x-42 ELISA kits (TMB)) following the manufacturer's instructions. This kit was selected based on past reports (Thakker *et al.*, 2009) and minimal cross-reactivity of pre-coated capture antibodies with other Aβ species. Samples were run in duplicates for each brain sample at 1:5, 1:10 or 1:20 dilutions to evaluate concentration within the standard curve range. Values have been reported as mean $\pm$ standard error (SEM).

Oligomeric Aβ estimation via western blots & semi-quantitative analysis

Soluble Aβ oligomeric levels were semi-quantitatively assessed by western blots using the NuPAGE system (Thermo Fisher Scientific) (Peng *et al.*, 2014). Briefly, 50 µg of total protein was mixed with, 4x NuPAGE lithium dodecyl sulphate (LDS) sample buffer, and 10x NuPAGE sample reducing agent (500 mM dithiothreitol) and further diluted to a 25µL final volume (1x LDS buffer, 50 mM dithiothreitol) in a 0.5 mL Eppendorf™ microcentrifuge tube (Thermo Fisher Scientific) by gentle mixing with a pipette. Contents were then heated on a dry bath (95°C, 10 min) and cooled to room temperature (20 min) prior to loading into wells on a PAGE 4-12% Bis-Tris gel (1 mm x 10 wells). Samples were run with NuPAGE 2-(N-morpholino) ethanesulfonic acid (MES) running buffer (50 mM MES, 50 mM Tris base, 0.1% SDS, 1 mM

EDTA, pH 7.3) at a constant voltage of 120 V from run start to mid-run and 90 V from mid-run to end of run. 10 µL Precision Plus Protein™ Dual Xtra prestained protein standards (Catalog #1610377; Biorad) was used as a molecular ladder. Protein was transferred from gels to nitrocellulose membrane using the iBlot™ dry blotting system (P1, 25 V, 7 min; Thermo Fisher Scientific) as per the manufacturer's protocol. Membranes were trimmed and placed in disposable plastic bags with 0.01M PBS and incubated for 20 min at a 95-97°C water bath for antigen retrieval. Membranes were then cooled to room temperature over 40 min in the same solution to maintain proteins in unfolded state. Next, membranes were incubated in 5% dry milk & 0.1% Tween-20 (Millipore-Sigma) dissolved in 0.01M PBS at pH 7.4 (blocking buffer) for 1 h, followed by overnight incubation with mouse Alexa Fluor™ 488-6E10 (Catalog #AF488-6E10; Biolegend; 1:500 dilution) and unlabeled donkey-anti-mouse glyceraldehyde-3-phosphate dehydrogenase (GAPDH; Catalog #AF5718; R&D Systems; 1:500 dilution) in blocking buffer at 4°C. This was followed by three washes of 0.01M PBS with 0.1% Tween-20 (PBST) followed by a secondary antibody incubation with donkey-anti-goat Alexa Fluor™ 594 IgG (AF594-IgG; Life Technologies/Thermo Fisher Scientific; 1:500 dilution) in blocking buffer for 1 h at room temperature. Membranes were washed with two more PBST washes followed by two PBS washes. Membranes were scanned on a Typhoon phosphor-imager system (GE Healthcare, Life Sciences) simultaneously for AF488-6E10 and AF594-IgG at normal sensitivity and 25 µm resolution. Membrane images were later processed using Fiji (Schindelin *et al.*, 2012) and semi-quantitative comparison of gel lanes across different membranes was performed using the Gel Analyzer plugin tutorials (Miller, 2010).

Results

Acute [^{125}I]-IgG biodistribution following intranasal and intraperitoneal administration

Emerging evidence suggests that intranasally administered large macromolecules can potentially access the CNS via systemic circulation through passive diffusion and entry across the BBB and BCSFBs, or through perineural channels, perivascular spaces or lymphatic routes in the nasal mucosa (Aspelund *et al.*, 2015;

Kumar *et al.* 2016; Kumar *et al.* 2018; Lochhead *et al*., 2015; Pizzo *et al.* 2018; Thorne *et al*., 2004; Thorne *et al*., 2008). We thus adapted previously described experimental paradigms for investigating intranasal delivery to the murine CNS (Thorne *et al*., 2004; Lochhead *et al*., 2015; Kumar *et al.* 2018; Hanson *et al.*, 2013). Modifications in our strategy included modifications in the dosing volume (4 x 2 µL drops for mice compared to 4 x 6-12 µL drops for rats), blood sampling method (retro-orbital blood draw in mice compared to abdominal aortic blood draw in rats), and perfusion techniques (transcardial perfusion using 26 GA needle compared to abdominal aortic cannulation used in rats). To confirm whether this strategy was optimal in mice, we performed equal-dose intranasal and intraperitoneal administrations with [^{125}I]-IgG in mice. These experiments provided us with a measure for maximal [^{125}I]-IgG entry to the CNS following BBB/BCSFB entry (intraperitoneal route access pathways) to contrast access through perineural/perivascular/lymphatic pathways following intranasal delivery. We then compared tissue concentrations within 2 standard deviations of mean (2 SD data range) and 3 standard deviations of mean (3 SD data range) to account for differences due to inter-animal variability and transcardial perfusion. Tables 1 and 2 summarize this information from acute (30 minute) biodistribution in the brain, vasculature, nervous system, lymph nodes and peripheral organs.

Similar blood [^{125}I]-IgG levels post equal-dose intranasal and intraperitoneal administration

[^{125}I]-IgG blood concentrations provided in Tables 1 and 2 were not significantly different for the two routes of administration in C57BL/6J mice, or in APPswe/PS1dE9 mice following intranasal administration with saline or MMP-9 pretreatment at 10 minutes following the first intranasal dose/bolus intraperitoneal injection. These values suggest that systemic exposure of [^{125}I]-IgG does not vary with the delivery strategy at 10 min following [^{125}I]-IgG administration.

Intranasally applied [^{125}I]-IgG enters the murine CNS through olfactory pathways

Following 30 min of exposure, animals were exsanguinated by saline (PBS) perfusion followed by a

mixture of aldehyde fixatives (2.5% glutaraldehyde + 2% PFA). Tissues (brain, lymph nodes, peripheral organs, nerves) were then extracted and microdissected to analyze [^{125}I]-IgG counts via gamma counting. Gamma counting results indicated significantly higher [^{125}I]-IgG concentrations in the olfactory bulb for intranasally applied [^{125}I]-IgG following saline (~22-fold higher for C57BL/6 mice, ~10-fold higher for APPswe/PS1dE9 mice) or MMP-9 pretreatment (~12-fold higher for C57Bl/6 mice, ~26-fold higher for APPswe/PS1dE9 mice) compared to intraperitoneal equal dose administration within the 3 SD data range (Table 1). These values continued to be significantly high for intranasally applied [^{125}I]-IgG compared to intraperitoneal controls when values outside the 2 SD data range were excluded (saline pretreatment: ~7-fold higher for C57BL/6 mice, ~4-fold higher for APPswe/PS1dE9 mice; MMP-9 pretreatment: ~12-fold higher for C57BL/6 mice, ~7-fold higher for APPswe/PS1dE9 mice), indicating that high values were not an artifact of the perfusion technique. Interestingly, tissue concentrations from intranasal [^{125}I]-IgG administration experiments fluctuated extensively between 2 SD and 3 SD data range values compared to no changes in intraperitoneal [^{125}I]-IgG administration experiments. Hence, inter-animal variabilities were considerably high for intranasal administration in mice as per our experimental paradigm. Values associated with other brain regions did not show a statistical significance across the two treatment groups but an apparent trend for higher [^{125}I]-IgG levels was observed in the rostral regions, followed by the brainstem and the subcortical regions. This trend was consistently observed after including or excluding values beyond 2SD. Values associated with the trigeminal nerves were not significantly different between any intranasal experiment when compared to intraperitoneal IgG experiments (intranasal-to-intraperitoneal ratios < 1), indicating that brain distribution of [^{125}I]-IgG was largely through the olfactory nerve associated pathways. These pathways have been described previously in rats (Kumar *et al.*, 2018) and for other macromolecules smaller than IgG in rodents and macaques (Thorne *et al.*, 2004; Thorne *et al.*, 2008). Lastly, isolated cerebral blood vessels values were not sufficient from independent experiments (i.e. $N = 1$) to delineate potential access via perivascular pathways in these experiments.

MMP-9 significantly enhanced [^{125}I]-IgG levels in APPswe/PS1dE9 mice but not in C57BL/6J mice

Matrix metalloproteinase-9 (MMP-9) has been demonstrated to improve CNS delivery and distribution profiles for large macromolecules such as IgG (150 kDa, Kumar *et al.*, 2018) and enzymes such as chloramphenicol acetyltransferase (75 kDa, Appu *et al.*, 2016) in rats. Similar studies have not been conducted in mice models. Interestingly, intranasal [^{125}I]-IgG administration following mouse MMP-9 pretreatment in C57BL/6J mice indicated no significant enhancement in [^{125}I]-IgG across different brain regions, nervous tissues, lymphoid tissues and peripheral organs. Apparent trend for increased [^{125}I]-IgG concentrations was observed for isolated anterior and middle cerebral arteries (~2-fold increase), basilar and vertebral arteries (~1.6-fold increase), primary somatosensory cortex (~4-fold increase), amygdala (~1.6-fold increase), hippocampus and occipital cortex (~2-fold increase), midbrain (~1.5-fold increase) and pons (~2.5-fold increase) (Fig. 1A1). This trend was lost for multiple regions, except for the primary somatosensory cortex, anterior and middle cerebral arteries and the amygdala when the data range outside 2 standard deviations (2SD) of mean were excluded (Fig, 1A2). Further, apparent increase in [^{125}I]-IgG concentrations for these regions suggests that enhancement of [^{125}I]-IgG access was likely occurring through the CSF, but high inter-animal variability and lack of significance prevents further interpretations. In contrast, intranasal MMP-9 pretreatment in APPswe/PS1dE9 mice led to significantly higher [^{125}I]-IgG levels at the olfactory bulbs (~2.4-fold increase within the 3 SD data range, ~1.8-fold increase within the 2 SD data range, Table 1 and 2). Apparent increase in intranasal [^{125}I]-IgG concentrations was also noted at the frontal lobe and the hippocampus, with a ~1.5-fold increase for both regions (Table 1 & 2; Fig. 1B1 & 1B2). Excluding values outside the 2 SD data range led to a ~1-2-fold increase in [^{125}I]-IgG levels for several other regions such as the anterior olfactory nucleus, motor cortex, piriform cortex, amygdala, cerebellum, cervical spinal cord, and trigeminal nerves (statistically significant 2-fold increase). Peripheral tissues such as the deltoid muscle indicated significantly lower [^{125}I]-IgG levels but no differences were noted in the blood levels of [^{125}I]-IgG.

Apparent increase in [^{125}I]-IgG brain levels for APPswe/PS1dE9 mice

We next compared IgG distribution profiles between C57BL/6J and APPswe/PS1dE9 mice within a given treatment paradigm. APPswe/PS1dE9 mice are double transgenic mouse model on a C57BL6 background that consist of two mutations, a gain-of-function mutation in the amyloid precursor protein (APP) and a loss-of-function mutation in the presenilin-1 subunit of gamma secretase, that lead to elevated production of $A\beta_{42}$ peptides (Jankowksy *et al.*, 2004). Physiological changes as a result of these genetic alterations (compensatory changes) have not been evaluated for APPswe/PS1dE9 mice. Fig. 2 highlights these comparisons in terms of fold-change in [^{125}I]-IgG levels relative to C57BL/6J experiments. Briefly, [^{125}I]-IgG levels in APPswe/PS1dE9 mice were noted to be apparently higher than C57BL/6J mice across treatment groups and data range considerations (Fig. 2).

Autoradiography images support [^{125}I]-IgG delivery to the murine CNS via olfactory pathways

Next, we employed autoradiography phosphor screens to image brain sections from intranasal [^{125}I]-IgG experiments (representative images in Fig. 3). Autoradiography images indicate [^{125}I]-IgG distribution to be associated with the olfactory bulb and rostral cortical regions in the sagittal sections from C57BL/6J (Fig. 2A1) mice and APPswe/PS1dE9 mice (Fig. 2B1). Signal intensity from brain sections subjected to MMP-9 pretreatment was relatively high compared to saline controls at multiple instances (n = 3, C57BL/6J; n = 1, APPswePS1dE9).

Hence, autoradiography scans and gamma-counting analysis collectively suggested that (a) intranasal administration of [^{125}I]-IgG leads to a higher CNS exposure compared to intraperitoneal equal-dose [^{125}I]-IgG administration, and (b) matrix metalloproteinase-9 has the likelihood of enhancing enhanced [^{125}I]-IgG distribution at the rostral brain regions in C57BL/6J and APPswe/PS1dE9 mice. Phosphor imaging of coronal brain sections indicated similar profiles (e.g. Fig. 2C1, C57BL/6J mice) but relative levels between dorsal/ventral or rostral/caudal cortical regions, as well as the precise location of [^{125}I]-IgG in the cortical regions could not be evaluated at the current imaging resolution. As a result, we employed *ex vivo* macro

fluorescence microscopy and high-resolution laser scanning confocal microscopy on brain section that received fluorescently-labeled mouse IgG following saline/MMP-9 pretreatment.

Acute intranasal AF594-IgG delivery in mice following intranasal saline / MMP-9 pretreatment

Here, we administered ~0.1 mg Alexa Fluor™-594 labeled IgG (AF594-IgG) following saline or MMP-9 pretreatment to replicate our findings with radiolabeled IgG, and to characterize the precise anatomical compartments encompassing AF594-IgG 30 min following intranasal administration. Brain sections were imaged by low resolution stereotaxic fluorescence microscopy (Fig. 4, 5) as well as high-resolution laser scanning confocal microscopy (Fig. 6).

Intranasally applied AF54-IgG enters the meningeal and perivascular spaces in the murine CNS

Fig. 4 depicts representative images from intranasal experiments where AF594-IgG was applied following saline/MMP-9 pretreatment to the nares of C57BL/6J and APPSwe/PS1dE9 mice. The likelihood of signal visibility for these experiments followed the order: C57BL/6J (saline) < APPswe/PS1dE9 (saline) < C57BL/6J (MMP-9) < APPswe/PS1dE9 (MMP-9). Across all animals, AF594-IgG signal was largely localized at the cortical surface/meninges and within perivascular spaces of large blood vessels penetrating the brain parenchyma at several locations (e.g. midline, rhinal fissure, olfactory bulb, base of lateral ventricle). Further, a decrease in surface AF594-IgG signal along the neural axis (anterior to posterior) was observed in coronal sections across all treatments (Fig. 4). Sections were also stained with Thioflavin-S (a dye that intercalates within fibrillar structures of amyloid oligomers but not monomers) and imaged to identify AF594-IgG signal localizing within fibrillar beta-amyloid species from AF594-IgG signal (Fig. 5). Instances of juxtaposed perivascular AF594-IgG and Thioflavin-S profiles were observed at the cortical surface/leptomeningeal interface (Fig. 5A).

Imaging these locations in APPswe/PS1dE9 mice via laser scanning confocal microscopy (Fig. 4) provided

a high-resolution view of the anatomical compartments encompassing AF-594-IgG at these interfaces. First, fluorescently-labeled IgG at the cortical surface corresponded to abluminal, vascular profiles that were closely associated but not in colocalization with PECAM-1-immunoreactive endothelial cells (Fig. 6A). Similar profiles were frequently observed at the midline (Fig. 6B-D), and at the base of the ventricles (Fig, 6E). Proximity with vascular markers together with the absence of colocalization suggests that AF594-IgG signal was overlapping PECAM-1-positive endothelial cells, potentially within the perivascular spaces associated with these microvessels. Further, punctate profiles were visible in regions in close proximity to a brain-CSF interface (e.g.: frontal cortex (Fig. 4A) and septal nuclei (Fig. 4B)) specific to the Texas Red™ filter, indicating potential cellular uptake in APPswe/PS1dE9 mice.

Chronic (14-week) survival/efficacy study paradigm

We further launched a chronic survival/efficacy endpoint study in which 16-week-old (4-month-old) female APPswe/PS1De9 mice were subjected to one of the following treatments over 14 weeks (i.e. until week 30) – (i) intranasal saline (8 x 2 µL per drop, 2 min intervals, 14 min), (ii) intranasal saline (4 x 2 µL per drop, 2 min intervals, 6 min) followed by intranasal 6E10 (20 µg, 4 x 2 µL per drop, 2 min intervals, 6 min), (iii) intranasal MMP-9 (100 nM, 4 x 2 µL per drop, 2 min intervals, 6 min) followed by intranasal saline (4 x 2 µL per drop, 2 min intervals, 6 min), (iv) intranasal MMP-9 (100 nM, 4 x 2 µL per drop, 2 min, 6 min) followed by intranasal 6E10 (20 µg, 4 x 2 µL per drop, 2 min intervals, 6 min), and (v) intraperitoneal 6E10 (20 µg, 100 µL bolus injection, 30 s). All animals survived till the end of the procedure. We selected 6E10, a mouse IgG1 antibody specific to the N-terminus of Aβ (1-16 amino acids), due to multiple reports of *in vivo* activity following semi-chronic intranasal (Chauhan *et al.*, 2011) administration and acute intracerebroventricular administration (Thakker *et al.*, 2009). Animals were evaluated for (a) olfactory sensitivity over 14 weeks (once every two weeks), (b) fibrillar plaque accumulation based on Thioflavin-S profiles per mm^2 slice area, (c) monomeric Aβ accumulation, and (d) soluble oligomeric Aβ accumulation.

Chronic MMP-9 exposure led to reduction in olfactory sensitivity

During the course of repeated intranasal/intraperitoneal dosing, we performed olfactory behaviour testing based on paradigm described in Witt *et al.*, 2009 to evaluate the effects of repeated MMP-9 exposure at the nasal mucosa (results have been summarized in Table 3 and Fig. 7). Briefly, animals were exposed to a scent (0.1 % cinnamon oil) in a test cage and behavior was recorded over 180 seconds. Recordings were subsequently analyzed for total sniff time (time of active investigation within 5 mm distance from the source of scent) and the latency (delay in first instance of investigation from t = 0 min). One-way ANOVA on ranks analysis of reading across treatment groups indicated no significant differences in sniff time or latency periods in any given week, except for week 15 where MMP-9 treated animals had significantly higher sniff time readout than saline controls. Further, a gradual decrease in sniff time was noted across all treatment groups – this decrease in sniff time was not significant for intranasal saline, intranasal saline + 6E10, and intranasal MMP-9 + 6E10 treatment groups. A significant reduction in sniff time readouts was noted for intranasal MMP-9 treatment group at week 10 ($p = 0.013$), week 14 ($p = 0.036$), and week 15 ($p = 0.012$). A similar pattern was noted for intraperitoneal 6E10 treated animals at week 14 ($p = 0.055$) and week 15 ($p = 0.004$). These results indicate that decrease in olfactory sensitivity was not exclusively due to MMP-9 induced regeneration of nasal epithelia; these might also be a consequence of 6E10-amyloid aggregate engagement in non-MMP-9 treated animals. Latency changes in scent exploration was not significant across treatment groups, indicating that decrease in sniff time readouts was not due to gain or loss of interest in exploring cinnamon oil during the chronic dosing paradigm.

Chronic 6E10 exposure led to reduction in Thioflavin-S profiles along the olfactory pathways

Table 4 and Fig. 8 indicate Thioflavin-S intensity profile estimates above a certain threshold for background autofluorescence. Briefly, Thioflavin-S intensity profiles were outlined in hemibrain coronal sections and areas were estimated using Fiji plugin-incorporating macro files (Schindelin *et al.*, 2012; macro files adapted from Pizzo *et al.*, 2018). Intensity values (in pixels) were then normalized by average pixel per mm^2 at a given magnification to calculate profiles per mm^2 slices area. Regions of interest have also been

shown in Fig.5 as olfactory bulb (OB), dorsal to rhinal fissure (dRF), ventral to rhinal fissure (vRF), cerebral cortex proximal to the lateral ventricles (LV), cerebral cortex caudal to the anterior commissure (pCTX) hippocampus (HC), and cerebellum (CBM). It was interesting to note that a dose-dependent pattern was present across section levels in the following order of treatment groups: intranasal saline $\geq$ intranasal 6E10 $\geq$ intranasal MMP-9 + intranasal 6E10 $\geq$ intraperitoneal 6E10. Further, values were lower at the OB and CBM regions but reached a global maximum at the LV region. In particular, values for intraperitoneal 6E10 treated mice were lower than saline controls at the olfactory bulbs ($p < 0.001$, one-way ANOVA on ranks with Dunn's *post hoc* test) and the lateral ventricle regions ($p = 0.01$, one-way ANOVA on ranks with Dunn's *post hoc* test). MMP-9/6E10 treatment led to significant reduction in plaque counts at the dRF ($p = 0.01$, one-way ANOVA on ranks with Dunn's *post hoc* test) and vRF ($p = 0.02$, one-way ANOVA on ranks with Dunn's *post hoc* test) regions. Of note, cerebellar profiles were significantly higher than saline controls for all treatment groups, indicating a 'tropism' along the neural axis (i.e. higher target engagement along the rostral brain regions, lower effects in subcortical and caudal brain regions). Plaque reductions for intranasal 6E10 + saline treatment were non-significant compared to saline-treated animals in the mouse brain.

Biochemical analysis of brain homogenates: 6E10 likely engaged higher oligomers (~100 kDa)

Snap-frozen hemibrains were further homogenized and proteins were extracted based on solubility in Tris-buffered saline (TBS protein fraction) or TBS with 0.6% sodium dodecyl sulfate (TBS-SDS protein fraction). The strength of SDS solution (0.6%) has been suggested to give a complete extraction of Aβ insoluble pool during early-onset of pathology (< 12-month-old mice) without using acid-based extraction methods that are usually incompatible with SDS-PAGE and western blot analysis (Biolegend technical datasheet). ELISA analysis following for total Aβ species did not reveal any differences in total $A\beta_{x-40}$ and $A\beta_{x-42}$ pools across different treatment groups in the TBS and TBS-SDS protein fractions (Fig. 9A). These results suggest that reduced Thioflavin-S profiles were a consequence of rearrangement among different Aβ species due to 6E10 engagement. We then analyzed the TBS protein fraction using Western Blots to

determine the relative intensities of two bands encompassing the spread of Aβ aggregates – Aβ trimer at 12 kDa and soluble APP fragment and 24-mer oligomers at 100 kDa (Fig. 9B, C). Band intensities were analyzed using the 'Gel Analyze' plugin in Fiji (Schindelin *et al.*, 2011) normalized first with their respective loading controls and then with the 37 kDa ladder to allow cross-comparison of membranes. Here, relative intensities of Aβ trimer bands were not significantly different across treatment groups, as was indicated by ELISA analysis. Similar analyses for 100 kDa band intensities highlight the dose-dependent increase in sAPP levels in the following order: intranasal saline $\leq$ intranasal 6E10 $\leq$ intranasal MMP-9 + intranasal 6E10 $\leq$ intraperitoneal 6E10. Taken together, reduction in Thioflavin-S intensities and increase in sAPP levels suggest that 6E10 is likely resolving insoluble fibrillar aggregates into higher-order soluble oligomers in a dose-dependent manner.

Discussion

Major findings from this study can be summarized as follows: (a) acute intranasal and intraperitoneal [^{125}I]-IgG administration in mice at equal-dose resulted in similar blood [^{125}I]-IgG levels but ~5-10-fold higher brain [^{125}I]-IgG concentrations at the olfactory bulbs with intranasal delivery; (b) MMP-9 enhances intranasal [^{125}I]-IgG delivery to the murine CNS, although the extent of enhancement (~1-2-fold) is lower than previously reported values for rats (~5-fold increase at the olfactory bulbs; Kumar *et al.*, 2018); (c) olfactory nerve-associated pathways may be more relevant than trigeminal nerve pathways for intranasal targeting to the CNS in mice, based on non-significant changes in trigeminal nerve [^{125}I]-IgG levels following intranasal [^{125}I]-IgG administration and intraperitoneal [^{125}I]-IgG administration; (d) subtle physiological differences in transgenic APPswe/PS1dE9 and wild-type C57BL/6J mice may be responsible for improved [^{125}I]-IgG distribution in the CNS with and without intranasal MMP-9 pretreatment; (e) APPswe/PS1dE9 mice may experience significant changes in olfactory sensitivity (reduced sniff time) due to chronic MMP-9 exposure as well as chronic intraperitoneal injections, and (f) chronic intranasal administration of an Aβ N-terminus-targeting antibody in APPswe/PS1dE9 mice may lead to dose-

dependent resolution of fibrillar plaques into higher-order soluble oligomers.

Maximal [^{125}I]-IgG exposure at the olfactory bulb following [^{125}I]-IgG intranasal delivery has been consistent across treatment strategies and autoradiography studies, and has been evolutionarily conserved across species based previous reports in rats and macaques (Kumar *et al.* 2018; Lochhead *et al.*, 2015; Thorne *et al.*, 2004). In this study, we did not observe significant differences in [^{125}I]-IgG associated with the trigeminal nerves. One possible explanation for these findings could be due to the reduced thickness of dural layer lining the trigeminal nerve, based on the ease of cranial window surgical preparations in mice compared to rats (Shih *et al.*, 2012 We also characterized MMP-9 induced nasal permeation enhancement in two different mouse models – while intranasal MMP-9 pre-treatment did result in brain exposure increases in these mice, it did so at levels (~2-fold enhancement) less than previously reported in rats (Kumar *et al.*, 2018). One conclusion from these observations that merits further study is the possibility that there are important differences in MMP-9 substrate activity in the nasal mucosa between rats, mice, and possibly other species. Early morphometric estimates suggest that the surface area of the respiratory and olfactory nasal mucosae increase by 60-70% between 7 and 16 weeks of age in rats, while no changes in nasal volume or surface area occur beyond 7 weeks of age in mice (Gross *et al.*, 1982). It may therefore be possible that the re-epithelialization rates (i.e. turnover and production of new epithelium) in adult rats and mice may be quite different over these time frames such that other related mechanistic differences (e.g. the expression of tissue inhibitors of metalloproteinases) may significantly affect nasal tissue responses to exogenous MMP-9.

Interestingly, we observed subtle differences in [^{125}I]-IgG brain levels following intranasal [^{125}I]-IgG delivery to C57BL/6J and APPswe/PS1dE9 mice irrespective of pretreatment strategy (saline or MMP-9). Intranasally applied [^{125}I]-IgG had similar distribution profiles in C57BL/6J mice with MMP-9 pretreatment (i.e. the enhanced brain delivery paradigm) compared to that observed for APPswe/PS1dE9 mice with saline pretreatment (i.e. the non-enhanced delivery paradigm), suggesting that the wild-type mice had a

poorer / more highly variable IgG distribution that needed nasal permeation enhancement just to reach the baseline IgG distribution observed in APPswe/PS1dE9 mice. The reasons underlying these differences are unknown but they may be due in part to abnormalities in the olfactory epithelium (reduced thickness, cell counts, neuronal density) following amyloid deposition in AD-model animals (Yao *et al.*, 2017). Such epithelial abnormalities might have resulted in a higher extent of transport (e.g. enhanced diffusion through the nasal mucosa, higher transcytosis rates across the nasal mucosa, increased access to the lamina propria, and/or a higher degree of perivascular entry with a subsequently higher flux into the brain as the end result) in our 7-to-10-month old APPswe/PS1dE9 mice (pathology initiating at 3 months of age). Indeed, IgG levels measured within the major cerebral arteries (and their associated perivascular spaces) were greater than ~2-fold higher for transgenic mice when compared to wild-type saline-treated mice.

Once in the lamina propria, the antibody is likely taken up by complex pathways associated with the olfactory and trigeminal nerves that eventually reflect onto the meningeal layers in the murine CNS. Indeed, widespread meningeal signal was observed in mouse brain sections following intranasal delivery of fluorescently-labeled IgG (AF594-IgG). High-resolution confocal microscopy images suggest it to be perivascular access based on abluminal and non-colocalizing AF594-IgG profiles associated with PECAM-1 immunoreactivity. Colocalization of Thioflavin-S profiles and AF594-IgG profiles was observed for amyloid deposits surrounding large surface blood vessels penetrating the brain parenchyma. Investigating these differences in a CAA-specific model might offer greater insights into pathology reduction within perivascular spaces.

Olfactory behavior tests suggest altered sensitivity for MMP-9 treated and intraperitoneal 6E10 treatment groups over time; however, differences across treatment groups were not observed. Additionally, latency times were not significantly different across treatment groups. Thioflavin-S intensity profiles further suggested a trend for reduced fibrillar amyloid species in specific brain regions. Studies in PD/APP mice indicate that IgG2a isotypes targeting the N-terminus may offer better outcomes in terms of fibrillar plaque

resolution (Bussière *et al.*, 2004).

Lastly, as already alluded to above, chronic antibody exposure following intranasal or systemic administration at equal doses may not scale in the same manner across species. Allometric scaling of intranasal administration dosing for direct brain delivery is thought to be primarily a function of nasal cavity volume (Thorne. PhD Thesis. 2002; Thorne *et al.*, 2008) and this volume is expected to increase by about ~20-30 times between mice and humans. Intraperitoneal injections scale allometrically based on body weight with a much higher fold-increase expected (~3500-fold increase for a 70 kg human being compared to an adult mouse). While conducting intranasal studies in human subjects utilizing a ~20-30-fold higher dose (0.5 – 0.6 mg) of intranasally applied antibody might be considered a realistic treatment strategy in terms of cost and inventory management, sustaining a chronic study at a ~3500-fold higher dose (70 g) intraperitoneal antibody injection is not only out of feasibility but may lead to amyloid-related imaging abnormalities (ARIA) such as edema and higher incidences of hemorrhages (Thakker *et al.*, 2009; Sperling *et al.*, 2011). The possibility to achieve a realistic, non-invasive dosing regimen using the intranasal route of administration will further help in achieving desired efficacy endpoints in clinical studies, if properly validated.

References

Abbott NJ, Patabendige AA, Dolman DE, Yusof SR & Begley DJ (2010). Structure and function of the blood-brain barrier. *Neurobiol Dis* **1**: 13-25.

Appu AP, Arun P, Krishnan JKS, Moffett JR & Namboodiri AMA (2016). Rapid intranasal delivery of chloramphenicol acetyltransferase in the active form to different brain regions as a model for enzyme therapy in the CNS. *J Neurosci Methods* **259**: 129-134.

Asgari M, de Zélicourt D & Kurtcuoglu V (2016). Glymphatic solute transport does not require bulk flow. *Sci Rep* **6**: 38635.

Aspelund A, Antila S, Proulx ST, Karlsen TV, Karaman S, Detmar M, Wiig H & Alitalo K (2015). A dural lymphatic vascular system that drains brain interstitial fluid and macromolecules. *J Exp Med* **212(7)**: 991-9.

Bussière T, Bard F, Barbour R, Grajeda H, Guido T, Khan K, Schenk D, Games D, Seubert P & Buttini M (2004). Morphological characterization of Thioflavin-S-positive amyloid plaques in transgenic Alzheimer mice and effect of passive Abeta immunotherapy on their clearance. *Am J Pathol* **165(3)**: 987-995.

Cattepoel S, Hanenberg M, Kulic L & Nitsch RM (2011). Chronic intranasal treatment with an anti-Aβ (30-42) scFv antibody ameliorates amyloid pathology in a transgenic mouse model of Alzheimer's disease. *PLoS One* 2011 **6(4)**: e18296.

Chauhan NB, Davis F & Xiao C (2011). Wheat germ agglutinin enhanced cerebral uptake of anti-Aβ antibody after intranasal administration in 5XFAD mice. *Vaccine* **29(44)**: 7631-7637.

Chauhan MB & Chauhan NB (2015). Brain Uptake of Neurotherapeutics after Intranasal versus Intraperitoneal Delivery in Mice. *J Neurol Neurosurg* **2(1). pii**: 009.

Cooper PR, Ciambrone GJ, Kliwinski CM, Maze E, Johnson L, Li Q, Feng Y & Hornby PJ (2013). Efflux of monoclonal antibodies from rat brain by neonatal Fc receptor, FcRn. *Brain Res* **1534**: 13-21.

Davydova TV, Gruden MA, Kudrin VS, Narkevich VB, Vetrile LA, Zakharova IA & Sewell RDE (2019). Effect of Antibodies to Glutamate on Age-Related Memory Changes in C57BL/6 Mice. *Bull Exp Biol Med*. **166(3)**: 326-329.

Dhuria SV, Hanson LR & Frey WH 2nd (2010). Intranasal delivery to the central nervous system: mechanisms and experimental considerations. *J Pharm Sci* **99(4)**: 1654-1673.

Eisenried A1, Meidahl ACN, Klukinov M, Tzabazis AZ, Sabbadini RA, Clark JD & Yeomans DC (2017). Nervous system delivery of antilysophosphatidic acid antibody by nasal application attenuates mechanical allodynia after traumatic brain injury in rats. *Pain* **158(11):** 2181-2188.

Engelhardt B & Sorokin L (2009). Blood-brain and the blood-cerebrospinal fluid barriers: function and dysfunction. *Semin Immunopathol* **31(4)**: 497-511.

Fraker PJ & Speck JC Jr (1978). Protein and cell membrane iodinations with a sparingly soluble chloroamide, 1,3,4,6-tetrachloro-3a,6a-diphrenylglycoluril. *Biochem Biophys Res Commun* **80(4)**: 849-857.

Franklin K & Paxinos G (2008). The Mouse Brain in Stereotaxic Coordinates. 3rd edition. Elsevier.

Gorbatov VY, Trekova NA, Fomina VG & Davydova TV (2010). Antiamnestic effects of antibodies to glutamate in experimental Alzheimer's disease. *Bull Exp Biol Med* **150(1)**: 23-25.

Gross EA, Swenberg JA, Fields S & Popp JA (1982). Comparative morphometry of the nasal cavity in rats and mice. *J Anat* **135(Pt 1):** 83-88.

Gueye Y, Ferhat L, Sbai O, Bianco J, Ould-Yahoui A, Bernard A, Charrat E, Chauvin JP, Risso JJ, Féron F, Rivera S, & Khrestchatisky M (2011). Trafficking and secretion of matrix metalloproteinase-2 in olfactory ensheathing glial cells: A role in cell migration? *Glia* **59(5)**: 750-770.

Hammarlund-Udenaes M (2014). Pharmacokinetic Concepts in Brain Drug Delivery, in Drug Delivery to the Brain Physiological Concepts, Methodologies and Approaches. Hammarlund-Udenaes M, de Lange E & Thorne RG (Eds.). 127-161. Springer.

Hanson LR, Fine JM, Svitak AL & Faltesek KA (2013). Intranasal administration of CNS therapeutics to awake mice. *J Vis Exp* 74.

Witt RM, Galligan MM, Despinoy JR & Segal R (2009). Olfactory behavioral testing in the adult mouse. *J Vis Exp* 23. pii: 949.

Hackel D1, Krug SM, Sauer RS, Mousa SA, Böcker A, Pflücke D, Wrede EJ, Kistner K, Hoffmann T, Niedermirtl B, Sommer C, Bloch L, Huber O, Blasig IE, Amasheh S, Reeh PW, Fromm M, Brack A, Rittner HL (2012). Transient opening of the perineurial barrier for analgesic drug delivery. *Proc Natl Acad Sci U S A* **109(29)**: E2018-27.

Illum L (2012). Nasal drug delivery - recent developments and future prospects. *J Control Release* **161(2)**: 254-263.

Jankowsky JL, Fadale DJ, Anderson J, Xu GM, Gonzales V, Jenkins NA, Copeland NG, Lee MK, Younkin LH, Wagner SL, Younkin SG & Borchelt DR (2004). Mutant presenilins specifically elevate the levels of the 42 residue beta-amyloid peptide in vivo: evidence for augmentation of a 42-specific gamma secretase. *Hum Mol Genet* **13(2):**159-170.

Kolobov VV, Davydova TV, Zakharova IA, Gorbatov VIu & Fomina VG (2012). [Repressional effects of the glutamate antibodies on expression of Dffb gene in the brain of rats with experimental Alzheimer's disease]. [Article in Russian] *Mol Biol (Mosk)* **46(5)**: 757-765.

Kolobov VV, Zakharova IA, Fomina VG, Gorbatov VY, Davydova TV (2013). Effect of antibodies to glutamate on caspase-3 activity in brain structures of rats with experimental Alzheimer's disease. *Bull Exp Biol Med* **154(4)**: 425-427.

Kumar NN, Pizzo ME, Nehra G, Wilken-Resman B, Boroumand S & Thorne RG (2018). Passive Immunotherapies for Central Nervous System Disorders: Current Delivery Challenges and New Approaches. *Bioconjug Chem* **29(12)**: 2937-3966.

Kumar NN, Lochhead JJ, Pizzo ME, Nehra G, Boroumand S, Greene G & Thorne RG (2018). Delivery of immunoglobulin G antibodies to the rat nervous system following intranasal administration: Distribution, dose-response, and mechanisms of delivery. *J Control Release* **286**: 467-484.

Kuznetsova LV, Karpova MN, Vetrile LA & Klishina NY (2013). Effects of antibodies to glutamate on focal penicillin-induced epileptic activity. *Bull Exp Biol Med* **155(5)**: 609-611.

Kumar NN, Gautam M, Lochhead JJ, Wolak DJ, Ithapu V, Singh V & Thorne RG (2016). Relative vascular permeability and vascularity across different regions of the rat nasal mucosa: implications for nasal physiology and drug delivery. *Sci Rep* **6**:31732.

Lochhead JJ & Thorne RG (2012). Intranasal delivery of biologics to the central nervous system. *Adv Drug Deliv Rev* **64(7)**: 614-628.

Lochhead JJ & Thorne RG (2014). Intranasal Drug Delivery to the Brain, in Drug Delivery to the Brain Physiological Concepts, Methodologies and Approaches. Hammarlund-Udenaes M, de Lange E & Thorne RG (Eds.). 401-431. Springer.

Mayo L, Cunha AP, Madi A, Beynon V, Yang Z, Alvarez JI, Prat A, Sobel RA, Kobzik L, Lassmann H, Quintana FJ & Weiner HL (2016). IL-10-dependent Tr1 cells attenuate astrocyte activation and ameliorate chronic central nervous system inflammation. *Brain* **139(Pt 7)**: 1939-1957.

Miller L (2010). Analyzing gels and western blots with ImageJ. https://lukemiller.org/index.php/2010/11/analyzing-gels-and-western-blots-with-image-j/ (accessed on Aug 3, 2019)

Nellan A, McCully CML, Cruz Garcia R, Jayaprakash N, Widemann BC, Lee DW & Warren KE (2018). Improved CNS exposure to tocilizumab after cerebrospinal fluid compared to intravenous administration in rhesus macaques. *Blood* **132(6)**: 662-666.

Paxinos G & Watson C (2007). The Rat Brain in Stereotaxic Coordinates. 6th edition. Elsevier.

Pizzo ME, Wolak DJ, Kumar NN, Brunette E, Brunnquell CL, Hannocks MJ, Abbott NJ, Meyerand ME, Sorokin L, Stanimirovic DB & Thorne RG (2018). Intrathecal antibody distribution in the rat brain: surface diffusion, perivascular transport and osmotic enhancement of delivery. *J Physiol* **596(3)**: 445-475.

Romanova GA, Shakova FM, Gorbatov VY, Kvashennikova YN & Davydova TV (2010). Effect of antibodies to glutamate on retention of conditioned passive avoidance response in rats with ischemic injury of the prefrontal cortex. *Bull Exp Biol Med* **149(3)**: 289-92.

Romanova GA, Kvashennikova YN, Shakova FM & Davydova TV (2012). Effect of antibodies to glutamate on the content of neurotransmitter amino acids in brain structures of rats with ischemic damage to the prefrontal cortex. *Bull Exp Biol Med* **153(1):** 13-15.

Rosso P, Moreno S, Fracassi A, Rocco ML & Aloe L (2015). Nerve growth factor and autophagy: effect of nasal anti-NGF-antibodies administration on Ambra1 and Beclin-1 expression in rat brain. *Growth Factors*. **33(5-6)**: 401-409.

Schindelin J, Arganda-Carreras I, Frise E, Kaynig V, Longair M, Pietzsch T, Preibisch S, Rueden C, Saalfeld S, Schmid B, Tinevez JY, White DJ, Hartenstein V, Eliceiri K, Tomancak P & Cardona A (2012). Fiji: an open-source platform for biological-image analysis. *Nat Methods*. **9(7):** 676-682.

Shakova FM, Kodt P, Kudrin VS, Davydova TV & Romanova GA (2013). [The saving role of glutamate antibodies with the acute ischemic damage of the rat brain prefrontal cortex]. *Patol Fiziol Eksp Ter* **3**: 19-22.

Shih AY, Driscoll JD, Drew PJ, Nishimura N, Schaffer CB & Kleinfeld D (2012). Two-photon microscopy as a tool to study blood flow and neurovascular coupling in the rodent brain. *J Cereb Blood Flow Metab* **32(7)**: 1277-1309

Sperling RA, Jack CR Jr, Black SE, Frosch MP, Greenberg SM, Hyman BT, Scheltens P, Carrillo MC, Thies W, Bednar MM, Black RS, Brashear HR, Grundman M, Siemers ER, Feldman HH & Schindler RJ (2011). Amyloid-related imaging abnormalities in amyloid-modifying therapeutic trials: recommendations from the Alzheimer's Association Research Roundtable Workgroup. *Alzheimers Dement* **7(4)**: 367-385.

Thakker DR, Weatherspoon MR, Harrison J, Keene TE, Lane DS, Kaemmerer WF, Stewart GR & Shafer LL (2009). Intracerebroventricular amyloid-beta antibodies reduce cerebral amyloid angiopathy and associated micro-hemorrhages in aged Tg2576 mice. *Proc Natl Acad Sci U S A*. **106(11)**: 4501-4506.

Thorne RG, Pronk GJ, Padmanabhan V & Frey WH 2nd (2004). Delivery of insulin-like growth factor-I to the rat brain and spinal cord along olfactory and trigeminal pathways following intranasal administration. *Neuroscience* **127(2)**: 481-496.

Thorne RG, Hanson LR, Ross TM, Tung D & Frey WH 2nd (2008). Delivery of interferon-beta to the monkey nervous system following intranasal administration. *Neuroscience* **152(3)**: 785-797.

Vetrile LA, Zakharova IA, Kudrin VS & Klodt PM (2013). Effects of antiglutamate antibodies on the development of stress response and neurotransmitter content in the hippocampus and hypothalamus of rats with different behavioral activity. 2013 *Bull Exp Biol Med* **155(3)**: 318-323.

Vetrile LA, Zakharova IA, Kudrin VS & Klodt PM (2016). [Effect of intranasally administered glutamate antibodies on the content of excitatory and inhibitory amino acids in the rat`s hippocampus and hypothalamus at the combined stress exposure] [Article in Russian]. *Patol Fiziol Eksp Ter* **(1)**: 4-10.

Wolburg H, Wolburg-Buchholz K, Sam H, Horvát S, Deli MA & Mack AF (2008). Epithelial and endothelial barriers in the olfactory region of the nasal cavity of the rat. *Histochem Cell Biol* **130(1)**: 127-140.

Xiao C, Davis FJ, Chauhan BC, Viola KL, Lacor PN, Velasco PT, Klein WL & Chauhan NB (2013). Brain transit and ameliorative effects of intranasally delivered anti-amyloid-β oligomer antibody in 5XFAD mice. *J Alzheimers Dis* **35(4)**: 777-788.

Yabluchanskiy A, Ma Y, Iyer RP, Hall ME & Lindsey ML (2013). Matrix metalloproteinase-9: Many shades of function in cardiovascular disease. *Physiology (Bethesda)*. **28(6)**: 391-403.

Yao ZG, Hua F, Zhang HZ, Li YY & Qin YJ (2017). Olfactory dysfunction in the APP/PS1 transgenic mouse model of Alzheimer's disease: Morphological evaluations from the nose to the brain. *Neuropathology* **37(6)**: 485-494.

Table 1. Tissue concentrations[a] (pM) of [^{125}I]-IgG following intranasal or intraperitoneal administration (3 SD data range)

	Intranasal IgG (saline, WT)	**Intranasal IgG (MMP-9, WT)**	**Intraperitoneal IgG (WT)**	**Intranasal IgG (saline, AD)**	**Intranasal IgG (MMP-9, AD)**
Blood (10 min)	462.65 ± 124.46 (10)	339.64 ± 88.66 (9)	302 + 74.11 (3)	238.78 ± 37.32 (10)	413.57 ± 78.22 (12)
ACA & MCA[b]	35.22 ± 8.95 (5)	86.18 ± 3.73 (5)		362.32 ± 182.07 (7)	117.09 ± 97.65 (7)
Bas. and vert. arteries[c]	37.67 ± 14.99 (7)	62.69 ± 28.23 (5)		119.98 ± 32.34 (7)[g]	53.18 ± 21.30 (9)
Olfactory bulb	95.11 ± 28.85 (10)[h]	55.85 ± 18.62 (9)[i]	4.31 ± 1.12 (6)	46.29 ± 9.93 (10)[j]	111.98 ± 32.10 (12)[k]
Ant. olfactory nucleus[d]	11.86 ± 2.02 (10)	9.79 ± 2.12 (8)	3.27 ± 1.71 (4)	22.99 ± 4.72 (9)	23.19 ± 3.85 (9)[l,m]
Frontal cortex	21.01 ± 10.72 (10)	13.42 ± 2.94 (7)		19.30 ± 7.31 (10)	29.80 ± 11.71 (13)
Olfactory tubercle	22.15 ± 5.93 (10)	7.81 ± 2.73 (6)	9.84 ± 4.01 (3)	11.72 ± 4.44 (9)	7.95 ± 2.62 (12)
Motor cortex	12.44 ± 3.03 (10)	11.11 ± 4.32 (9)	3.89 ± 0.29 (3)	23.08 ± 11.77 (10)	11.02 ± 2.28 (13)
Somatosensory cortex[e]	8.01 ± 2.44 (8)	32.22 ± 22.07 (6)	4.72 ± 1.27 (3)	21.63 ± 11.43 (9)	14.15 ± 5.55 (12)
Piriform cortex	12.10 ± 4.33 (10)	14.63 ± 7.07 (8)		11.61 ± 6.15 (8)	7.64 ± 1.63 (13)
Parietal cortex	11.76 ± 3.57 (9)	7.68 ± 2.86 (7)		11.32 ± 4.20 (8)	7.64 ± 1.63 (13)
Caudoputamen	5.28 ± 1.24 (10)[h]	4.30 ± 1.11 (8)	18.38 ± 8.12 (3)	8.61 ± 2.69 (10)	7.67 ± 1.53 (13)
Amygdala	17.00 ± 7.89 (8)	24.51 ± 14.01 (6)	6.85 ± 2.08 (3)	31.48 ± 17.56 (7)	27.36 ± 9.69 (10)
Hippocampus	4.82 ± 0.48 (10)	9.19 ± 6.12 (9)	6.85 ± 1.86 (3)	4.48 ± 0.68 (10)	10.31 ± 2.53 (13)
Occipital cortex	7.74 ± 2.37 (10)	13.83 ± 8.68 (9)	5.94 ± 1.32 (3)	13.54 ± 3.75 (10)	6.37 ± 1.01 (12)
Medulla	19.20 ± 7.83 (9)	10.45 ± 6.22 (9)	7.51 ± 2.05 (3)	20.11 ± 11.85 (9)	10.26 ± 4.04 (11)
Pons	9.35 ± 1.85 (10)	23.22 ± 18.39 (9)	6.64 ± 2.60 (3)	19.94 ± 13.22 (9)	7.52 ± 1.34 (13)

Midbrain	7.98 ± 1.50 (10)	11.65 ± 6.22 (9)	6.01 ± 1.05 (3)	7.34 ± 1.19 (10)	6.11 ± 0.68 (11)
Cerebellum	9.44 ± 3.26 (10)	9.50 ± 2.83 (9)	6.61 ± 1.08 (3)	21.02 ± 8.44 (10)	7.07 ± 0.95 (13)
Cervical spinal cord	24.54 ± 13.56 (9)	20.35 ± 4.85 (9)	13.62 ± 3.41 (3)	25.07 ± 8.94 (10)	15.88 ± 3.42 (10)
Trigeminal nerves	215.55 ± 46.08 (10)	162.34 ± 47.41 (7)	325.20 ± 109.60 (3)	256.54 ± 111.28 (10)	158.06 ± 51.12 (10)
Optic nerve	46.77 ± 11.93 (8)	155.56 ± 97.33 (6)		46.44 ± 35.30 (7)	108.88 ± 47.07 (10)
Pituitary gland	14.38 ± 6.01 (6)	363.12 ± 269.40 (6)		47.67 ± 24.47 (7)	85.63 ± 32.12 (8)
Lung	93.84 ± 45.22 (9)	42.87 ± 25.79 (8)	48.20 ± 22.48 (3)	52.48 ± 23.97 (10)	102.21 ± 46.88 (13)
Heart	46.44 ± 15.90 (10)	49.89 ± 26.01 (9)	155.56 ± 104.60 (3)	34.69 ± 14.40 (10)	21.73 ± 5.28 (13)
Kidney	54.11 ± 18.34 (10)	76.52 ± 23.22 (9)	115.22 ± 1.12 (3)	57.44 ± 8.18 (10)	88.51 ± 19.60 (13)
Liver	62.73 ± 16.62 (10)	39.84 ± 7.03 (9)	78.76 ± 21.61 (3)	56.11 ± 8.55 (10)	47.54 ± 5.80 (13)
Deltoid muscle	64.73 ± 11.89 (10)	55.69 ± 32.79 (9)	42.56 ± 8.71 (3)	22.17 ± 5.11 (10)[n]	15.01 ± 3.32 (13)[o]
Axillary lymph nodes	51.32 ± 11.45 (10)	69.94 ± 14.76 (5)	194.92 ± 151.91 (3)	120.94 ± 97.04 (10)	43.73 ± 9.45 (12)
Deep cervical LN[f]	90.91 ± 26.49 (10)	1799.76 ± 932.02 (9)		839.61 ± 266.82 (9)	274.57 ± 58.43 (12)
Superficial cervical LN	754.95 ± 326.00 (10)	339.64 ± 88.66 (9)[p]	602.70 ± 389.77 (3)	198.86 ± 31.39 (10)	245.03 ± 185.12 (13)[q]

Blood, brain, nervous system, peripheral organ, and lymph node radiolabel concentrations following intranasal or intraperitoneal administration of [^{125}I]-mouse IgG at a low tracer dose (20 µg). Intranasal administrations were performed over 8 min (4 x 2 µL per drop) following saline pre-administration (4 x 2 µL per drop). Intraperitoneal administration was performed as a bolus injection of 0.5 mg/mL (20 µg; 100 µL) over 30 s into the abdominal cavity. Blood was sampled through the retro-orbital vein at 10 min following the first intranasal dose of [^{125}I]-mouse IgG or intraperitoneal [^{125}I]-mouse IgG bolus injection. [a]Values are depicted as mean ± S.E.M (*n* independent experiments); [b]Anterior cerebral artery and middle cerebral artery; [c]Basilar and vertebral artery; [d]Anterior olfactory nucleus; [e]Primary somatosensory cortex; [f]lymph nodes; statistical

values for Kruskal-Wallis one-way ANOVA on ranks analysis with Dunn's or Holm-Sidak *post hoc* test(s): [g] $p = 0.04$ (compared to intranasal IgG (saline, WT)), [h] $p = 0.039$ (compared to IP IgG (WT)), [i] $p = 0.025$ (compared to IP IgG (WT)), [j] $p = 0.006$ (compared to IP IgG (WT)), [k] $p < 0.001$ (compared to IP IgG (WT)), [l] $p = 0.027$ (compared to IP IgG (WT)), [m] $p = 0.005$ (compared to intranasal IgG (MMP-9, WT)), [n] $p = 0.031$ (compared to intranasal IgG (saline, WT)), [o] $p < 0.001$ (compared to intranasal IgG (saline, WT)), [p] $p < 0.001$ (compared to IP IgG (WT)),[q] $p = 0.004$ (compared to intranasal IgG (MMP-9, WT)).

Table 2. Tissue concentrations[a] (pM) of [^{125}I]-IgG following intranasal or intraperitoneal administration (2 SD data range)

	Intranasal IgG (saline, WT)	Intranasal IgG (MMP-9, WT)	Intraperitoneal IgG (WT)	Intranasal IgG (saline, AD)	Intranasal IgG (MMP-9, AD)
Blood (10 min)	284.73 ± 45.01 (8)	339.64 ± 88.66 (9)	302 + 74.11 (3)	211.41 ± 28.37 (9)	351.03 ± 51.47 (11)
ACA & MCA[b]	35.22 ± 8.95 (5)	86.18 ± 3.73 (5)		197.24 ± 90.86 (7)	19.51 ± 4.30 (9)
Bas. and vert. arteries[c]	37.67 ± 14.99 (7)	62.69 ± 28.23 (5)		119.98 ± 32.34 (7)[g]	23.89 ± 6.82 (8)
Olfactory bulb	30.16 ± 5.29 (8)[h]	55.85 ± 18.62 (9)	4.31 ± 1.12 (6)	19.12 ± 2.40 (7)	34.16 ± 6.02 (9)[i]
Ant. olfactory nucleus[d]	11.86 ± 2.02 (10)	9.79 ± 2.12 (8)	3.27 ± 1.71 (4)	12.37 ± 1.99 (7)	18.96 ± 2.77 (8)[j,k]
Frontal cortex	10.51 ± 2.39 (9)	13.42 ± 2.94 (7)		8.56 ± 1.54 (8)	8.95 ± 2.19 (10)
Olfactory tubercle	14.15 ± 3.00 (8)	7.81 ± 2.73 (6)	9.84 ± 4.01 (3)	5.67 ± 1.75 (7)	4.30 ± 0.60 (10)
Motor cortex	12.44 ± 3.03 (10)	3.45 ± 0.89 (6)	3.89 ± 0.29 (3)	4.98 ± 1.01 (7)	11.02 ± 2.28 (13)
Somatosensory cortex[e]	8.01 ± 2.44 (8)	10.29 ± 3.02 (5)	4.72 ± 1.27 (3)	10.86 ± 4.34 (8)	6.92 ± 1.65 (10)
Piriform cortex	8.05 ± 1.73 (9)	8.05 ± 2.97 (7)		5.48 ± 0.71 (7)	7.64 ± 1.63 (13)
Parietal cortex	9.00 ± 2.57 (8)	4.91 ± 0.85 (6)		7.55 ± 2.16 (7)	3.27 ± 0.54 (9)
Caudoputamen	3.61 ± 0.50 (8)	4.30 ± 1.11 (8)	18.38 ± 8.12 (3)	8.61 ± 2.69 (10)	5.73 ± 0.90 (11)
Amygdala	9.34 ± 2.19 (7)	24.51 ± 14.01 (6)	6.85 ± 2.08 (3)	14.73 ± 6.23 (6)	27.36 ± 9.69 (10)
Hippocampus	4.82 ± 0.48 (10)	3.14 ± 1.00 (8)	6.85 ± 1.86 (3)	4.48 ± 0.68 (10)	6.92 ± 1.12 (11)
Occipital cortex	4.63 ± 0.65 (8)	5.25 ± 1.46 (8)	5.94 ± 1.32 (3)	13.54 ± 3.75 (10)	5.50 ± 0.57 (11)
Medulla	11.76 ± 1.63 (8)	7.67 ± 2.23 (8)	7.51 ± 2.05 (3)	8.49 ± 2.61 (8)	6.40 ± 1.31 (10)
Pons	9.35 ± 1.85 (10)	4.85 ± 1.06 (8)	6.64 ± 2.60 (3)	6.74 ± 0.78 (8)	4.87 ± 0.63 (9)
Midbrain	7.98 ± 1.50 (10)	5.55 ± 1.44 (8)	6.01 ± 1.05 (3)	7.34 ± 1.19 (10)	6.11 ± 0.68 (11)

Cerebellum	6.34 ± 1.13 (9)	7.09 ± 1.68 (8)	6.61 ± 1.08 (3)	5.22 ± 0.21 (6)	6.39 ± 0.72 (12)
Cervical spinal cord	11.10 ± 2.04 (8)	20.35 ± 4.85 (9)	13.62 ± 3.41 (3)	9.51 ± 2.51 (7)	15.88 ± 3.42 (10)
Trigeminal nerves	215.55 ± 46.08 (10)	122.05 ± 27.00 (7)	325.20 ± 109.60 (3)	32.94 ± 4.42 (6)[l,m]	70.88 ± 15.48 (9)[n]
Optic nerve	46.77 ± 11.93 (8)	155.56 ± 97.33 (6)		11.37 ± 4.68 (6)	49.61 ± 15.56 (9)
Pituitary gland	14.38 ± 6.01 (6)	94.81 ± 29.64 (5)		24.20 ± 8.21 (6)	85.63 ± 32.12 (8)
Lung	20.37 ± 3.64 (6)	17.82 ± 7.07 (7)	48.20 ± 22.48 (3)	29.43 ± 7.35 (9)	26.78 ± 4.52 (10)
Heart	24.53 ± 4.63 (8)	15.84 ± 6.21 (7)	155.56 ± 104.60 (3)	16.76 ± 2.95 (8)	11.29 ± 1.52 (9)
Kidney	28.29 ± 6.23 (8)	76.52 ± 23.22 (9)	115.22 ± 1.12 (3)	57.44 ± 8.18 (10)	74.77 ± 15.20 (12)
Liver	48.99 ± 10.44 (9)	34.35 ± 4.97 (8)	78.76 ± 21.61 (3)	56.11 ± 8.55 (10)	47.54 ± 5.80 (13)
Deltoid muscle	64.73 ± 11.89 (10)	19.16 ± 2.82 (7)[o]	42.56 ± 8.71 (3)	17.98 ± 3.28 (9)[p]	12.92 ± 2.80 (12)[q, r]
Axillary lymph nodes	51.32 ± 11.45 (10)	69.94 ± 14.76 (5)	194.92 ± 151.91 (3)	19.82 ± 2.54 (8)	43.73 ± 9.45 (12)
Deep cervical LN[f]	69.43 ± 17.34 (9)	509.70 ± 102.26 (6)[s]		839.61 ± 266.82 (9)	234.14 ± 46.22 (11)
Superficial cervical LN	275.78 ± 49.15 (7)	247.43 ± 47.33 (7)	602.70 ± 389.77 (3)	198.86 ± 31.39 (10)	122.13 ± 12.67 (11)

Blood, brain, nervous system, peripheral organ, and lymph node radiolabel concentrations following intranasal or intraperitoneal administration of [^{125}I]-mouse IgG at a low tracer dose (20 µg). Intranasal administrations were performed over 8 min (4 drops of 2 µL each) following saline pre-administration (4 drops of 2 µL each). Intraperitoneal administration was performed as a bolus injection of 0.5 mg/mL (20 µg; 100 µL) over 0.5 min into the abdominal cavity. Blood was sampled through the retro-orbital vein at 10 min following the first intranasal dose of [^{125}I]-mouse IgG or intraperitoneal bolus [^{125}I]-mouse IgG injection. [a]Values are depicted as mean ± S.E.M (*n* independent experiments); [b]Anterior cerebral artery and middle cerebral artery; [c]Basilar and vertebral artery; [d]Anterior olfactory nucleus; [e]Primary somatosensory cortex; [f]lymph nodes; statistical values for Kruskal-Wallis one-way ANOVA on ranks analysis with Dunn's or Holm-Sidak *post hoc* test(s): [g]$p = 0.004$ (compared to

intranasal IgG (saline, WT)); [h]$p = 0.001$ (compared to IP IgG (WT)); [i]$p = 0.003$ (compared to IP IgG (WT)); [j]$p = 0.005$ (compared to intranasal IgG (MMP-9, WT)),[k]$p = 0.006$ (compared to IP IgG (WT)), [l]$p = 0.003$ (compared to IP IgG (WT)), [m]$p = 0.003$ (compared to intranasal IgG (saline, WT)), [n]$p = 0.035$ (compared to IP IgG (WT)), [o]$p = 0.041$ (compared to intranasal IgG (saline, WT)), [p]$p = 0.012$ (compared to intranasal IgG (saline, WT)), [q]$p < 0.001$ (compared to intranasal IgG (saline, WT)), [r]$p = 0.041$ (compared to IP IgG (WT)), [s]$p = 0.004$ (compared to intranasal IgG (saline, WT)).

Table 3. Summary of olfactory sensitivity testing results (*N*)

	IN saline (12)	IN 6E10 (12)	IN MMP-9 (12)	IN MMP-9 / 6E10 (12)	IP 6E10 (12)
			Sniff Time (s)		
Week 0	6.42 + 2.49 (8)	9.50 + 1.60 (10)	10.70 + 1.88 (11)	11.31 + 2.28 (10)	10.39 + 1.64 (6)
Week 2	6.45 + 2.10 (8)	4.05 + 0.91 (10)	4.25 + 4.36 (11)	6.15 + 1.78 (10)	7.76 + 2.29 (6)
Week 4	2.63 + 0.57 (8)	6.10 + 2.45 (10)	4.36 + 0.81 (12)	3.44 + 0.81 (10)	8.70 + 3.57 (6)
Week 6	2.90 + 0.92 (8)	3.23 + 0.65 (10)	3.39 + 1.14 (12)	2.64 + 0.25 (10)	6.40 + 1.34 (6)
Week 8	4.06 + 0.92 (8)	4.89 + 1.28 (10)	6.70 + 3.09 (12)	3.86 + 0.60 (10)	4.35 + 1.83 (6)
Week 10	1.75 + 0.35 (8)	3.79 + 1.04 (10)	3.21 + 0.65 (12)[a]	4.35 + 0.72 (10)	3.29 + 1.54 (6)
Week 12	1.33 + 0.33 (7)	1.86 + 0.61 (9)	3.29 + 1.13 (11)	4.75 + 1.16 (8)	4.22 + 1.63 (6)
Week 14	1.16 + 1.56 (6)	3.48 + 0.75 (8)	3.94 + 0.70 (10)[b]	6.53 + 2.06 (9)	2.62 + 0.85 (5)[c]
Week 15	1.52 + 0.53 (8)	5.27 + 1.76 (10)	5.62 + 1.09 (12)[d,e]	4.48 + 1.28 (10)	1.86 + 1.01 (6)[f]
			Latency (s)		
Week 0	20.77 + 14.06 (8)	11.18 + 4.88 (10)	34.32 + 12.54 (11)	13.06 + 4.88 (10)	9.92 + 5.19 (6)
Week 2	17.87 + 9.94 (8)	11.64 + 3.36 (10)	16.45 + 5.94 (12)	26.43 + 14.35 (10)	6.54 + 2.05 (6)
Week 4	30.36 + 13.13 (8)	15.41 + 7.99 (10)	23.92 + 8.24 (12)	8.73 + 2.60 (10)	22.04 + 8.38 (6)
Week 6	12.56 + 3.34 (8)	24.50 + 5.99 (10)	41.76 + 16.62 (11)	28.63 + 10.94 (10)	11.40 + 4.01 (6)
Week 8	12.21 + 2.84 (8)	11.16 + 4.40 (10)	20.81 + 10.87 (12)	15.18 + 8.20 (10)	37.58 + 13.04 (6)
Week 10	19.40 + 3.26 (8)	24.06 + 11.21 (10)	15.01 + 5.14 (11)	11.38 + 3.98 (10)	7.72 + 4.20 (6)
Week 12	51.84 + 21.28 (7)	14.84 + 5.84 (9)	22.75 + 10.12 (11)	18.08 + 5.47 (8)	35.60 + 12.16 (6)
Week 14	74.02 + 39.29 (5)	3.65 + 0.67 (8)	14.44 + 6.85 (10)	6.76 + 1.75 (9)	12.36 + 1.99 (5)

Week 15	24.17 + 8.88 (8)	10.03 + 6.72 (10)	22.63 + 7.90 (12)	19.44 + 6.78 (10)	33.46 + 17.39 (6)

Olfactory sensitivity testing parameters from chronic survival/efficacy study adapted from the procedure described in Witt *et al.*, 2009. Briefly, animal behavior was recorded over 180 seconds and readouts for sniff time and latency were retrospectively evaluated. Sniff time refers to the total time spent in active exploration time within 5 mm radius from the source of scent (0.1% cinnamon oil in distilled water). Latency refers to the delay from introduction to source of scent (t = 0 s) until first instance of sniff/active exploration was observed. Values are depicted as mean $\pm$ S.E.M (*n* independent experiments). *N*: number of animal per treatment group at the start of chronic study. Animals with readouts outside 3 standard deviations of mean value were excluded from these calculations. Dosing was initiated 24 h after olfaction testing for weeks 0-14; animals were euthanized by exsanguination 24 h after week 15 testing. Statistical values for Kruskal-Wallis one-way ANOVA on ranks analysis with Dunn's or Holm-Sidak *post hoc* test(s): [a]$p = 0.013$ (compared to week 0); [b]$p = 0.036$ (compared to week 0); [c]$p = 0.012$ (compared to week 0); [d]$p = 0.044$ (compared to intranasal saline control); [e]$p = 0.055$ (compared to week 0); [f]$p = 0.004$ (compared to week 0); IN: intranasal; IP: intraperitoneal.

Table 4. Summary of Thioflavin-S profiles per mm^2 slice area (*N*, *n*) from *ex vivo* fluorescence imaging analysis

	IN saline (12)	IN 6E10 (12)	IN MMP-9 (12)	IN MMP-9 / 6E10 (12)	IP 6E10 (12)
Olfactory bulb (OB)[a, #]	7.70 ± 1.47 (4, 12)	4.71 ± 1.48 (5, 15)	5.34 ± 1.22 (6, 18)	4.09 ± 0.88 (5, 15)	1.63 ± 0.15 (6, 18)[f, g]
Rhinal fissure[b, #]					
Dorsal (dRF)	20.13 ± 2.79 (8, 24)	22.82 ± 3.15 (10, 30)	14.29 ± 2.08 (10, 30)	13.91 ± 2.60 (10, 30)[h]	14.48 ± 2.76 (8, 24)[i, j]
Ventral (vRF)	10.68 ± 2.00 (8, 24)	14.46 ± 2.12 (10, 30)	11.36 ± 1.47 (10, 30)[k]	7.61 ± 1.48 (10, 30)[l]	6.68 ± 1.46 (8, 24)[m]
Lateral ventricle (LV)[c, #]	17.60 ± 2.49 (8, 24)	16.11 ± 2.34 (10, 30)	16.20 ± 2.48 (10, 30)	13.73 ± 1.71 (8, 24)	10.94 ± 1.71 (8, 24)[n]
Posterior cortex (pCTX)[d, #]	22.87 ± 2.01 (8, 24)	12.92 ± 1.94 (10, 30)	17.26 ± 3.39 (10, 30)	14.42 ± 2.52 (10, 30)	11.24 ± 2.01 (8, 24)
Hippocampus (HC)[d, #]	10.85 ± 1.00 (8, 24)	10.90 ± 1.05 (10, 30)	11.27 ± 1.24 (10, 30)[o]	10.77 ± 1.97 (10, 30)	8.52 ± 1.09 (8, 24)
Cerebellum (CBM)[e, #]	6.75 ± 1.12 (8, 24)	9.89 ± 2.41 (9, 27)[p]	11.62 ± 1.36 (10, 30)	8.86 ± 1.35 (10, 30)[q]	8.67 ± 1.95 (6, 18)[r]

Thioflavin-S intensity profiles above white matter background threshold was quantified using Fiji plugins (Schindelin *et al*., 2012) and macros generated for Pizzo *et al.*, 2018 to measure the number of fibrillar plaque load. Profiles were further normalized by slice area (mm^2). Values are depicted as mean ± SEM (*N, n*); *N*: number of animals per treatment group; n: number of sections per treatment group; IN: Intranasal; IP: Intraperitoneal; MMP-9: matrix metalloproteinase-9; [a]+3 mm to +4 mm; [b]+2 mm to +3 mm; [c]+2 mm to 0 mm; [d]0 mm to -5 mm; [e]-5 mm to -8 mm; [#]relative to bregma (0 mm) as per Franklin & Watson, 2008; statistical values for Kruskal-Wallis one-way ANOVA on ranks analysis with Dunn's *post hoc* test: [f]$p < 0.001$ (compared to IN saline), [g]$p = 0.04$ (compared to IN MMP-9), [h]$p = 0.00$ (compared to IN 6E10), [i]$p < 0.001$ (compared to IN 6E10), [j]$p = 0.04$ (compared to IN MMP-9), [k]$p = 0.02$ (compared to IN 6E10), [l]$p = 0.01$ (compared to IN 6E10), [m]$p = 0.02$ (compared to IN 6E10), [n]$p = 0.01$ (compared to IN saline), [o]$p = 0.01$ (compared to IN saline), [p]$p < 0.001$ (compared to IN saline), [q]$p = 0.00$ (compared to IN saline), [r]$p < 0.001$ (compared to IN saline); IN: Intranasal; IP: Intraperitoneal.

Table 5. Summary of protein analysis following chronic intranasal / systemic 6E10 administration

	IN saline (12)	IN 6E10 (12)	IN MMP-9 (12)	IN MMP-9 / 6E10 (12)	IP 6E10 (12)
			ELISA protein levels (pg/mg brain tissue)[a]		
TBS[c] / $A\beta_{40}$	73.85 ± 7.87 (5)	123.24 ± 27.15 (7)	92.73 ± 17.70 (6)	107.26 ± 19.81 (7)	98.86 ± 12.60 (8)
TBS / $A\beta_{42}$	55.46 ± 13.09 (7)	53.91 ± 10.53 (8)	79.96 ± 23.47 (10)	46.27 ± 9.57 (10)	54.97 ± 11.82 (8)
TBS-SDS[d] / $A\beta_{40}$	119.86 ± 29.64 (7)	152.34 ± 28.80 (7)	108.28 ± 19.17 (9)	110.39 ± 13.54 (9)	105.93 ± 10.78 (9)
TBS-SDS / $A\beta_{42}$	24.40 ± 14.88 (8)	29.60 ± 7.70 (10)	46.22 ± 12.03 (8)	46.029 ± 15.39 (10)	43.58 ± 13.71 (9)
			[b]Western Blot protein band densities relative to 37 kDa molecular ladder (37 kDa = 1000 units)		
12 kDa (3-mer[e])	15.67 ± 2.76 (7)	34.57 ± 3.42 (9)	-	13.64 ± 1.75 (10)	20.06 ± 5.41 (8)
100 kDa (sAPP[f])	4.76 ± 0.70 (7)	10.94 ± 2.26 (9)	-	13.80 ± 7.42 (10)	17.85 ± 4.47 (8)

[a]ELISA values were estimated using a 4-parameter logisitic regression curve on the standard curve values for $A\beta_{40}$ and $A\beta_{43}$. [b]Relative densities were quantified using Gel Analyzer Fiji plugin to measure the area under the curve for a given well's intensity. Values are depicted as mean ± SEM (N); N: number of animals. [b]Tris-buffered saline; [c]Tris-buffered saline with 0.6% sodium dodecyl sulfate; [e]trimer; [f]soluble amyloid precursor protein fragment or higher order (24-mer) oligomers. No statistical significance was observed across different treatment groups in these analyses; IN: Intranasal; IP: Intraperitoneal.

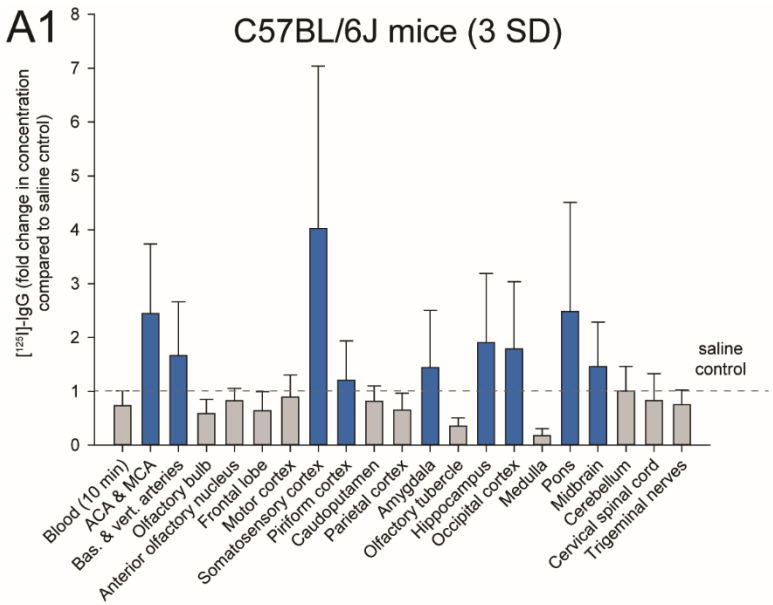
A1
C57BL/6J mice (3 SD)
[125I]-IgG (fold change in concentration compared to saline cntrol)
saline control
Blood (10 min)
ACA & MCA
Bas. & vert. arteries
Olfactory bulb
Anterior olfactory nucleus
Frontal lobe
Motor cortex
Somatosensory cortex
Piriform cortex
Caudoputamen
Parietal cortex
Amygdala
Olfactory tubercle
Hippocampus
Occipital cortex
Medulla
Pons
Midbrain
Cerebellum
Cervical spinal cord
Trigeminal nerves

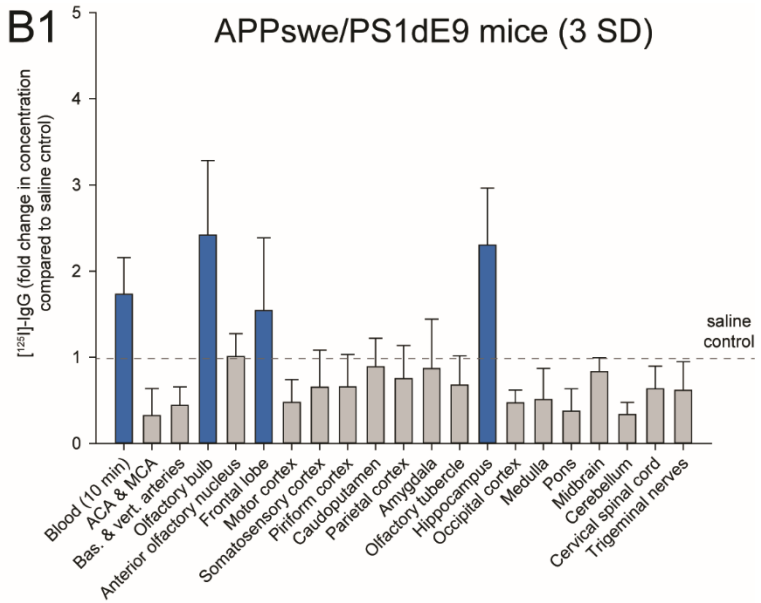
B1
APPswe/PS1dE9 mice (3 SD)
[125I]-IgG (fold change in concentration compared to saline cntrol)
saline control
Blood (10 min)
ACA & MCA
Bas. & vert. arteries
Olfactory bulb
Anterior olfactory nucleus
Frontal lobe
Motor cortex
Somatosensory cortex
Piriform cortex
Caudoputamen
Parietal cortex
Amygdala
Olfactory tubercle
Hippocampus
Occipital cortex
Medulla
Pons
Midbrain
Cerebellum
Cervical spinal cord
Trigeminal nerves

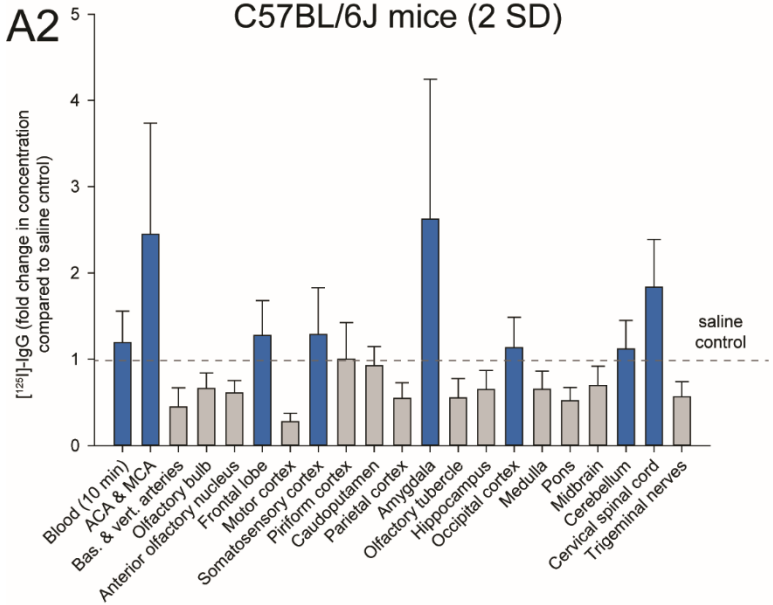
A2
C57BL/6J mice (2 SD)
[125I]-IgG (fold change in concentration compared to saline cntrol)
saline control
Blood (10 min)
ACA & MCA
Bas. & vert. arteries
Olfactory bulb
Anterior olfactory nucleus
Frontal lobe
Motor cortex
Somatosensory cortex
Piriform cortex
Caudoputamen
Parietal cortex
Amygdala
Olfactory tubercle
Hippocampus
Occipital cortex
Medulla
Pons
Midbrain
Cerebellum
Cervical spinal cord
Trigeminal nerves

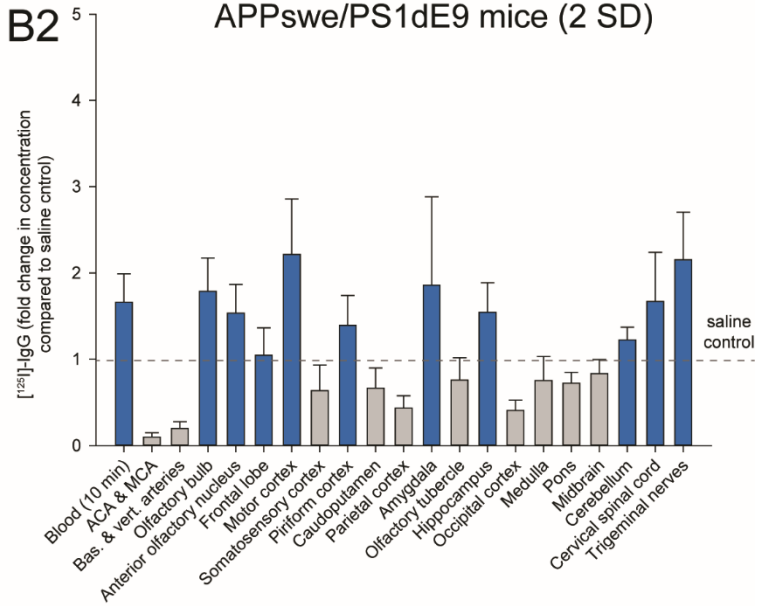
B2
APPswe/PS1dE9 mice (2 SD)
[125I]-IgG (fold change in concentration compared to saline cntrol)
saline control
Blood (10 min)
ACA & MCA
Bas. & vert. arteries
Olfactory bulb
Anterior olfactory nucleus
Frontal lobe
Motor cortex
Somatosensory cortex
Piriform cortex
Caudoputamen
Parietal cortex
Amygdala
Olfactory tubercle
Hippocampus
Occipital cortex
Medulla
Pons
Midbrain
Cerebellum
Cervical spinal cord
Trigeminal nerves

Figure 1. **Fold-change in [^{125}I]-IgG levels in the brain, nervous tissue, and blood following mouse matrix metalloproteinase-9 (mMMP-9) pre-treatment in C57Bl/6J and APPswe/PS1dE9 mice**. Values are normalized with respect to saline controls receiving intranasal [^{125}I]-IgG followed by saline pre-treatment. Fold change values are derived from Tables 1 and 2 as mean $\pm$ S.E.M (standard error of mean). S.E.M values for fold-change were estimated as the squared root of sum of squared errors (i.e. S.E.M. / mean). Grey dashed line indicates 1 fold-change with respect to the intranasal saline control experiments. Data was visualized within 3 (A1, B1) and 2 (A2, B2) standard deviation of mean values to account for inter-animal variabilities in intranasal administration or transcardial perfusion technique. In C57BL/6J, certain regions (primary somatosensory cortex, amygdala, anterior cerebral and middle cerebral arteries, occipital cortex) were consistently above the saline control mean values, however S.E.M. values were also high for these regions. Inter-animal variabilities were lower in APPswe/PS1dE9 mice with ~1-2 fold higher [^{125}I]-IgG levels in the olfactory bulbs, hippocampus, and blood compared to APPSwe/PS1dE9 mice receiving saline pre-treatment prior to intranasal [^{125}I]-IgG administration. ACA: anterior cerebral artery; MCA: middle cerebral artery; Bas.: basilar artery; Vert.: Vertebral artery; 2 SD: 2 standard deviations from mean value; 3 SD: 3 standard deviations from mean value.

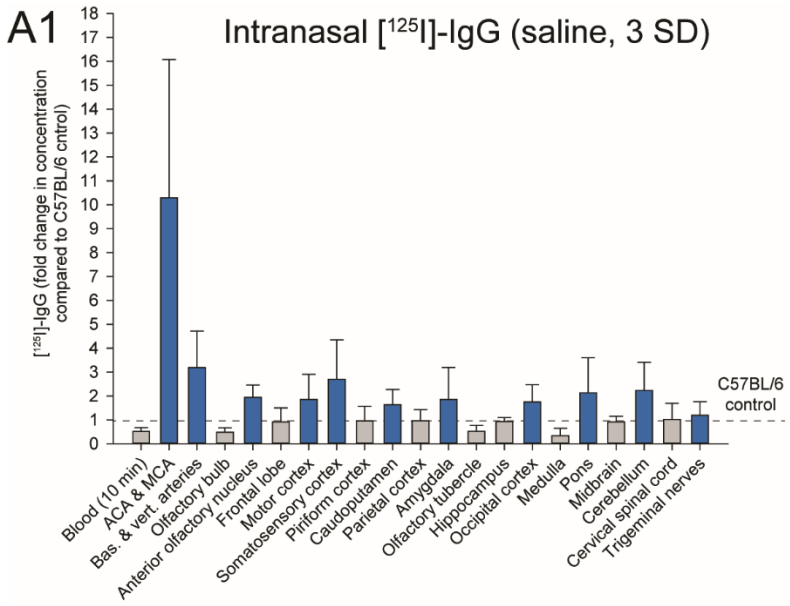
A1
Intranasal [125I]-IgG (saline, 3 SD)
[125I]-IgG (fold change in concentration compared to C57BL/6 cntrol)
C57BL/6 control
Blood (10 min)
ACA & MCA
Bas. & vert. arteries
Olfactory bulb
Anterior olfactory nucleus
Frontal lobe
Motor cortex
Somatosensory cortex
Piriform cortex
Caudoputamen
Parietal cortex
Amygdala
Olfactory tubercle
Hippocampus
Occipital cortex
Medulla
Pons
Midbrain
Cerebellum
Cervical spinal cord
Trigeminal nerves

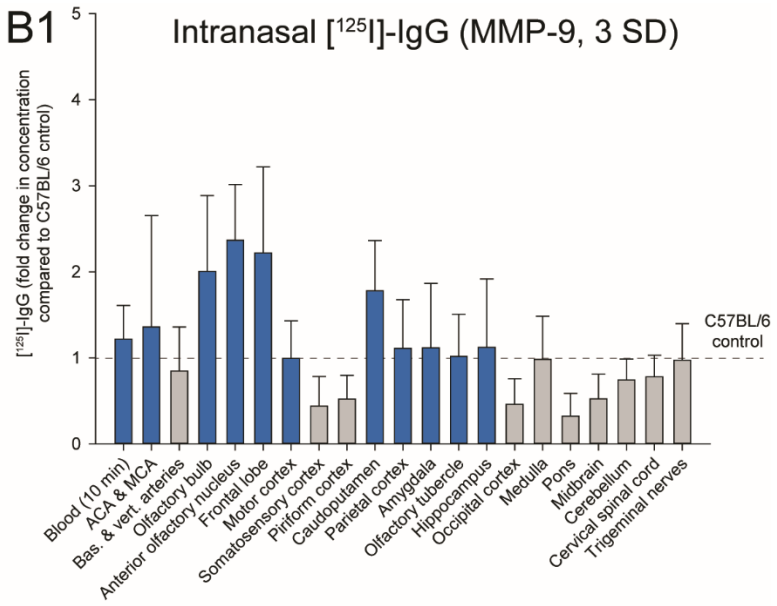
B1
Intranasal [125I]-IgG (MMP-9, 3 SD)
[125I]-IgG (fold change in concentration compared to C57BL/6 cntrol)
C57BL/6 control
Blood (10 min)
ACA & MCA
Bas. & vert. arteries
Olfactory bulb
Anterior olfactory nucleus
Frontal lobe
Motor cortex
Somatosensory cortex
Piriform cortex
Caudoputamen
Parietal cortex
Amygdala
Olfactory tubercle
Hippocampus
Occipital cortex
Medulla
Pons
Midbrain
Cerebellum
Cervical spinal cord
Trigeminal nerves

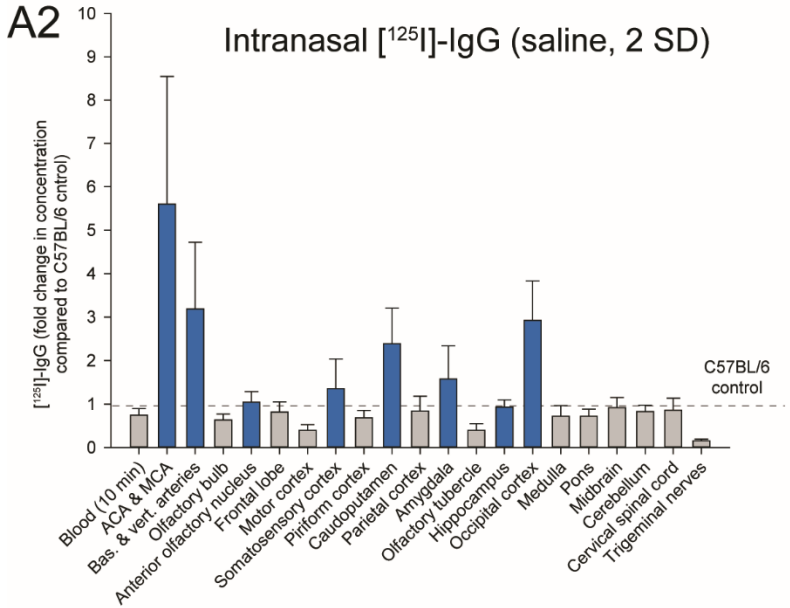
A2
Intranasal [125I]-IgG (saline, 2 SD)
[125I]-IgG (fold change in concentration compared to C57BL/6 cntrol)
C57BL/6 control
Blood (10 min)
ACA & MCA
Bas. & vert. arteries
Olfactory bulb
Anterior olfactory nucleus
Frontal lobe
Motor cortex
Somatosensory cortex
Piriform cortex
Caudoputamen
Parietal cortex
Amygdala
Olfactory tubercle
Hippocampus
Occipital cortex
Medulla
Pons
Midbrain
Cerebellum
Cervical spinal cord
Trigeminal nerves

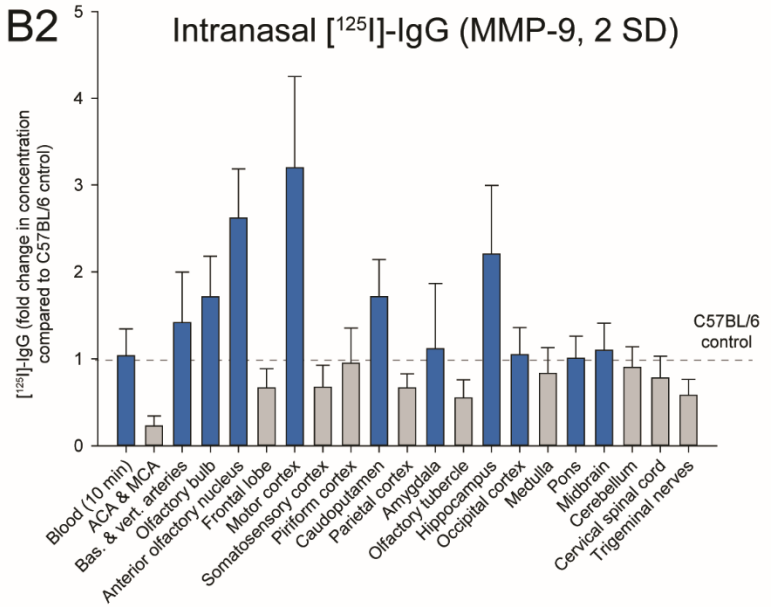
B2
Intranasal [125I]-IgG (MMP-9, 2 SD)
[125I]-IgG (fold change in concentration compared to C57BL/6 cntrol)
C57BL/6 control
Blood (10 min)
ACA & MCA
Bas. & vert. arteries
Olfactory bulb
Anterior olfactory nucleus
Frontal lobe
Motor cortex
Somatosensory cortex
Piriform cortex
Caudoputamen
Parietal cortex
Amygdala
Olfactory tubercle
Hippocampus
Occipital cortex
Medulla
Pons
Midbrain
Cerebellum
Cervical spinal cord
Trigeminal nerves

Figure 2. **Fold-change in [^{125}I]-IgG levels in the brain, nervous tissue, and blood for APP/PS1 mouse model compared to background strain with saline and MMP-9 pre-administration**. Values are normalized with respect to saline controls receiving intranasal [^{125}I]-IgG followed by saline pre-treatment. Fold change values are derived from Tables 1 and 2 as mean $\pm$ S.E.M (standard error of mean). S.E.M values for fold-change were estimated as the squared root of sum of squared errors (i.e. S.E.M. / mean). Grey dashed line indicates 1 fold-change with respect to the intranasal saline control experiments. Data was visualized within 3 (A1, B1) and 2 (A2, B2) standard deviation of mean values to account for inter-animal variabilities in intranasal administration or transcardial perfusion technique. APPswe/PS1dE9 mice had consistently high [^{125}I]-IgG levels for major cerebral arteries and associated perivascular compartments, caudoputamen and occipital cortex compared to C57BL/6J mice with saline pre-administration. [^{125}I]-IgG levels following MMP-9 pretreatment led to a ~1-2-fold increase in [^{125}I]-IgG concentrations across brain regions for APPswe/PS1dE9 mice when compared to C57BL/6J mice receiving MMP-9 pre-administration. ACA: anterior cerebral artery; MCA: middle cerebral artery; Bas.: basilar artery; Vert.: Vertebral artery; 2 SD: 2 standard deviations from mean value; 3 SD: 3 standard deviations from mean value.

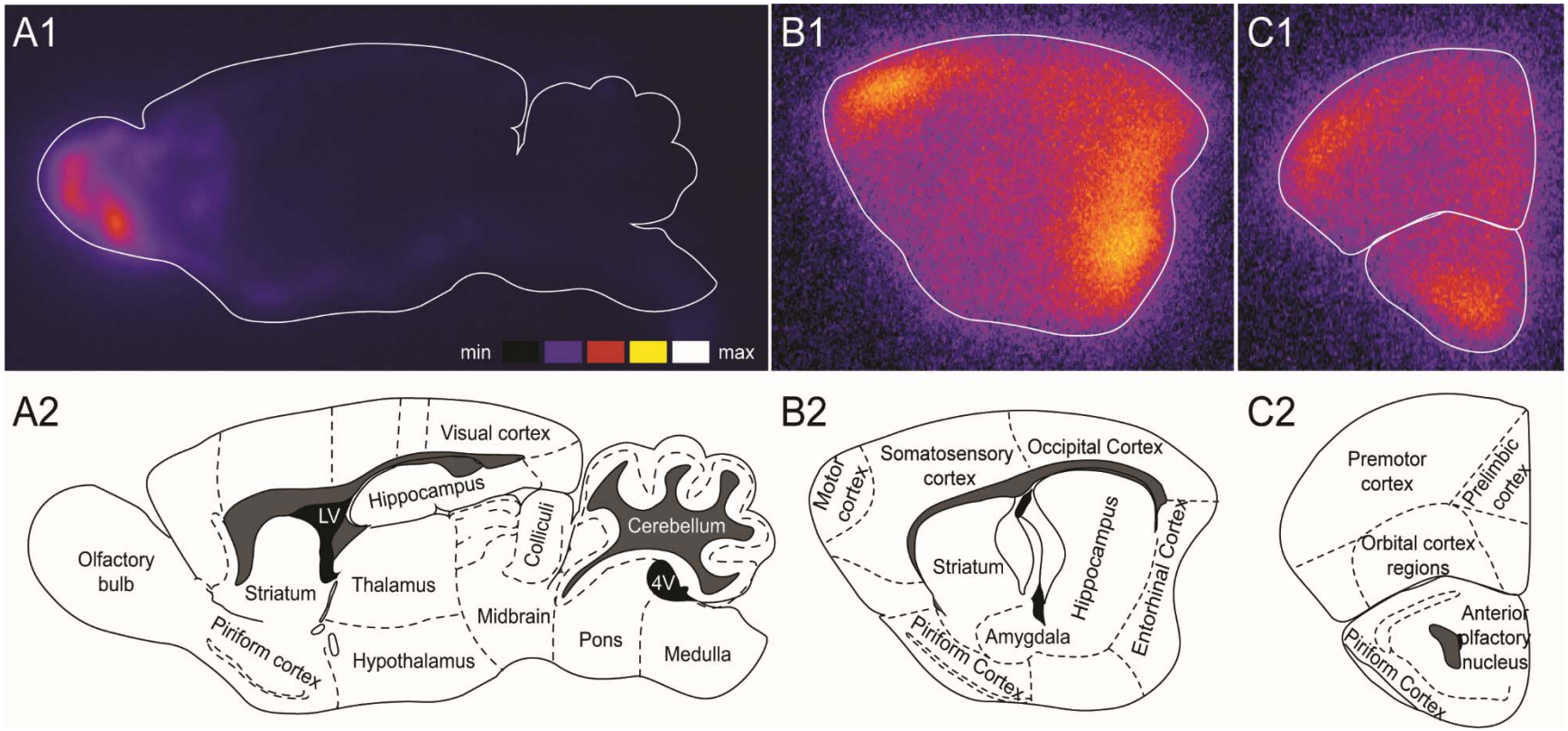

Figure 3. Representative autoradiography images of [^{125}I]-IgG distribution in C57BL6 and APPswe/PS1dE9 brains following intranasal [^{125}I]-IgG delivery with MMP-9 pretreatment (with corresponding schematics). (A1) Sagittal brain section autoradiograph (approximately 1.5 mm lateral to the midline; Paxinos & Watson, 2007) revealed high signal associated with the olfactory bulb and rostro, and ventral brain regions following MMP-9 pretreatment. (A2) Schematic corresponding to sagittal section autoradiograph. (B1) Sagittal brain section autoradiograph (approximately 3 mm lateral to the midline; Paxinos & Watson, 2007) revealed higher signal associated with cortical regions in APPswe/PS1dE9 mice. (B2) Schematic corresponding to sagittal brain section autoradiograph in (B1), adapted from Paxinos & Watson, 2007. (C1) Coronal brain

section autoradiograph (approximately 2.5 mm anterior to the bregma; Franklin & Watson, 2008) from APPswe/PS1dE9 mice revealed high signal in the dorsal and ventral regions. (C2) Schematic for (C1) coronal brain section autoradiograph adapted from Franklin & Watson, 2008. LV: Lateral ventral; 4V: fourth ventricle.

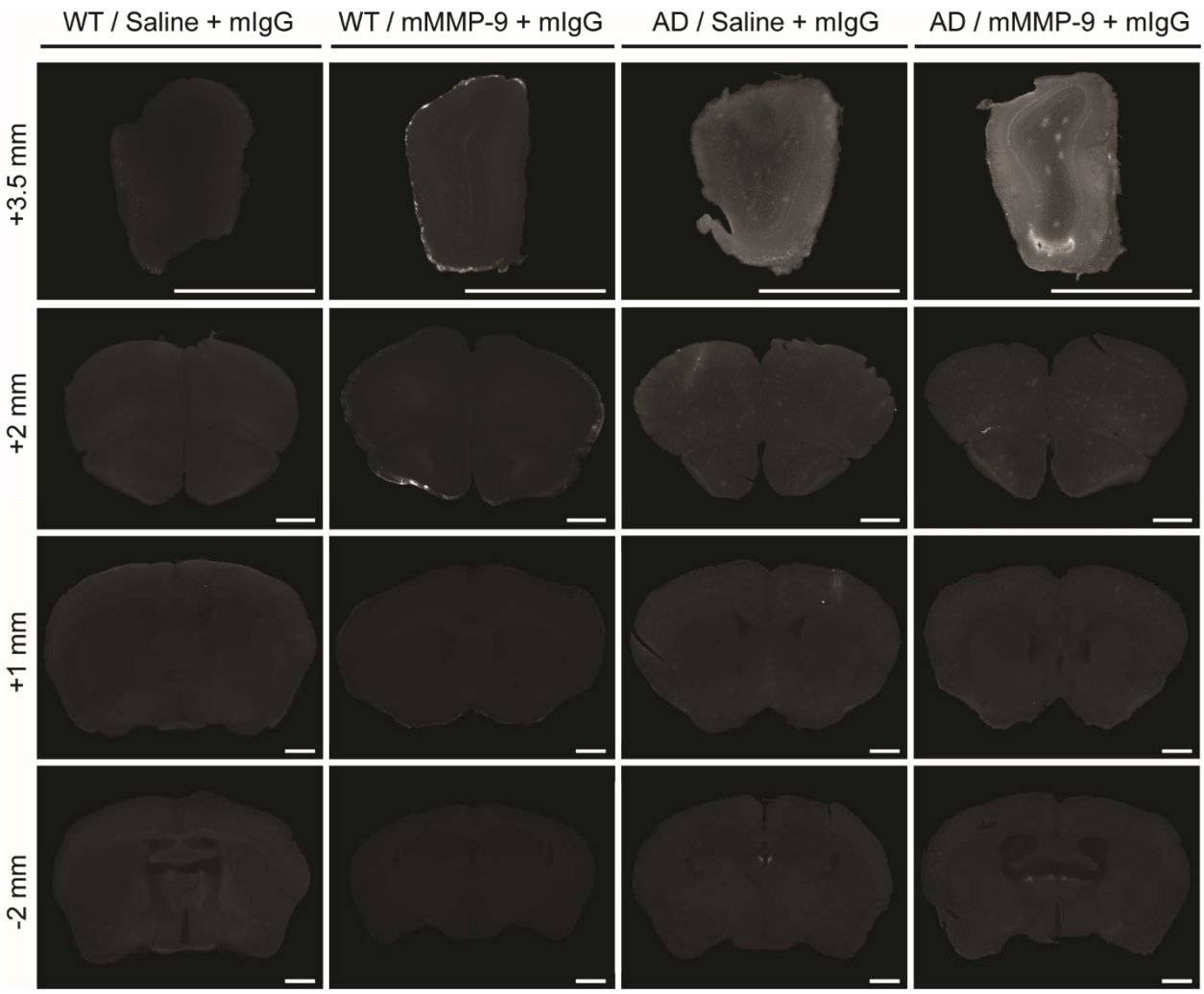

Figure 4. Coronal brain sections highlight intranasal AF594-IgG access in the mouse brain following MMP-9 pre-treatment. Differences were evident at the olfactory bulbs in WT and AD mice (*n* = 2 each). Section levels indicate approximate distances from bregma (0 mm) as per Franklin & Watson (2008). Scale bar = 1 mm. Concentration AlexaFlour^{TM} 594-IgG (15-20 mg/mL) was largely associated with the meningeal compartment and ventricular spaces 30 min following intranasal administration.

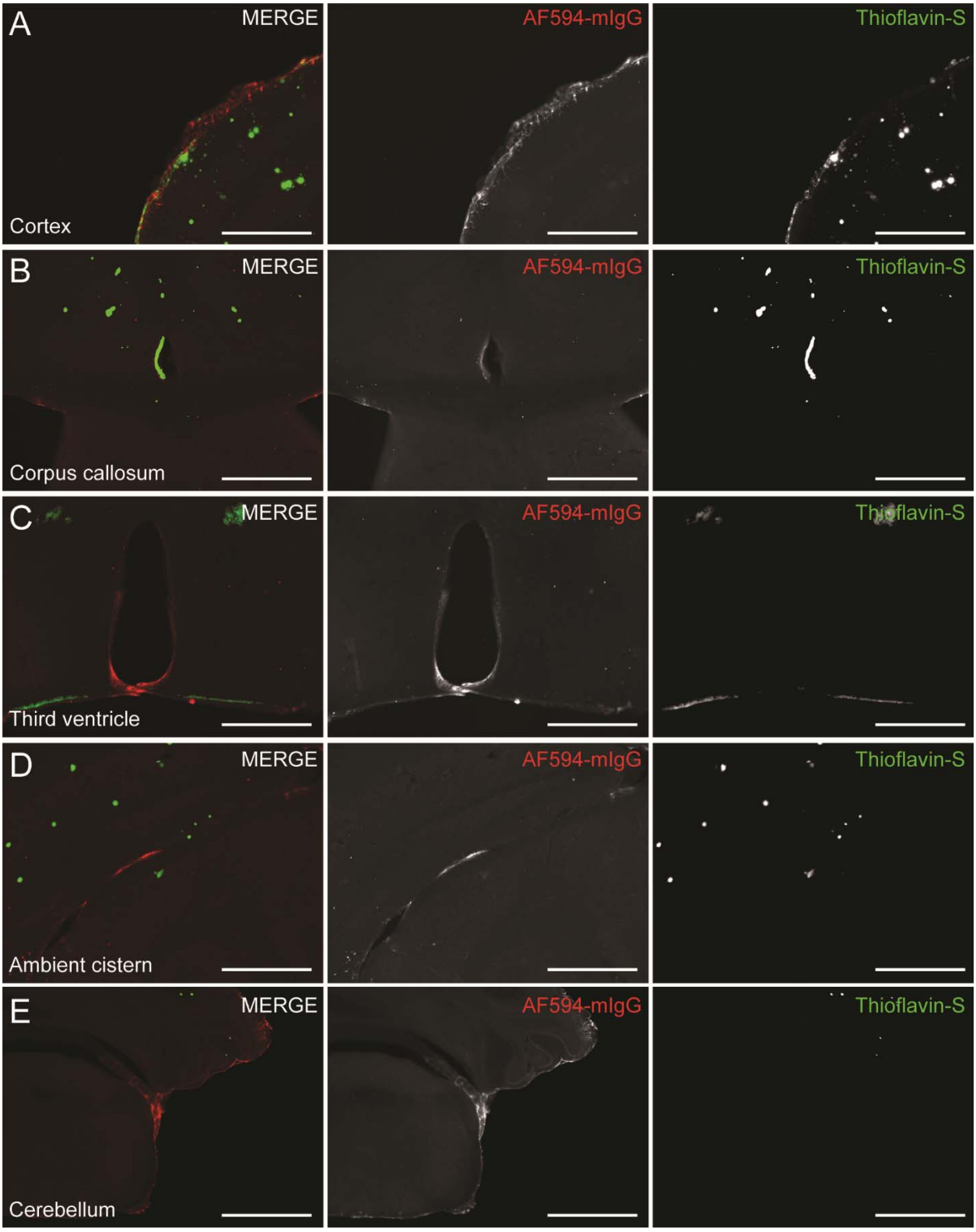

Figure 5. Low resolution *ex vivo* fluorescence images of AF594-mIgG distribution in the APPswe/PS1dE9 mouse brain following intranasal AF594-mIgG delivery. Intranasally applied AF594-

mIgG was consistently observed at the leptomeningeal surface (A, B, E), at the base of the lateral ventricles (C), and within cells associated with the cisternal spaces (D). Thioflavin-S staining of 100 µm thick brain sections indicated perivascular amyloid deposits in close proximity with AF594-mIgG signal (A). Scale bar = 0.5 mm.

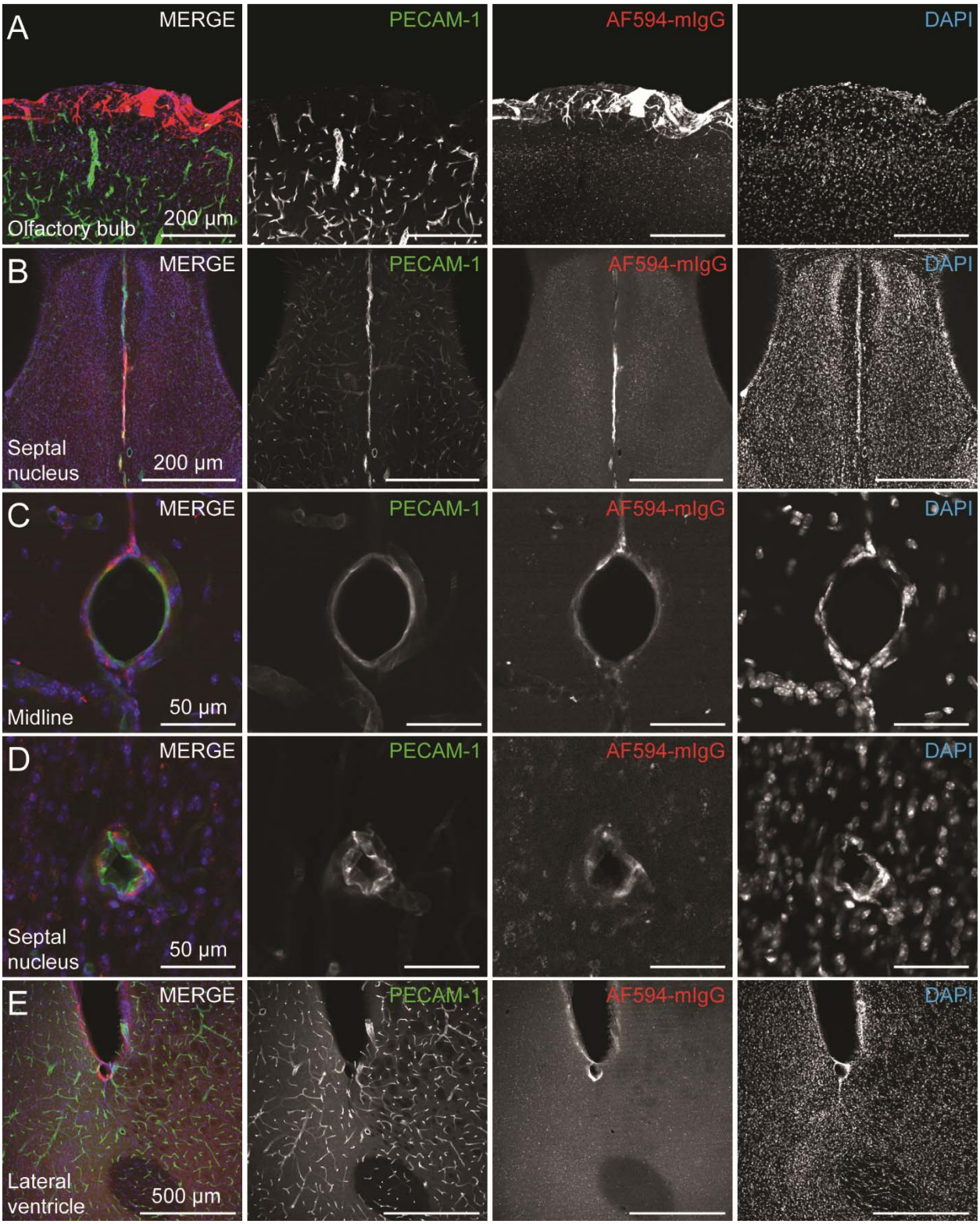

Figure 6. Laser scanning confocal microscopy images suggest perivascular localization of AF594-mIgG in the brain sections of APPswe/PS1dE9 mice. Coronal brain sections from mice receiving

intranasal AF594-mIgG were immunolabeled with platelet endothelial cell adhesion molecule-1, an endothelial cell specific protein following perfusion fixation. Confocal images indicated that AF594-mIgG signal was overlapping PECAM-1 profiles but colocalization was not observed (B, C, D). AF594-mIgG signal was also observed to be associated with PECAM-1-negative surfaces e.g. the leptomeningeal surface (A) and the ependymal layer (D).

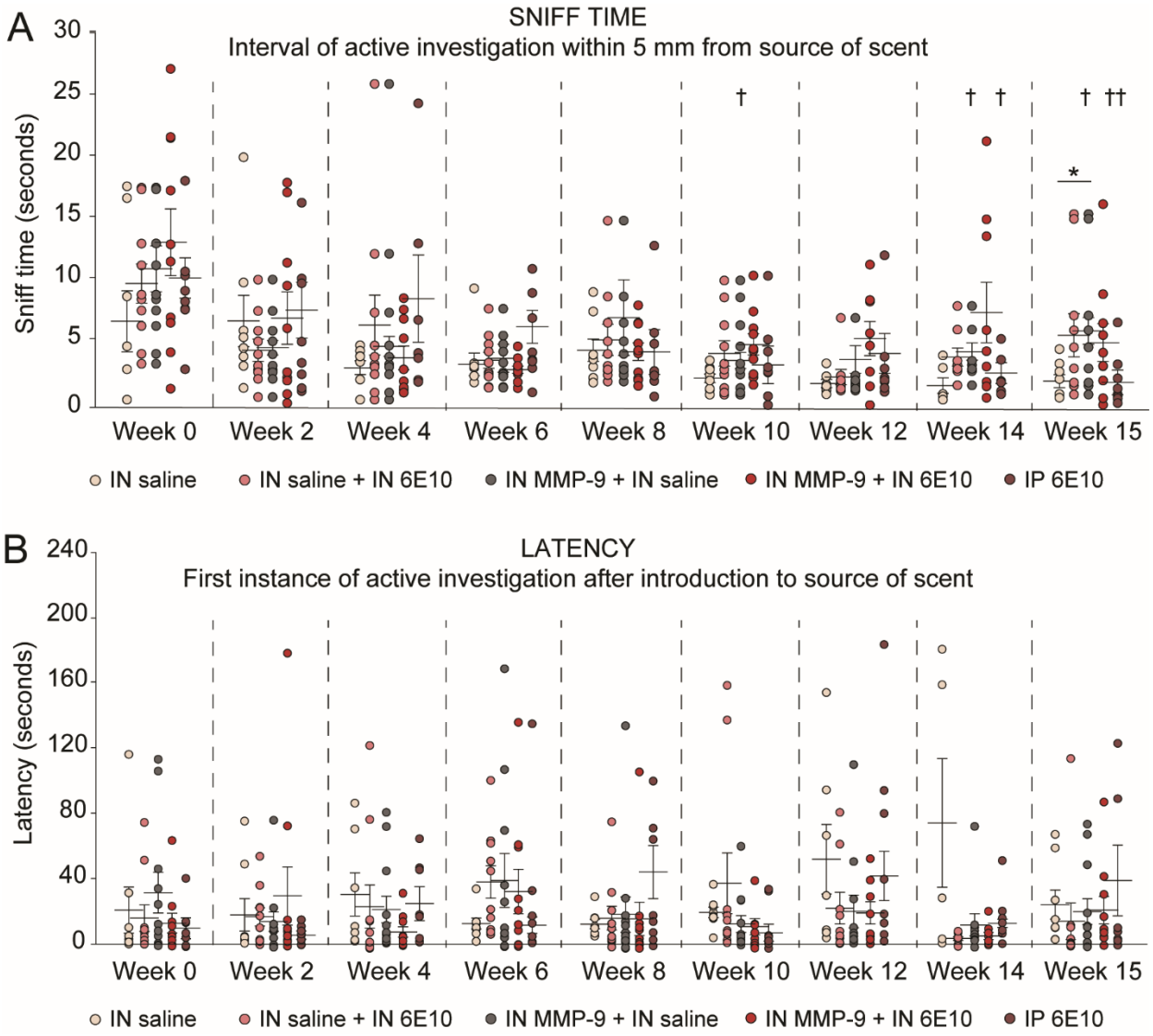

Figure 7. Olfactory sensitivity testing in chronically treated APPswe/PS1dE9 mice. Animal were exposed to a source of scent (0.5% cinnamon oil in distilled water) 24 h before dosing and activities were recorded over 180 seconds of exposure. Recordings were later timed for two parameters: (i) sniff time i.e. total time of active investigation within a 5 mm radius from the source of scent, and (ii) latency or delay in first instance of active investigation. Statistical values for Kruskal-Wallis one-way ANOVA with Dunn's *post hoc* test: $^{*}p < 0.05$ (compared to IN saline control), $^{\dagger}p < 0.05$ (compared to week 0 readouts); $^{\dagger\dagger}p < 0.005$ (compared to week 0 readouts). IN: intranasal; MMP-9: matrix metalloproteinase-9.

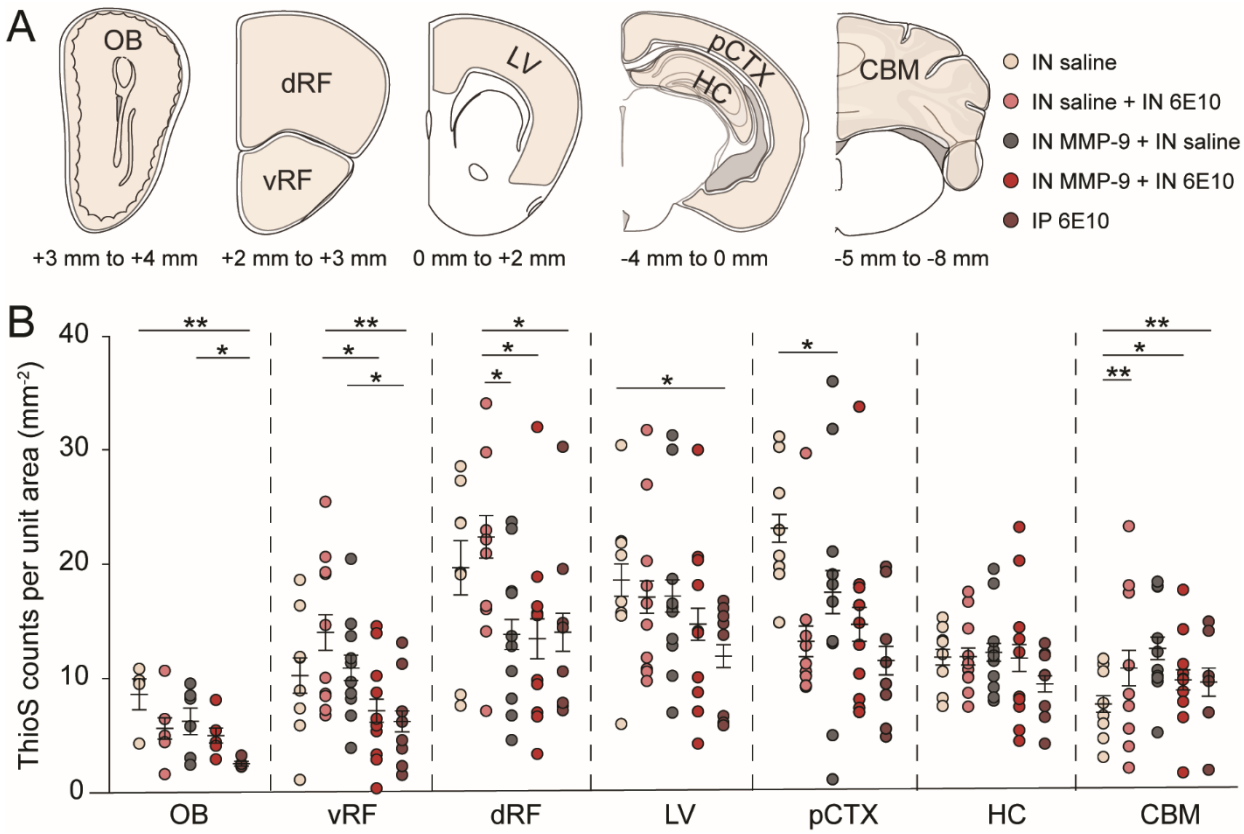

Figure 8. ***Ex vivo*** **fluorescence images of Thioflavin-S stained coronal brain sections indicated a ladder-like trend in accumulation of fibrillar amyloid aggregates species**. (A) Schematic for outlined regions of interest were adapted from Franklin & Watson (2008). Fluorescence intensity (in pixels) were measured for these regions using previously generated macros to run Fiji plugins in a sequential order (Schindelin *et al.*, 2012; Pizzo *et al.*, 2018). Intensity values at each magnification level were normalized by its corresponding pixel/mm^2 values to achieve profiles per mm^2 readouts. (B) Graphs derived from mean $\pm$ S.E.M values in Table 4. A ladder-like reduction in Thioflavin-S profiles was observed across multiple cortical regions (excluding the hippocampus and cerebellum). Thioflavin-S positive profiles were higher in the dRF, LV, and pCTX regions compared to OB, vRF, CBM, HC regions across all treatment groups. *$p < 0.05$, Kruskal-Wallis one-way analysis of variance on ranks with Dunn's *post hoc* test; **$p < 0.005$, Kruskal-Wallis one-way analysis of variance on ranks with Dunn's *post hoc* test. IN: intranasal; MMP-9: matrix metalloproteinase-9; OB: Olfactory bulb; dRF: dorsal to rhinal fissure; vRF: ventral to rhinal fissure; LV: lateral ventricle associated cortex; pCTX: posterior cortex; HC: hippocampus; CBM: cerebellum.

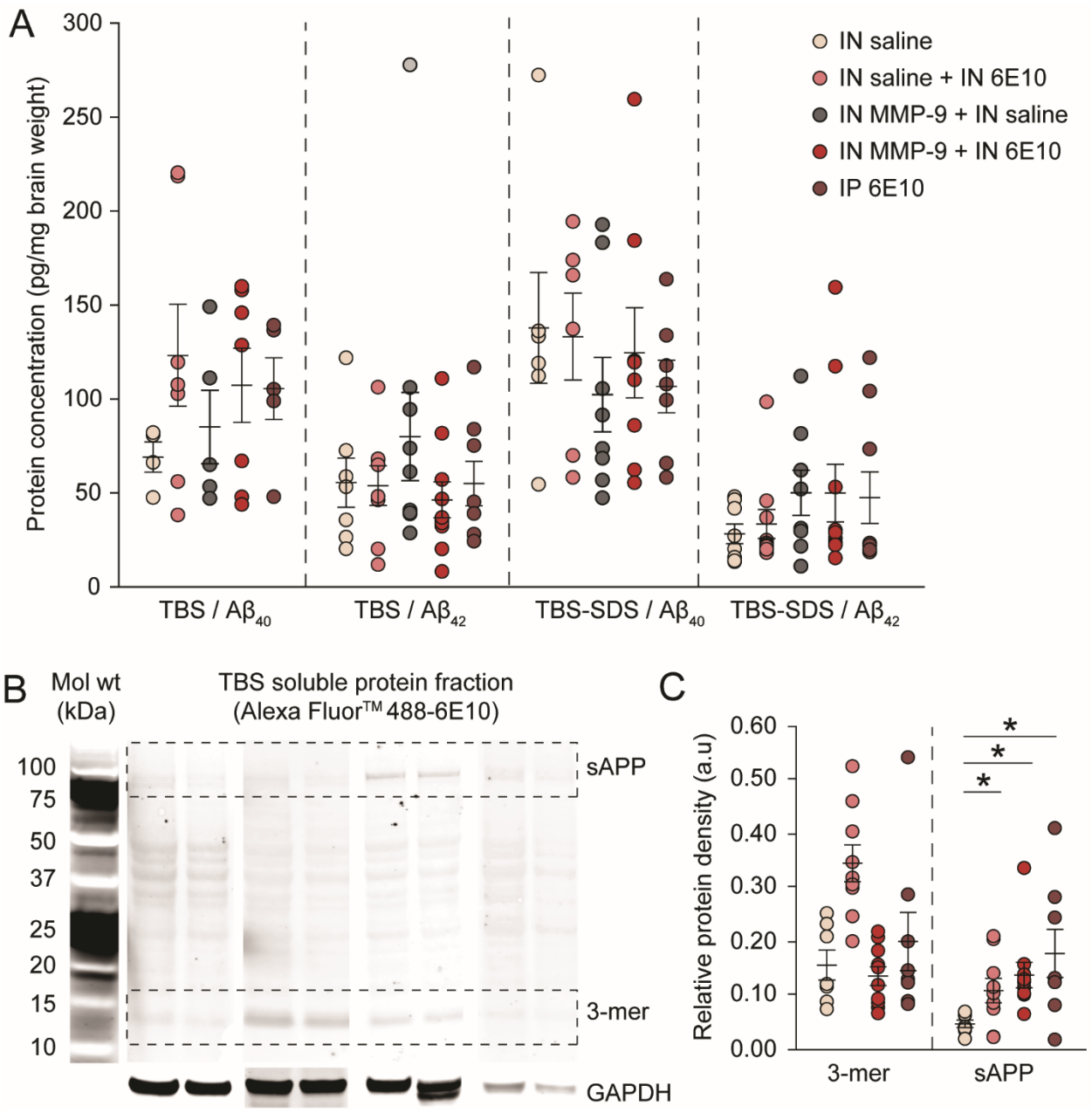

Figure 9. Enyzme-linked immunosorbent assay (ELISA) and Western Blot analysis demonstrated a shift in Aβ load for higher oligomers but not for $A\beta_{40}$ and $A\beta_{42}$ with chronic intranasal 6E10 exposure. (A) TBS soluble protein fractions and TBS-SDS soluble protein fractions were analyzed for $A\beta_{40}$ and $A\beta_{42}$ levels by ELISA; no significant differences were observed across treatment groups. (B) Representative Western Blot(s) for TBS soluble fraction of IN saline, IN 6E10, IN MMP-9 ± IN 6E10, and IP 6E10 treatment groups (left to right). Bands were detected with Alexa Fluor™ 488 conjugated 6E10 antibody.

(C) Relative band densities were quantified for ~12 kDa (trimer) and ~100 kDa (secreted amyloid precursor protein, sAPP and 24-mer amyloid aggregates) using Fiji 'Gel Analyze' plugin (Schindelin *et al.*, 2012; Miller, 2010). These values were normalized by the corresponding loading control band densities (loading control: glyceraldehyde 3-phosphate dehydrogenase or GAPDH). Normalized values were further standardized to the 37 kDa molecular ladder band density to allow cross-comparison of multiple membranes. Here, 12 kDa band levels were not significantly different across treatment groups. However, a trend for significantly higher sAPP/24-mer levels (100 kDa band density) was observed in 6E10-treated animals compared to saline-treated animals. These values suggested that 6E10 was potentially resolving fibrillar plaques (Fig. 8) to higher-end Aβ oligomers. IN: intranasal; MMP-9: matrix metalloproteinase-9.

CHAPTER 3

Passive immunotherapies for central nervous system disorders: current delivery challenges and new approaches

Niyanta N. Kumar[1], Michelle E. Pizzo[1], **Geetika Nehra[1]**, Brynna Wilken-Resman[1], Sam Boroumand[1], Robert G. Thorne[1,2,3]

[1]Pharmaceutical Sciences Division, School of Pharmacy, University of Wisconsin-Madison, Madison, Wisconsin, USA; [2]Denali Therapeutics, South San Francisco, California, USA; [3]Department of Pharmaceutics, College of Pharmacy, University of Minnesota Twin Cities, Minneapolis, Minnesota, USA

*Represents sections co-authored by Geetika Nehra

Reproduced in part with permission from:

Kumar NN, Pizzo ME, Nehra G, Wilken-Resman B, Boroumand S & Thorne RG (2018). Passive Immunotherapies for Central Nervous System Disorders: Current Delivery Challenges and New Approaches. *Bioconjugate Chem* **29**, 3957-3966.

Abstract

Passive immunotherapy i.e. administration of antibodies that recognize a specific target antigen, has gained significant momentum as a potential treatment strategy for several central nervous system (CNS) disorders, including Alzheimer's disease, Parkinson's disease, Huntington's disease, and brain cancer, among others. Advances in antibody engineering to create therapeutic antibody fragments or antibody conjugates have introduced new strategies that may also be applied to treat CNS disorders. However, drug delivery to the CNS for antibodies and other macromolecules has thus far proven challenging, due in large part to the blood-brain barrier and blood-cerebrospinal fluid barriers that greatly restrict transport of peripherally administered molecules from the systemic circulation into the CNS. Here, we summarize the various passive immunotherapy approaches under study for the treatment of CNS disorders, with a primary focus on disease-specific and target site-specific challenges to drug delivery and new, cutting edge methods.

Introduction

Antibodies are a group of serum glycoproteins called immunoglobulins (Igs) that assist in generating an adaptive humoral immune response in vertebrates (Kindt *et al*., 2007). Immunoglobulin G (IgG; ~150 kDa), in particular, is the most abundant serum isotype that elicits an immune response by recognizing a specific target antigen using two antigen-binding fragments (Fab; ~ 50 kDa each), and a crystallizable fragment (Fc; ~ 50 kDa) that binds to endogenous Fc receptors (Kindt *et al*., 2007) (see schematic in Fig.1). Administration of Ig-based antibodies to target disease-specific antigens ('passive immunotherapy') has significantly advanced ever since César Milstein and Georges Köhler demonstrated the production of monoclonal antibodies using hybridoma cells (Köhler & Milstein, 1975). Indeed, antibody-based therapeutics have been one of the fastest emerging drug candidates (Urquhart, 2019) that are highly amenable yet maintain target-specificity (Chiu & Gilliland, 2016). These can be full-length antibodies (e.g., IgG) with a long half-life due to pH-sensitive Fc domain - Brambell receptor/ neonatal Fc receptor (FcRn) interactions (Pyzik *et al.*, 2019) and immune effector functions through Fc domain – Fc gamma receptor

interactions (Nimmerjahn & Ravetch, 2007; Nimmerjahn & Ravetch, 2008; Nimmerjahn & Ravetch, 2008; Nimmerjahn & Ravetch, 2010), or antibody fragments (e.g. Fab, single domain antibodies (sdAbs)) if long half-lives and effector functions are not required (Holliger & Hudson, 2005). Additionally, antibody fragments may better penetrate physiological barriers better and recognize inaccessible epitopes (Holliger & Hudson, 2005). Engineered antibody fusion proteins, bispecific antibodies, and antibody-drug conjugates have further widened the scope of antibody-based treatment strategies (Chiu & Gilliland, 2016; Holliger & Hudson, 2005; Wu & Senter, 2005).

Given the massive socio-economic burden that disorders of the central nervous system (CNS) have placed on the healthcare system, efforts to develop effective disease-modifying strategies in the CNS has gained significant attention in the past decade (Hammarlund-Udenaes *et al.* 2014). Many of these efforts utilize antibodies that interfere with abnormal protein aggregation and aid their clearance, or have cytotoxic effects on degenerating neurons in the brain. However, therapeutic antibodies are large proteins that may not access the CNS at desired levels through systemic injection due to restrictive blood-brain barrier (BBB) (Reese & Karnovsky, 1967) and blood-cerebrospinal fluid barriers (BCSFBs) (Becker *et al*, 1967; Nabeshima *et al.*, 1975) properties. Here, we will briefly discuss the development of antibody-based therapies for CNS disorders as well as strategies for their successful delivery to the brain.

Brain Cancer

There are several types of cancers that occur within the CNS and they may be classified based on their site of origin (primary or metastatic), the cell type they are derived from (e.g., astrocyte, neuron, meningeal cell, etc.), their level of malignancy, and the CNS region they affect. Primary and metastatic brain tumors may have adverse effects due to several reasons: increased mass causing a rise in intracranial pressure (Mokri, 2001), physical encroachment on normal brain areas, and necrosis in tumors which may cause inflammation and cognitive decline due to neuronal cell death. Brain metastases from peripheral cancers are the most common type of intracranial tumors and typically arise from non-small cell lung cancer, breast

cancer, or melanoma (Chamberlain *et al.*, 2017). Brain metastases are associated with a poor (8%) 2-year survival rate (Hall *et al.*, 2000) and a median survival time of 4-12 months (Maher *et al.*, 2009), with few treatment options thus far (Chamberlain *et al.*, 2017). Primary brain cancers originate from abnormal cells within the brain. The most common type of primary brain cancer is the glioma, which as the name suggests originates from glial cells. Gliomas cause the second highest level of morbidity in individuals under 15 and the fourth highest level of morbidity in individuals between 35 and 54 (Black & Loeffler, 2004) and account for over 60% of primary neoplasms (Russel & Rubinstein, 1989). The prognosis for the most malignant form referred to as glioblastoma multiforme (GBM) continues to be poor, with most patients dying within a year of the initial diagnosis (Black & Loeffler, 2004). The median survival time for GBM patients following diagnosis is 14.6 months and the 5-year survival rate is 9.8 % (Johnson & O'Neil, 2012; Stupp *et al.*, 2005; Stupp *et al.*, 2009). Gliomas and brain metastases are typically diagnosed by neuroimaging in patients who present with symptoms such as chronic headaches, onset of seizures, nausea and vomiting, neurological deficits, and signs of increased intracranial pressure (Hall *et al.*, 2000; Miyauchi & Tsirka, 2018). Despite advances in new cancer therapeutics, the typical standard of care consists of surgical resection (when possible) followed by a combination of radio and chemotherapy with temozolomide (TMZ), which has limited benefit (Stupp *et al.*, 2005).

Passive immunotherapies for brain cancers

Passive immunotherapies have emerged as a promising class of therapeutics for the treatment of brain cancers and can overcome several challenges specific to this pathology. First, there is significant heterogeneity in brain tumors observed across individuals, between different cells within a tumor, as well as at different stages of tumor growth (Patel *et al.*, 2014; Sampson *et al.*, 2017). This heterogeneity underlies the need for therapies that are combinatorial and can be tailored to a specific antigen profile at different stages of brain cancer in a patient and across patients. Passive immunotherapy lends itself well to this purpose since antibody-based therapeutics have the ability to be highly selective in recognizing tumor-specific or relevant anti-tumor immunomodulatory antigens that can be targeted to either directly inhibit

tumor growth or selectively target a cytotoxic payload of chemo or radiotherapy to kill tumor cells. Another challenge in the treatment of brain cancers is their aggressive growth. For example, gliomas often cannot be fully surgically resected due to their infiltrative and diffuse spread (Claes *et al*., 2007). Surgical resection is also far more challenging in the case of many pediatric glioma patients since the tumors are often in non-hemispheric regions such as the brainstem (Green & Kieran, 2015). Additionally, it is often challenging to strike a balance between the efficacy, pharmacokinetic characteristics, and safety profile for small molecule therapeutics, putting them at a disadvantage compared to highly specific and potent antibody-based therapies (Ferrara *et al*., 2004). Overall, passive immunotherapies have many potential advantages for the treatment of brain cancers. To facilitate our discussion of antibodies investigated as potential therapies for brain cancer, we will describe them in the context of five categories based on their targets and modes of action: (i) anti-angiogenic antibodies, (ii) checkpoint inhibitors, (iii) lymphocyte target, (iv) antibody drug conjugates, and (v) metastatic brain tumor target.

Anti-angiogenic antibodies

The strategy to use anti-angiogenic agents as anti-cancer therapies was founded based on the correlation between pathological angiogenesis and tumorigenesis, first established by Judah Folkman over 40 years ago (Folkman, 1971; Folkman *et al*., 1971); it is summarized schematically in Fig. 2. Folkman's findings spurred the eventual isolation of the pro-angiogenic vascular endothelial growth factor (VEGF) (Leung *et al*., 1989; Senger *et al*., 1983; Senger *et al*., 1986). $VEGF_{165}$ or VEGFA is the most physiologically relevant isoform and may get cleaved by plasmin or matrix metalloproteinase-9 (MMP-9) to release bioactive fragments that promote angiogenesis. In January 1997, Genentech filed an Investigational New Drug application and initiated clinical trials for bevacizumab (commercial name – Avastin) – a humanized monoclonal recombinant antibody that binds to all VEGFA isoforms and their bioactive fragments with high affinity and specificity, inhibiting their interaction with VEGFRs, and thus suppressing VEGF signaling (Ferrara *et al*., 2004). The US Food and Drug Administration (FDA) approved the use of bevacizumab first for the treatment of colorectal cancer in 2004 and later expanded the range of approved

oncology indications to include the treatment of lung, breast, brain, cervical, and ovarian cancer over the next decade in keeping with new clinical trial data. Since GBM is associated with significant necrosis and high VEGF mRNA expression within clusters of necrotic tumor cells (Plate *et al*., 1992), it was hoped that 'anti-angiogenesis' therapies might offer a powerful treatment strategy for gliomas, which demonstrate the highest degree of angiogenesis of all human neoplasms (Brem *et al*., 1972; *et al*., 1992).

Initial Phase 2 clinical studies investigating systemically administered bevacizumab monotherapy or combinatorial therapies for recurrent glioblastoma demonstrated a reduced radiological contrast enhancement and increase in progression free survival (PFS) with bevacizumab (Field *et al*., 2015; Vredenburgh *et al*., 2007; Vredenburgh *et al*., 2007; Friedman *et al*., 2009; Kreisl *et al*., 2009). The FDA subsequently provided accelerated approval for systemically administered bevacizumab as a monotherapy to treat patients with recurrent GBMs that had progressed following initial treatment with chemotherapy and radiation (Cohen *et al*., 2009). However, the benefit of systemically administered bevacizumab for the treatment of recurrent glioblastoma as a monotherapy or in combination with radiotherapies and chemotherapies remains controversial (Field *et al*., 2015). Results from initial phase 2 clinical studies (Field *et al*., 2015; Vredenburgh *et al*., 2007; Vredenburgh *et al*., 2007; Friedman *et al*., 2009; Kreisl *et al*., 2009) must be interpreted with care and have several caveats such as small sample sizes, insufficient controls, instances of poor correlation between radiological contrast enhancement and anti-tumor effects, and no significant indication of increased overall survival (Field *et al*., 2015; Vredenburgh *et al*., 2007; Vredenburgh *et al*., 2007; Friedman *et al*., 2009; Kreisl *et al*., 2009). The more recent bevacizumab and lomustine for recurrent GBM (BELOB) clinical trial was a randomized controlled multicenter phase 2 study that included three treatment arms receiving bevacizumab monotherapy, lomustine monotherapy, or bevacizumab in combination with lomustine. By including a treatment group that did not receive bevacizumab the BELOB trial provided the first objective phase 2 clinical assessment of bevacizumab monotherapy versus chemotherapy alone or in combination with bevacizumab (Field *et al*., 2015; Tall *et al*., 2014). The primary outcome of overall survival at 9 months was lowest in the group receiving

bevacizumab alone and did not justify further clinical study for systemically administered bevacizumab monotherapy for recurrent GBM. Additionally, initial clinical investigation in a randomized controlled trial also demonstrated that systemically administered bevacizumab provided no benefit for newly diagnosed glioblastoma (Gilbert *et al*., 2014). The poor clinical outcomes of systemically administered bevacizumab for GBM may be attributed in some part to insufficient delivery to the brain target site. The elevated production of VEGF by tumor cells (Treps *et al*., 2017) and the occurrence of VEGF/VEGFRs on both luminal and abluminal sides of tumor vasculature underscores the importance of successful delivery of anti-angiogenic therapies to the brain tumor and migrating tumor cells by overcoming or circumventing the blood-tumor barrier (BTB) and BBB (Stefanini *et al*., 2009). Furthermore, many of the adverse side-effects of bevacizumab treatment, e.g., hypertension, fatigue, headache, hemorrhage, and thromboembolic events (Armstrong *et al*., 2012), may in fact be a consequence of off-target anti-angiogenic effects at non-tumor sites (Yu *et al*., 2016). Thus, drug delivery strategies that minimize exposure to non-tumor sites will prove beneficial.

Checkpoint inhibitors

To ensure specific targeting of abnormal or pathogenic entities versus normal host tissue, the immune system relies on the recognition of molecular checkpoints to make go/no-go decisions. Cancer cells have the ability to modulate these molecular checkpoints and thus escape attack from the immune system. Therefore, checkpoint inhibitors that may be antibodies or small molecules have emerged as a promising strategy to prevent checkpoint modulation by cancer cells and thus improve anti-tumor immune responses.

For example, although cancer cells often express antigens that can be recognized by T cells of the host immune system, they often escape T cell mediated elimination. This is because the appropriate priming and accomplishment of T cell effector functions requires not only the engagement of the T cell receptor (TCR) by antigen peptides presented on the major histocompatibility complex (MHC) of antigen presenting cells (APCs) and tumor cells, but also activation of additional co-stimulatory signals and suppression of

inhibitory signals (immune check points) expressed by APCs and tumor cells (Fig. 3) (Driessens *et al*., 2009). TCR engagement without the support of co-stimulatory signals results in a suppressed T cell immune responsive state referred to as 'anergy' (Driessens *et al*., 2009). Both co-stimulatory and inhibitory signals that influence T cell response occur in peripheral lymphoid organs as well as in the tumor microenvironment. Augmenting co-stimulatory signals and blocking inhibitory signals to increase anti-tumor T cell activity has thus emerged as a viable strategy for cancer therapy (Driessens *et al*., 2009).

Checkpoint inhibitor immunotherapies for cancer currently include six FDA approved IgG antibodies that target CTLA-4 (ipilimumab), PD-1 (pembrolizumab, nivolumab), or PD-L1 (atezolimumab, avelumab, and durvalumab). Ipilimumab (commercial name - Yervoy; Bristol-Myers Squibb; approved in 2011) was the first checkpoint inhibitor immunotherapy approved by the FDA for the treatment of melanoma. Pembrolizumab (commercial name – Keytruda; Merck), nivolumab (commercial name – Opdivo; Bristol-Myers Squibb) were approved by the FDA in 2014 for advanced melanoma. Atezolimumab (commercial name – Tecentriq; Genentech) was approved by the FDA in 2016 for urothelial carcinoma and metastatic lung cancer. Avelumab (commercial name – Bavencio; Merck, Pfizer, & Eli Lilly) was approved in 2017 for urothelial carcinoma and metastatic merkel cell carcinoma). Durvalumab (commercial name – Imfinzi; Medimmune/AstraZeneca) was approved in 2017 for advanced bladder cancer and in 2018 for advanced non-small cell lung cancer.

The CD-28 receptor on T cells and its B7-1/B7-2 ligands expressed by APCs constitute an important co-stimulatory pathway that can increase anti-tumor T cell activity. Conversely, CTLA-4 (cytotoxic T lymphocyte antigen-4) (Brunet *et al*., 1987), an inducible CD-28 homologue expressed by T cells, binds to B7-1/B7-2 ligands with a higher affinity than CD-28 (Azuma *et al*., 1993) and initiates an inhibitory response that can suppress anti-tumor T cell activity (Driessens *et al*., 2009). CTLA-4 expression has been shown to be upregulated on anti-tumor T cells and in particular on an immunosuppressive T cell population called regulatory T cells or Tregs. Thus, blocking CTLA-4 with antibodies such as ipilimumab offers a

potentially promising strategy to allow immune recognition of cancer cells (Fig. 4). Initial clinical investigation in a small cohort of glioblastoma patients testing ipilimumab in combination with bevacizumab showed that the combination was well tolerated and was associated with positive radiographic responses over a 3-month period (Carter *et al*., 2016), possibly warranting further clinical examination.

The expression of a receptor called PD-1 (programmed cell death-1) on activated T cells (Ishida *et al*., 1992) and its ligand PD-L1 (programmed cell death ligand-1) (Dong *et al*., 1999) on APCs constitutes an important inhibitory pathway that under normal physiological conditions plays an important role in preventing autoimmunity. However, the high expression of PD-L1 on several tumor cell types results in the PD-1/PD-L1 inhibitory pathway preventing an appropriate anti-tumor T cell response (Zang *et al*., 2007). PD-L1 is highly expressed by GBM tumor cells, in particular at the tumor periphery, resulting in the formation of a "molecular shield" between the tumor boundary and host anti-tumor T cells (Xue *et al*., 2017) and is a promising target for passive immunotherapy (Fig. 4). Nivolumab and pembrolizumab are anti-PD-1 monoclonal antibodies that are currently being clinically investigated for the treatment of primary and metastatic brain cancers as monotherapies and in combination with radiation therapies, chemotherapies, or other immunotherapies (Huang *et al*., 2017; Xue *et al*., 2017; Long *et al*., 2018; Goldberg *et al*., 2016). It remains to be seen whether CNS access of antibodies acting as checkpoint inhibitors is needed and, if so, whether such access is sufficient to alter the course of primary as well as metastatic brain cancers. As checkpoint inhibitors have been expected to primarily act in the periphery on T cells, it has been suggested that CNS access may not be needed for effects (Chamberlain *et al*., 2017); however, the observation that brain metastases continue to occur with systemic application of these newer therapies and that extracranial responses are generally superior to intracranial responses suggests that CNS delivery may in fact be needed for more robust responses (Chamberlain *et al*., 2017). Indeed, clinical trials are under way in which checkpoint inhibitor immunotherapies are administered both systemically and intrathecally (e.g., nivolumab; clinicaltrials.gov).

Lymphocyte target

Lymphocytes are not typically present in the central compartment (cerebrospinal fluid (CSF) and CNS tissue) in large numbers except in disease conditions (e.g., multiple sclerosis); however, T cells commonly perform a CNS immune surveillance function even in healthy individuals (Sallusto *et al*., 2012; Engelhardt *et al*., 2016). Although lymphocyte numbers in the CSF are very low under normal physiological conditions, recirculating lymphocytes have been shown to migrate into the CSF at levels similar to those observed in subcutaneous lymph (Seabrook *et al*., 1998). Primary CNS lymphoma (PCNSL) is a rare form of non-Hodgkin lymphoma that occurs in the brain, leptomeninges, or eyes (Mrugala *et al*., 2009; Pfannl & Harris, 2004). Median survival of PCNSL patients is 13 months with a 5-year survival rate less than 5% (Neuwelt *et al*., 1991). Immunodeficiency is a major risk factor for PCNSL, with a high rate of incidence observed in patients infected with the human immunodeficiency virus (HIV) or organ transplant recipients (Pfannl *et al*., 2004; Cote *et al*., 1996; Ferry & Harris, 1994). PCNSL is thought to typically involve the malignant transformation of B cells within the brain microenvironment, although the precise biological details are still lacking (Mrugala *et al*., 2009). Malignant lymphocytes from the periphery extravasate at the level of arterioles and venules to first enter and spread along enlarged perivascular spaces, and eventually move into the CNS parenchyma as the outer boundary of the perivascular space is compromised (Aho *et al*., 1993). Once malignant lymphocytes enter the CNS they are not easily eradicated since the CNS is a relatively immune-privileged site. The adhesion molecule CD44 and its ligands likely play an important role in the extravasation of malignant lymphocytes; high CD44 expression is observed within PCNSL lesions in the white matter (Aho *et al*., 1993). Due to their diffuse progression, surgical resection is not a useful strategy for CNS lymphomas. High dose methotrexate (HD-MTX) chemotherapy for newly diagnosed PCNSL and whole brain radiotherapy (WBRT) for recurring PCNSL are the current standard of care (Phillips *et al*., 2014). Poor penetration of methotrexate through the BBB due to the presence of efflux transporters (methotrexate is a substrate for many such transporters, including p-glycoprotein and breast cancer resistance protein; Loshner & Potschka, 2005) and toxicity associated with high doses of methotrexate pose additional challenges for this treatment strategy (Li *et al*., 2013). Passive immunotherapy

approaches targeting abnormal lymphocytes in PCNSLs are currently being explored (Fig. 5). For example, systemic administration of rituximab, a chimeric murine monoclonal antibody that recognizes the B cell specific cell surface antigen CD20 (Citterio *et al*., 2017), has been reported to elicit radiographic responses in 4 out of 12 patients in a small clinical study, and these may be synergistic when delivered in combination with chemotherapy (Batchelor *et al*., 2011). Osmotic disruption of the BBB in combination with intra-arterial methotrexate has also been demonstrated to improve patient outcomes by improving chemotherapeutic delivery to the CNS (Neuwelt *et al*., 1991; Angelov *et al*., 2009).

Antibody drug conjugates

Antibody drug conjugates (ADCs) are targeted antibodies linked to anti-tumor cytotoxic moieties and have been successfully used in the treatment of peripheral solid tumors (Gan *et al*., 2017). ADCs may allow tumor specific targeting of radio and chemotherapies, while reducing off-target side effects. However, the benefit of ADCs may be lost over chronic application if the expression of the targeted tumor antigen gets downregulated (Miyauchi & Tsirka, 2018). Most passive immunotherapies with naked (unconjugated) antibodies for brain cancers have thus far demonstrated limited success in improving overall survival (e.g., bevacizumab in GBM). There are two possible reasons for these disappointing outcomes – (i) unconjugated mAbs are not eliciting sufficient pharmacological efficacy at their target site, possibly due to downregulation of target antigens or other tumor compensatory mechanisms, and (ii) antibodies are not being delivered effectively to the target sites due to challenges posed by CNS barriers such as the BBB and the BCSFBs. Using ADCs as a therapy for brain cancers is a potential way to navigate the first pharmacological challenge since they provide an additional benefit of delivering an effective cytotoxic payload (Figure. 6). Several radioimmuno-conjugates are being investigated in clinical trials for the treatment of brain cancer. For example, ^{188}Re-nimotuzumab, a beta-emitting radioisotope of rhenium linked to an anti-epithelial growth factor receptor (EGFR) antibody is being investigated for the treatment of gliomas overexpressing EGFR (Casaco *et al*., 2008). ^{211}At-ch81C6, an alpha-emitting radioisotope of astatine linked to an anti-tenascin antibody and ^{131}I-BC2/BC4, a beta and gamma emitting radioisotope of

iodine linked to an anti-tenascin antibody are being investigated for the treatment of GBM (Riva *et al*., 1999). Tenascin C is an extracellular matrix protein whose expression is controlled by Notch signaling; in GBM tumor cells, aberrant notch signaling results in over-expression of Tenascin C resulting in increased tumor cell migration which aids the invasiveness of GBM tumors (Sivasankaran *et al*., 2009; Zalutsky *et al*., 2008). Bacterial toxins conjugated to proteins such as transferrin and interleukin-13 are being investigated in the treatment of high-grade gliomas. A similar strategy with bacterial toxins conjugated to targeted antibodies might also serve as a related promising strategy. These toxins include molecules such as the diphtheria toxin and the *Pseudomonas aeruginosa* exotoxin A, among others (Gan *et al*., 2017). ABT-414 (AbbVie) – anti-EGFR antibody conjugated to the cytotoxin monomethyl auristatin F (MMAF) – an anti-mitotic agent that inhibits cell division – is currently under clinical evaluation for newly diagnosed GBM with EGFR amplification (Phillips *et al*., 2016). AMG-595 (Amgen), an anti-EGFR antibody conjugated to the cytotoxin maytansinoid emtansine (DM1), is currently under clinical evaluation for newly diagnosed GBM with EGFR amplification; DM1 binds to the ends of microtubules and thereby destabilizes the cytoskeleton of tumor cells (Lopus *et al*., 2010).

Metastatic brain tumor target

Primary tumors in the periphery can metastasize to the brain (Chamberlain *et al*., 2017; Parrish *et al*., 2015). Metastatic brain cancers are as much as ten times more common than primary brain cancers, with brain metastases from lung (~50%), breast (~15-25%) and melanoma (~5-20%) being the most common (Chamberlain *et al*., 2017; Parrish *et al*., 2015; Gavrilovic *et al*., 2005). Brain cancer metastases are often non-angiogenic tumors, i.e., the metastatic cancer cells co-opt the existing brain vasculature, which may make anti-angiogenic therapies less effective in treating these tumors (Valiente *et al*., 2014). Systemic treatment with trastuzumab, an anti-human epidermal growth factor receptor 2 (HER2) antibody (commercial name – Herceptin; Genentech/Roche) has been used to effectively treat extracranial breast cancer that overexpresses HER2 (Hudis, 2007; Fig. 7). However, systemic trastuzumab treatment also has a significant correlation to increased incidence of brain metastasis (Paik *et al*., 1990) and this correlation is

most likely the consequence of trastuzumab not being effectively delivered to the metastatic brain tumors across the BTB and BBB (Kirsch & Hochberg, 2003). Intrathecal administration of trastuzumab in breast cancer patients with leptomeningeal carcinomatosis has shown some promise warranting further investigation in a larger study (Park *et al*., 2016; Lu *et al*., 2015). Similar considerations hold true of passive immunotherapies for the treatment of other types of brain metastases as such as non-small cell lung cancer (treatment – nivolumab; anti-PD1 antibody; commercial name – Opdivo; Bristol-Myers Squibb; Watanbe *et al*., 2017), and melanoma (treatment – ipilimumab; anti-CTLA-4 antibody; commercial name – Yervoy; Bristol-Myers Squibb; Margolin, 2012; Margolin *et al*., 2012).

Current strategies and challenges in delivering passive immunotherapies to brain tumors

Delivering passive immunotherapies to treat brain cancers is difficult. Both systemic and central delivery approaches used clinically face unique challenges in the treatment of brain cancers, emphasizing the need for new approaches and strategies for tumor drug delivery. Targeting passive immunotherapies to brain tumors via systemic delivery suffers the inherent drawback of having a large fraction of the administered dose being potentially lost to the rest of the body and is heavily dependent on the capacity of antibodies to not only cross the BTB but also areas of normal BBB that tumor cells may be hidden behind. Hydrophilic macromolecules like antibodies are thought to cross the walls of peripheral microvessels typically via passive movement across fenestrations and interendothelial clefts or via active receptor-mediated transcytosis (Wang *et al*., 2008). In order of increasing permeability, brain tumor microvasculature may include non-fenestrated, continuous capillaries, which closely resemble those observed in normal brain tissue, fenestrated continuous capillaries, and fenestrated capillaries with interendothelial gaps as large as 1 μm (Groothuis, 2000; Schlageter *et al*., 1999); importantly, BTB permeability in animal models of brain cancer has been shown to exhibit marked heterogeneity ranging from minimal to marked permeability that is not easily predictable (Lockman *et al*., 2010). Passive movement of large biologics like antibodies may only occur appreciably across capillaries with open fenestrations, large interendothelial gaps, or via transcytosis (Sarin, 2010; Michel, 1996). To harness the potential of receptor mediated transcytosis across

the walls of tumor microvessels, bispecific antibodies that recognize both a transcytosis receptor at the BTB and an anti-tumor antigen within the brain tumor may be used (Razpotnik *et al*., 2017). However, transcytosis receptors at the BTB may also be expressed elsewhere within the body, which increases the possibility of off-target side effects (Gatter *et al*., 1983; Yu *et al*., 2013). Therapeutic antibodies designed to exploit receptor-mediated transcytosis at the BTB for transport into the tumor may also face the challenge of having to compete with the endogenous ligand of the receptor (Groothuis, 2000). Typically, microvessel permeability within the tumor core is high and drops sharply at the tumor margins (van Tellingen *et al*., 2015). However, cancer cells may reside in the tumor periphery and remain protected by the BBB, facilitating the possibility of tumor spread or recurrence. Overall, the permeability of microvessels within brain tumors and surrounding brain varies considerably depending on the type of tumor and the location of the microvessels (Groothuis, 2000), making systemic delivery of passive immunotherapies to brain tumors a complex task. Strategies such as transiently disrupting the BTB to enhance systemic drug delivery to brain tumors by systemic infusion of hyperosmolar mannitol appear to have some benefit (Neuwelt *et al*., 1991; Angelov *et al*., 2009). However, permeability of the BBB in normal brain tissue may be relatively more affected than the BTB by systemic osmotic approaches (Zunkeler *et al*., 1996), resulting in neurotoxic sequelae in healthy tissue. Distribution of antibody-based therapeutics within solid tumors has often been found to be heterogeneous and sites of antibody accumulation often do not correlate with sites of high antigen expression (Jones *et al*., 1986). This phenomenon of problematic and uneven distribution of systemically administered antibody-based therapeutics within tumors has been attributed to the high interstitial pressure that builds within tumors due to the increased angiogenesis and vascular hydraulic conductivity in tumors (Munson & Shieh, 2014), although other factors may also be at play. The more or less uniformly high interstitial pressure within tumors and sharp drop in pressure at the tumor periphery may result in systemically administered macromolecules like antibody-based therapeutics to accumulate close to blood vessels (points of entry) and the tumor periphery, with little delivery occurring to the rest of the tumor (Baxter & Jain, 1989; Jain & Baxter, 1998).

Strategies involving the direct administration of antitumor drugs into the CNS have emerged to overcome some of the challenges faced by systemic delivery. Methods such as convection-enhanced delivery (CED) (Bobo *et al*., 1994) or injection/infusion of drugs directly into cavities following surgical tumor resection, can deliver passive immunotherapies directly to the brain while bypassing the BTB, the BBB, and the BCSFBs. However, in addition to being highly invasive, such strategies are likely to be practically restricted to local drug delivery due to the transport limitations associated with the brain extracellular spaces where long range distribution is limited by diffusion (Hannocks *et al*., 2018; Wolak *et al*., 2015); diffusive transport in brain extracellular spaces is size-dependent and will be particularly limited for large macromolecules like antibodies (Wolak *et al*., 2015). While this transport limitation may be desirable to 'target' drugs to a small area of a brain tumor, cancer cells within the tumor periphery may still be beyond reach. Direct injection or infusion (including the aforementioned CED) into brain tumors (intratumoral, intracystic, and intralesional) or surrounding tissue has been utilized clinically to deliver a variety of antibody therapeutics (clinicaltrials.gov). Examples of passive immunotherapies administered via CED to treat brain cancers include: ^{131}I-chTNT-1/B (commercial name – Cotara; Peregrine Pharmaceuticals/Avid bioservices) – an ADC consisting of an iodine radioisotope conjugated to an anti-DNA-histone H1 complex monoclonal antibody [115]; ^{123}I- or ^{131}I-labeled 81C6 (commercial name – Neurodiab; Bradmer Pharmaceuticals) – an ADC consisting of an iodine radioisotope conjugated to an anti-tenascin monoclonal antibody (Sampson *et al*., 2006); ^{131}I-8H9 (commercial name – Burtomab; Y-mAbs Therapeutics) – an ADC consisting of an iodine radioisotope conjugated to a murine anti-human B7-H3 monoclonal antibody (Ivasyk *et al*., 2017; Larson *et al*., 2015); D2C7-IT – an ADC consisting of a *Pseudomonas* exotoxin (PE38KDEL) conjugated to a single chain variable fragment of an anti-EGFRwt/EGFRvIII monoclonal antibody (Bao *et al*., 2016); and Me1-14 F(ab')$_2$ – a F(ab')$_2$ antibody fragment of the anti-proteoglycan chondroitin sulfate-associated protein murine monoclonal antibody Me1-14 (Bigner *et al*., 1995). Clinical trials infusing antibodies into a surgically created resection cavity have also been conducted with ADCs (e.g., ^{123}I- or ^{131}I-labeled 81C6 [121]).

Other methods of delivery that circumvent the BTB, BBB, and BCSFBs are intrathecal and intracerebroventricular (ICV) administration into the CSF; these routes may provide more global delivery of antibody-based therapeutics within the CNS due to their capacity to access low-resistance pathways such as perivascular spaces surrounding leptomeningeal and cerebral blood vessels that potentially allow rapid distribution throughout the brain and exchange between the interstitial fluid and CSF (Pizzo *et al*., 2018). Numerous clinical trials have been or are currently being conducted for treatment of CNS cancer using CSF-administered antibodies. Intrathecal/ICV rituximab - an anti-CD20 monoclonal antibody (commercial name – MabThera/Rituxan; Genentech/Roche) - has been administered to treat CNS lymphoma (Perissinotti & Reeves, 2010). Intrathecal/ICV ^{131}I-3F8 - a radiolabeled anti-GD2 ganglioside monoclonal antibody - has been used to treat primary and metastatic leptomeningeal or brain tumors, including a trial for medulloblastoma (Larson *et al*., 2015). Intrathecal/ICV administration of two anti-HER2 antibodies has been investigated for the treatment of leptomeningeal metastases associated with HER2+ breast cancer - trastuzumab (commercial name – Herceptin; Genentech/Roche) monotherapy or in combination with pertuzumab (commercial name – Perjeta; Genentech/Roche; Perissinotti & Reeves, 2010; Calias *et al*., 2014). Intrathecal/ICV ^{131}I-8H9 has been given Breakthrough Therapy Designation by the FDA for the treatment of neuroblastoma (Larson *et al*., 2015). ^{123}I- or ^{131}I-labeled 81C6, Me1-14 F(ab')$_2$, and LMB-7 (or B3(Fv)-PE38, a single-chain variable fragment of the murine B3 anti-Lewis Y-related carbohydrate monoclonal antibody conjugated to a portion of the *Pseudomonas* exotoxin PE38; Pastan *et al*., 2006) have also been administered into the CSF for primary or metastatic brain cancer and leptomeningeal cancer. Finally, other non-conventional routes of administration (e.g., intranasal delivery) are also being actively investigated to target therapies to brain tumors (Lochhead & Thorne, 2012). The intranasal route for drug delivery is thought to achieve some degree of CNS targeting by accessing pathways associated with the olfactory and trigeminal nerve systems in the nasal mucosae that allow brain entry at the level of the olfactory bulbs and brainstem, respectively (Thorne *et al*., 2004). Intranasal delivery in particular may prove to be relevant for the treatment of brainstem gliomas, which are not particularly amenable to surgical resection or invasive drug delivery methods (Goodwin *et al*., 2016).

*Alzheimer's disease**

Alzheimer's disease (AD) and related dementia are estimated to affect more than 50 million patients worldwide (World Alzheimer's Report 2018), with more than 5.8 million patients in the United States as of 2018 (Alzheimer's association, 2019). These numbers are likely to double in the US and triple worldwide by 2050, partly due to the rise of a more susceptible ageing demographic (Alzheimer's association, 2019; World Alzheimer's Report 2018). The clinical definition for AD has evolved over the last three decades from a cognitive syndrome (McKhann *et al.*, 1984) to a multi-faceted gamut of pathological changes that gradually lead to cognitive impairment over decades (Serrano-Pozo *et al.*, 2011). Cognitive impairment among AD patients often manifests as one or more progressively declining core domains (memory, executive function, language, visuospatial perception, and intellect) (McKhann *et al.*, 2011; Jack *et al.*, 2011). Further, AD can be difficult to diagnose overlapping symptoms with a variety of other neurological conditions, including (but not limited to) vascular dementia, dementia with Lewy bodies, frontotemporal dementia and cardiovascular disease (McKhann *et al.*, 2011).

Passive Immunotherapies for Alzheimer's disease*

AD can be characterized by simultaneous accumulation of two abnormal proteins and their aggregates – amyloid-beta and hyperphosphorylated tau (Jack *et al.*, 2011). These proteins can occur in several different forms and aggregation states during AD progression and offer a wide range of targets for clinical intervention strategies. Amyloid beta (Aβ), for instance, refers to a heterogeneous set of monomeric peptides resulting from the sequential cleavage of amyloid precursor protein (APP) through several different enzymes. These peptides are typically in the range of 38-43 amino acids among other isoforms (Selkoe & Hardy, 2016; Chow *et al.*, 2010). Enzymes that cleave APP (alpha and beta secretase) generate multiple protein fragments at the amino (e.g. secreted APP proteins or sAPPs) and carboxy (C) termini (e.g. carboxy terminal fragments or CTFs) (Chow *et al.*, 2010), while gamma-secretase (γ-secretase) acts downstream by cleaving these membrane-bound fragments (e.g. CTF83, CTF99) into smaller peptides (e.g.

p3, Aβ, APP intracellular domain or AICD) (Chow *et al.*, 2010). APP is primarily cleaved by β-secretases (e.g. beta-site APP-cleaving enzyme 1, or BACE1, in the brain) and γ-secretases resulting in the production of pathogenic Aβ isoforms (Chow *et al.*, 2010; Haass *et al.*, 2012; Finder & Glockshuber, 2007) as per the amyloidogenic or Aβ-generating pathway. In the non-amyloidogenic pathway observed in healthy individuals, APP is primarily cleaved by α-secretases and γ-secretase within the Aβ peptide sequence that prevent the formation of pathogenic Aβ species (Chow *et al.*, 2010). The less amyloidogenic isoform, Aβ40, is largely associated with the smooth muscle layer of cerebral arteries while Aβ42 is the earliest and most abundant isoform in the brain parenchyma (Serrano-Pozo *et al.*, 2011; Tarasoff-Conway *et al.*, 2015). N-terminally truncated forms of Aβ40 and Aβ42 have also been demonstrated to form harmful pyroglutamate Aβ isomers (pGlu-Aβ (3-40/42)) following cyclization at the N-terminus (Hook *et al.*, 2014). Increased Aβ production or the lack of efficient Aβ clearance spurs CNS buildup and aggregation as multiple units fuse together to form toxic, soluble oligomeric species (Musiek & Holtzman, 2015; Benilova *et al*, 2012). These soluble oligomers further act as seeds for aggregation of insoluble, fibrillar Aβ species (Ahmed *et al.*, 2010; Roher *et al.*, 2000) and accumulate within the brain parenchyma. Fibrillar Aβ may deposit around the smooth muscle layer of cerebral arteries, commonly referred to as cerebral amyloid angiopathy (CAA) (Serrano-Pozo *et al.*, 2011). Both of these processes (among others) are ultimately responsible for the neurodegeneration observed in AD (Serrano-Pozo *et al.*, 2011; Selkoe & Hardy, 2016). While therapeutic strategies have historically focused on insoluble fibrillar oligomers or 'plaques', recent reports suggest engaging soluble oligomers may have a greater likelihood of intervening Aβ aggregation effectively (Selkoe & Hardy, 2016; Sengupta *et al.*, 2016). Likewise, microtubule associated tau protein (MAPT) may get abnormally hyperphosphorylated and detach from cytoskeletal proteins to form several different types of pathologic conformations such as paired helical filaments (PHFs), pre-neurofibrillary tangles (pre-NFTs) and eventually neurofibrillary tangles (NFTs) that lead to cellular atrophy or eventually cell death (Iqbal *et al.*, 2016). Passive immunotherapy lends itself well to the task of targeting these different Aβ and hyperphosphorylated tau antigens over the course of AD progression and has therefore emerged as a promising treatment strategy (Lannfelt *et al.*, 2014; St-Amour *et al.*, 2016). The fact that no disease-

modifying therapies have currently reached FDA approval status for AD (Cummings *et al.* 2017) further emphasizes the need to develop antibody-based therapies for AD. In this review, we will discuss these therapies (Fig. 8) based on their antigen/target as (i) anti-beta amyloid antibodies, (ii) anti-tau antibodies, (iii) anti-BACE 1antibodies, (iv) anti-apolipoprotein E (APOE) antibodies, and (v) anti-inflammatory antibodies.

Anti-beta amyloid antibodies

Aβ was the first antigen target investigated for potential AD passive immunotherapies based on two independent studies where two monoclonal antibodies (3D6 and m266) demonstrated a reduction in brain Aβ levels via different mechanisms following repeated systemic administration (Bard *et al.*, 2000; DeMattos *et al.*, 2001). Studies at Elan Pharmaceuticals with 3D6 suggested that repeated systemic injections of an antibody targeting fibrillar Aβ species led to plaques reduction via Fc-receptor-mediated phagocytosis (Bard *et al.*, 2000). In contrast, m266 developed by David Hotlzman's group against soluble Aβ species indicating indicated a shift in the Aβ aggregates equilibrium between CNS and peripheral compartments by repeated m266 administration (DeMattos *et al.*, 2001). In 2006, both of these 'first-generation' antibodies were developed into their humanized version under the labels bapineuzumab (Jannsen/Pfizer) and solanezumab (Eli Lilly) (Panza *et al.*, 2014) for Phase 2 clinical trials. However, clinical trials for bapineuzumab were discontinued in 2013 due to its inability to meet clinical endpoints (Salloway *et al.*, 2014). Systemic administration of solanezumab also failed to show significant improvement in primary cognitive outcomes in two phase 3 clinical trials (EXPEDITION 1 and EXPEDITION 2) in patients diagnosed with mild-to-moderate AD (Doody *et al.*, 2014). Disappointing outcomes of the bapineuzumab and solanezumab clinical trials may potentially be attributed to many possible factors: (i) initiation of treatment too late in the disease process (Doody *et al.*, 2014); (ii) the possibility that targeting Aβ alone may be insufficient to alter disease progression in some cases (Doody *et al.*, 2014); and (iii) insufficient central delivery of systemically applied antibodies to the appropriate target sites (St-Amour *et al.*, 2013. Further investigation into the possibility of therapeutic effects at an earlier

stage of AD was spurred by secondary analysis of the EXPEDITION 1 and 2 trial data which showed that solanezumab treatment resulted in lesser cognitive and functional decline than placebo among trial participants diagnosed with mild AD (Siemers *et al.*, 2016). However, investigation of systemic solanezumab passive immunotherapy in a third Phase 3 trial specifically for mild AD (EXPEDITION 3; 400 mg solanezumab or placebo administered intravenously every 4 weeks for 76 weeks) also recently failed to show any significant effect on cognitive outcomes (Honig *et al.*, 2018). Higher doses of solanezumab are currently being investigated in prodromal populations at risk for AD in two major clinical studies: (i) the Dominantly Inherited Alzheimer Network (DIAN) clinical trial investigating solanezumab as a preventative treatment in individuals at risk for early onset AD due to a dominantly inherited genetic mutation (Panza *et al.*, 2018) and (ii) the A4 trial investigating solanezumab as a preventative treatment in older individuals at risk for AD due to amyloid plaque build-up but who do not yet show any cognitive impairment (Sperling *et al.*, 2014). The results of these later trials may ultimately better inform on solanezumab efficacy and its limitations.

Other anti-Aβ passive immunotherapies for which (i) clinical investigation has been discontinued due to failure to meet clinical endpoints and/or (ii) clinical study outcomes have not been fully reported include: ponezumab (Rinat Neuroscience/Pfizer), an anti-Aβ monoclonal antibody that specifically binds to the Aβ40 fragment that accumulates in the walls of blood vessels as part of the CAA process; GSK933776 (GlaxoSmithKline), an anti-Aβ monoclonal antibody that binds with higher affinity to Aβ monomers and has a modified Fc region that reduces effector-mediated functions to minimize the risk of side effects such cerebral edema or microhaemorrhages that are detected as amyloid-related imaging abnormalities (ARIA) (Andreasen *et al.*, 2015); AAB-003 (Pfizer/Janssen), a modified version of bapineuzumab that has a modified Fc region that reduces effector-mediated functions to minimize the risk of ARIA (Delnomdedieu *et al.*, 2016); SAR228810 (Sanofi), an anti-Aβ monoclonal antibody that binds with higher affinity to Aβ protofibrils than Aβ oligomers or monomers and has reduced effector-mediated function to minimize the

risk of ARIA; and MEDI1814 (AstraZeneca and Eli Lilly), an anti-Aβ monoclonal antibody that binds with high affinity to Aβ42.

Numerous anti-Aβ passive immunotherapy trials are still under clinical investigation (clinicaltrials.gov), e.g., BAN2401 (Biogen/Eisai), gantenerumab (Hoffman-La Roche), crenezumab (Genentech/Hoffman-La Roche), and KHK6640 (Kyowa Hakko Kirin), anti-Aβ monoclonal antibodies that bind with higher affinity to more aggregated insoluble conformations of Aβ such as protofibrils and/or fibrils compared to soluble Aβ monomers and/or oligomers; aducanumab (Biogen), an anti-Aβ monoclonal antibody that binds with higher affinity to soluble oligomeric as well as insoluble fibrillar Aβ aggregates compared to monomeric Aβ; LY3002813 (Eli Lilly), an anti-Aβ monoclonal antibody that recognizes the pyroglutamate Aβ monomer Aβp3-42; and intravenous immunoglobulin (IVIg; Octapharm), an immunoglobulin serum fraction obtained from healthy donors, used to supplement/replace the immunoglobulin fraction in AD patients.

Anti-tau antibodies

Analogous to anti-amyloid therapeutic interventions, anti-tau antibodies targeting hyperphosphorylated toxic tau conformations are being investigated as potential passive immunotherapies for AD (Pedersen & Sigurdsson, 2015; Asuni *et al.*, 2007). Immunotherapy approaches for intracellular tau aggregates faced several initial hurdles given that antibodies are too large to effectively target intracellular antigens (Iqbal *et al.*, 2005). Emerging evidence now suggests that secreted extracellular tau species may be involved in initiating the spread of pathology as seeds for tau aggregation (Yamada *et al.*, 2017; Yamada *et al.*, 2017a; de Calignon *et al.*, 2012), thus providing a clear rationale for developing tau immunotherapy strategies. Anti-tau passive immunotherapy trials that are still under clinical investigation (clinicaltrials.gov) include: RO7105705 (Hoffman-La Roche), an anti-tau antibody that specifically recognizes a phosphorylated serine residue (Tau/pS409) present in intracellular pre-NFTs as well as extracellular neuropil threads and mature NFTs; LY3303560 (Eli Lilly), an anti-tau antibody that specifically binds to the N-terminus of tau

aggregates over monomers; ABBV-8E12 (AbbVie), an anti-tau antibody that has high affinity for all forms of extracellular aggregated tau; and BIIB092 (Bristol-Myers Squibb and Biogen), an anti-tau antibody that has high affinity for tau residues 15-24 and specificity for extracellular secreted forms of tau, as well as tau aggregates. Gene therapy strategies to target intracellular tau are also being investigated; these include the use of anti-tau intracellular antibodies or 'intrabodies' (Ising *et al*., 2017). Intrabodies are antibody fragments (e.g., single chain variable fragments) that can recognize specific antigens such as tau and are expressed intracellularly using viral gene therapy approaches to transduce desired cell populations (Ising *et al*., 2017; Marasco, 1997; Chen *et al*., 1994).

Anti-BACE1 antibodies

Another strategy to reduce the production of Aβ is to inhibit BACE1, one of the enzymes that cleaves APP to produce Aβ. Anti-BACE1 antibodies are being investigated to inhibit APP cleavage by either sterically blocking the BACE1 active site or by blocking the allosteric site that regulates enzyme activity. Preclinical testing has shown that this strategy holds promise (Atwal *et al.*, 2011; Arbel *et al.*, 2005) and clinical investigation will likely follow.

Anti-ApoE antibodies

Apolipoprotein E (ApoE) is the primary carrier of lipids and cholesterol within the brain (Puglielli *et al.*, 2003) and the ε4 isoform of ApoE has been identified as one of the strongest genetic risk factors for late-onset AD (Corder *et al*., 1993; Strittmatter *et al*., 1993). Recent studies have highlighted the potential of anti-ApoE antibodies as passive immunotherapy candidates in AD (Luz *et al.*, 2016; Liao *et al.*, 2018) and clinical investigation is likely to follow.

Anti-inflammatory antibodies

Several preclinical studies have shown that systemic inflammatory stimuli in the periphery can trigger an adverse central immune response, which subsequently leads to neurotoxicity (Perry & Holmes, 2014; Cunnigham *et al*, 2005). Indeed, AD patients with elevated levels of the pro-inflammatory cytokine TNF-α have a typically faster cognitive decline (Perry *et al.*, 2007). Etanercept (Amgen and Pfizer) is a fusion protein consisting of human IgG1 Fc portion linked to a dimeric ligand-binding region of tumor necrosis factor alpha cell surface receptor (p75 TNF-α) (Decourt *et al.*, 2017) that was under clinical investigation as a potential passive immunotherapy for AD. However, the inability to meet clinical endpoints has currently halted further investigation of this strategy.

Current strategies and challenges in delivering passive immunotherapies for Alzheimer's disease*

Pathological changes in AD initiate as localized protein aggregation but spread globally throughout the course of disease progression (Braak *et al.* 2011; Thal *et al*., 2002). Hence, whole brain delivery of antibodies will eventually become crucial to obtain widespread CNS effects and acceptable clinical efficacy. Currently, most AD passive immunotherapy clinical trials utilize the systemic route of administration. Unfortunately, it is likely that systemically administered exogenous antibodies do not cross the BBB or BCSFBs to an appreciable extent and often remain restricted to the endothelial compartment where they cannot engage target antigens (St-Amour *et al*., 2013). High doses of systemic exogenous antibodies, often administered in order to attempt overcoming poor delivery to the CNS, have been linked to adverse events such as vasogenic edema and microhemorrhages (ARIA-E or ARIA-H respectively) (Sperling *et al.*, 2011). Strategies to enhance delivery of systemically administered exogenous antibodies to the CNS such as transient disruption of the BBB with focused ultrasound (e.g., BAM-10; Jordão *et al.*, 2010), or shuttling antibodies across CNS barriers using bispecific antibodies (e.g., anti-BACE-1/TfR; Yu *et al*., 2011; Zuchero *et al*., 2016; Kanodia *et al*., 2016) are also being tested.

Strategies exploring the administration of passive immunotherapies for AD directly into the central compartment have also received increasing interest. For example, preclinical studies have shown that intracerebroventricular (ICV) administration of anti-amyloid antibodies results in widespread brain delivery and reduces parenchymal plaque burden (Chauhan *et al.*, 2001; Chauhan *et al.*, 2004; Chauhan *et al.*, 2004; Chauhan *et al.*, 2005). ICV administration of passive immunotherapies for AD also outperforms systemic delivery approaches, both in efficacy and safety (reduced incidence of ARIAs; Thakker *et al.*, 2009). Perispinal administration has received renewed attention as a potential means to deliver drugs to the intracranial venous system, which is potentially in communication with the cerebrospinal fluid (CSF) (Tobinik, 2016). Perispinal injection involves injecting the drug between the spinous processes of the lower dorsal vertebrae, outside the spinal canal, and posterior to the ligamentous flavum with the expectation that the drug is rapidly absorbed by local vertebral venous vasculature and eventually drains into the external vertebral venous plexus (EVVP) (Tobinik, 2016). Vertebral veins are valveless and are in communication with intracranial veins allowing drug in the EVVP to access the intracranial venous system, and eventually the CSF (Tobinik, 2016) potentially via communication between the intracranial venous system, arachnoid villi (Sakka *et al.*, 2011), dural lymphatics (Aspelund *et al.*, 2015; Louveau *et al.*, 2015), and other extracellular pathways (Broadwell & Sofroniew, 1993). Perispinal administration of etanercept has showed rapid anti-inflammatory response in some studies (Tobinik, 2008; Tobinik & Gross, 2008; Tobinik & Gross, 2008; Tobinik, 2009); however, the outcomes of this route are somewhat controversial (Roerink, 2015). Intranasal delivery is also emerging as a promising non-invasive central delivery approach to target passive immunotherapies to the CNS; indeed, delivery of antibodies (Chauhan & Chauhan, 2015; Kolobov *et al.*, 2012; Kolobov *et al.*, 2013), as well as antibody fragments (Cattepoel *et al.*, 2011), have been reported to reduce pathology in rodent models of AD. However, the detailed CNS distribution, mechanisms responsible for transport from the nasal epithelia to the CNS, and strategies to optimize CNS delivery of intranasally applied antibodies have only recently been explored (Kumar *et al.*, 2018). Further work is clearly needed to better define alternative delivery approaches for targeting antibodies to the CNS.

Parkinson's disease

Parkinson's disease (PD) affects nearly 10 million individuals worldwide and nearly 1 million individuals in the United States alone and, like other neurodegenerative disorders, PD poses a significant financial burden due to large healthcare costs and lost earning potential associated with those afflicted and their caregivers (e.g., it may be estimated that PD accounts for over $20 billion in direct and indirect costs in the U.S. today with PD prevalence / costs expected to rise dramatically by 2040; Kowal *et al.*, 2013; Elkouzi, 2018). Bradykinesia, postural instability, rigidity, and tremor are the major clinical symptoms observed in Parkinsonian disorders (Dickson, 2012). Accumulation of an abnormal form of the presynaptic neuronal protein alpha synuclein within neuronal perikarya as Lewy bodies is a hallmark of idiopathic PD (Dickson, 2012). As with AD, there are currently no disease-modifying therapeutics for the treatment of PD; strategies that can target different alpha synuclein aggregation profiles and other pathological targets observed with PD progression will be crucial for success. Passive immunotherapies are well suited to this challenge and are therefore currently being investigated for the treatment of PD (Valera & Masliah, 2013).

Passive immunotherapies for Parkinson's disease

In this section, we will limit the discussion to antibodies as potential therapies for PD (Fig. 9) in the context of three broad categories based on their antigen/target: (i) anti-alpha synuclein antibodies, (ii) fusion proteins, and (iii) anti-LAG3 antibodies.

Anti-alpha synuclein antibodies

A study by Masliah and coworkers showing a reduction in alpha-synuclein pathology in the CNS was the first preclinical study to investigate passive immunotherapy targeting alpha-synuclein for PD treatment [218]. Several other preclinical studies followed to investigate the efficacy of anti-alpha synuclein antibodies in PD therapy (George & Brundin, *et al.*, 2015). These antibodies demonstrated varied specificity for epitopes

and conformations of alpha synuclein and included the C-terminus (Bae *et al.*, 2012; Games *et al.*, 2014), N-terminus (Shahaduzzaman *et al.*, 2015), or central region of alpha synuclein (Shahaduzzaman *et al.*, 2015), as well as alpha synuclein protofibrils (Fagerqvist *et al.*, 2013). Clinical investigation of passive immunotherapies for PD has been fairly limited thus far. A monoclonal anti-alpha synuclein antibody PRX002 (Prothena Corp.) has been shown to be safe in humans but its efficacy remains to be demonstrated in a clinical setting (Schenk *et al.*, 2017).

Fusion proteins

Glial-derived neurotrophic factor (GDNF) has been shown to promote neuronal cell survival and has long been thought to be a promising potential therapy for PD. However, GDNF cannot appreciably cross the barriers of the CNS following systemic administration; several different strategies have been tried in the hope of successful central GDNF therapy over the years (e.g., intraventricular or intraparenchymal GDNF infusions) but these have so far met with challenges (Sherer *et al.*, 2006). This initially spurred efforts to engineer an immunoglobulin fusion protein that might utilize a putative BBB transcytosis system (e.g., the transferrin receptor or the human insulin receptor) to shuttle GDNF from the blood circulation into the brain parenchyma (Zhou *et al.*, 2010); however, despite initially positive pre-clinical findings, systemic delivery of a GDNF-human insulin receptor antibody fusion protein ultimately did not show behavioral or anatomical efficacy in a macaque PD model and, further, produced metaplastic and neoplastic pancreatic lesions in rhesus monkeys that caution against use of such a systemically applied growth factor-insulin receptor antibody conjugate for future clinical trials (Emborg *et al.*, 2013).

Anti-LAG3 antibodies

Although Lewy bodies and other alpha synuclein aggregates typically occur intracellularly, a secreted form of abnormal alpha synuclein has also been reported to contribute to the spread of pathology to other brain regions in a prion-like manner (Tyson *et al.*, 2016; Tyson *et al.*, 2017; Dehay *et al.*, 2016). This transfer of

abnormal alpha synuclein between neurons was recently reported to involve the lymphocyte-activation gene 3 (LAG3) transmembrane protein (Mao *et al.*, 2016). LAG3 is a transmembrane protein that structurally resembles the T cell co-receptor CD4, which binds MHC class II molecules and is expressed by neurons in the cortex and cerebellum, as well as cells/cellular processes in developing white matter and the choroid plexus (Workman *et al.*, 2002). Although the physiological function of LAG3 remains largely unknown, it has been demonstrated that LAG3 binds to abnormal alpha synuclein preformed fibrils (PFFs) but not monomers and facilitates the entry of pathologic alpha synuclein PFFs into neurons via clathrin-mediated endocytosis (Mao *et al.*, 2016); based on these findings an anti-LAG3 passive immunotherapy approach to inhibit the spread of pathologic alpha synuclein within the CNS may be promising and warrants future investigation.

Current strategies and challenges in delivering passive immunotherapies for Parkinson's disease

Among the innovative approaches that have been considered to enable anti-alpha synuclein antibodies to access and engage intracellular aggregates, is the use of intracellular antibodies (i.e., intrabodies; Zhou *et al.*, 2004; Lynch *et al.*, 2008). Expression of antigen specific intrabodies within the CNS requires that brain cells be transfected with anti-alpha synuclein scFv cDNA containing plasmids or viruses (Chen *et al.*, 1994). However, delivering plasmids and viral vectors to brain tissue remains challenging due to their highly limited capacity to cross CNS barriers following systemic delivery (Gray *et al.*, 2010) and their limited spread away from the site of administration following central delivery approaches such as direct intraparenchymal or intrathecal administration (Gray *et al.*, 2010; Wolak & Thorne, 2013; Sykova & Nicholson, 2008). Delivering viral vectors to the CNS also may pose safety concerns with certain vector types (Raper *et al.*, 2002). Another unique challenge for intrabodies to engage their target is the instability of antibody disulfide bonds in the reducing environment of the cell cytoplasm (Valera & Masliah, 2013). Endogenous immunoglobulin disulfide bonds are formed under highly controlled redox potential conditions within the endoplasmic reticulum; these conditions favor the formation and stability of disulfide bonds (Hwang *et al.*, 1992). Endogenous immunoglobulins remain protected from the reducing environment of

the cell cytoplasm by vesicles until they are secreted (Baumal & Scharff, 1973) into a physiological fluid (e.g., blood or CSF), which has a redox potential that can sustain disulfide bond stability (Ouellette *et al.*, 2010); intrabodies may fail to fully access this complex intracellular protein trafficking pathway.

In general, the challenges faced for delivering passive therapies to the CNS for the treatment of PD faces some of the same challenges as those for other neurodegenerative disorders. Systemically administered exogenous therapeutic antibodies may not appreciably cross CNS barriers to engage their pathologic target (St-Amour *et al.*, 2013), while most central routes of delivery are limited by their invasiveness and, at least so far, a suspected inability to provide global drug delivery (Wolak & Thorne, 2013; Sykova & Nicholson, 2008).

Summary of systemic administration strategies to deliver passive immunotherapies for CNS disorders

Systemic administration (i.e., delivery of drugs via the blood circulation) of passive immunotherapies to investigate potential treatments for CNS disorders has historically been the primary focus of both industry and academic studies for several reasons. First, most biologics, such as antibody-based therapeutics are susceptible to protease degradation and permeate poorly across physiological barriers (e.g., the gastrointestinal mucosa) due to their large size and charge (Jitendra *et al*., 2011; Thorne & Frey, 2001). Second, the pharmacokinetics of the most typical parenteral routes of administration (i.e., intravenous, intramuscular, or subcutaneous) are relatively simpler and better understood than that for other routes of administration such as oral or intranasal where an often complex initial absorption step must be accounted for. Third, the brain is a highly vascularized organ with capillary density as high as several thousand mm/mm^3 (total capillary length per tissue volume; Thorne, 2014). The typical distance between capillaries and neurons within the brain ranges between 8-25 μm (Thorne, 2014). However, a major hurdle to systemic drug delivery to the CNS is the existence of the BBB and BCSFBs (Abbott *et al*., 2010; Abbott, 2013; Abbott, 2014). While it has been reported that a small fraction of endogenous IgG circulating in the blood may access the CNS (Podulso & Curran, 1994; Davson & Segal, 1995) via sites where the BBB is absent

(e.g., the circumventricular organs; Broadwell & Sofroniew, 1993; Balin *et al*., 1986) the capacity of these pathways to allow entry of exogenous systemically administered antibodies into the CNS at therapeutically relevant levels is limited (St-Amour *et al*., 2013). Indeed, only 0.009% of IVIg has been detected in the brain and a large portion of this fraction has been observed to be sequestered within the endothelial compartment of cerebral microvessels, i.e., it is unable to access the brain parenchyma to engage with target antigens (St-Amour *et al*., 2013). The difficulty in being able to distinguish between the systemically administered exogenous antibody fraction sequestered within the cerebral endothelial cells versus the antibody fraction that truly gains access to the brain parenchyma has resulted in an overall poor quantitative estimation of antibody CNS levels following systemic delivery (St-Amour *et al*., 2013; Banks *et al*., 2002; Petereit & Rubbert-Roth, 2009). Fourth, it is often assumed that the BBB is compromised under pathological conditions and that its ability to restrict systemically administered drugs from entering the brain is altered under such conditions. However, the degree of BBB disruption varies greatly depending on the stage of disease progression and may be heterogeneous in different brain regions (de Lange, 2014); indeed, careful study of BBB permeability to systemically applied human IgG in several common mouse models of AD (mutant PS2-APP, tau and APOE lines) and amyotrophic lateral sclerosis (mutant superoxide dismutase 1(SOD1) line) revealed no change in IgG levels in cortex, cerebellum, or spinal cord (Bien-LY *et al*., 2015).

The poor outcomes of clinical trials investigating systemically administered passive immunotherapies for CNS disorders and a better understanding of the limited levels of exogenous IgG capable of passively reaching the CNS has spurred new efforts to enhance transport across or around the CNS barriers. For example, one such strategy has involved the transient disruption of the BBB via methods such as MRI-guided focused ultrasound with microbubbles (Fan *et al*., 2014; Chen *et al*., 2013) or systemic infusion of hyperosmolar solutions (e.g., hyperosmolar mannitol; Pappius *et al*., 1979; Rapoport *et al*., 1972; Rapoport *et al*., 1972). However, it has long been appreciated that disruption of the BBB poses a risk since it non-specifically allows entry of not just drugs but other serum macromolecules into the CNS (Kovacs *et al*.,

2017). A more specific approach being investigated to enhance the CNS delivery of antibodies across the BBB is the application of methods (sometimes referred to as 'Trojan Horse' strategies) that utilize endogenous receptor-mediated vesicular transport systems (primarily clathrin-coated vesicles; Preston *et al*., 2014) to shuttle their ligands (nutrients, metabolites, proteins etc.) from the luminal to the abluminal surface of the brain endothelium, i.e., from the blood to the brain (Lajoie & Shusta, 2015). Endogenous receptors involved in putative receptor-mediated transport (RMT) at the BBB include the transferrin receptor, insulin receptor, and low-density lipoprotein-receptor related protein, among others (Lajoie & Shusta *et al*., 2015; Fishman *et al*., 1987). Although RMT in brain endothelium is relatively downregulated compared to endothelium in other parts of the body, it may be crucial for macromolecule transport across the BBB (Preston *et al*., 2014). Such BBB-crossing strategies typically involve a drug consisting of an antibody, antibody-fusion protein, or antibody-decorated nanoparticle with two main components, the first of which targets one of the aforementioned RMT pathways in brain endothelial cells while the second consists of a therapeutic payload (e.g., lysosomal enzyme) or disease-modifying Fab portion directed against CNS pathology (e.g., amyloid beta or alpha-synuclein; Preston *et al*., 2014; Lajoie & Shusta, 2015; Watts & Dennis, 2013; Bell & Ehlers, 2014). However, 'molecular hitchhiking' of therapeutic molecules across the BBB by harnessing endogenous transport mechanisms (Bell & Ehlers, 2014) may sometimes come at a price, e.g., the expression of transcytosis receptor targets (e.g., transferrin receptor) in other regions of the body poses the risk of off-target side effects, depending on the nature of the antibody (Gatter *et al*., 1983; Yu & Watts, 2013; Couch *et al*., 2013). Additionally, it has been suggested that antibodies directed against BBB RMT systems should ideally demonstrate low affinity binding in order to allow the antibody to be successfully released following transit across endothelial cells of the BBB; such low affinity interactions will often require larger systemic doses to be administered in order to achieve therapeutically relevant levels within the brain parenchyma (Yu & Watts, 2013; Yu *et al*., 2011). Lastly, exogenous antibodies targeted to an endogenous RMT system at the BBB may compete with the endogenous ligand of the receptor in some cases, a situation that may cause complications over time depending on the nature of the receptor system being targeted (Groothuis, 2000). Identification of new RMT pathways at the BBB

is under investigation (Zuchero *et al*., 2016) in order find delivery mechanisms with a larger transport capacity and fewer off-target side effects. An important caveat to such approaches is that any antibody or antibody conjugate that first crosses the brain endothelium must then navigate endothelial-, pericyte-, and astrocyte-associated basement membranes in crossing the perivascular compartment (which may consist of fused basement membranes or a potential pericapillary space), before finally moving beyond astrocytic endfeet to reach the brain extracellular spaces and then diffuse to target neurons (Pizzo *et al*., 2018; Abbott *et al*., 2018; Wolak *et al*., 2015). These steps may pose a particular barrier to larger macromolecule therapeutics like antibodies, which may not always easily escape the perivascular spaces to enter the parenchyma (Pizzo *et al*., 2018; Kumar *et al*., 2018); however, further studies are needed to better understand the distribution of endothelial cell-crossing therapeutics between the PVS and brain ECS.

Summary of central administration strategies to deliver passive immunotherapies for CNS disorders

Central administration strategies that bypass the BBB and BCSFBs entirely are emerging as a necessary tool to facilitate the delivery of large biologics like therapeutic antibodies to the CNS. One approach to bypass the BBB is direct injection or infusion of substances into the brain parenchyma; this may be particularly suitable when narrow, focal delivery to specific brain regions is desired. Transport within the brain extracellular spaces is particularly limited to short range distribution by diffusion (Wolak & Thorne, 2013; Sykova & Nicholson, 2008), a size-dependent process that may be slow and inefficient over longer distances for large macromolecules like antibodies (Wolak *et al*., 2015). This transport limitation may be desirable to 'target' drugs to a small area of the brain, e.g., a brain tumor (although invading cancer cells migrating away from tumors to other brain sites may still be beyond reach). Treatment of whole brain disorders that may require chronic drug administration paradigms (e.g., Alzheimer's disease, neuropathic lysosomal storage disorders, Parkinson's disease, and Huntington's disease, to name a few) with direct parenchymal injections will likely be neither practical nor feasible due to the number of injection sites required for therapeutic delivery.

One well-described drug delivery method for direct brain injection is CED (Bobo *et al*., 1994). It was originally thought that this technique could accomplish delivery to a larger brain volume than simple injections due to a resulting pressure gradient imposed between the catheter tip and the tissue interstitium that might force an infusate to flow through the extracellular space. However, it is now better appreciated that parenchymally-infused substances are much more likely to distribute via faster bulk flow along low-resistance pathways in the brain, e.g., cerebral perivascular spaces and white matter tracts (Pizzo *et al*., 2018; Rennels *et al*., 1985; Iliff *et al*., 2012; Cserr *et al*., 1977; Szentistvanyi *et al*., 1984; Ichimura *et al*., 1991; Hadaczek *et al*., 2006; Carare *et al*., 2008), than along narrow gray matter extracellular spaces that exhibit high hydraulic resistance to flow of any kind (Wolak & Thorne, 2013); indeed, these low-resistance pathways associated with the perivascular spaces and white matter are now more commonly credited for the large area of tracer distribution following CED (Hadaczek *et al*., 2006; Salegio *et al*., 2014). Important considerations for CED include optimal injection volumes and rates that ideally achieve the desired target volume of distribution. In keeping with these considerations, the FDA approved the 'iPlan Flow' software to help target therapies more accurately to specific brain regions and without significantly losing the drug to the CSF via white matter tracts or the pial/ependymal surfaces (Buonerba *et al*., 2011). Improved cannula designs (Yin *et al*., 2010; Yin *et al*., 2010) that may help prevent backflow are also under active investigation. Recent work includes the investigation of multifunctional microfabricated devices (e.g., a miniaturized neural drug delivery system, or MiNDS) with smaller catheters that can more precisely deliver smaller volumes at lower flow rates (e.g., an order of magnitude lower than typical CED) and with rapid on/off dosing; such devices have recently been tested for feasibility and functionality in both rodents and non-human primates (Dagdeviren *et al*., 2018). Though the above strategies are invasive, and the transport of large molecules may still be limited with some of them, intraparenchymal delivery methods nonetheless continue to hold promise for certain types of targeted therapies. To date there are no approved macromolecule therapeutics delivered directly into the brain parenchyma; a recent FDA approval (the Cleveland Multiport Catheter CED device; Vogelbaum, 2017) may open the way for further studies (this

particular device has so far been utilized in clinical trials administering topotecan, a small molecule chemotherapeutic, intratumorally; clinicaltrials.gov).

Another central delivery approach to bypass the BBB and BCSFBs involves administration directly into the CSF within and surrounding the brain and spinal cord. Possible routes of administration include lumbar intrathecal (into the lower/caudal spinal CSF space), cisternal intrathecal (into the cisterna magna, near the brainstem, the reason this route is rarely used clinically), or ICV (into the lateral, third, or fourth ventricles in the brain's interior; Kaufman, 1998). A recent study reviewed the safety and usage of ICV devices in patients and suggested that it is a reasonable long-term drug delivery strategy C0hen-Pfeffer *et al*., 2017). CSF-administration shows some promise for larger macromolecules, though clinically almost all are still in trials (Calias *et al*., 2014). It is important to note that many clinical trials listing 'intrathecal' as the route of delivery actually administer the therapeutic agent into the CSF by intrathecal injection/lumbar puncture or by administration into the ventricles using a device such as the Ommaya reservoir or the Rickham device (subcutaneous implanted reservoirs with a catheter placed into a ventricle or surgically created resection cavity that can be accessed through the skin); indeed, some clinical trials require an implanted ventricular access device for eligibility. Intraventricular delivery is not technically equivalent to intrathecal, (with obvious differences in location and application) so caution should be exercised when assuming the actual route of delivery based on use of the term 'intrathecal'; the implications of an entirely different site of delivery may be important for drug distribution between the cranial and spinal CSF compartments and critical for understanding the pharmacokinetics. There are currently three biologics approved in the United States by the FDA for CSF-administration: (i) ziconotide, a 2.6 kDa peptide delivered via lumbar intrathecal infusion approved in 2004 for chronic pain (Wallace *et al*., 2006; Wallace, 2006), (ii) nusinersen, a 7.5 kDa antisense oligonucleotide delivered via lumbar intrathecal injection approved in 2016 for spinal muscular atrophy (Scoto *et al*., 2017; Chiriboga *et al*., 2016; Finkel *et al*., 2016; Hache *et al*., 2016), and (iii) cerliponase alfa, a 66 kDa enzyme delivered via intracerebroventricular infusion approved in 2017 for late infantile neuronal ceroid lipofuscinosis type 2 (CLN2; Kaufman, 2017). The latter disorder is unarguably a

whole-brain disease, for which delivery of the enzyme to every cell is desired; however, the actual distribution of this enzyme throughout the brain is has not been fully described. The lack of published studies describing detailed distribution profiles for intracerebroventricularly and intrathecally applied macromolecules is something that needs to be addressed in the future; indeed, there is an urgent need for preclinical studies focused on the mechanisms governing macromolecule transport to and distribution within the brain so that the potential translatability of different methods can be better understood across different therapeutic classes (e.g., peptide versus oligonucleotide versus larger proteins).

CSF administration to target drugs to the brain relies on communication between the CSF and the brain interstitial fluid (ISF), the governing physiology of which is an area of great interest but also a topic with significant questions and some recent controversies (Pizzo *et al*., 2018; Hladky & Barran, 2014). Modern studies have confirmed that diffusion appears to hinder the transport of substances between the CSF and bordering brain extracellular spaces, for a variety of macromolecules, including antibodies (Pizzo *et al*., 2018); this finding is somewhat in line with older work where CSF-administered macromolecule delivery into the brain was previously thought to be minimal (Pardridge, 1997; Billiau *et al*., 1981). However, the low-resistance pathways (the cerebral perivascular spaces and white matter tracts, discussed above) have increasingly been appreciated to play perhaps a key role in rapid exchange between the CSF and brain ISF (Pizzo *et al*., 2018; Iliff *et al*., 2012; Cserr *et al*., 1977; Szentistvanyi *et al*., 1984; Ichimur1991; Hadaczek *et al*., 2006). Transport along the perivascular space (defined here as the fluid-filled vascular connective tissue space of the vessel adventitia and also possibly the extracellular space associated with the smooth muscle basement membrane of the tunica media) has been suggested to occur in part due to vessel pulsatility driving convective flow along the vessel wall (Rennels *et al*., 1985; Hadaczek *et al*., 2006; Iliff *et al*., 2013) or alternatively, dispersion (Asgari *et al*., 2016). Most importantly, substantial entry into the perivascular compartment from the CSF may theoretically provide access to the whole brain (by reaching down to the level of the capillaries) so it is critically important to better understand what factors (physiological and physicochemical) govern this access and how to tune it for better delivery (Pizzo *et al*., 2018).

The intranasal route of administration has also received recent attention as a potentially non-invasive method to deliver biologics to the CNS (Lochhead & Thorne, 2012; Thorne *et al*., 2004; Kumar *et al*., 2016; Lochhead & Thorne, 2014; Lochhead *et al*., 2015; Thorne *et al*., 1995; Thorne *et al*., 2008). Several groups have demonstrated that intranasal administration of specific full length IgG antibodies (Chauhan & Chauhan, 2015; Kolobov *et al*., 2012; Kolobov *et al*., 2013), and smaller antibody fragments (Cattepoel *et al*., 2011), may result in CNS delivery sufficient to show efficacy in rodent models of AD. Recent published work from our laboratory shows that intranasally administered IgG can rapidly access the CNS at therapeutically relevant levels via transport along extracellular perineural and perivascular pathways associated the olfactory and trigeminal nerves with further widespread distribution within the brain via the perivascular spaces of cerebral blood vessels (Kumar *et al*., 2018). Evidence supporting access to olfactory and trigeminal pathways in the nasal lamina propria and subsequent transport to and distribution within the CNS following intranasal delivery has now been demonstrated for untargeted antibodies (Kumar *et al*., 2018), and targeted antibodies (Chauhan & Chauhan, 2015), as well as other protein (Valera & Masliah, 2013; Thorne *et al*., 2008) and dextran tracers (Lochhead *et al*., 2015). This accumulating evidence suggests (i) the transport pathways from the nasal mucosa to the CNS are unique to the nasal route of administration and (ii) that these unique anatomical pathways themselves do not appear to vary considerably for different intranasally administered macromolecules. However, specific binding (e.g., binding to antigens or Fc receptors) or non-specific binding (e.g., binding to extracellular matrix components) interactions will likely affect the efficiency of transport of different antibodies along these nose-to-brain pathways. Intranasal delivery to the CNS may be influenced by several factors: formulation (Illum, 2012; Costantino *et al*., 2007), molecular size (Lochhead *et al*., 2015; Sakane *et al*., 1995), use of nasal epithelial permeability enhancers (Lochhead *et al*., 2015; Davis & Illum, 2003), and body position (Merkus *et al*., 2006; Djupesland, 2013) among others. Size-dependent aspects of intranasal antibody delivery to the CNS can now be addressed due to significant advances in protein engineering and the rise of antibody fragment-based therapies (Holliger & Hudson, 2005). Molecular size may potentially influence intranasal delivery to the CNS at several stages of the transport process. Intranasally administered molecules must first cross the

nasal epithelium via transcellular or paracellular pathways (Lochhead & Thorne, 2013; Lochhead & Thorne, 2014), prior to accessing perineural and perivascular pathways to the CNS. However, tight junction proteins expressed at the nasal epithelium (e.g., occludin, claudins-1, -3, and -5, and zonula occludens-1 and -2 expressed in the apical olfactory epithelium; Wolburg *et al*., 2008) impose a size-dependent barrier to paracellular transport (Lochhead & Thorne, 2012; Lochhead & Thorne, 2014; Lochhead *et al*., 2015). Smaller molecules are thus able to cross the nasal epithelium to reach the underlying lamina propria and access pathways to the CNS more efficiently than larger molecules; such a size-dependence has been demonstrated using fluorophore-labeled 3 and 10 kDa dextrans (Lochhead *et al*., 2015). Preliminary studies from our laboratory also suggest a similar trend for intranasally administered antibodies, with better brain delivery for smaller sdAbs (hydrodynamic diameter (d_H) ~ 4.5 nm) and Fab fragments (d_H ~ 6.5 nm) than for full length IgG (~ 10 nm; Kumar *et al*., 2018 & unpublished observations). It has been suggested that IgG transport across the nasal epithelium following intranasal administration may also be attributed to FcRn-dependent transcytosis (Perissinotti & Reeves, 2010; Ye *et al*., 2011; Heidl *et al*., 2016). Once in the nasal lamina propria, intranasally administered molecules would need to escape clearance into the sink of the systemic circulation or nasal lymphatics in order to access perineural and perivascular pathways to the CNS (Kumar *et al*., 2016). Larger hydrophilic molecules are more likely to escape clearance into the systemic circulation and lymphatics than smaller molecules (Kumar *et al*., 2016). Entry of intranasally administered macromolecules into the CSF has also been shown to be size-dependent (Sakane *et al*., 1995). As with nasal epithelial transport, IgG access to the CSF following intranasal delivery may partly be attributed to FcRn-dependent transport processes at lining cells of nerves and leptomeningeal vessels (Pizzo *et al*., 2018; Kumar *et al*., 2018; Abbott *et al*., 2018), although this will require further study. Our work has shown that intranasally administered IgG accesses the brain more efficiently than the CSF compartment, suggesting that some degree of CNS entry/distribution can occur without access to the CSF first (Kumar *et al*., 2018). Taken together, the size-dependent entry of intranasally administered antibodies to the CNS appears most likely attributed to size-dependent transport across the nasal epithelium, although other mechanisms influenced by molecular size may also play important roles.

Our work investigating the distribution of antibodies within the CNS following intraparenchymal (Wolak *et al*., 2015), intrathecal (Pizzo *et al*., 2018), and intranasal administration (Kumar *et al*., 2018) (Fig. 11) emphasizes that drug access to perivascular spaces and subsequent distribution along these spaces into the brain may likely govern whole brain delivery and thus therapeutic efficacy (Pizzo *et al*., 2018; Wolak & Thorn, 2013; Abbott *et al*., 2018). Several physiological factors may influence the capacity of antibodies to access the perivascular compartments of cerebral blood vessels and subsequently diffuse from the perivascular space and into the brain parenchyma. First, size-dependent entry of protein tracers into the perivascular spaces of cerebral blood vessels has been shown to play a large role in brain distribution from the CSF, with smaller sdAbs having greater access to the perivascular spaces compared to full length IgG (Pizzo *et al*., 2018). Size-dependent access to the perivascular spaces likely serves additional physiological roles; e.g., insulin-like growth factor 1 (IGF1, 7.6 kDa) binding to insulin-like growth factor binding protein 2 (IGFBP-2; 32 kDa) in the CSF may prevent substantial brain access of IGF-1 under some conditions, and release of IGF-1 from this same binding protein may allow free IGF-1 to enter the brain more easily (Loddick *et al*., 1998), possibly via non-saturable perivascular pathways (Guan *et al*., 2000). Second, binding of immunoglobulin G to Fc receptors (e.g., the Fcγ receptor 2b) in the brain at key interfaces (e.g., the pial surfaces, the glia limitans, and around cerebral blood vessels) may impede the ability of IgG to enter the brain from the CSF and hinder its exit from the perivascular compartment by diffusion. Surprisingly, very little information is available on Fc receptor distribution in the CNS so such a 'binding' barrier cannot yet be fully appreciated. Third, the astrocyte basement membrane may also pose a barrier to substances attempting to enter the extracellular space from the perivascular spaces [288]. Indeed, previous studies have demonstrated that full-length IgG exhibits limited diffusion out of the perivascular spaces and into the surrounding neuropil (Pizzo *et al*., 2018; Hannocks *et al*., 2018). Finally, the impact of administration parameters, e.g., infusion rates, delivery volumes (Davson & Segal, 1995), and body positioning (Merkus *et al*., 2006; Lee *et al*., 2015), etc. may ultimately prove quite significant when carefully studied across the different routes.

Pathological changes that occur with the progression of CNS disorders may also have an important, disease-specific impact on the ability of centrally administered drugs to access the perivascular compartment of cerebral blood vessels and diffuse within the brain target regions. For example, brain tumors often have an astrocytic border that likely serves to hinder diffusion between surrounding brain and the tumor. Increased laminin content in the tumor extracellular matrix may also further impede antibody diffusion within the tumor microenvironment (Vargova *et al*., 2003). Perivascular access and transport may also be physically blocked by cancer cells that have been shown to reside and disperse along cerebral perivascular compartments (Scherer, 1938; Calabrese *et al*., 2007; Gilbertson & Rich, 2007; Thorsen & Tysnes, 1997), the subpial spaces (Scherer, 1938), nerves (Scherer, 1938), and white matter tracts (Scherer, 1938); remarkably, and perhaps not coincidentally, such pathways are likely the same ones important for drug transport to and from deeper brain regions following central delivery (Cserr *et al*., 1977; Szentistvanyi *et al*., 1984; Ichimura *et al*., 1991). The disease pathology in Alzheimer's disease and related dementias has been shown to influence the architecture of cerebral perivascular compartments due to either deposition of hyperphosphorylated tau or Aβ40 within the perivascular compartment (Merlini *et al*., 2016), sometimes accompanied by enlargement of the perivascular space (Chen *et al*., 2011). Similar abnormally enlarged cerebral perivascular spaces have also been demonstrated in patients with traumatic brain injuries (Inglese *et al*., 2005), acute ischemic stroke (Doubal *et al*., 2010), and certain lysosomal storage disorders (Zafeiriou & Batzios, 2013). Whether such a physiologically enlarged perivascular space affects perivascular drug transport remains an open question.

A final important consideration is systemic exposure, which is often relatively low with intra-CSF administration compared to systemic or intranasal routes of administration (Pizzo *et al*., 2018; Lochhead & Thorne, 2013; Lochhead & Thorne, 2014). However, CSF-administered substances do eventually drain from the central compartment via arachnoid granulations into the blood of the dural sinuses (Pollay, 2010)

as well as via lymphatic pathways that ultimately drain into systemic circulation as well (Louveau *et al*., 2015; Aspelund *et al*., 2015).

Conclusions and Future Perspectives

The development of passive immunotherapies for CNS disorders has lagged behind that of other non-CNS indications (Pangalos *et al*., 2007). The reasons for this development lag for CNS indications are varied but they are thought to include insufficient mechanistic understanding of the brain, a paucity of reliable biomarkers to monitor disease progression and drug efficacy, and perhaps most significantly, the tremendous challenge of effective drug delivery to target brain regions (Hammarlund-Udenaes *et al*., 2014). However, this review emphasizes that we have nonetheless made significant strides toward better understanding the challenges in overcoming the various physiological and pathological barriers that may impede therapeutic antibody delivery to the CNS. Creative strategies that harness the capacity of pre-existing anatomical pathways and mechanisms to deliver antibodies to their target site, coupled with rapid advances in antibody engineering that facilitate customization of antibody target selectivity, effector functions, and distribution properties, provide a promising outlook for the future of passive immunotherapies to treat CNS disorders.

In this review, we primarily focused on passive immunotherapies for the treatment of proteinopathies (e.g., PD, AD, and HD) and brain cancers. However, passive immunotherapies are also being investigated and applied for treating other CNS disorders such as multiple sclerosis, stroke, and traumatic brain injury among others. Multiple sclerosis (MS), an autoimmune neuroinflammatory disorder of unknown etiology causes demyelination of axons within the CNS. There are currently no treatments that can entirely stop disease progression or reverse existing disabilities in MS patients (Wootla *et al*., 2016; Hemmer *et al*., 2006; Baecher-Allan *et al*., 2018). Acute inflammatory episodes in MS are typically treated with intravenously administered corticosteroids that cause immunosuppression; however, the symptomatic relief and response to corticosteroids diminishes with repeated use (Wootla *et al*., 2016). Several passive immunotherapies that

largely target immune responses in the periphery have been approved for treatment in MS (Wootla *et al*., 2016; Baecher-Allan *et al*., 2018): (i) natalizumab (Tysabri; Biogen/Élan; FDA approval – 2004) targets the cell adhesion molecule α4-integrin and blocks lymphocyte migration into the CNS (Baecher-Allan *et al*., 2018; Engelhardt & Kappos, 2007; Polman *et al*., 2006; Sellebjerg *et al*., 2016); (ii) alemtuzumab (Lemtrada; Genzyme/Sanofi; FDA approval – 2014) depletes lymphocytes via antibody-mediated cell cytotoxicity (ADCC) and by activating the complement system (Baecher-Allan *et al*., 2018; Coles *et al*., 2008; Jones & Coles, 2014; Gross *et al*., 2016); (iii) daclizumab (Zinbryta; Biogen/Abbvie; FDA approval – 2016) targets the IL2 receptor (Baecher-Allan *et al*., 2018; Gross *et al*., 2016) but was recently withdrawn (April, 2018) due to complex and significant adverse events; and (iv) ocrelizumab (Ocrevus; Genentech/Roche; FDA approval – 2017) targets CD20+ B cells and is the first and only therapy currently that has been approved for the treatment of both primary and progressive forms of MS (Baecher-Allan *et al*., 2018; Hauser *et al*., 2017; Hauser *et al*., 2017; Montalban *et al*., 2017). However, therapies that directly target the inflammation in the central compartment in MS could potentially be more effective (Hemmer *et al*., 2006). The BBB appears to be intact during the first 6 weeks of lesion formation in MS when activation of microglia and macrophages begins with very few peripheral lymphocytes infiltrating the brain at this stage (Hemmer *et al*., 2006; Engelhardt, 2008). Thus, strategies targeting passive immunotherapies to the CNS at the earliest stages of MS to prevent steps that lead to lesion formation could potentially alter the course of the disease but face the challenge of delivering antibodies across the BBB. Systemic immunosuppressive therapies that deplete lymphocyte populations also pose a risk of CNS infections (Hemmer *et al*., 2006) and investigating unique passive immunotherapy targets that prevent pathological infiltration of lymphocytes into the CNS without hampering CNS immune surveillance is crucial.

Ischemic strokes have the highest incidence among all cases of stroke and are caused due to obstruction of blood flow within cerebral vessels that may be attributed to one or more factors, e.g., fatty deposits along vessel walls that narrow the vessel lumen (atherosclerosis), elevated blood pressure, diabetes, and genetic predisposition (Lo *et al*., 2003; Yu *et al*., 2013) The obstruction in the cerebral blood vessel may be caused

either due to the formation of a blood clot (thrombus) within the brain itself (referred to as cerebral thrombosis) or a blood clot that migrates from the periphery into the brain (referred to as a cerebral embolism; Tomura *et al*., 1990). Arterial occlusion in stroke triggers a sequence of events leading to cell death and subsequent cognitive damage due to ischemia and neuroinflammatory responses in the brain (Lo *et al*., 2003). Elimination of the cerebral blood clot either by dissolving it using a thrombolytic agent such as tissue plasminogen activator (tPA) or by surgical removal (embolectomy) are currently the most effective treatments available for ischemic stroke (Yu *et al*., 2013). However, due to the narrow therapeutic time window (e.g., less than 4.5 h post-stroke for tPA treatment) and invasiveness (e.g., embolectomy), currently available treatment options only benefit a small number of stroke patients (Yu *et al*., 2013). Passive immunotherapies are an attractive means to modulate neuroinflammation and neuroplasticity in stroke patients both as a means to widen the therapeutic window of current revascularization strategies and to minimize brain damage (Yu *et al*., 2013). For example, antibodies against myelin-associated proteins that inhibit neurite growth (such as Nogo-A and its receptor Nogo-66) are being explored as a way to increase neuroplasticity following stroke (Kilic *et al*., 2010; Gillani *et al*., 2010; Ma *et al*., 2007). tPA therapy has side-effects such as cerebral edema and hemorrhage that may partly be attributed to its interaction with the N-methyl-D-aspartate (NMDA) receptor, resulting in Ca^{2+} ion influx and the triggering of cell death signaling cascades (Nicole *et al*., 2001). Antibodies that block the interaction between tPA and NMDA receptors are being investigated as a neuroprotective strategy in stroke (Yu *et al*., 2013). Since the BBB often appears compromised following ischemic stroke (Haley *et al*., 2017), it may pose less of a barrier for therapeutic antibody delivery to brain target sites. However, it may very well be crucial to administer the antibody-based therapy at specific points in the time course of post-stroke pathological events for central delivery and efficacy. For instance, systemic administration of anti-Nogo-A antibodies immediately post-stroke during the hyperacute phase (when tissue damage pathways are more active than tissue repair) may result in deleterious rather than beneficial effects (Kilic *et al*., 2010).

Traumatic brain injuries are typically grouped based on severity of the impact/injury as mild, moderate, or severe. Mild traumatic brain injury (TBI), commonly referred to as a concussion, is often caused by a blunt non-penetrating trauma and its repeated occurrence (often seen in athletes playing high impact contact sports) has been linked to neurodegenerative conditions such as chronic traumatic encephalopathy (CTE) (McKee *et al*., 2015; McKee & Daneshvar, 2015). Although primary mechanical injury in TBI may cause hematoma, edema, hemorrhage, and axonal injury, it is becoming apparent that secondary injury due to sterile neuroinflammation, excitotoxicity, and oxidative stress may ultimately result in more progressive long-term detrimental effects (Blennow *et al*., 2016; Putatunda *et al*., 2018). Passive immunotherapies that can inhibit neurotoxic innate and adaptive immune responses without disrupting physiological CNS immune surveillance are therefore being investigated as potential treatment strategies for TBI (Putatunda *et al*., 2018). These strategies include intravenous immunoglobulin (IVIg) to 'normalize' the immune environment and monoclonal antibodies that can inhibit lymphocyte trafficking to the CNS (e.g., anti-CD20 and anti-CXCL10 antibodies; Putatunda *et al*., 2018). Finally, it bears noting that BBB disruption observed in TBI correlates with adverse neurological effects, so restoration of normal BBB function is also being investigated as a therapeutic strategy (Chodobski *et al*., 2011).

An important physiological distinction between proteinopathies such as AD, PD, and HD versus conditions such as MS, stroke, and TBI appears related to differences in the intactness of the CNS barriers. For example, work with experimental models and clinical studies have demonstrated that the BBB may be profoundly compromised over the course of disease progression in conditions like MS but remain relatively intact during the course of pathological processes associated with AD (Bien-Ly *et al*., 2015). Future endeavors to translate passive immunotherapies for the treatment of CNS disorders will therefore have to take into consideration the spatial and temporal heterogeneity in the extent the BBB and the BCSFBs restrict antibody transport to brain target sites in different diseases and stages of pathology.

References

Abbott J (2014). In Drug Delivery to the Brain. Advances in the Pharmaceutical Sciences Series. (eds Margareta Hammarlund-Udenaes, Elizabeth de Lange, & Robert Thorne) Ch. 1, 4. AAPS Press. Springer.

Abbott NJ, Patabendige AA, Dolman DE, Yusof SR & Begley DJ (2010). Structure and function of the blood-brain barrier. *Neurobiol Dis* **37**, 13-25

Abbott NJ, Pizzo ME, Preston JE, Janigro D & Thorne RG (2018). The role of brain barriers in fluid movement in the CNS: is there a 'glymphatic' system? *Acta Neuropathol* **135**, 387-407.

Abbott NJ. Blood-brain barrier structure and function and the challenges for CNS drug delivery. *J Inherit Metab Dis* **36**, 437-449.

Ahmed M *et al* (2010). Structural conversion of neurotoxic amyloid-beta (1-42) oligomers to fibrils. *Nat Struct Mol Biol* **17**, 561-567.

Aho R, Ekfors T, Haltia M & Kalimo H (1993). Pathogenesis of primary central nervous system lymphoma: invasion of malignant lymphoid cells into and within the brain parenchyma. *Acta Neuropathol* **86**, 71-76.

Alzheimer's association (2018). alz.org (access Jul 29, 2019)

Andreasen N *et al* (2015). First administration of the Fc-attenuated anti-β amyloid antibody GSK933776 to patients with mild Alzheimer's disease: a randomized, placebo-controlled study. *PLoS One* **10**, e0098153.

Angelov L *et al* (2009). Blood-brain barrier disruption and intra-arterial methotrexate-based therapy for newly diagnosed primary CNS lymphoma: a multi-institutional experience. *J Clin Oncol* **27**, 3503-3509.

Arbel M, Yacoby I & Solomon B (2005). Inhibition of amyloid precursor protein processing by beta-secretase through site-directed antibodies. *Proc Natl Acad Sci U S A* **102**, 7718-7723.

Armstrong TS, Wen PY, Gilbert MR & Schiff D (2012). Management of treatment-associated toxicities of anti-angiogenic therapy in patients with brain tumors. *Neuro Oncol* **14**, 1203-1214.

Asgari M, de Zélicourt D & Kurtcuoglu V (2016). Glymphatic solute transport does not require bulk flow. *Sci Rep* **6**, 38635.

Aspelund A *et al* (2015). A dural lymphatic vascular system that drains brain interstitial fluid and macromolecules. *J Exp Med* **212**, 991-999.

Asuni AA, Boutajangout A, Quartermain D & Sigurdsson EM (2007). Immunotherapy targeting pathological tau conformers in a tangle mouse model reduces brain pathology with associated functional improvements. *J Neurosci* **27**, 9115-9129.

Atwal JK *et al* (2011). A therapeutic antibody targeting BACE1 inhibits amyloid-β production in vivo. *Sci Transl Med* **3**, 84ra43.

Azuma M *et al* (1993). B70 antigen is a second ligand for CTLA-4 and CD28. *Nature* **366**, 76-79.

Bae EJ *et al* (2012). Antibody-aided clearance of extracellular α-synuclein prevents cell-to-cell aggregate transmission. *J Neurosci* **32**, 13454-13469.

Baecher-Allan C, Kaskow BJ & Weiner HL (2018). Multiple Sclerosis: Mechanisms and Immunotherapy. *Neuron* **97**, 742-768.

Balin BJ, Broadwell RD, Salcman M. & el-Kalliny M (1986). Avenues for entry of peripherally administered protein to the central nervous system in mouse, rat, and squirrel monkey. *J Comp Neurol* **251**, 260-280.

Banks WA *et al*. (2002). Passage of amyloid beta protein antibody across the blood-brain barrier in a mouse model of Alzheimer's disease. Peptides 23, 2223-2226.

Bao X, Pastan I, Bigner DD & Chandramohan V (2016). EGFR/EGFRvIII-targeted immunotoxin therapy for the treatment of glioblastomas via convection-enhanced delivery. *Receptors Clin Investig* **3**

Bard F *et al* (2000). Peripherally administered antibodies against amyloid beta-peptide enter the central nervous system and reduce pathology in a mouse model of Alzheimer disease. *Nat Med* **6**, 916-919.

Batchelor TT *et al* (2011). Rituximab monotherapy for patients with recurrent primary CNS lymphoma. *Neurology* **76**, 929-930.

Baumal R & Scharff, M. D. (1973). Synthesis, assembly and secretion of mouse immunoglobulin. *Transplant Rev* **14**, 163-183 (1973).

Baxter LT & Jain RK (1989). Transport of fluid and macromolecules in tumors. I. Role of interstitial pressure and convection. *Microvasc Res* **37**, 77-104.

Becker NH, Novikoff AB & Zimmerman HM (1967). Fine structure observations of the uptake of intravenously injected peroxidase by the rat choroid plexus. *J Histochem Cytochem* **15**, 160-165.

Bell RD & Ehlers MD (2014). Breaching the blood-brain barrier for drug delivery. *Neuron* **81**, 1-3.

Benilova I, Karran E & De Strooper B (2012). The toxic Aβ oligomer and Alzheimer's disease: an emperor in need of clothes. *Nat Neurosci* **15**, 349-357.

Bien-Ly N *et al* (2014). Lack of Widespread BBB Disruption in Alzheimer's Disease Models: Focus on Therapeutic Antibodies. *Neuron* **88**, 289-297.

Bigner DD *et al* (1995). Phase I studies of treatment of malignant gliomas and neoplastic meningitis with 131I-radiolabeled monoclonal antibodies anti-tenascin 81C6 and anti-chondroitin proteoglycan sulfate Me1-14 F (ab')2--a preliminary report. *J Neurooncol* **24**, 109-122.

Billiau A *et al* (1981). Tissue distribution of human interferons after exogenous administration in rabbits, monkeys, and mice. *Arch Virol* **68**, 19-25.

Black P & Loeffler J (2004). Cancer of the Nervous System. 2nd edition. Lippincott Williams & Wilkins.

Blennow K *et al* (2016). Traumatic brain injuries. *Nat Rev Dis Primers* **2**, 16084.

Bobo RH *et al* (1994). Convection-enhanced delivery of macromolecules in the brain. *Proc Natl Acad Sci USA* **91**, 2076-2080.

Braak H, Thal DR, Ghebremedhin E & Del Tredici, K (2011). Stages of the pathologic process in Alzheimer disease: age categories from 1 to 100 years. *J Neuropathol Exp Neurol* **70**, 960-969.

Brem S, Cotran R & Folkman J (1972. Tumor angiogenesis: a quantitative method for histologic grading. *J Natl Cancer Inst* **48**, 347-356.

Brem SS *et al*. (1990). Inhibition of angiogenesis and tumor growth in the brain. Suppression of endothelial cell turnover by penicillamine and the depletion of copper, an angiogenic cofactor. *Am J Pathol* **137**, 1121-1142.

Broadwell RD & Sofroniew MV (1993). Serum proteins bypass the blood-brain fluid barriers for extracellular entry to the central nervous system. *Exp Neurol* **120**, 245-263.

Brown MT *et al* (1996). Intrathecal 131I-labeled antitenascin monoclonal antibody 81C6 treatment of patients with leptomeningeal neoplasms or primary brain tumor resection cavities with subarachnoid communication: phase I trial results. *Clin Cancer Res* **2**, 963-972.

Brunet JF *et al* (1987). A new member of the immunoglobulin superfamily--CTLA-4. *Nature* **328**, 267-270.

Buchbinder EI & Desai A (2016). CTLA-4 and PD-1 Pathways: Similarities, Differences, and Implications of Their Inhibition. *Am J Clin Oncol* **39**, 98-106.

Buonerba C *et al* (2011). A comprehensive outlook on intracerebral therapy of malignant gliomas. *Crit Rev Oncol Hematol* **80**, 54-68.

Calabrese C (2007). A perivascular niche for brain tumor stem cells. *Cancer Cell* **11**, 69-82.

Calias P, Banks WA, Begley D, Scarpa M & Dickson P (2014). Intrathecal delivery of protein therapeutics to the brain: a critical reassessment. *Pharmacol Ther* **144**, 114-122.

Carare RO *et al* (2008). Solutes, but not cells, drain from the brain parenchyma along basement membranes of capillaries and arteries: significance for cerebral amyloid angiopathy and neuroimmunology. *Neuropathol Appl Neurobiol* **34**, 131-144.

Carter T, Shaw H, Cohn-Brown D, Chester K & Mulholland P (2016). Ipilimumab and Bevacizumab in Glioblastoma. *Clin Oncol (R Coll Radiol)* **28**, 622-626.

Casacó, A. *et al* (2008). Phase I single-dose study of intracavitary-administered Nimotuzumab labeled with 188 Re in adult recurrent high-grade glioma. *Cancer Biol Ther* **7**, 333-339.

Cattepoel S, Hanenberg M, Kulic L & Nitsch RM (2011). Chronic intranasal treatment with an anti-Aβ (30-42) scFv antibody ameliorates amyloid pathology in a transgenic mouse model of Alzheimer's disease. *PLoS One* **6**, e18296.

Chamberlain MC, Baik CS, Gadi VK, Bhatia S & Chow LQ (2017). Systemic therapy of brain metastases: non-small cell lung cancer, breast cancer, and melanoma. *Neuro Oncol* **19**, 1-24

Chauhan MB & Chauhan NB (2015). Brain Uptake of Neurotherapeutics after Intranasal versus Intraperitoneal Delivery in Mice. *J Neurol Neurosurg* **2**.

Chauhan NB & Siegel GJ (2004). Efficacy of anti-Abeta antibody isotypes used for intracerebroventricular immunization in TgCRND8. *Neurosci Lett* **375**, 143-147.

Chauhan NB & Siegel GJ (2004). Intracerebroventricular passive immunization in transgenic mouse models of Alzheimer's disease. *Expert Rev Vaccines* **3**, 717-725.

Chauhan NB, Siegel GJ & Lichtor T (2001). Distribution of intraventricularly administered anti-amyloid-beta peptide (Abeta) antibody in the mouse brain. *J Neurosci Res* **66**, 231-235.

Chauhan NB, Siegel GJ & Lichtor T (2004). Effect of age on the duration and extent of amyloid plaque reduction and microglial activation after injection of anti-Abeta antibody into the third ventricle of TgCRND8 mice. *J Neurosci Res* **78**, 732-741.

Chen CC *et al* (2013). Targeted drug delivery with focused ultrasound-induced blood-brain barrier opening using acoustically-activated nanodroplets. *J Control Release* **172**, 795-804.

Chen SY, Bagley J & Marasco WA (1994). Intracellular antibodies as a new class of therapeutic molecules for gene therapy. *Hum Gene Ther* **5**, 595-601.

Chen W, Song X, Zhang Y & Initiative (2011). Assessment of the Virchow-Robin Spaces in Alzheimer disease, mild cognitive impairment, and normal aging, using high-field MR imaging. *Am J Neuroradiol* **32**, 1490-1495.

Chiriboga CA *et al* (2016). Results from a phase 1 study of nusinersen (ISIS-SMN(Rx)) in children with spinal muscular atrophy. *Neurology* **86,** 890-897.

Chiu ML & Gilliland GL (2016). Engineering antibody therapeutics. *Curr Opin Struct Biol* **38**, 163-173.

Chodobski A, Zink BJ & Szmydynger-Chodobska J (2011). Blood-brain barrier pathophysiology in traumatic brain injury. *Transl Stroke Res* **2**, 492-516.

Chow VW, Mattson MP, Wong PC & Gleichmann M (2010). An overview of APP processing enzymes and products. *Neuromolecular Med* **12**, 1-12.

Citron M (2010). Alzheimer's disease: strategies for disease modification. *Nat Rev Drug Discov* **9**, 387-398.

Citterio G, Reni M, Gatta G & Ferreri AJM (2017). Primary central nervous system lymphoma. *Crit Rev Oncol Hematol* **113**, 97-110.

Claes A, Idema AJ & Wesseling P (2007). Diffuse glioma growth: a guerilla war. *Acta Neuropathol* **114**, 443-458.

ClinicalTrials.gov (2019). clinicaltrials.gov (accessed August 4, 2019)

Cohen MH, Shen YL, Keegan P & Pazdur R (2009). FDA drug approval summary: bevacizumab (Avastin) as treatment of recurrent glioblastoma multiforme. *Oncologist* **14**, 1131-1138.

Cohen-Pfeffer JL *et al* (2017). Intracerebroventricular Delivery as a Safe, Long-Term Route of Drug Administration. *Pediatr Neurol* **67**, 23-35.
Coles AJ *et al* (2008). Alemtuzumab vs. interferon beta-1a in early multiple sclerosis. *N Engl J Med* **359**, 1786-1801.

Corder EH *et al* (1993). Gene dose of apolipoprotein E type 4 allele and the risk of Alzheimer's disease in late onset families. *Science* **261**, 921-923 (1993).

Costantino HR, Illum L, Brandt G, Johnson PH & Quay SC (2007). Intranasal delivery: physicochemical and therapeutic aspects. *Int J Pharm* **337**, 1-24.

Coté TR, Manns A, Hardy CR, Yellin FJ & Hartge P (1996). Epidemiology of brain lymphoma among people with or without acquired immunodeficiency syndrome. AIDS/Cancer Study Group. *J Natl Cancer Inst* **88**, 675-679.

Couch JA *et al*. (2013). Addressing safety liabilities of TfR bispecific antibodies that cross the blood-brain barrier. *Sci Transl Med* **5**, 183ra157, 181-112.

Cserr HF, Cooper DN & Milhorat TH (1977). Flow of cerebral interstitial fluid as indicated by the removal of extracellular markers from rat caudate nucleus. *Exp Eye Res* **25 Suppl** 461-473.

Cummings J, Lee G, Mortsdorf T, Ritter A & Zhong K (2017). Alzheimer's disease drug development pipeline: 2017. *Alzheimers Dement (N Y)* **3**, 367-384.

Cunningham C, Wilcockson DC, Campion S, Lunnon K & Perry VH (2005). Central and systemic endotoxin challenges exacerbate the local inflammatory response and increase neuronal death during chronic neurodegeneration. *J Neurosci* **25**, 9275-9284.

Dagdeviren C *et al* (2018). Miniaturized neural system for chronic, local intracerebral drug delivery. *Sci Transl Med* 10

Davis SS & Illum L (2003). Absorption enhancers for nasal drug delivery. *Clin Pharmacokinet* **42**, 1107-1128.

Davson H. & Segal M (1995). Physiology of the CSF and Blood-brain barriers., 506-507. CRC Press.

de Calignon A *et al* (2012). Propagation of tau pathology in a model of early Alzheimer's disease. Neuron 73, 685-697.

de Lange E (2014). In Drug delivery to the brain - Physiological concepts, Methodologies and Approaches (eds M Hammarlund-Udenaes, R Thorne, & E de Lange). AAPS Press. Springer.

Decourt B, Lahiri DK & Sabbagh MN (2017). Targeting Tumor Necrosis Factor Alpha for Alzheimer's Disease. *Curr Alzheimer Res* **14**, 412-425.

Dehay B, Vila M, Bezard E, Brundin P & Kordower JH. (2016). Alpha-synuclein propagation: New insights from animal models. *Mov Disord* **31**, 161-168.

Delnomdedieu M *et al* (2016). First-In-Human safety and long-term exposure data for AAB-003 (PF-05236812) and biomarkers after intravenous infusions of escalating doses in patients with mild to moderate Alzheimer's disease. *Alzheimers Res Ther* **8**, 12.

DeMattos RB *et al* (2001). Peripheral anti-A beta antibody alters CNS and plasma A beta clearance and decreases brain A beta burden in a mouse model of Alzheimer's disease. *Proc Natl Acad Sci U S A* **98**, 8850-8855.

Dickson DW (2012). Parkinson's disease and parkinsonism: neuropathology. *Cold Spring Harb Perspect Med* **2**.

Djupesland PG (2013). Nasal drug delivery devices: characteristics and performance in a clinical perspective-a review. *Drug Deliv Transl Res* **3**, 42-62.

Dong H, Zhu G, Tamada K & Chen L (1999). B7-H1, a third member of the B7 family, co-stimulates T-cell proliferation and interleukin-10 secretion. *Nat Med* **5**, 1365-1369.

Doody RS *et al* (2014). Phase 3 trials of solanezumab for mild-to-moderate Alzheimer's disease. *N Engl J Med* **370**, 311-321.

Doody RS, Farlow M, Aisen PS & Committee (2014) Phase 3 trials of solanezumab and bapineuzumab for Alzheimer's disease. *N Engl J Med* **370**, 1460.

Doubal FN, MacLullich AM, Ferguson KJ, Dennis MS & Wardlaw JM (2010). Enlarged perivascular spaces on MRI are a feature of cerebral small vessel disease. *Stroke* **41**, 450-454.

Driessens G, Kline J & Gajewski TF (2009). Costimulatory and coinhibitory receptors in anti-tumor immunity. *Immunol Rev* **229**, 126-144.

Elkouzi A. (www.parkinson.org/understanding-parkinsons) (Accessed Aug 7, 2019).

Emborg ME *et al*. (2013). Intracerebral transplantation of differentiated human embryonic stem cells to hemiparkinsonian monkeys. *Cell Transplant* **22**, 831-838.

Engelhardt B & Kappos L (2008). Natalizumab: targeting alpha4-integrins in multiple sclerosis. *Neurodegener Dis* **5**, 16-22.

Engelhardt B (2008). The blood-central nervous system barriers actively control immune cell entry into the central nervous system. *Curr Pharm Des* **14**, 1555-1565.

Engelhardt B *et al* (2016). Vascular, glial, and lymphatic immune gateways of the central nervous system. *Acta Neuropathol* **132**, 317-338.

Fagerqvist T *et al*. (2013). Monoclonal antibodies selective for α-synuclein oligomers/protofibrils recognize brain pathology in Lewy body disorders and α-synuclein transgenic mice with the disease-causing A30P mutation. *J Neurochem* **126**, 131-144.

Fan CH *et al*. (2014). Contrast-enhanced ultrasound imaging for the detection of focused ultrasound-induced blood-brain barrier opening. *Theranostics* **4**, 1014-1025.

Ferrara N, Hillan KJ, Gerber HP & Novotny W (2004). Discovery and development of bevacizumab, an anti-VEGF antibody for treating cancer. *Nat Rev Drug Discov* **3**, 391-400.

Ferry J & Harris N (1994). In Pathology and Rejection Diagnosis in Solid Organ Transplantation (eds K Solez, L Racusen, & M Billingham) 277-301. Marcel Dekker.

Field KM, Jordan JT, Wen PY, Rosenthal MA & Reardon DA (2015). Bevacizumab and glioblastoma: scientific review, newly reported updates, and ongoing controversies. *Cancer* **121**, 997-1007.

Finder VH & Glockshuber R (2007). Amyloid-beta aggregation. *Neurodegener Dis* **4**, 13-27.

Finkel RS *et al* (2016). Treatment of infantile-onset spinal muscular atrophy with nusinersen: a phase 2, open-label, dose-escalation study. *Lancet* **388**, 3017-3026.

Fishman JB, Rubin JB, Handrahan JV, Connor JR & Fine RE. (1987). Receptor-mediated transcytosis of transferrin across the blood-brain barrier. *J Neurosci Res* **18**, 299-304.

Folkman J (1971). Tumor angiogenesis: therapeutic implications. *N Engl J Med* **285**, 1182-1186.

Folkman J, Merler E, Abernathy C & Williams G (1971). Isolation of a tumor factor responsible for angiogenesis. *J Exp Med* **133**, 275-288.

Friedman HS *et al.* (2009). Bevacizumab alone and in combination with irinotecan in recurrent glioblastoma. *J Clin Oncol* **27**, 4733-4740.

Games D *et al*. (2014). Reducing C-terminal-truncated alpha-synuclein by immunotherapy attenuates neurodegeneration and propagation in Parkinson's disease-like models. *J Neurosci* **34**, 9441-9454.

Gan HK, van den Bent M, Lassman AB, Reardon DA & Scott AM (2017). Antibody-drug conjugates in glioblastoma therapy: the right drugs to the right cells. *Nat Rev Clin Oncol* **14**, 695-707.

Gatter KC, Brown G, Trowbridge IS, Woolston RE & Mason DY (1983). Transferrin receptors in human tissues: their distribution and possible clinical relevance. *J Clin Pathol* **36**, 539-545.

Gavrilovic IT & Posner JB (2005). Brain metastases: epidemiology and pathophysiology. *J Neurooncol* **75**, 5-14.

George S & Brundin P (2015). Immunotherapy in Parkinson's Disease: Micromanaging Alpha-Synuclein Aggregation. *J Parkinsons Dis* **5**, 413-424.

Gilbert MR *et al.* (2014). A randomized trial of bevacizumab for newly diagnosed glioblastoma. *N Engl J Med* **370**.

Gilbertson RJ & Rich JN (2007). Making a tumor's bed: glioblastoma stem cells and the vascular niche. *Nat Rev Cancer* **7**, 733-736.

Gillani RL *et al* (2010). Cognitive recovery in the aged rat after stroke and anti-Nogo-A immunotherapy. *Behav Brain Res* **208**, 415-424.

Goldberg SB *et al* (2016). Pembrolizumab for patients with melanoma or non-small-cell lung cancer and untreated brain metastases: early analysis of a non-randomised, open-label, phase 2 trial. *Lancet Oncol* **17**, 976-983.

Goodwin CR *et al* (2016). Local delivery methods of therapeutic agents in the treatment of diffuse intrinsic brainstem gliomas. *Clin Neurol Neurosurg* **142**, 120-127.

Gray SJ, Woodard KT & Samulski RJ (2010). Viral vectors and delivery strategies for CNS gene therapy. *Ther Deliv* **1**, 517-534.

Green AL & Kieran MW (2015). Pediatric brainstem gliomas: new understanding leads to potential new treatments for two very different tumors. *Curr Oncol Rep* **17**, 436.

Groothuis DR (2000). The blood-brain and blood-tumor barriers: a review of strategies for increasing drug delivery. *Neuro Oncol* **2**, 45-59.

Gross CC *et al* (2016). Impaired NK-mediated regulation of T-cell activity in multiple sclerosis is reconstituted by IL-2 receptor modulation. *Proc Natl Acad Sci U S A* **113**, E2973-2982.

Guan J, Beilharz EJ, Skinne SJ, Williams CE & Gluckman PD (2000). Intracerebral transportation and cellular localization of insulin-like growth factor-1 following central administration to rats with hypoxic-ischemic brain injury. *Brain Res* **853**, 163-173.

Haass C, Kaether C, Thinakaran G & Sisodia S (2012). Trafficking and proteolytic processing of APP. *Cold Spring Harb Perspect Med* **2**, a006270.

Haché M *et al* (2016). Intrathecal Injections in Children with Spinal Muscular Atrophy: Nusinersen Clinical Trial Experience. *J Child Neurol* **31**, 899-906.

Hadaczek P *et al* (2006). The "perivascular pump" driven by arterial pulsation is a powerful mechanism for the distribution of therapeutic molecules within the brain. *Mol Ther* **14**, 69-78.

Haley MJ & Lawrence CB (2017). The blood-brain barrier after stroke: Structural studies and the role of transcytotic vesicles. *J Cereb Blood Flow Metab* **37**, 456-470.

Hall WA, Djalilian HR, Nussbaum ES & Cho KH (2000). Long-term survival with metastatic cancer to the brain. *Med Oncol* **17**, 279-286.

Hammarlund-Udenaes M, de Lange E & Thorne R (2014). Drug Delivery to the Brain. 1st edition. AAPS Press. Springer.

Hannocks MJ *et al*. (2018) Molecular characterization of perivascular drainage pathways in the murine brain. *J Cereb Blood Flow Metab* **38**, 669-686.

Hauser SL *et al* (2017). Ocrelizumab versus Interferon Beta-1a in Relapsing Multiple Sclerosis. *N Engl J Med* **376**, 221-234.

Hauser SL, Belachew S & Kappos L (2017). Ocrelizumab in Primary Progressive and Relapsing Multiple Sclerosis. *N Engl J Med* **376**, 1694

Havrdova E, Horakova D & Kovarova I (2015). Alemtuzumab in the treatment of multiple sclerosis: key clinical trial results and considerations for use. *Ther Adv Neurol Disord* **8**, 31-45.

Heidl S, Ellinger L, Niederberger V, Waltl EE & Fuchs R (2016). Localization of the human neonatal Fc receptor (FcRn) in human nasal epithelium. *Protoplasma* **253**, 1557-1564.

Hemmer B, Frohman E, Hartung HP & Stüve O (2006). Central nervous system infections - a potential complication of systemic immunotherapy. *Curr Opin Neurol* **19**, 271-276.

Hemmer B, Nessler S, Zhou D, Kieseier B & Hartung HP (2006). Immunopathogenesis and immunotherapy of multiple sclerosis. *Nat Clin Pract Neurol* **2**, 201-211.

Hladky SB & Barrand MA (2014). Mechanisms of fluid movement into, through and out of the brain: evaluation of the evidence. *Fluids Barriers CNS* **11**, 26.

Holliger P & Hudson PJ (2005). Engineered antibody fragments and the rise of single domains. *Nat Biotechnol* **23**, 1126-1136.

Honig LS *et al* (2018). Trial of Solanezumab for Mild Dementia Due to Alzheimer's Disease. *N Engl J Med* **378**, 321-330.

Hook G, Yu J, Toneff T, Kindy M & Hook V (2014). Brain pyroglutamate amyloid-β is produced by cathepsin B and is reduced by the cysteine protease inhibitor E64d, representing a potential Alzheimer's disease therapeutic. *J Alzheimers Dis* **41**, 129-149.

Huang B *et al* (2017). Advances in Immunotherapy for Glioblastoma Multiforme. *J Immunol Res* **2017**, 3597613

Huang J *et al* (2017). Immune Checkpoint in Glioblastoma: Promising and Challenging. *Front Pharmacol* **8**, 242.

Hudis CA (2007). Trastuzumab--mechanism of action and use in clinical practice. *N Engl J Med* **357**, 39-51.

Hudson N *et al* (2014). Differential apicobasal VEGF signaling at vascular blood-neural barriers. *Dev Cell* **30**, 541-552.

Hwang C, Sinskey AJ & Lodish HF (1992). Oxidized redox state of glutathione in the endoplasmic reticulum. *Science* **257**, 1496-1502.a

Ichimura T, Fraser PA. & Cserr HF (1991). Distribution of extracellular tracers in perivascular spaces of the rat brain. *Brain Res* **545**, 103.

Iliff JJ *et al* (2012). A paravascular pathway facilitates CSF flow through the brain parenchyma and the clearance of interstitial solutes, including amyloid β. *Sci Transl Med* **4**, 147ra111.

Iliff JJ *et al* (2013). Cerebral arterial pulsation drives paravascular CSF-interstitial fluid exchange in the murine brain. *J Neurosci* **33**, 18190-18199.

Illum L (2012). Nasal drug delivery - recent developments and future prospects. *J Control Release* **161**, 254-263.

Inglese M *et al* (2005). Dilated perivascular spaces: hallmarks of mild traumatic brain injury. *Am J Neuroradiol* **26**, 719-724.

Iqbal K *et al* (2005). Tau pathology in Alzheimer disease and other tauopathies. *Biochim Biophys Acta* 1739, 198-210.

Iqbal K, Liu F & Gong CX (2016). Tau and neurodegenerative disease: the story so far. *Nat Rev Neurol* **12**, 15-27.

Ishida Y, Agata Y, Shibahara K & Honjo T (1992). Induced expression of PD-1, a novel member of the immunoglobulin gene superfamily, upon programmed cell death. *EMBO J* **11**, 3887-3895.

Ising C *et al* (2017). AAV-mediated expression of anti-tau scFvs decreases tau accumulation in a mouse model of tauopathy. *J Exp Med* **214**, 1227-1238.

Ivasyk I, Morgenstern PF, Wembacher-Schroeder E & Souweidane MM (2017). Influence of an intratumoral cyst on drug distribution by convection-enhanced delivery: case report. *J Neurosurg Pediatr* **20**, 256-260.

Jack CR *et al* (2011). Introduction to the recommendations from the National Institute on Aging-Alzheimer's Association workgroups on diagnostic guidelines for Alzheimer's disease. *Alzheimers Dement* **7**, 257-262.

Jain RK & Baxter LT (1988). Mechanisms of heterogeneous distribution of monoclonal antibodies and other macromolecules in tumors: significance of elevated interstitial pressure. *Cancer Res* **48**, 7022-7032.

Jitendra Sharma, PK Bansal, S & Banik A. (2011). Noninvasive routes of proteins and peptides drug delivery. *Indian J Pharm Sci* **73**, 367-375.

Johnson DR & O'Neill BP (2012). Glioblastoma survival in the United States before and during the temozolomide era. *J Neurooncol* **107**, 359-364.

Jones JL & Coles AJ (2014). Mode of action and clinical studies with alemtuzumab. *Exp Neurol* **262** Pt A, 37-43.

Jones PL, Gallagher BM & Sands H (1986). Autoradiographic analysis of monoclonal antibody distribution in human colon and breast tumor xenografts. *Cancer Immunol Immunother* **22**, 139-143.

Jordão JF *et al* (2010). Antibodies targeted to the brain with image-guided focused ultrasound reduces amyloid-beta plaque load in the TgCRND8 mouse model of Alzheimer's disease. *PLoS One* **5**, e10549.

Kanodia JS *et al* (2016). Prospective Design of Anti-Transferrin Receptor Bispecific Antibodies for Optimal Delivery into the Human Brain. *CPT Pharmacometrics Syst Pharmacol* **5**, 283-291.

Kaufman H (1998). Cerebrospinal fluid collections. Thieme

Kaufman MB (2017). Pharmaceutical Approval Update. P T 42, 562-580.

Kilic E *et al* (2010). Role of Nogo-A in neuronal survival in the reperfused ischemic brain. *J Cereb Blood Flow* Metab **30**, 969-984.

Kindt TJ, Goldsby RA & Osborne BA (2007). *Kuby Immunology*. 6th edition. W. H. Freeman and Co.

Kirsch DG & Hochberg FH (2003). Targeting HER2 in brain metastases from breast cancer. *Clin Cancer Res* **9**, 5435-5436.

Köhler G & Milstein C (1975). Continuous cultures of fused cells secreting antibody of predefined specificity. *Nature* **256**, 495-497.

Kolobov VV, Davydova TV, Zakharova IA, Gorbatov VI & Fomina VG (2012). [Repressional effects of the glutamate antibodies on expression of Dffb gene in the brain of rats with experimental Alzheimer's disease]. *Mol Biol (Mosk)* **46**, 757-765 (2012).

Kolobov VV, Zakharova IA, Fomina VG, Gorbatov VY & Davydova TV (2013). Effect of antibodies to glutamate on caspase-3 activity in brain structures of rats with experimental Alzheimer's disease. *Bull Exp Biol Med* **154**, 425-427 (2013).

Kovacs ZL *et al*. (2017). Disrupting the blood-brain barrier by focused ultrasound induces sterile inflammation. *Proc Natl Acad Sci U S A* **114**, E75-E84.

Kowal SL, Dall TM, Chakrabarti R, Storm MV & Jain A (2013). The current and projected economic burden of Parkinson's disease in the United States. *Mov Disord* **28**, 311-318

Kreisl TN *et al.* (2009). Phase II trial of single-agent bevacizumab followed by bevacizumab plus irinotecan at tumor progression in recurrent glioblastoma. *J Clin Oncol* **27**, 740-745.

Kumar NN *et al* (2016). Relative vascular permeability and vascularity across different regions of the rat nasal mucosa: implications for nasal physiology and drug delivery. *Sci Rep* **6**, 31732.

Kumar NN *et al* (2018). Delivery of immunoglobulin G antibodies to the rat nervous system following intranasal administration: Distribution, dose-response, and mechanisms of delivery. J Control Release **286**, 467-484.

Kuo TT & Aveson VG (2011). Neonatal Fc receptor and IgG-based therapeutics. *MAbs* **3**, 422-430.

Lajoie JM & Shusta EV (2015). Targeting receptor-mediated transport for delivery of biologics across the blood-brain barrier. *Ann Rev Pharmacol Toxicol* **55**, 613-631.

Lannfelt L *et al* (2014). Perspectives on future Alzheimer therapies: amyloid-β protofibrils - a new target for immunotherapy with BAN2401 in Alzheimer's disease. *Alzheimers Res Ther* **6**, 16.

Larson SM, Carrasquillo JA, Cheung NK & Press OW (2015). Radioimmunotherapy of human tumours. *Nat Rev Cancer* **15**, 347-360.

Lee H *et al* (2015). The Effect of Body Posture on Brain Glymphatic Transport. *J Neurosci* **35**, 11034-11044.

Leung DW, Cachianes G, Kuang WJ, Goeddel DV & Ferrara N (1989). Vascular endothelial growth factor is a secreted angiogenic mitogen. *Science* **246**, 1306-1309.

Levites Y *et al* (2006). Insights into the mechanisms of action of anti-Abeta antibodies in Alzheimer's disease mouse models. *FASEB J* **20**, 2576-2578.

Li L, Agarwal S & Elmquist WF (2013). Brain efflux index to investigate the influence of active efflux on brain distribution of pemetrexed and methotrexate. *Drug Metab Dispos* **41**, 659-667.

Liao F *et al* (2018). Targeting of nonlipidated, aggregated apoE with antibodies inhibits amyloid accumulation. *J Clin Invest*, JCI96429

Lo EH, Dalkara T & Moskowitz MA (2003). Mechanisms, challenges and opportunities in stroke. *Nat Rev Neurosci* **4**, 399-415.

Lochhead JJ & Thorne RG (2012). Intranasal delivery of biologics to the central nervous system. *Adv Drug Deliv Rev* **64**, 614-628.

Lochhead JJ & Thorne RG (2014). In Drug delivery to the brain - Physiological concepts, Methodologies and Approaches. Advances in the Pharmaceutical Sciences (eds Hammarlund-Udenaes, de Lange, & Thorne) Ch. 14, 401-431. AAPS Press. Springer.

Lochhead JJ, Wolak DJ, Pizzo ME & Thorne RG (2015). Rapid transport within cerebral perivascular spaces underlies widespread tracer distribution in the brain after intranasal administration. *J Cereb Blood Flow Metab* **35**, 371-381.

Lockman PR *et al* (2010). Heterogeneous blood-tumor barrier permeability determines drug efficacy in experimental brain metastases of breast cancer. *Clin Cancer Res* **16**, 5664-5678.

Loddick SA *et al* (1998). Displacement of insulin-like growth factors from their binding proteins as a potential treatment for stroke. *Proc Natl Acad Sci U S A* **95**, 1894-1898.

Long GV *et al* (2018). Combination nivolumab and ipilimumab or nivolumab alone in melanoma brain metastases: a multicenter randomised phase 2 study. *Lancet Oncol* **19**, 672-681.

Lopus M *et al* (2010). Maytansine and cellular metabolites of antibody-maytansinoid conjugates strongly suppress microtubule dynamics by binding to microtubules. *Mol Cancer Ther* **9**, 2689-2699.

Löscher W & Potschka H (2005). Drug resistance in brain diseases and the role of drug efflux transporters. *Nat Rev Neurosci* **6**, 591-602.

Louveau A *et al* (2015). Structural and functional features of central nervous system lymphatic vessels. *Nature* **523**, 337-341.

Lu NT *et al* (2015). Intrathecal trastuzumab: immunotherapy improves the prognosis of leptomeningeal metastases in HER-2+ breast cancer patient. *J Immunother Cancer* **3**, 41.

Luz I, Liraz O & Michaelson DM (2016). An Anti-apoE4 Specific Monoclonal Antibody Counteracts the Pathological Effects of apoE4 in vivo. *Curr Alzheimer Res* **13**, 918-929.

Lynch SM *et al* (2008). An scFv intrabody against the nonamyloid component of alpha-synuclein reduces intracellular aggregation and toxicity. *J Mol Biol* **377**, 136-147.

Ma J *et al* (2007). An experimental test of stroke recovery by implanting a hyaluronic acid hydrogel carrying a Nogo receptor antibody in a rat model. *Biomed Mater* **2**, 233-240.

Maher EA, Mietz J, Arteaga CL, DePinho RA & Mohla S (2009). Brain metastasis: opportunities in basic and translational research. *Cancer Res* **69**, 6015-6020.

Mao X *et al* (2016). Pathological α-synuclein transmission initiated by binding lymphocyte-activation gene 3. *Science* **353**.

Marasco WA (1997). Intrabodies: turning the humoral immune system outside in for intracellular immunization. *Gene Ther* **4**, 11-15.

Margolin K (2012). Ipilimumab in a Phase II trial of melanoma patients with brain metastases. *Oncoimmunol* **1**, 1197-1199.

Margolin K *et al* (2012). Ipilimumab in patients with melanoma and brain metastases: an open-label, phase 2 trial. *Lancet Oncol* **13**, 459-465.

Masliah E *et al* (2011). Passive immunization reduces behavioral and neuropathological deficits in an alpha-synuclein transgenic model of Lewy body disease. *PLoS One* **6**, e19338.

Mckee AC & Daneshvar DH (2015). The neuropathology of traumatic brain injury. *Handb Clin Neurol* **127**, 45-66

McKee AC, Stein TD, Kiernan PT & Alvarez VE (2015). The neuropathology of chronic traumatic encephalopathy. *Brain Pathol* **25**, 350-364.

McKhann G *et al* (1984). Clinical diagnosis of Alzheimer's disease: report of the NINCDS-ADRDA Work Group under the auspices of Department of Health and Human Services Task Force on Alzheimer's Disease. *Neurology* **34**, 939-944.

McKhann GM *et al* (2011). The diagnosis of dementia due to Alzheimer's disease: recommendations from the National Institute on Aging-Alzheimer's Association workgroups on diagnostic guidelines for Alzheimer's disease. *Alzheimers Dement* **7**, 263-269.

Merkus P, Ebbens FA, Muller B & Fokkens WJ (2006). Influence of anatomy and head position on intranasal drug deposition. *Eur Arch Otorhinolaryngol* **263**, 827-832.

Merlini M, Wanner D & Nitsch RM (2016). Tau pathology-dependent remodelling of cerebral arteries precedes Alzheimer's disease-related microvascular cerebral amyloid angiopathy. *Acta Neuropathol* **131**, 737-752.

Michel CC (1996). Transport of macromolecules through microvascular walls. *Cardiovasc Res* **32**, 644-653.

Miyauchi JT & Tsirka SE (2017). Advances in immunotherapeutic research for glioma therapy. *J Neurol*, s00415

Mokri B (2001). The Monro-Kellie hypothesis: applications in CSF volume depletion. *Neurology* **56**, 1746-1748.

Montalban XX *et al* (2017). Ocrelizumab versus Placebo in Primary Progressive Multiple Sclerosis. *N Engl J Med* **376**, 209-220.

Mrugala MM, Rubenstein JL, Ponzoni M & Batchelor TT (2009). Insights into the biology of primary central nervous system lymphoma. *Curr Oncol Rep* **11**, 73-80.

Munson JM & Shieh AC (2014). Interstitial fluid flow in cancer: implications for disease progression and treatment. *Cancer Manag Res* **6**, 317-328.

Musiek ES & Holtzman DM (2015). Three dimensions of the amyloid hypothesis: time, space and 'wingmen'. *Nat Neurosci* **18**, 800-806.

Nabeshima S, Reese TS, Landis DM & Brightman MW (1975). Junctions in the meninges and marginal glia. J *Comp Neurol* **164**, 127-169.

Neuwelt EA *et al* (1991). Primary CNS lymphoma treated with osmotic blood-brain barrier disruption: prolonged survival and preservation of cognitive function. *J Clin Oncol* **9**, 1580-1590.

Nicole O *et al*. The proteolytic activity of tissue-plasminogen activator enhances NMDA receptor-mediated signaling. *Nat Med* **7**, 59-64, doi:10.1038/83358 (2001).

Nimmerjahn F & Ravetch JV (2006). Fc-receptors: old friends & new family members. *Immunity* **1**, 19-28.

Nimmerjahn F & Ravetch JV (2007). Fc-receptors as regulators of immunity. *Adv Immunol* **96**, 179-204.

Nimmerjahn F & Ravetch JV (2008). Analyzing antibody-Fc-receptor interactions. *Methods Mol Biol* **415**, 151-162.

Nimmerjahn F & Ravetch JV (2008). Fcgamma receptors as regulators of immune responses. *Nat Rev Immunol* **8**, 34-47.

Nimmerjahn, F. & Ravetch, J. V. FcγRs in health and disease. Curr Top Microbiol Immunol 350, 105-125, doi:10.1007/82_2010_86 (2011).

Ouellette D *et al*. (2010). Studies in serum support rapid formation of disulfide bond between unpaired cysteine residues in the VH domain of an immunoglobulin G1 molecule. *Anal Biochem* **397**, 37-47.

Paik S *et al* (1990). Pathologic findings from the National Surgical Adjuvant Breast and Bowel Project: prognostic significance of erbB-2 protein overexpression in primary breast cancer. *J Clin Oncol* **8**, 103-112.

Pangalos MN, Schechter LE & Hurko O (2007). Drug development for CNS disorders: strategies for balancing risk and reducing attrition. *Nat Rev Drug Discov* **6**, 521-532.

Panza F *et al* (2018). The potential of solanezumab and gantenerumab to prevent Alzheimer's disease in people with inherited mutations that cause its early onset. *Expert Opin Biol Ther* **18**, 25-35.

Panza F, Solfrizzi V, Imbimbo BP & Logroscino G (2014). Amyloid-directed monoclonal antibodies for the treatment of Alzheimer's disease: the point of no return? *Expert Opin Biol Ther* **14**, 1465-1476.

Pappius HM, Savaki HE, Fieschi C, Rapoport SI. & Sokoloff L (1979). Osmotic opening of the blood-brain barrier and local cerebral glucose utilization. *Ann Neurol* **5**, 211-219.

Pardridge WM (1997). Drug delivery to the brain. *J Cereb Blood Flow Metab* **17**, 713-731.

Park WY *et al* (2016). Intrathecal Trastuzumab Treatment in Patients with Breast Cancer and Leptomeningeal Carcinomatosis. *Cancer Res Treat* **48**, 843-847.

Parrish KE, Sarkaria JN & Elmquist WF (2015). Improving drug delivery to primary and metastatic brain tumors: strategies to overcome the blood-brain barrier. *Clin Pharmacol Ther* **97**, 336-346.

Pastan I, Hassan R, Fitzgerald DJ & Kreitman RJ (2006). Immunotoxin therapy of cancer. *Nat Rev Cancer* **6**, 559-565.

Patel AP *et al*. (2014). Single-cell RNA-seq highlights intratumoral heterogeneity in primary glioblastoma. *Science* **344**, 1396-1401.

Patel SJ *et al* (2005). Safety and feasibility of convection-enhanced delivery of Cotara for the treatment of malignant glioma: initial experience in 51 patients. *Neurosurgery* **56**, 1243-1252.

Pedersen JT & Sigurdsson EM (2015). Tau immunotherapy for Alzheimer's disease. *Trends Mol Med* **21**, 394-402.

Perissinotti AJ & Reeves DJ (2010). Role of intrathecal rituximab and trastuzumab in the management of leptomeningeal carcinomatosis. *Ann Pharmacother* **44**, 1633-1640.

Perry VH & Holmes C (2014). Microglial priming in neurodegenerative disease. *Nat Rev Neurol* **10**, 217-224.

Perry VH, Cunningham C & Holmes C (2007). Systemic infections and inflammation affect chronic neurodegeneration. *Nat Rev Immunol* **7**, 161-167.

Petereit HF & Rubbert-Roth (2009). A. Rituximab levels in cerebrospinal fluid of patients with neurological autoimmune disorders. *Mult Scler* **15**, 189-192.

Pfannl R & Harris F (2004). Pathology of primary central nervous system lymphoma and related conditions. 29-41. Butterworth-Heinemann.

Phillips AC *et al* (2016). ABT-414, an Antibody-Drug Conjugate Targeting a Tumor-Selective EGFR Epitope. *Mol Cancer Ther* **15**, 661-669.

Phillips EH, Fox CP & Cwynarski K (2014). Primary CNS lymphoma. *Curr Hematol Malig Rep* **9**, 243-253.

Pizzo ME *et al* (2018). Intrathecal antibody distribution in the rat brain: surface diffusion, perivascular transport, and osmotic enhancement of delivery. *J Physiol*, 275105.

Plate KH, Breier G, Weich HA & Risau W (1992). Vascular endothelial growth factor is a potential tumor angiogenesis factor in human gliomas in vivo. *Nature* **359**, 845-848.

Poduslo JF, Curran GL & Berg CT (1994). Macromolecular permeability across the blood-nerve and blood-brain barriers. Proc Natl Acad Sci U S A 91, 5705-5709.

Pollay M (2010). The function and structure of the cerebrospinal fluid outflow system. *Cerebrospinal Fluid Res* **7**, 9.

Polman CH *et al* (2006). A randomized, placebo-controlled trial of natalizumab for relapsing multiple sclerosis. *N Engl J Med* **354**, 899-910.

Preston JE, Joan Abbott N & Begley, DJ (2014). Transcytosis of macromolecules at the blood-brain barrier. *Adv Pharmacol* **71**, 147-163.

Prince M, Comas-Herrera A, Knapp M, Guerchet M & Karagiannidou M (2016). *World Alzheimer Report*

Puglielli L, Tanzi RE & Kovacs DM (2003). Alzheimer's disease: the cholesterol connection. *Nat Neurosci* 6, 345-351.

Putatunda R, Bethea JR & Hu WH (2018). Potential immunotherapies for traumatic brain and spinal cord injury. *Chin J Traumatol* **21**, 125-136.

Raper SE *et al* (2002). A pilot study of in vivo liver-directed gene transfer with an adenoviral vector in partial ornithine transcarbamylase deficiency. *Hum Gene Ther* **13**, 163-175.

Rapoport SI, Bachman DS. & Thompson HK (1972). Chronic effects of osmotic opening of the blood-brain barrier in the monkey. *Science* **176**, 1243-1245.

Rapoport SI, Hori M & Klatzo I (1972). Testing of a hypothesis for osmotic opening of the blood-brain barrier. *Am J Physiol* **223,** 323-331.

Razpotnik R, Novak N, Čurin Šerbec V & Rajcevic U (2017). Targeting Malignant Brain Tumors with Antibodies. *Front Immunol* **8**, 1181.

Reese TS & Karnovsky MJ (1967). Fine structural localization of a blood-brain barrier to exogenous peroxidase. J *Cell Biol* **34**, 207-217.

Rennels ML, Gregory TF, Blaumanis OR, Fujimoto K & Grady PA (1985). Evidence for a 'paravascular' fluid circulation in the mammalian central nervous system, provided by the rapid distribution of tracer protein throughout the brain from the subarachnoid space. *Brain Res* **326**, 47-63.

Riva P *et al* (1999). 131I radioconjugated antibodies for the locoregional radioimmunotherapy of high-grade malignant glioma--phase I and II study. *Acta Oncol* **38**, 351-359.

Roerink ME *et al* (2015). Central delivery of iodine-125-labeled cetuximab, etanercept and anakinra after perispinal injection in rats: possible implications for treating Alzheimer's disease. *Alzheimers Res Ther* **7**, 70.

Roher AE *et al* (2000). Oligomerizaiton and fibril assembly of the amyloid-beta protein. *Biochim Biophys Acta* **1502**, 31-43.

Russel DC & Rubinstein LJ (1989). Pathology of tumors of the nervous system. 5th edition.

Sakane T *et al* (1995). Direct drug transport from the rat nasal cavity to the cerebrospinal fluid: the relation to the molecular weight of drugs. *J Pharm Pharmacol* **47**, 379-381.

Sakka L, Coll G & Chazal J (2011). Anatomy and physiology of cerebrospinal fluid. *Eur Ann Otorhinolaryngol Head Neck Dis* **128**, 309-316.

Salegio EA *et al* (2014). Distribution of nanoparticles throughout the cerebral cortex of rodents and non-human primates: Implications for gene and drug therapy. *Front Neuroanat* **8**, 9.

Salloway S *et al* (2014). Two phase 3 trials of bapineuzumab in mild-to-moderate Alzheimer's disease. *N Engl J Med* **370**, 322-333.

Sallusto F *et al* (2012). T-cell trafficking in the central nervous system. *Immunol Rev* **248**, 216-227.

Sampson JH *et al* (2006). Comparison of intratumoral bolus injection and convection-enhanced delivery of radiolabeled antitenascin monoclonal antibodies. *Neurosurg Focus* **20**, E14.

Sampson JH, Maus MV & June CH (2017). Immunotherapy for Brain Tumors. *J Clin Oncol* **35**, 2450-2456.

Sarin H *et al* (2010). Physiologic upper limits of pore size of different blood capillary types and another perspective on the dual pore theory of microvascular permeability. *J Angiogenes Res* **2**, 14.

Schenk DB *et al*. (2017). First-in-human assessment of PRX002, an anti-α-synuclein monoclonal antibody, in healthy volunteers. *Mov Disord* **32**, 211-218.

Scherer H (1938). Structural development in gliomas. *Am J Cancer* **34**, 333-351.

Schlageter KE, Molnar P, Lapin GD & Groothuis DR (1999). Microvessel organization and structure in experimental brain tumors: microvessel populations with distinctive structural and functional properties. *Microvasc Res* **58**, 312-328.

Scoto M, Finkel RS, Mercuri E & Muntoni F (2017). Therapeutic approaches for spinal muscular atrophy (SMA). *Gene Ther* **24**, 514-519.

Seabrook TJ, Johnston M & Hay JB (1998). Cerebral spinal fluid lymphocytes are part of the normal recirculating lymphocyte pool. *J Neuroimmunol* **91**, 100-107.

Selkoe DJ & Hardy J (2016). The amyloid hypothesis of Alzheimer's disease at 25 years. *EMBO Mol Med* **8**, 595-608.

Sellebjerg F *et al* (2016). Exploring potential mechanisms of action of natalizumab in secondary progressive multiple sclerosis. *Ther Adv Neurol Disord* **9**, 31-43.

Senger DR *et al.* (1983). Tumor cells secrete a vascular permeability factor that promotes accumulation of ascites fluid. *Science* **219**, 983-985.

Senger DR, Perruzzi CA, Feder J & Dvorak HF (1986). A highly conserved vascular permeability factor secreted by a variety of human and rodent tumor cell lines. *Cancer Res* **46**, 5629-5632.

Sengupta U, Nilson AN & Kayed R (2016). The Role of Amyloid-β Oligomers in Toxicity, Propagation, and Immunotherapy. *EBioMedicine* **6**, 42-49.

Serrano-Pozo A, Frosch MP, Masliah E & Hyman BT (2011). Neuropathological alterations in Alzheimer disease. *Cold Spring Harb Perspect Med* **1**, a006189.

Shahaduzzaman M *et al*. (2015). Anti-human α-synuclein N-terminal peptide antibody protects against dopaminergic cell death and ameliorates behavioral deficits in an AAV-α-synuclein rat model of Parkinson's disease. *PLoS One* **10**, e0116841.

Sherer TB, Fiske BK, Svendsen CN, Lang AE & Langston JW. (2006). Crossroads in GDNF therapy for Parkinson's disease. *Mov Disord* **21**, 136-141.

Siemers ER *et al* (2016). Phase 3 solanezumab trials: Secondary outcomes in mild Alzheimer's disease patients. *Alzheimers Dement* **12**, 110-120.

Sivasankaran B *et al* (2009). Tenascin-C is a novel RBPJkappa-induced target gene for Notch signaling in gliomas. *Cancer Res* **69**, 458-465.

Sperling RA *et al* (2011). Amyloid-related imaging abnormalities in amyloid-modifying therapeutic trials: recommendations from the Alzheimer's Association Research Roundtable Workgroup. *Alzheimers Dement* **7**, 367-385.

Sperling RA *et al* (2014). The A4 study: stopping AD before symptoms begin? *Sci Transl Med* **6**, 228fs213.

St-Amour I *et al* (2013). Brain bioavailability of human intravenous immunoglobulin and its transport through the murine blood-brain barrier. *J Cereb Blood Flow Metab* **33**, 1983-1992.

St-Amour I, Cicchetti F & Calon F (2016). Immunotherapies in Alzheimer's disease: Too much, too little, too late or off-target? *Acta Neuropathol* **131**, 481-504.

Stefanini MO, Wu FT, Mac Gabhann F & Popel AS (2009). The presence of VEGF receptors on the luminal surface of endothelial cells affects VEGF distribution and VEGF signaling. *PLoS Comput Biol* **5,** e1000622.

Strittmatter W *et al* (1993). Apolipoprotein E: high-avidity binding to beta-amyloid and increased frequency of type 4 allele in late-onset familial Alzheimer disease. *Proc Natl Acad Sci U S A* **90**, 1977-1981.

Stupp R *et al* (2005). Radiotherapy plus concomitant and adjuvant temozolomide for glioblastoma. *N Engl J Med* **352**, 987-996.

Stupp R *et al* (2009). Effects of radiotherapy with concomitant and adjuvant temozolomide versus radiotherapy alone on survival in glioblastoma in a randomised phase III study: 5-year analysis of the EORTC-NCIC trial. *Lancet Oncol* **10**, 459-466.

Syková E & Nicholson C (2008). Diffusion in brain extracellular space. *Physiol Rev* **88**, 1277-1340

Szentistványi I, Patlak CS, Ellis RA & Cserr HF (1984). Drainage of interstitial fluid from different regions of rat brain. *Am J Physiol* **246**, F835-844.

Taal W *et al.* (2014). Single-agent bevacizumab or lomustine versus a combination of bevacizumab plus lomustine in patients with recurrent glioblastoma (BELOB trial): a randomised controlled phase 2 trial. *Lancet Oncol* **15,** 943-953.

Taguchi H *et al* (2008). Catalytic antibodies to amyloid beta peptide in defense against Alzheimer disease. *Autoimmun Rev* **7**, 391-397.

Tarasoff-Conway JM *et al* (2015). Clearance systems in the brain-implications for Alzheimer disease. *Nat Rev* Neurol **11**, 457-470.

Thakker DR *et al* (2009). Intracerebroventricular amyloid-beta antibodies reduce cerebral amyloid angiopathy and associated micro-hemorrhages in aged Tg2576 mice. *Proc Natl Acad Sci U S A* **106**, 4501-4506.

Thal DR, Rüb U, Orantes M & Braak H (2002). Phases of A beta-deposition in the human brain and its relevance for the development of AD. *Neurology* **58**, 1791-1800.

Thorne R (2014). in Drug delivery to the brain - Physiological concepts, Methodologies and Approaches. Advances in the Pharmaceutical Sciences (eds Hammarlund-Udenaes, de Lange, & Thorne) Ch. Appendix, 685-707 (Springer, 2014).

Thorne RG & Frey WH (2001). Delivery of neurotrophic factors to the central nervous system: pharmacokinetic considerations. *Clin Pharmacokinet* **40**, 907-946.

Thorne RG, Emory CR, Ala TA & Frey WH (1995). Quantitative analysis of the olfactory pathway for drug delivery to the brain. *Brain Res* **692**, 278-282.

Thorne RG, Hanson LR, Ross TM, Tung D & Frey WH (2008). Delivery of interferon-beta to the monkey nervous system following intranasal administration. *Neuroscience* **152**, 785-797.

Thorne RG, Pronk GJ, Padmanabhan V & Frey WH (2004). Delivery of insulin-like growth factor-I to the rat brain and spinal cord along olfactory and trigeminal pathways following intranasal administration. *Neuroscience* **127**, 481-496.

Thorsen F & Tysnes BB (1997). Brain tumor cell invasion, anatomical and biological considerations. *Anticancer Res* **17**, 4121-4126.

Tobinick E (2008). Perispinal etanercept produces rapid improvement in primary progressive aphasia: identification of a novel, rapidly reversible TNF-mediated pathophysiologic mechanism. *Medscape J Med* **10**, 135.

Tobinick E (2009). Perispinal etanercept for neuroinflammatory disorders. *Drug Discov Today* **14**, 168-177

Tobinick EL & Gross H (2008). Rapid cognitive improvement in Alzheimer's disease following perispinal etanercept administration. *J Neuroinflammation* **5**, 2.

Tobinick EL & Gross H. Rapid improvement in verbal fluency and aphasia following perispinal etanercept in Alzheimer's disease. *BMC Neurol* **8**, 27.

Tobinick EL. Perispinal Delivery of CNS Drugs. *CNS Drugs* **30**, 469-480.

Tomura N *et al* (1990). Differentiation between cerebral embolism and thrombosis on sequential CT scans. *J Comput Assist Tomogr* **14**, 26-31.

Treps L, Perret R, Edmond S, Ricard D & Gavard J (2017). Glioblastoma stem-like cells secrete the pro-angiogenic VEGF-A factor in extracellular vesicles. *J Extracell Vesicles* **6**, 1359479.

Tyson T *et al*. (2017). Novel animal model defines genetic contributions for neuron-to-neuron transfer of α-synuclein. *Sci Rep* **7**, 7506.

Tyson, T, Steiner JA & Brundin P (2016). Sorting out release, uptake and processing of alpha-synuclein during prion-like spread of pathology. *J Neurochem* **139 Suppl 1**, 275-289.

Urquhart L (2018). Market watch: Top drugs and companies by sales in 2017. *Nat Rev Drug Discov* **17**, 232.

Valera E & Masliah E (2013). Immunotherapy for neurodegenerative diseases: focus on α-synucleinopathies. *Pharmacol Ther* **138**, 311-322.

Valiente M *et al* (2014). Serpins promote cancer cell survival and vascular co-option in brain metastasis. *Cell* **156**, 1002-1016.

van Tellingen O *et al* (2015). Overcoming the blood-brain tumor barrier for effective glioblastoma treatment. *Drug Resist Updat* **19**, 1-12.

Vargová L *et al* (2003). Diffusion parameters of the extracellular space in human gliomas. *Glia* **42**, 77-88.

Vogelbaum M (2017). Novel convection enhanced drug delivery device. http://consultqd.clevelandclinic.org/novel-convection-enhanced-delivery-device-wins-fda-clearance. (accessed Jul 29, 2019)

Vredenburgh JJ *et al.* (2007). Bevacizumab plus irinotecan in recurrent glioblastoma multiforme. *J Clin Oncol* **25**, 4722-4729.

Vredenburgh JJ *et al.* (2007). Phase II trial of bevacizumab and irinotecan in recurrent malignant glioma. *Clin Cancer Res* **13**, 1253-1259.

Wallace MS (2006). Ziconotide: a new nonopioid intrathecal analgesic for the treatment of chronic pain. Expert Rev *Neurother* **6**, 1423-1428.

Wallace MS *et al* (2006). Intrathecal ziconotide in the treatment of chronic nonmalignant pain: a randomized, double-blind, placebo-controlled clinical trial. *Neuromodulation* **9**, 75-86.

Wang W, Wang EQ & Balthasar JP (2008). Monoclonal antibody pharmacokinetics and pharmacodynamics. Clin Pharmacol Ther 84, 548-558.

Watanabe H *et al* (2017). The effect of nivolumab treatment for central nervous system metastases in non-small cell lung cancer. *J Clin Oncol* **35**

Watts RJ & Dennis MS (2013). Bispecific antibodies for delivery into the brain. *Curr Opin Chem Biol* **17**, 393-399.

Weiner HL & Frenkel D (2006). Immunology and immunotherapy of Alzheimer's disease. *Nat Rev Immunol* **6**, 404-416.

Wolak DJ & Thorne RG (2013). Diffusion of Macromolecules in the Brain: Implications for Drug Delivery. *Mol Pharm*, 300495e

Wolak DJ, Pizzo ME & Thorne RG (2018). Probing the extracellular diffusion of antibodies in brain using in vivo integrative optical imaging and ex vivo fluorescence imaging. *J Control Release* **197**, 78-86

Wolburg H *et al* (2008). Epithelial and endothelial barriers in the olfactory region of the nasal cavity of the rat. Histochem Cell Biol 130, 127-140, doi:10.1007/s00418-008-0410-2 (2008).

Wootla B *et al* (2016). Recent Advances in Monoclonal Antibody Therapies for Multiple Sclerosis. *Expert Opin Biol Ther* **16**, 827-839.

Workman CJ, Rice DS, Dugger KJ, Kurschner C & Vignali DA (2002). Phenotypic analysis of the murine CD4-related glycoprotein, CD223 (LAG-3). *Eur J Immunol* **32**, 2255-2263

Wu AM & Senter PD (2005). Arming antibodies: prospects and challenges for immunoconjugates. *Nat Biotechnol* **23**, 1137-1146.

Xue S, Hu M, Iyer V & Yu J (2017). Blocking the PD-1/PD-L1 pathway in glioma: a potential new treatment strategy. *J Hematol Oncol* **10**, 81.

Yamada K *et al* (2017). Extracellular Tau and Its Potential Role in the Propagation of Tau Pathology. *Front Neurosci* **11**, 667.

Yamada K *et al* (2017). In Vivo Microdialysis of Brain Interstitial Fluid for the Determination of Extracellular Tau Levels. *Methods Mol Biol* **1523**, 285-296.

Ye L, Zeng R, Bai Y, Roopenian DC & Zhu X (2011). Efficient mucosal vaccination mediated by the neonatal Fc receptor. *Nat Biotechnol* **29**, 158-163.

Yin D *et al* (2010). Cannula placement for effective convection-enhanced delivery in the nonhuman primate thalamus and brainstem: implications for clinical delivery of therapeutics. *J Neurosurg* **113**, 240-248.

Yin D, Forsayeth J & Bankiewicz KS (2010). Optimized cannula design and placement for convection-enhanced delivery in rat striatum. *J Neurosci Methods* **187**, 46-51.

Yu CY, Ng G & Liao P (2013). Therapeutic antibodies in stroke. *Transl Stroke Res* **4**, 477-483.

Yu YJ & Watts RJ (2013). Developing therapeutic antibodies for neurodegenerative disease. *Neurotherapeutics* **10**, 459-472.

Yu YJ *et al* (2011). Boosting brain uptake of a therapeutic antibody by reducing its affinity for a transcytosis target. *Sci Transl Med* **3**, 84ra44.

Yu Z *et al* (2016). Efficacy and safety of bevacizumab for the treatment of glioblastoma. *Exp Ther Med* **11**, 371-380.

Zafeiriou DI & Batzios SP (2013). Brain and spinal MR imaging findings in mucopolysaccharidoses: a review. *Am J Neuroradiol* **34**, 5-13.

Zalutsky MR *et al* (2008). Clinical experience with alpha-particle emitting 211At: treatment of recurrent brain tumor patients with 211At-labeled chimeric antitenascin monoclonal antibody 81C6. *J Nucl Med* **49**, 30-38.

Zang X & Allison JP (2007). The B7 family and cancer therapy: costimulation and coinhibition. *Clin Cancer Res* **13**, 5271-5279.

Zhou C, Emadi S, Sierks MR & Messer A (2004). A human single-chain Fv intrabody blocks aberrant cellular effects of overexpressed alpha-synuclein. *Mol Ther* **10**, 1023-1031.

Zhou QH, Boado RJ, Lu JZ, Hui EK & Pardridge WM. (2010). Monoclonal antibody-glial-derived neurotrophic factor fusion protein penetrates the blood-brain barrier in the mouse. *Drug Metab Dispos* **38**, 566-572.

Zuchero YJ *et al* (2016). Discovery of Novel Blood-Brain Barrier Targets to Enhance Brain Uptake of Therapeutic Antibodies. *Neuron* **89**, 70-82.

Zünkeler B *et al* (1996). Quantification and pharmacokinetics of blood-brain barrier disruption in humans. *J Neurosurg* **85**, 1056-1065.

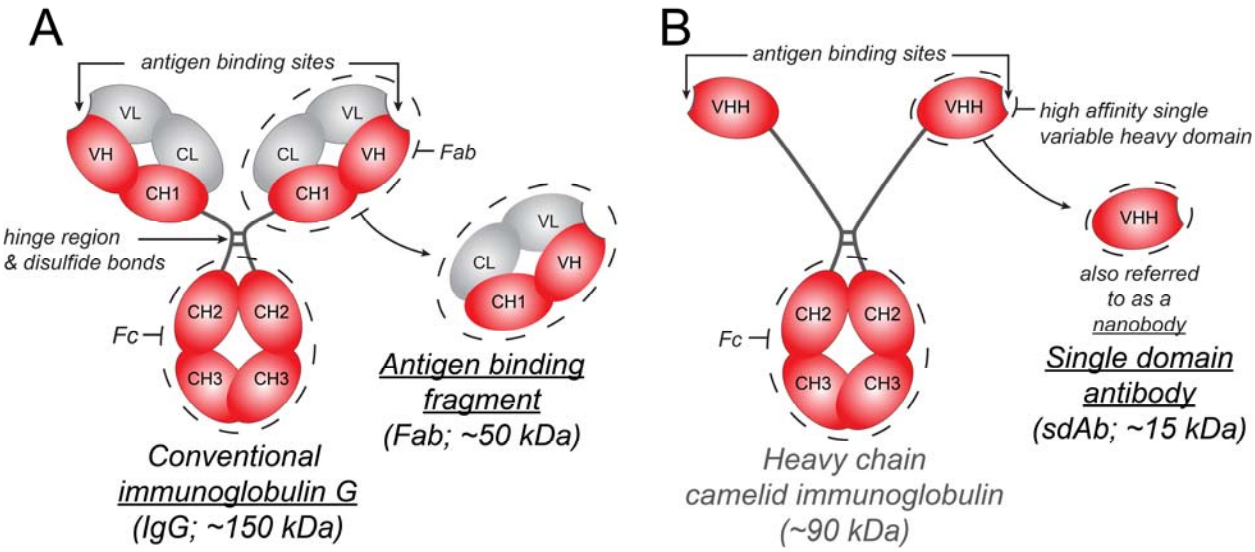

Figure 1. Summary of IgG, Fab, and sdAb structure and sizes. (A) Full length IgG is a Y shaped molecule made up of four polypeptide chains – two heavy chains (red) and two light chains (grey) that are linked by disulfide bonds. Each polypeptide chain has constant domains (C) and variable domains (V). There are two Fab arms, each containing an antigen-binding site made up of the variable domains of the heavy and light chains, which can recognize antigens with high specificity. The crystallizable fragment or Fc arm can interact with Fc receptors. (B) Camelids, sharks and other cartilaginous fish (Chondrichthyes) produce a unique IgG molecule consisting of heavy chains alone. A camelid IgG molecule is depicted here. A single heavy chain variable domain is also referred to as a single domain antibody or nanobody. Unlike the antibody variable domains in other species, camelid and cartilaginous fish variable domains do not aggregate when isolated and retain their antigen binding capacity; this has generated interest in their use as therapeutics when a smaller size and no Fc interactions are desired (Holliger & Hudson, 2005).

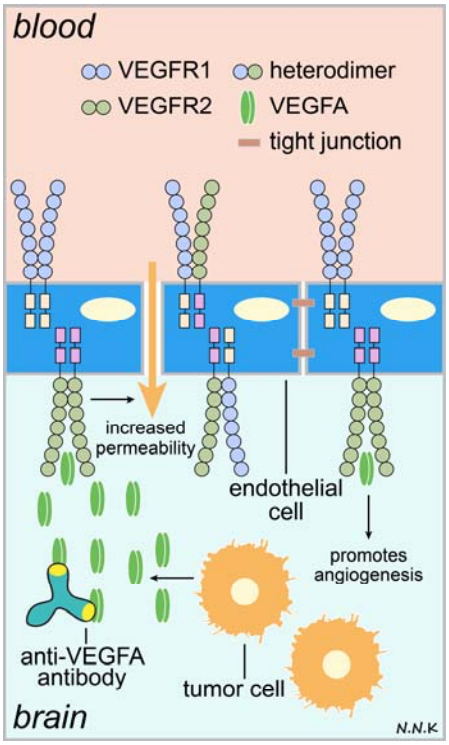

Figure 2. Passive immunotherapy strategies for brain cancer using anti-angiogenic antibodies. VEGFA binding to VEGFR2 triggers an increase in paracellular permeability, downregulation of tight junctional proteins, and the promotion of angiogenesis. Anti-VEGFA antibodies can bind to VEGFA and prevent angiogenesis thus inhibiting tumor growth and survival. Adapted from Hudson *et al.*, 2014. Abbreviations: VEGF – vascular endothelial growth factor; VEGFR – VEGF receptor.

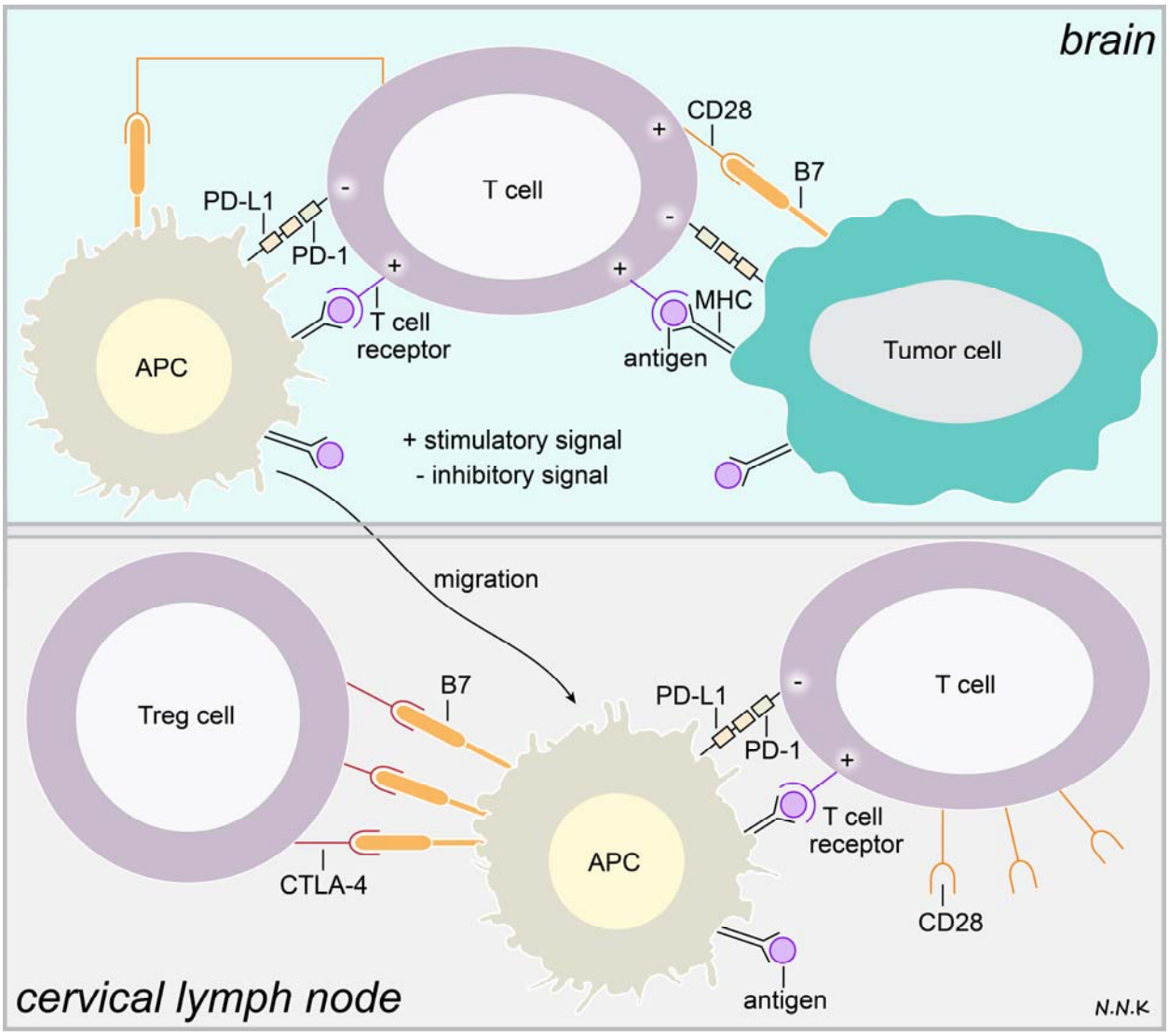

Figure 3. T cell immune response and immune checkpoints in brain cancer. T cells may recognize tumor antigen peptides presented via MHC class I/II molecules on tumor cells or APCs via the TCR, resulting in a weak immune stimulatory signal. Interaction between the TCR and tumor antigen peptide/MHC complex can only activate the T cell in the presence of other co-stimulatory immune signaling. However, tumor cells and APCs in the tumor microenvironment express high levels of programmed cell death-ligand-1 (PD-L1), a ligand for the programmed cell death - (PD-1) receptor expressed by T cells, which inhibits T cell activation. APCs presenting the tumor antigen peptide/MHC complex may migrate to the cervical lymph nodes where T cells recognizing the tumor antigen may be activated and directed to the tumor. In addition to the TCR-tumor antigen/MHC interaction, the T cell must

receive co-stimulatory signals in order to be activated. This co-stimulatory signal is typically received when the classification determinant 28 (CD28) receptor on T cells interacts with the B7 ligand expressed by APCs. However, regulatory T cells (Treg cells) express high amounts of cytotoxic T-lymphocyte-associated protein 4 (CTLA-4) – a receptor that mimics CD28 and has an even higher affinity for the B7 ligand. Thus, CTLA-4-B7 interaction can compete with the CD28-B7 interaction, resulting in the lack of appropriate co-stimulatory signaling to activate tumor antigen recognizing T cells. Adapted from Buchbinder & Desai, 2016; Huang *et al.*, 2017; Huang *et al.*, 2017. Abbreviations: PD-1 – programmed cell death protein-1; PD-L1 – programmed cell death protein ligand-1; CTLA-4 – cytotoxic T-lymphocyte-associated protein 4; Treg – regulatory T cells; CD28 – classification determinant 28.

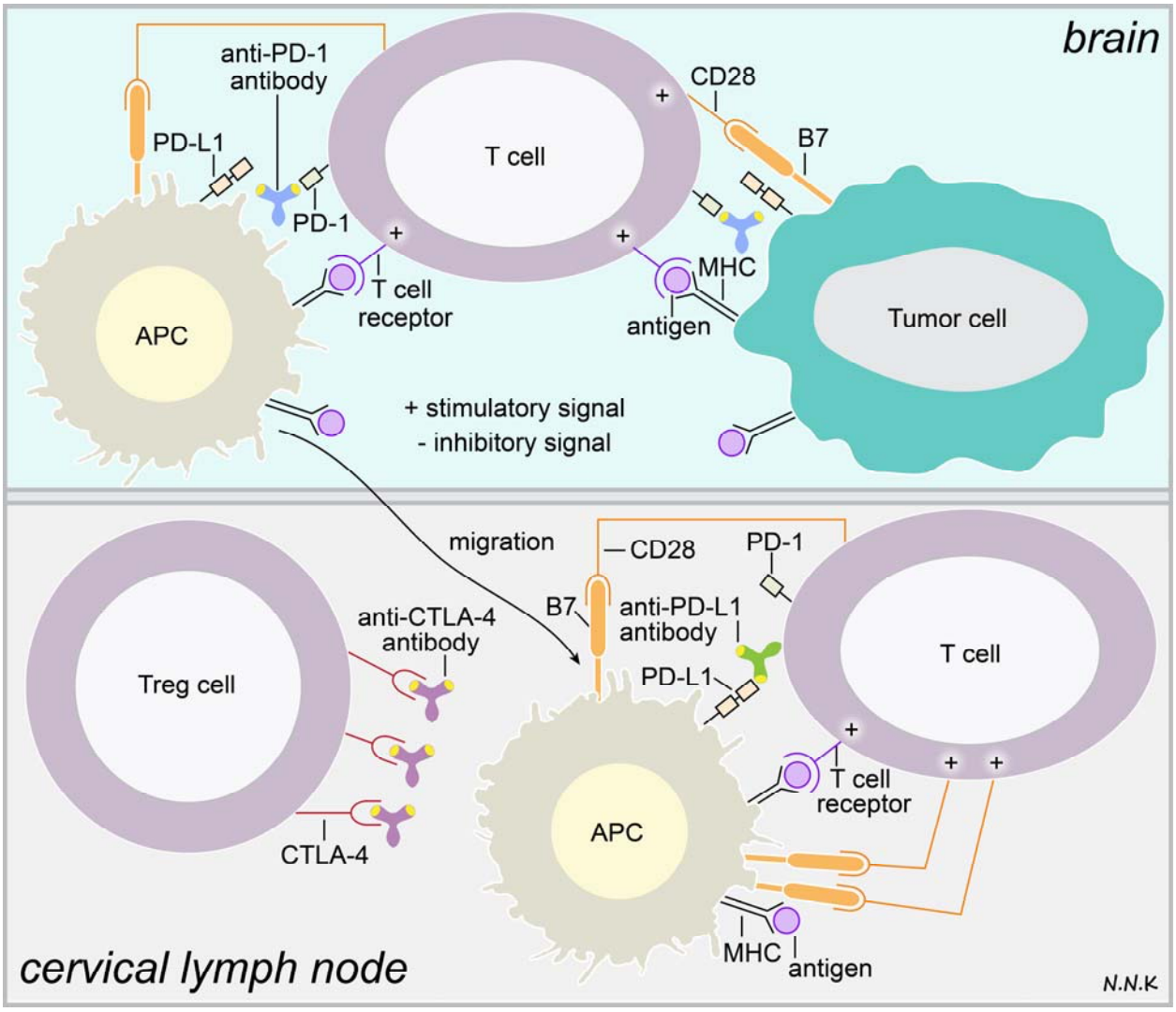

Figure 4. Passive immunotherapy strategies for brain cancer using immune checkpoint inhibitory antibodies. Interactions between T cells, antigen presenting cells (APCs), and tumor cells that inhibit appropriate activation of T cell cytotoxic immune responses may be modulated via passive immunotherapy. For example, anti-PD-1 antibodies can bind to the PD-1 receptor that is expressed by T cells and disrupt PD-1's interaction with its ligand PD-L1, which is highly expressed on tumor cells and APCs in the tumor microenvironment. Alternatively, anti-PD-L1 antibodies can neutralize the PD-L1 ligand's ability to bind to PD-1. Anti-CTLA-4 antibodies may be used to block the interaction between the CTLA-4 receptor on Treg cells and the B7 ligand on tumor cells and APCs; this would subsequently allow B7 interaction with the CD28 receptor on T cells, which provides a stimulatory signal for T cell activation. Adapted from

Buchbinder & Desai, 2016; Huang *et al.*, 2017; Huang *et al.*, 2017. Abbreviations: PD-1 – programmed cell death protein-1; PD-L1 – programmed cell death protein ligand-1; CTLA-4 – cytotoxic T-lymphocyte-associated protein 4; Treg – regulatory T cells; CD28 – classification determinant 28.

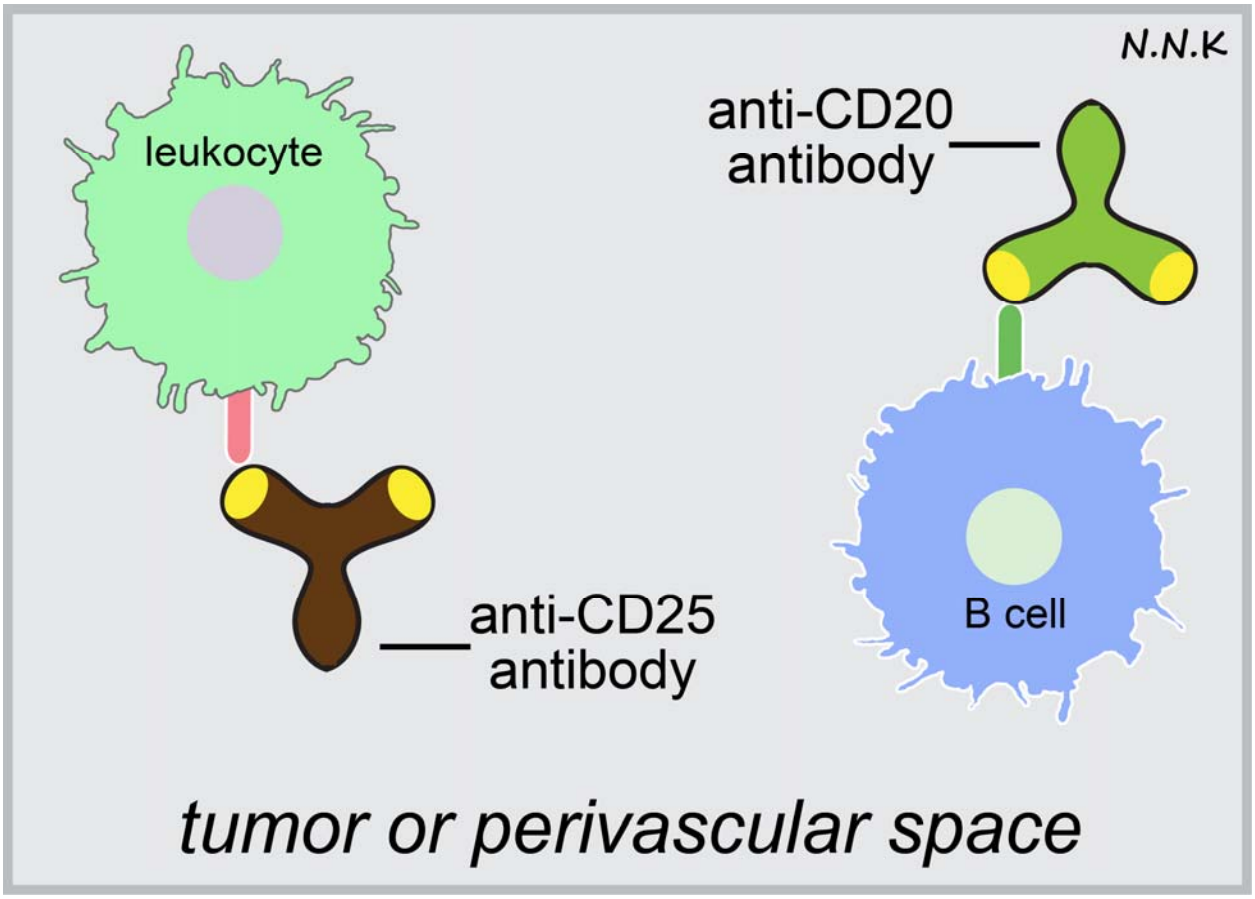

Figure 5. Passive immunotherapy strategies for antibodies recognizing lymphocyte antigens. Antibodies that recognize molecules expressed by malignant infiltrating lymphocytes may be used to treat certain CNS lymphomas. Adapted from Aho *et al.*, 1993; Citterio *et al*., 2017.

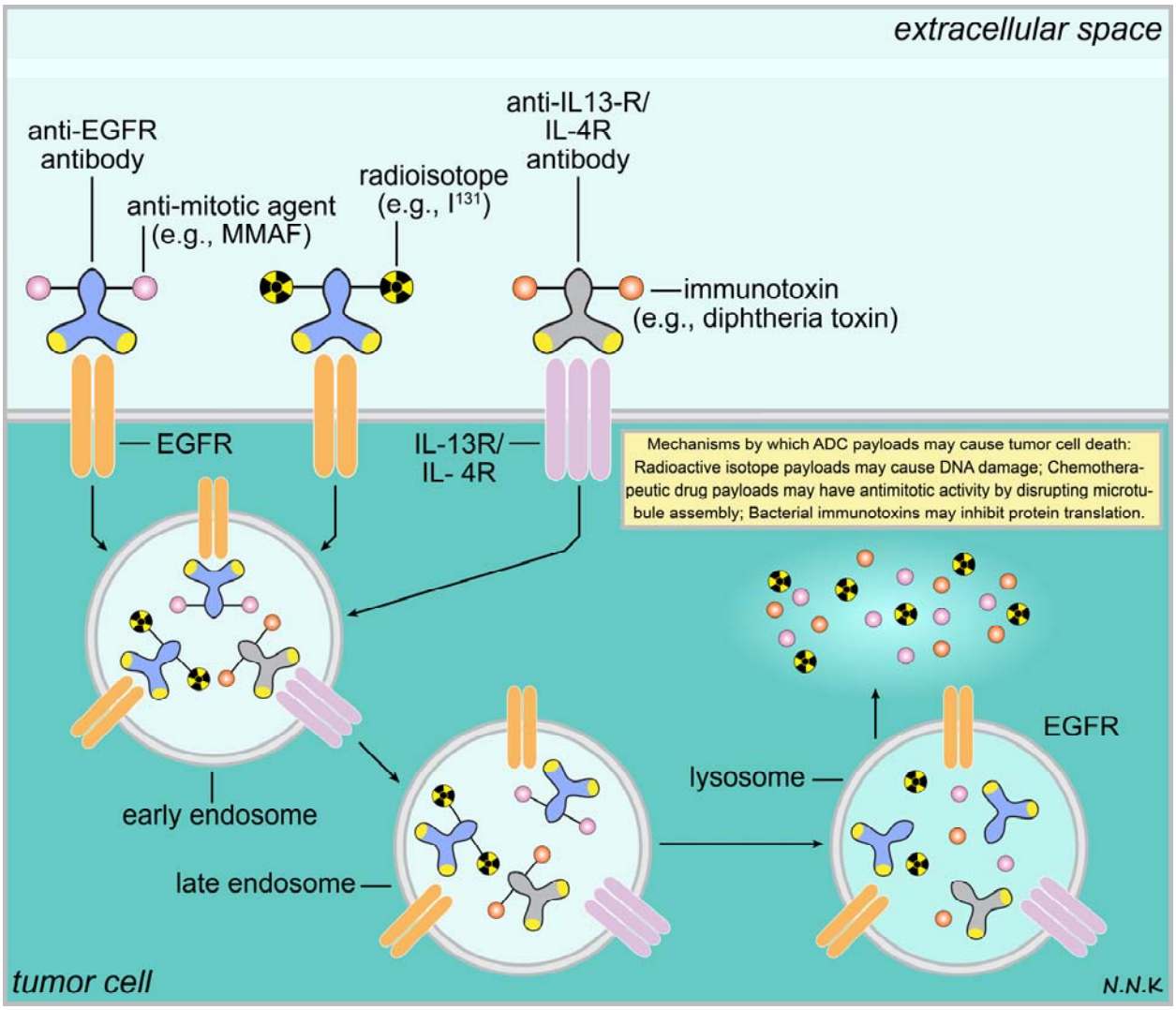

Figure 6. Passive immunotherapy strategies for brain cancer using antibody drug conjugates (ADCs). ADCs combine the ability of antibodies to recognize specific antigens overexpressed by tumor cells (e.g., EGFR, IL-13R, or IL-4R) and the ability to deliver a cytotoxic payload that can lead to tumor cell death or arrest tumor growth. Typically, an ADC has 3 main components – an antibody that can recognize a tumor antigen, a linker, and a cytotoxic payload. The cytotoxic payloads may be radioisotopes (e.g., I^{131}) that can cause DNA damage within the tumor cell, bacterial immunotoxins (e.g., diphtheria toxin) that may interfere with microtubule assembly or protein translation, or anti-tumor chemotherapeutic drugs (e.g., MMAF). Since ADCs can deliver a cytotoxic payload to the tumor target with high specificity they minimize off-

target effects. Adapted from Gan *et al.*, 2017. Abbreviations: EGFR – epidermal growth factor receptor; IL – interleukin; I^{131} – iodine radioisotope; MMAF – monomethyl auristatin F

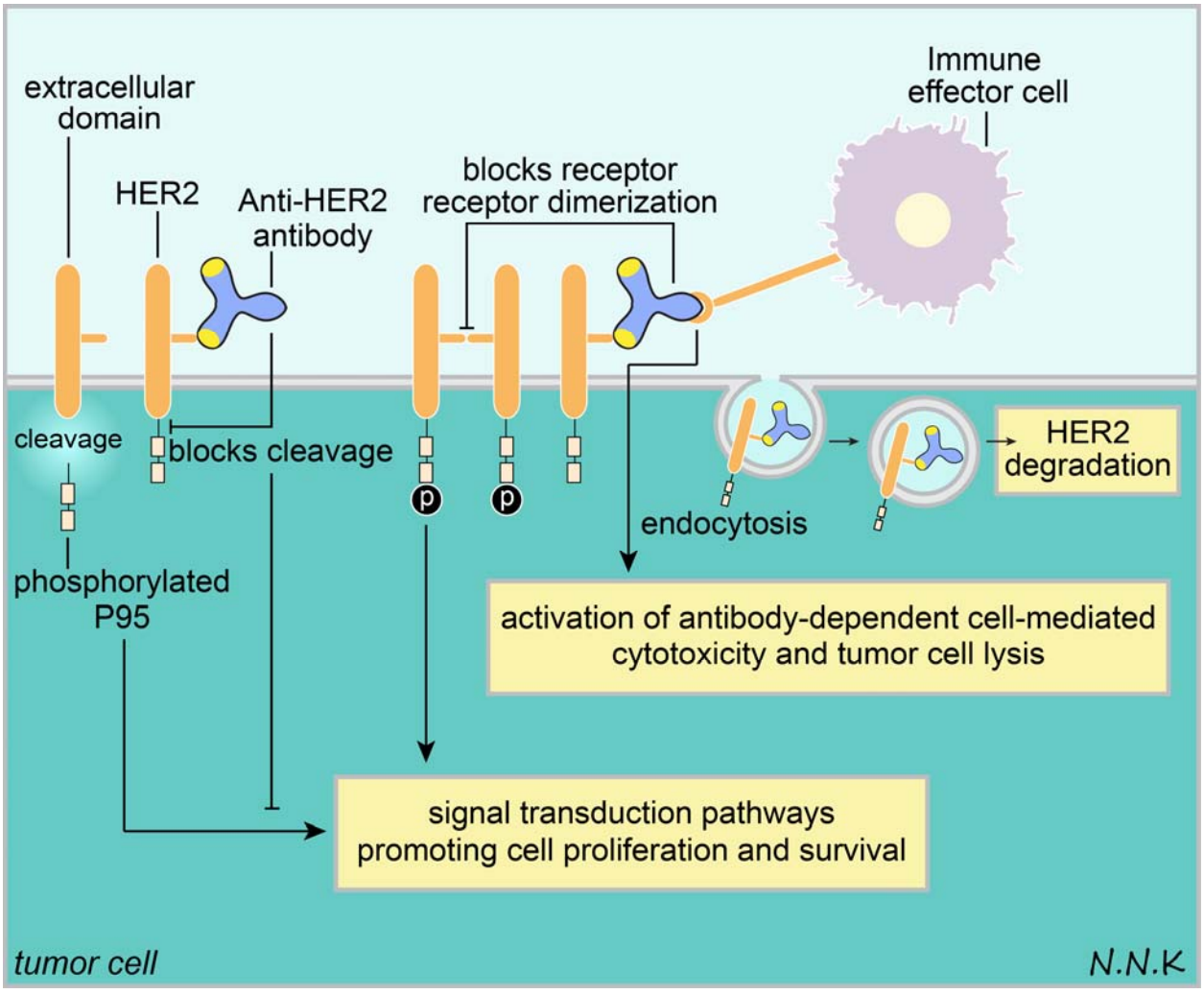

Figure 7. Passive immunotherapy strategy to treat breast cancer brain metastases using anti-HER2 antibodies. HER2 overexpressing breast cancer brain metastases may be treated with anti-HER2 antibodies. Anti-HER2 passive immunotherapy may have several effects. First, HER2 homo or hetero dimerization that drives downstream signaling that promotes tumor cell survival may be disrupted using anti-HER2 antibodies. Second, the extracellular domain of HER2 is typically shed in tumor cells, leaving behind a phosphorylated P95 that is membrane bound and can drive downstream signaling promoting tumor cell growth and survival; anti-HER2 antibodies can bind to the HER2 extracellular domain and prevent its cleavage. Third, anti-HER2 antibodies may bind to HER2 expressed on tumor cell surfaces and initiate an Fc-mediated immune effector function that targets tumor cells. Fourth and finally, anti-HER2 antibodies

may bind to HER2 and cause its internalization by endocytosis, resulting in HER2 degradation. Adapted from: [91]. Abbreviations: HER2 – human epidermal growth factor receptor 2.

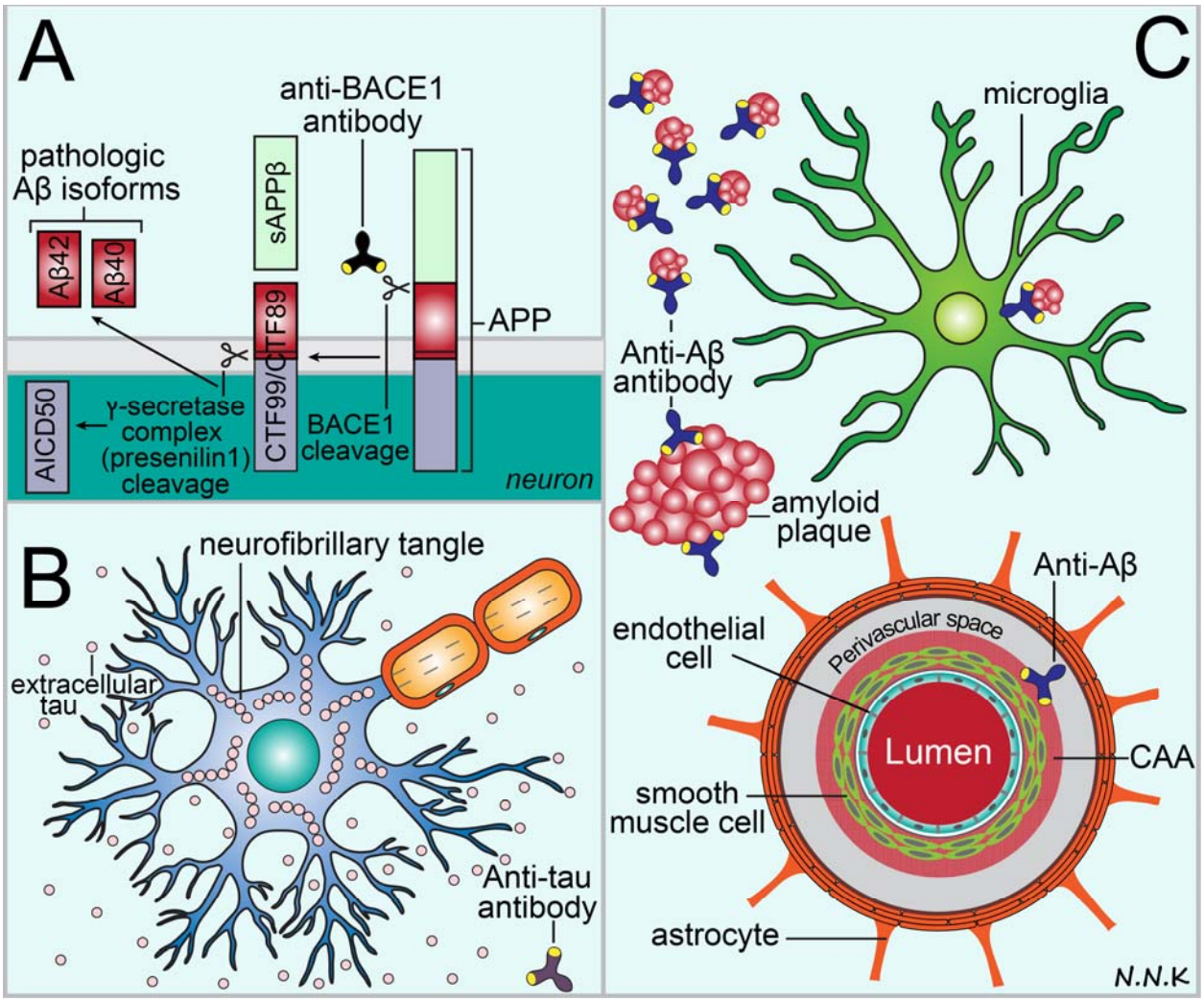

Figure 8. Passive immunotherapy strategies to treat Alzheimer's disease (AD). Some of the major hallmarks of pathology in AD include: (i) excess production of amyloid β-peptide (Aβ) fragments catalyzed by the beta-site APP-cleaving enzyme 1 (BACE1) and γ-secretase enzyme complex cleavage of the amyloid precursor protein (APP); (ii) accumulation and aggregation of hyperphosphorylated tau within neurons leading to cell death and cell-to-cell transmission of extracellular tau; and (iii) accumulation and aggregation of Aβ within the brain parenchyma (Aβ42) and the perivascular compartments of cerebral arteries (Aβ40). Passive immunotherapy may be used to target these different features of AD pathology. (A) Anti-BACE1 antibodies can be used to block the BACE1 cleavage of APP and thus minimize abnormal and excess production of Aβ fragments. (B) Anti-tau antibodies that target hyperphosphorylated tau can be used to block intracellular tau aggregation (likely using intrabodies; Ising *et al.*, 2017) and prevent the

extracellular cell-to-cell transmission of pathologic tau (conventional antibodies; Pederson & Sigurdsson, 2015; Asuni *et al.*, 2007). (C) Anti-Aβ42 antibodies can be used to target Aβ42 in the brain parenchyma and halt or reverse disease pathology by aiding microglia mediated Aβ42 clearance via Fc interactions, binding to monomers and oligomers and preventing their aggregation, and resolving plaques via serine protease activity. Anti-Aβ40 antibodies may be used to target Aβ40 accumulation in the perivascular compartment of cerebral arteries (also referred to as cerebral amyloid angiopathy or CAA) in a similar manner. Adapted from Chow *et al.*, 2010; Citron, 2010; Weiner & Frenkel, 2006; Taguchi *et al.*, 2008).

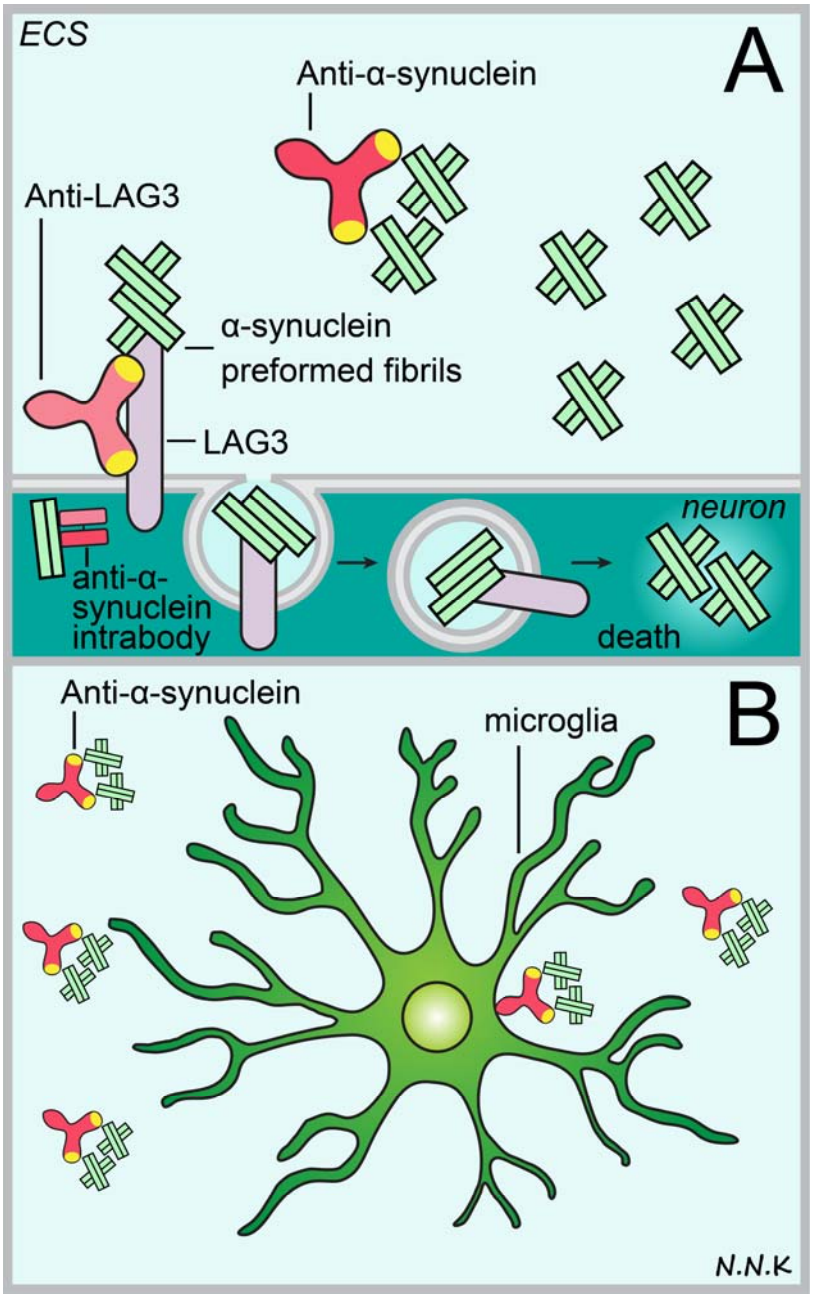

Figure 9. Passive immunotherapy strategies to treat Parkinson's disease (PD). Disease pathology in Parkinson's disease typically entails the accumulation and aggregation of abnormal alpha synuclein protein, subsequently leading to neuronal cell death and cognitive decline. Anti-alpha synuclein antibodies may be used to block the intracellular aggregation of abnormal alpha synuclein which typically leads to the formation of intracellular Lewy bodies (thus the most likely strategy would be to use intrabodies) or prevent the cell-to-cell transmission of extracellular abnormal alpha synuclein (using conventional antibodies).

Extracellular anti-alpha synuclein antibodies may prevent abnormal alpha synuclein monomers and oligomers from aggregating further and may recruit microglia to phagocytose abnormal protein via Fc mediated interactions. Lymphocyte activation gene 3 (LAG3) protein was recently implicated in the internalization of pathologic alpha synuclein during cell-to-cell transmission so an anti-LAG3 antibody strategy may therefore be promising to prevent the spread of alpha synuclein pathology. Abbreviations: ECS – extracellular space. Adapted from Valera & Masliah, 2013; Mao *et al.*, 2016.

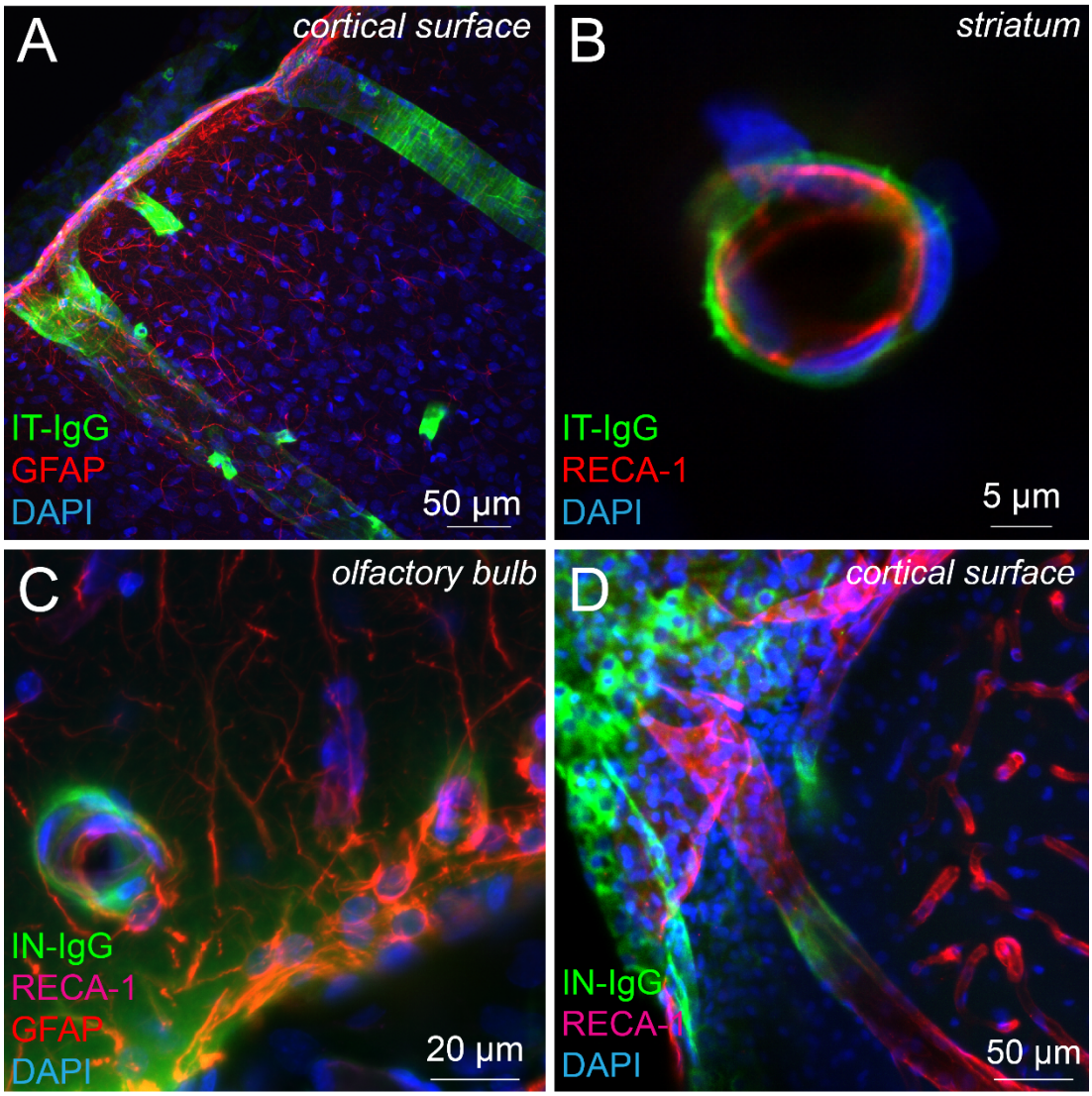

Figure 10. Immunoglobulin G (IgG) access to the perivascular space (PVS) surrounding cerebral blood vessels following intrathecal and intranasal delivery. (A, B) Examples of blood vessels at the rat the cortical surface and in the striatum respectively showing intrathecally administered rat IgG accessing the PVS. (C, D) Examples of blood vessels in the rat olfactory bulb and at the cortical surface respectively showing intranasally administered rat IgG accessing the PVS. Abbreviations: IT – intrathecal; IN – intranasal; RECA-1 – rat endothelial cell antigen-1 (endothelial cell marker); GFAP – glial fibrillary acidic protein (astrocyte marker); DAPI – 4', 6-diamidino-2-phenylindole (cell nucleus marker).

CHAPTER 4

Evident astrocytic and macrophageal FcRn and FcγRIIb immunoreactivity at the rodent brain-cerebrospinal fluid interfaces

Geetika Nehra[1, §], Maj S. Thomsen[2, §], Niyanta N. Kumar[1], Michelle E. Pizzo[1], Gretchen Greene[1], Svend Birkelund[3], Torben Moos[2, *], Robert G. Thorne[1,4,5, *]

[1]Pharmaceutical Sciences Division, School of Pharmacy, University of Wisconsin-Madison, Madison, Wisconsin, USA; [2]Laboratory of Neurobiology, Department of Health Science and Technology, Aalborg University, Aalborg, Denmark; [3]Laboratory of Medical Mass Spectrometry, Department of Health Science and Technology, Aalborg University, Aalborg, Denmark; [4]Denali Therapeutics, South San Francisco, California, USA; [5]Department of Pharmaceutics, College of Pharmacy, University of Minnesota Twin Cities, Minneapolis, Minnesota, USA; [§]Equal contribution

*Represents experiments designed and executed by Geetika Nehra

In preparation for first submission to *The Journal of Physiology*

Abstract

Distribution of antibody-based therapeutics in the central nervous system (CNS) could govern their successful translation for treating CNS disorders as their regulation may rely on their interaction with endogenous Fc receptors. However, Fc receptor expression has been described through pharmacokinetic studies or IgG immunostaining of brain tissues in the past, especially at the interfaces surrounding the specialized vascular and fluidic barriers of the CNS that suggest interactions between IgG and Fc receptors account for minimal binding. In this study, we took morphological and gene expression analysis to investigate the localization of two key Fc receptors at these interfaces - (a) the neonatal Fc receptor (FcRn) that binds to IgG in a pH dependent manner, and (b) the low affinity-binding inhibitory Fc gamma receptor (FcγRIIb). Immunolabeling was performed on brain sections of adult Sprague-Dawley rats, wild-type C57BL/6N (WT) mice, and double transgenic APPswe/PS1dE9 (APP/PS1) mice to assess species differences. Primary cell cultures of rat and mouse brain capillary endothelial cells and astrocytes were labeled with identical anti-Fc receptor antibodies to confirm positive findings. Our results suggest that immunoreactivities for FcRn and FcγRIIb in the rat brain were observed at the brain-cerebrospinal fluid (CSF) interfaces relevant for central drug delivery strategies such as the olfactory nerve layer, leptomeninges, glia limitans, perivascular spaces, ventricles, and choroid plexus. Specifically, FcRn and rat FcγRIIb labeled meningeal cells, perivascular macrophages, choroid plexus epithelial cells, and perivascular astrocytes. Immunolabeling was also observed for neocortical neurons and astrocytes in white matter tracts. In the mouse brain, high levels of endogenous mouse IgG prevented the ability to conclude findings from anti-FcRn antibodies. However, mouse FcγRIIb immunoreactivity was consistently present in neurons. Brain endothelial cells remained minimally labeled or unlabeled in thus study for both rats and mice. FcRn messenger RNA (*Fcgrt*) levels for endothelial cell lines were significantly higher than primary astrocytes for mice but not rats. FcγRIIb messenger RNA (*Fcgr2b*) levels were not detected in endothelial cells. These results provide insights into exploring non-endothelial Fc receptor expression, specific to astrocytes and perivascular macrophages, for antibody distribution studies utilizing central delivery routes to the CNS.

Introduction

Immunoglobulin G (IgG) based immunotherapies have been a preferred treatment strategy for several neuropathological conditions in clinical trials (Kumar *et al*., 2018) due to the unusually long systemic half-life of IgG (Vieira & Rajewsky, 1988; Spiegelberg & Fishkin, 1972) (through interactions with endogenous Fc receptors (Woof & Burton, 2004)). Most of systemic IgG, however, is restricted from entering the central nervous system (CNS) (Preterit & Rubbert-Roth, 2003; Banks *et al*., 1972; Wang *et al*., 1972; Wurster & Haas, 1994) due to the presence of blood-brain barrier (BBB) (Abbott *et al*., 2010; Abbott *et al*., 2013; Engelhardt *et al*., 2009) and blood-cerebrospinal fluid (CSF) barriers (BCSFB) (Engelhardt *et al*., 2009). A fraction of systemic IgG that accesses the CNS enters through fenestrated vessels in the circumventricular organs and the choroid plexus stroma (Griffin & Giffels, 1982; Hochwald, 1970; Rappaport & Pettigrew, 1979; Shrestha *et al*., 2014; Wurster & Haas, 1994). However, serum IgG remains encapsulated within the lysosomal compartments (St. Amour *et al*., 2013, Villaseñor *et al*., 2016) or basal lamina of endothelial cells (Aihara *et al*., 1994), hence, restricted access into the brain parenchyma.

Several drug development strategies are now investigating (novel) drug delivery system based on IgG structure and biology. Some of these strategies are fusion proteins (Pardridge & Boado, 2012), polymerosomes (Tian *et al*., 2015), IgGs with altered glycosylation (Mimura *et al*., 2018; Podulso & Curran, 1994) or receptor affinity (Cooper *et al*., 2013; Booth *et al*., 2018; Borrok *et al*., 2017), single-domain antibodies (Abulrob *et al*., 2004; Pizzo *et al*., 2018), IgGs with dual variable domains (Karaoglu Hanzatian et al., 2018), and bispecific antibodies (Stanimirovic *et al*., 2014; Webster *et al*., 2016). Many of these strategies suggest an enhanced antibody distribution (Pizzo *et al*., 2018) or uptake (Croll *et al*., 1998) if the IgG-Fc receptor (IgG-FcR) interactions are incorporated into the experimental design. However, our understanding on the sites of these interactions is based on in situ hybridization maps (Allen Institute for Brain Science, 2004), inferences from pharmacokinetics studies in knockout animals (Abuqayyas & Balthasar, 2013) or IgG immunoreactivity analysis (Aihara *et al*., 1994; Goldsmith, 2002; Shreshtha *et al*.,

2014). While these studies have been key to initiate the discussion on the IgG-FcR interactions in the central nervous system, they mainly provide an indirect estimate for cerebral FcR protein expression. Considering these issues, investigating the localization of specific IgG FcRs in the CNS can potentially facilitate efforts to enhance IgG delivery to the brain. In this study, we explore the distribution of two such receptors having widespread mRNA expression profiles in the mouse brain (Allen Institute for Brain Science, 2004) – the neonatal Fc receptor (FcRn) and the inhibitory Fc receptor (FcγRIIb).

FcRn is structurally similar to major histocompatibility complex (MHC) class I molecules, consisting of a large p51 subunit with three extracellular immunoglobulin (Ig) domains (α1, α2, and α3), a transmembrane domain and a cytoplasmic tail (Simister & Mostov, 1989). The α3 domain dimerizes with *β*2-microglobulin (*β*2m) (Raghavan *et al*., 1994). All FcRn subunits act as contact sites for one IgG molecule, while the CH2-CH3 junction of the IgG Fc region is available for binding to two FcRn molecules (Burmeister *et al*. 1994). FcRn-IgG binding occurs in a pH-dependent manner as shown in human syncytiotrophoblasts transporting IgG across the placental barrier (Firan *et al*., 2001; Kristoffersen & Matre, 1996; Leach *et al*., 1996; Simister *et al*., 1996). It has been generally agreed upon that IgG is taken up by cells through fluid-filled (non-specific) pinocytosis in physiological environments (pH 7.4) as well as surface FcRn-IgG binding under acidic conditions (Waldmann & Jones, 2008; Rodewald & Kraehenbuhl, 1984). Once internalized, FcRn binds to IgG in acidified endosomes, salvages it from lysosomal degradation (Anderson, 2014; He *et al*., 2008; Popov *et al*., 1996; Raghavan *et al*., 1994; Roberts *et al*., 1990; Ward & Ober, 2015). The effect is saturable in endothelial cells at exceptionally high serum IgG concentrations (Junghans, 1997; Van Gog *et al*., 1997; Waldmann & Jones, 2008) and can be deleterious in autoimmune disorders where pathogenic antibodies have a longer systemic circulation (Akilesh *et al*., 2004; Baryr *et al*., 2007). Hence, FcRn-mediated transcytosis is considered to dictate the fate of IgG in terms of catabolism, immune activation, and circulation (Roopenian *et al*., 2003; Pyzik *et al*., 2015; Rojas & Apodaca, 2002; Roopenian & Akilesh, 2007). FcRn was initially demonstrated to be important for maternal-to-fetal IgG transfer at the mucosal lining in neonatal intestines (Brambell, 1969; Hemmings & Brambell, 1961; Waldmann & Jones, 2008;

Wallace & Rees, 1980). With recent advancements in histology, FcRn expression was also confirmed in epithelial cells (Claypool *et al*., 2004), mammary gland (Cianga *et al*., 2003), intestine (Shah *et al*. 2003; Zhu *et al*. 2001), liver (Zhu *et al*., 2008), lungs (Spiekermann *et al*., 2002), placenta (Roopenian & Akilesh, 2007), and the nasal passages (Heidl *et al*., 2016; Ladel *et al*., 2018; Ye *et al*., 2011) in various species. Subsequently, endothelial cells at the placenta (Radulescu *et al*., 2004), retina (Deissler *et al*., 2017), liver, and muscles (Borvak *et al*., 1998) have also been demonstrated to express FcRn protein. In the CNS, FcRn has been observed in vitro in neurons (Andoh & Kuraishi, 2004) and endothelial cells (Caram-Salas *et al*., 2011) of primary murine cell cultures. FcRn has also been detected ex vivo at the choroid plexus, and along cerebral microvessels in the developing rat brain (Strazielle & Ghersi-Egea, 2013), adult rat (Latvala *et al*., 2017; Schlachetzki *et al*., 2002), and murine brain tissue sections (Dean *et al*., 2005; Latvala *et al*., 2017). Yet, the precise localization of FcRn at these sites (luminal vs abluminal) remains unclear. In addition, pharmacokinetic analyses evaluating the role of FcRn in IgG uptake and efflux in the CNS have not reached a unanimous consensus (Abuqayyas & Balthasar, 2013; Cooper *et al*., 2013; Deane *et al*., 2005); confounding any alternative functions FcRn may have in the CNS.

Unlike FcRn, the FcγR consists of an alpha subunit with only two extracellular Ig domains (α1 and α2), one transmembrane domain and a cytoplasmic tail. The α2 domain of nearly all FcγRs binds to an epitope between the hinge region and CH2 Fc region of IgG in a 1:1 stoichiometric ratio (Woof & Burton, 2004), while the cytoplasmic tail consists of a tyrosine-based motif for activating or inhibitory immune effector function, and a gamma chain for signal transduction (Nimmerjahn & Ravetch, 2006; Nimmerjahn & Ravetch, 2008; Takai, 2002). Consequently, FcγR are classified as activating (FcγRI, FcγRIII, FcγRIV for rats and mice; FcγRI, FcγRIIa, FcγRIIc, FcγRIIIa, FcγRIIIb for humans) or inhibitory (FcγRIIb) receptors. Of note, Fc gamma receptor IIb (FcγRIIb) is the only known inhibitory Fc receptor in the body, primarily responsible for internalizing antigen-antibody complexes through phagocytosis (Ravetch & Bolland, 2001), maintaining peripheral tolerance towards endogenous antigens (Nimmerjahn & Ravetch, 2006, Takai, 2002), protecting plasma cells from generating autoantibodies (Nimmerjahn & Ravetch, 2008; Li *et al*.,

2014) and for in vivo activity of intravenous Ig (IVIG) (Nimmerjahn & Ravetch, 2008; Takai, 2002). FcγRIIb is peripherally expressed by sinusoidal endothelial cells (Ganesan *et al*., 2012), placental endothelial cells (Ishikawa *et al*. 2015; Takizawa *et al*., 2005; Stapleton *et al*., 2018), reactive lymphoid tissue (Camilleri-Broet *et al*., 2004), and in nervous tissue in spinal neurons (Zhang *et al*., 2013). Schwann cells, endothelial cells, and perineural cells around nerve capillaries (Vedeler *et al*., 1989; Vedeler *et al*., 1991) also express FcγRIIb in the periphery. In situ hybridization data depicts FcγRIIb mRNA in the adult human (Peress *et al*., 1989) and mouse brain (Allen Institute for Brain Science, 2004; Lein *et al*. 2006), predominantly at the leptomeninges, arachnoid granulations, ventricles, perivascular spaces, and choroid plexuses (Peress *et al*., 1989; Perry *et al*., 1985). On the contrary, FcγRI and FcγRIII mRNA levels were localized to the choroid plexus and ventricles respectively (Peress *et al*., 1989). Immunolabeling studies show FcγRIIb expression in Purkinje cells (Nakamura *et al*., 2007), primary murine astrocytes (Nitta *et al*., 1992), oligodendrocytes (Nakahara *et al*., 2003; Okun *et al*., 2010), and neuronal cell cultures (Okun *et al*., 2010) but in vivo FcγRIIb distribution has not been well-characterized in the rodent CNS.

Our recent report suggests extracellular spaces as a potential site for IgG-FcR interaction, based on altered IgG diffusion profile following intracranial co-infusion with an excess Fc fragments (Wolak *et al*., 2015). We also hypothesize IgG-FcR interactions within perivascular spaces (PVS) around cerebral blood vessels, based on widespread IgG distribution along these routes following intrathecal delivery of species-matched IgG (Pizzo *et al*., 2018) (in the rat). However, these sites have not been extensively characterized for specific FcR immunoreactivity. To confirm these hypotheses, we investigated the distribution and cellular origin of rodent FcRn and FcγRIIb using ex vivo and in vitro immunolabeling, and relative gene expression analysis. These results might be useful for exploring the functional aspects of IgG-FcR interactions at key interfaces for IgG distribution in the CNS.

Materials and Methods

Ethics Approval

All *ex vivo* animal experiments were conducted at the University of Wisconsin-Madison as per the *NIH Guide for the Care and Use of Laboratory Animals* (8th edition, 2011) following the approval of Institutional Animal Care and Use Committee regulations at the University of Wisconsin-Madison. Rats and mice were housed under 12 h light/12 h dark cycle, climate-controlled conditions with *ad libitum* access to food and water. All animal experiments were terminal and efforts were made to ensure minimal animal pain and distress during anesthesia and cannulations.

*Animal preparation**

Adult female Sprague Dawley rats (180 - 210 g; 2 to 4-month-old; Envigo/Harlan, Indianapolis, IN), adult female C57BL/6N mice (18 - 24 g; 3-month-old; Strain #044; Envigo/Harlan), and adult female APP/PS1 mice (20 - 30; g 5 to 7-month-old; Strain #000644; MMRRC at Jackson Laboratory, Bar Harbor, ME) were anesthetized with urethane (1.2 - 1.5 g/kg, i.p.) until surgical plane was reached. Animals were maintained at physiological body temperature (37°C) using a homeothermic monitoring system (Harvard Apparatus, Holliston, MA, USA) prior to perfusion.

*Abdominal aortic cannulation and euthanasia in rats**

Rats under surgical plane underwent terminal abdominal aorta cannulation by a previously described procedure (Kumar *et al.* 2016; Kumar *et al.*, 2018, Lochhead *et al.*, 2015; Pizzo *et al.*, 2018; Thorne *et al.*, 2004; Wolak *et al.*, 2015). Briefly, an incision was made along the midline over the abdominal cavity, skin was retracted, and visceral organs were abducted to obtain a clear view of the abdominal vasculature. Connective tissue between blood vessels was separated to widen the intervascular distance two pieces of general-purpose thread (~12 in) were either tied at the anal end to severe lower body circulation or held

loosely close to the xiphoid end using hemostats (Fine Science Tools, Foster City, CA, USA) for securing the cannula. Next, a horizontal aortic incision was made and enlarged using vannas scissors (Harvard Apparatus) followed by the insertion of a 20 GA 1.25-inch catheter (Exelint International Co., Redondo Beach, CA) connected to a three-way stop cock pre-filled with heparinized (1:100) saline. Cannula was secured in place with the general-purpose thread to prevent leakage. Organs were reassembled inside the abdominal opening after cannulation. Animals were then transferred to a laminar fume hood for exsanguination where the cannula was connected to the peristaltic pump tubing (Minipuls, Gilson Incorporated, Middleton, WI) in a laminar hood and the vena cava was incised at the start of 15 mL/min perfusion flow rate with 50 mL of 0.01M phosphate buffered saline at pH 7.4 (PBS) followed by 500 mL of 4% paraformaldehyde (Alfa Aesar, Haverhill, MA) in 0.1 M phosphate buffer at pH 7.4 (PFA).

Transcardial cannulation and euthanasia in mice*

Anesthetized mice were transferred to a surgical tray in a laminar hood for transcardial perfusion. An abdominal incision was made using sharp scissors, followed up with blunt scissors (Fine Science Tools) to reach the thoracic cavity. Skin and muscles were retracted, diaphragm and ribcage were horizontally, and laterally incised, and sternal-xiphoid muscles were inverted using hemostats to exposure the pericardial space. Connective tissues surrounding the left ventricle was removed using forceps (Fine Science Tools) and a 26 GA 1.5 in needle (AgTech, Inc., Manhattan, KS), trimmed to 2 mm and connected to the peristaltic pump, was inserted. Right atrium was snipped shortly after the start of perfusion process (50 mL PBS followed by 250 mL PFA; 7.5 mL/min).

Postmortem tissue processing*

Following perfusion fixation, whole brains were dissected and post-fixed overnight in PFA at 4°C. Brains were coronally sectioned into 100 μm thick slices on a vibratome (Leica VT100S; Leica Biosystems,

Wetzlar, Germany) and stored as free-floating sections in PBS at 4°C until further processing. Dura mater was removed during tissue extraction and preserved in PBS at 4°C.

Immunohistochemistry buffers*

All tissue sections were washed with PBS. Blocking and incubation buffers were PBS solutions containing 0.3% Triton-X (Sigma-Aldrich/Millipore-Sigma, St. Louis, MO, USA), 3-5% goat serum (Sigma-Aldrich/Millipore-Sigma) or donkey serum (Sigma-Aldrich/Millipore-Sigma) depending on the host species of secondary antibodies. Occasionally, PBS containing 5% Bovine Serum Albumin (Sigma-Aldrich/Millipore-Sigma) was used as a blocking buffer when immunostaining tissues for alpha smooth muscle actin (αSMA). A detailed list of primary and secondary antibodies has been provided in Table 5 and 6, respectively.

Immunohistochemistry procedure*

Free-floating sections were washed with PBS for 5 min and incubated in blocking buffer at room temperature for 1 h, followed by incubation with appropriate primary antibodies overnight at 4°C. Next day, tissue sections were washed three times (10 min per wash, 1 mL per well) in PBS and incubated with blocking buffer containing appropriate secondary antibodies for 1 h at room temperature. Sections were subsequently washed three times with PBS. Sections were incubated with 4',6-diamidino-2-phenylindole (DAPI; Life Technologies/Thermo Fisher Scientific, Carlsbad, CA, USA) in PBS at 2 µg/mL for 20 min at most instances to label cell nuclei, followed by three sets of 10 min PBS washes. Free-floating brain sections were mounted onto glass slides after the final wash and air-dried in the dark overnight, prior to rehydration with traces of PBS and coverslipping with ProLong Diamond Antifade Mountant (Thermo Fisher Scientific). Coverslipped slides were cured in the dark overnight at room temperature and stored at -20°C.

Isolation and culture of murine brain capillary endothelial cells (BCECs) and mixed glial cells

BCECs and mixed glial cells were isolated from C57BL6 mice and Sprague-Dawley rat brains based on recent protocols (Burkhardt *et al.*, 2015; Thomsen *et al.*, 2016). Briefly, BCECs were seeded at a cell density of 1×10^4 cells/cm^2 on collagen IV-fibronectin coated 1 µm Millicell® hanging inserts for 24 hours. Inserts were transferred to a 12-well plate containing mixed glial cells and grown to confluence on the bottom. To induce BBB properties, the top growth medium (BCEC growth medium; Dulbecco's Modified Eagle Medium (DMEM)-F12, GlutaMax™ with 10% plasma derived serum (PDS; Life Technologies, Naerum, Denmark, DK), heparin (100 µg/mL; Sigma-Aldrich/Millipore-Sigma, Brondby, Denmark, DK), insulin-transferrin sodium selenite (0.1 mg/mL; Roche, Hvidovre, Denmark, DK), and gentamicin sulphate (10 µg/mL, Lonza)) were supplemented with 1 µg/mL basic fibroblast growth factor (bFGF; 550 nM hydrocortisone, 17.4 µM Ro 20-1724 (Sigma-Aldrich/Millipore-Sigma), 250 nM 8-(4-Chlorophenylthio)adenosine 3',5'-cyclicmonophosphate sodium salt (pCPT-cAMP; Sigma-Aldrich/Millipore-Sigma)). Medium in the bottom chamber consisted of 1:1 BCEC growth medium and mixed glial cell conditioned medium (DMEM GlutaMax™ (Sigma-Aldrich/Millipore-Sigma), 10% fetal calf serum (FCS), gentamicin sulphate (10 µg/mL), 0.5 µg/mL bFGF, 550 nM hydrocortisone). Cells were maintained in an incubator at 37°C with 5% CO_2 humidified environment.

Murine brain endothelial cell culture

Immortalized murine brain endothelial cell line (bEnd.3) was grown in DMEM, high glucose, GlutaMax™ (Thermo Fisher Scientific, Hvidovre, Denmark, DK) supplemented with 10% FCS and gentamicin sulphate (10µg/mL) (Gosk *et al.* 2008). For transfection, cells at a density of 1×10^4 cells/cm^2 were seeded in a 24-well plate or in an 8-well Permanox chamber and incubated at 37°C with 5% CO_2 in a humidified environment.

Transfection of rodent FcRn in bEnd.3 cells

Coding sequences of mouse *Fcgrt* (accession number NM_010189) and rat *Fcgrt* (accession number NM_033351) in pCMV-Entry encoding C-terminal Myc-DDK tag (OriGene, Rockville, MD) were propagated in DH5α. Plasmids were purified using NucleoBond® Xtra Midi kit as per the manufacturer's protocol (Macherey-Nagel) but with an additional round of polyethylene precipitation. Purified plasmids were reconstituted in Tris-ethylenediaminetetraacetic acid (EDTA) buffer and concentration was measured using NanoDrop® (Thermo Fisher Scientific). For transfection of the bEnd.3 cells, 0.25 µg deoxyribonucleic acid (DNA) of mouse or rat FcRn plasmid was mixed with serum-free medium and commercially available transfection agent TurboFect™ (Thermo Fisher Scientific). Transfection mixture was incubated at room temperature for 20 min before distributing into wells containing bEnd.3 cells. Cells were maintained at 37°C in 5% CO_2 in a humid environment for 24 hours before transgene expression was analyzed using immunofluorescence.

Production of monoclonal 1G3 antibody

Mouse 1G3 hybridoma cell line (ATCC® CRL-2434) was grown in HL-1™ medium (Lonza) supplemented with 1 mM sodium pyruvate, 1 mM L-glutamine, 1% FCS and gentamicin sulphate (10µg/mL) and kept at 37°C with 5% CO_2 humidified atmosphere. Cells were passaged upon reaching a cell density of 30×10^4 cells/mL. The medium was harvested and centrifuged at 1200 RPM for 5 min at 4°C. The medium containing 1G3 monoclonal antibody was stored as one-time use aliquots at -20°C until further use. The antibody production was tested on both rat and mouse *Fcgrt* transfected bEnd.3 cells using immunofluorescence.

Immunofluorescent labeling of cell cultures

Different cell cultures were washed twice in potassium phosphate-buffered saline (KPBS) and fixed using 4% paraformaldehyde (PFA) for 10 min at room temperature. Cells were then blocked with 3% bovine

serum albumin (BSA) with 0.3% Triton X-100 for 30 min at room temperature to block non-specific antibody interactions. Primary antibodies were added to the blocking buffer (see Table 5). Cells were incubated at 4°C overnight with gentle agitation and washed 3 times in PBS before the addition of secondary antibodies (see Table 6) diluted in incubation buffer for 30 min at room temperature. Subsequently, cells were washed twice with PBS, and nuclei stained for 4 min with 1 µg/mL 4',6-diamidino-2-phenylindole (DAPI; Sigma-Aldrich/Millipore-Sigma) in PBS before mounting with fluorescent mounting medium (Dako).

Quantitative reverse transcription polymerase chain reaction (RT-qPCR)

To assess FcR gene expression, ribonucleic acid (RNA) was isolated from rBCECs (n = 4), mBCECs (n = 4), primary rat astrocytes (n = 4) and primary mouse astrocytes (n = 4) using GeneJET RNA Purification Kit (Life technologies, #K0731). Each sample contained a pool of cells from 3-4 wells/filters from 2-4 different isolations. The isolation of RNA was followed by DNA removal using deoxyribonuclease (DNase) I reagent (Life technologies, #EN0525) as per manufacturer's instructions. 100 ng RNA was used as template for cDNA synthesis following the procedure described for Maxima H Minus First Strand Synthesis Kit (Life technologies, #K1652). β -actin and hypoxanthine-guanine phosphoribosyltransferase (*Hprt1*) were used as housekeeping control genes. 2.5 ng cDNA and 10 pmol of each primer were used with Maxima™ SYBR green qPCR Master Mix in a final PCR reaction volume of 10 µL. QuantStudio 6 Flex Real-Time PCR System was used for sample analysis (1 x (95°C, 10 min) $\pm$ 40 x (95°C, 30 s; 60°C, 1 min)) followed by the creation of a melting curve to verify the product. Nuclease-free water and non-reversed transcribed RNA were included as controls for each sample. Relative gene expression in each sample was calculated by the 2ΔΔ CT method (Pfaffl 2001) with the gene expression of the astrocyte cultures being the calibration sample. Accordingly, for each sample based on rBCECs and mBCECs, data were depicted as fold-difference compared to those of rat and mouse astrocytes respectively. Statistical differences were analyzed using unpaired Students t-test via GraphPad Prism version 5.0 for Windows (GraphPad Software, San Diego, California USA, www.graphpad.com). Data were presented as mean ± standard error of the

mean (SEM). A p-value < 0.05 was considered statistically significant (see Tables 7 and 8 for references sequences).

Microscopy and Image Analysis*

Immunofluorescently labeled cells were visualized using an Observer Z1 (Carl-Zeiss, Germany) fluorescence microscope equipped with ApoTome.2 (Carl-Zeiss). Brain sections were visualized using an Olympus FV1000 laser scanning confocal microscope with FLUOVIEW software or a Nikon A1R laser scanning confocal microscope with NIS Elements software. Specific regions of interest (ROIs) were selected for *ex vivo* analysis (see Figure 1). Confocal images of brain sections are representative for each ROI since imaging settings were optimized for each ROI/antibody/magnification. Images were analyzed using Fiji/ImageJ (v.1.47 and v.1.51h) (Linkert *et al.*, 2010; Schindelin *et al.*, 2012; Schneider *et al.*, 2012; Schindelin *et al.*, 2015;) and optimized in Adobe Photoshop (Adobe Systems) with RGB histogram adjustments. Gamma values remained unaltered during image processing for all channels. Line intensity plots were performed on processed images with RGB setting (0-255) to identify colocalization patterns. Grey boxes indicate regions with similar trends in signal intensity across two channels. Confocal images for antibody controls (mouse IgG1; rabbit IgG) were imaged at the highest settings used for corresponding targeted antibodies.

Results

Anti-FcRn antibodies used in this study have been referred to by their commercial names (1G3, M-255, H-4, CD32B). M-255 and H-4 and rat IgG and mouse IgG1 respectively, are raised against the extracellular region (aa 22-276) of FcRn large p51 subunit/α chain/Fcgrt. 1G3 is a mouse IgG1 antibody raised against purified soluble FcRn/Fcgrt-β2m heterodimer with an unidentified epitope. Anti-FcγRIIb antibodies (CD32B) detecting the extracellular N-terminal and intracellular C-terminal residues are denoted by $CD32B_N$ and $CD32B_C$ respectively. Specific regions of interest (ROIs) are shown in Figure 2. Signal

intensity plots for each multichannel image are used to show overlap between cellular markers. The findings are summarized in Table 1 and 2.

Setting the baseline for non-specific immunolabeling with isotype controls

Brain sections were initially tested for non-specific antibody interactions using non-targeted polyclonal rabbit IgG (rIgG) and monoclonal mouse IgG1 (mIgG1) at a fairly high antibody concentration (10 μg/mL). Confocal imaging of these tissues revealed low surface immunolabeling with polyclonal rIgG (Fig. 3A-C) but high levels of mIgG1 immunolabeling at key brain-CSF interfaces (meninges, glia limitans, ventricles, choroid plexus, cerebral perivascular spaces; Fig. 3D-F) in rats. These profiles were likely due to secondary anti-mouse IgG antibodies cross-reacting with endogenous rat IgG at these sites (Pizzo, unpublished). Indeed, preabsorbed secondary anti-mouse IgG secondary antibodies alleviated a large extent of non-specific immunoreactivity in rats (Fig. 3G-I). However, endogenous mouse IgG levels in the mouse brain sections prevented from validating anti-FcRn antibodies (mouse IgG) in wild-type C57BL6 mice (Fig. 3J-L) and transgenic APPswe/PS1dE9 (Fig. 3M-O) mice. Hence, *ex vivo* immunofluorescence results are suggestive of high FcRn immunoreactivity sites in the rat brain but speculative for the same in the mouse brain. Instead, we used *in vitro* immunocytochemical methods and gene expression analysis to evaluate the latter in this study (discussed later in this section).

FcRn and FcγRIIb immunoreactivity associated with meningeal cells

Rat dura (n = 1 per antibody) and underlying meninges (n = 4 per antibody) were probed with M-255, 1G3, $CD32B_C$ and $CD32B_N$ to examine FcR localization relative to markers for vascular endothelial cells (rat endothelial cell antigen-1, RECA-1), lymphatic endothelial cells (lymphatic vessel endothelial hyaluronic acid receptor 1, LYVE-1; Podoplanin) macrophages and other cells of myeloid origin (LYVE-1). Signal from all four antibodies was detected inside these LYVE-1/podoplanin-positive cells lining (Fig. 4) with varying degree of colocalization. M-255 and $CD32B_C$ immunolabeling was also associated with large dural blood

vessels (labeled with RECA-1, Fig. 4A) in the dura, but not lymphatic capillaries (labeled with Podoplanin, Fig. 4D). Isotype controls (rIgG, mIgG1) were not probed for the dura mater. Further, leptomeningeal cells underlining major cerebral arteries were immunoreactive for FcRn and FcγRIIb (Fig. 5). M-255 and 1G3 immunoreactivity was continuous along the leptomeningeal surface (Fig. 5A, B) while $CD32B_N$ and $CD32B_C$ immunoreactivity was associated with non-continuous (Fig. 5D, F). 1G3 immunoreactivity was also present in these cells overlaying the glia limitans, indicating soluble FcRn could be specific to intracellular compartments. These cells could be putative macrophages as confirmed by colocalization with ionized calcium binding adaptor molecule 1 (Iba1; Fig 10D).

Astrocytic FcRn and FcγRIIb immunoreactivity at the glia limitans in the rat

At the cortical surface, Fc receptor immunoreactivity was associated with astrocytic foot processes (indicated by glial fibrillary acidic protein, GFAP) forming the glia limitans. M-255 and 1G3 demonstrated extensive colocalization with GFAP at the glia limitans and to a certain depth along blood vessels penetrating the brain parenchyma (Fig. 6A, B). FcγRIIb immunoreactivity was also observed in astrocytes at the glia limitans. Extensive GFAP/$CD32B_C$ (Fig. 6C) but limited GFAP/$CD32B_N$ colocalization (Fig. 6D) was observed throughout the brain parenchyma, indicating that $CD32B_N$ was potentially detecting non-astrocytic FcγRIIb subpopulations of at the cortical surface. Instead, a strong Iba1/$CD32B_N$ colocalization (data not shown) suggested that these cells could be macrophages and/or microglia.

Perivascular FcRn and FcγRIIb immunoreactivity among macrophages and astrocytes

Transverse cross-section images of large (> 25 μm) cerebral blood vessels reveal positive immunoreactivity for astrocytes with all antibodies, albeit with differences in extent of colocalization with GFAP. M-255 immunostaining was present in cells within the perivascular space and along the astrocytic coverage of endothelial cells (Fig. 7A, 8A). 1G3 immunolabeling was specific to perivascular cells (Fig. 6B) and relatively low at the astrocytic boundaries (Fig. 8B). Iba1/1G3 colocalization (Fig. 10B) suggests these cells could be

putative perivascular macrophages. Low endothelial immunoreactivity were observed for M-255 (Fig. 7A) and 1G3 (Fig. 7B). Luminal/abluminal intensity distribution was not investigated for M-255, 1G3, and RECA-1. $CD32B_C$ and $CD32B_N$ immunoreactivity was non-endothelial around cerebral blood vessels. Perivascular $CD32B_C$ signal was associated with GFAP-positive astrocytes and Iba-1-positive perivascular macrophages (Fig. 7C, 8C). Minimal $CD32B_N$ immunoreactivity was observed with astrocytic end-feet (Fig. 7D) These findings suggest that perivascular astrocytes and macrophages potentially express FcγRIIb and FcRn around endothelial cells of large blood-vessels of the brain. A similar pattern was seen in the choroid plexus stroma (< 25 μm, labeled with RECA-1, red). Here, endothelial cells had relatively low M-255 and 1G3 immunoreactivity compared to adjacent epithelial cells or macrophages (Fig. 9A, D). $CD32B_C$ and $CD32B_N$ were not immunoreactive with endothelial cells in the parenchyma and choroid plexus.

Ventricular Fc receptor profiles associated with ependymal cells, subventricular astrocytes, choroid plexus epithelial cells, and macrophages

Fc receptor immunoreactivity was consistently observed at the basal side of ependymal cells and within subventricular astrocytes for three out of four FcR antibodies but with varying degrees of GFAP colocalization (Fig. 9A-D). 1G3 targeting soluble FcRn complexes minimally labeled subventricular astrocytes, compared to perfect overlap between GFAP and M-255 that targets the Fcgrt alpha chain. Similarly, GFAP/$CD32B_C$ colocalization was extensively observed in these cells but $CD32B_N$ immunoreactivity was minimal. Choroid plexus immunoreactivity was higher for macrophages followed by epithelial cells for all four anti-FcR antibodies (Fig. 10A-D). Macrophage-like cells (identified by Iba1 labeling) and choroid plexus epithelial cells were both labeled by M-255 (Fig. 10A), 1G3 (Fig. 10B), and $CD32B_N$ (Fig. 10D), but not $CD32B_C$ (Fig. 10C).

Astrocytes and macrophages immunoreactive for Fc receptors at the olfactory nerve layer

Next, we investigated FcRn immunoreactivity at the olfactory nerve layer-glomerular layer interface where olfactory nerve layer and associated perineural channels have potential connections with the meninges (Kumar

et al., 2018). Connections between the CSF and olfactory routes have also been demonstrated (Norwood *et al.*, 2019; Pizzo *et al.*, 2018). Evaluating FcR immunoreactivity at this interface could thus initiate a discussion on the role of Fc receptors in the central delivery of antibodies in the CNS. Recent studies have already suggested the presence of FcRn in the olfactory (Ladel *et al.*, 2018) and respiratory epithelial cells (Heidl *et al.*, 2016). Consistent with these findings, we observed M-255 (Fig. 11A) and 1G3 (Fig. 11B) immunoreactivity at the olfactory nerve layer that perfectly colocalized with GFAP for astrocytes overlying the glomerular layer. Cellular 1G3 profiles could be putative perivascular macrophages based on Iba1 co-immunoreactivity for these cells (not shown). $CD32B_N$ immunoreactivity was associated with astrocytes (Fig. 11C) while $CD32B_N$ immunoreactivity was associated with macrophages (labeled with LYVE-1, Fig. 11D) but not microglia.

Astrocytic and neuronal Fc receptor immunoreactivity in the rat brain parenchyma

FcRn and FcγRIIb expression in the brain neocortex (Fig. 12A-D) was largely neuronal (labeled with neuronal nuclei (NeuN) or ubiquitin carboxyl-terminal esterase L1 (UCHL1); red). GFAP colocalization was extensively observed for anti-FcRn antibodies (Fig. 13A, B) and $CD32B_C$ (Fig. 13C) whereas $CD32B_N$ profiles specifically detected Iba1-positive microglia (Fig. 13D).

Astrocytic mIgG1 immunoreactivity in wild-type and transgenic APP/PS1 mouse brain

Immunolabeling of mouse brain tissues ($n = 4$) with non-targeted mIgG1 (Fig. 1J-O), H-4 (mIgG1 alias of M-255; Fig. 14), and 1G3 (Fig. 15) detected GFAP-positive profiles at key brain-CSF interfaces i.e. cortical surface and the ventricles. Further, vascular profiles around surface blood vessels were detected with H-4 (Fig. 14C, D) and 1G3 (Fig. 15C, D) in the AD brain sections but not in WT brain sections.

Neuronal, non-astrocytic FcγRIIb immunoreactivity in wild-type and transgenic APP/PS1 mouse brain

Mouse brain FcγRIIb immunoreactivity was largely non-astrocytic based on immunofluorescence data (Fig. 16). Cortical surface was $CD32B_C$ immunoreactive (Fig. 16A) but these profiles were also observed with non-

targeted rabbit IgG (Fig. 14C). Additionally, astrocytes in the glia limitans were non-$CD32B_C$ immunoreactive, confirming non-specificity of surface $CD32B_C$ signal. In the cortex, $CD32B_C$ and $CD32B_N$ profiles were associated with UCHL-1-positive neurons (Fig. 14B, 14E).

M-255, not 1G3, detects transfected mouse Fcgrt protein in bEnd.3 cells

Next, we validated the specificity of 1G3 and M-255 antibodies in immortalized murine endothelial cells (bEnd.3) transfected with myc-DDK-tagged rat or mouse *Fcgrt*. Myc-DDK immunofluorescence suggested an approximately 5% success rate for bEnd.3 cells for mouse and rat *Fcgrt* transfection and was used as a positive control for evaluating immunoreactivity (Fig. 17A, D). M-255 immunolabeling of bEnd.3 cells revealed a similar distribution for transfected rat *Fcgrt* (Fig. 17B) and mouse *Fcgrt* (Figure 17C), however 1G3 immunolabeling detected rat *Fcgrt* (Fig. 17E) but not mouse *Fcgrt* (Figure 17F). Efforts to detect mouse FcRn at higher 1G3 concentrations led to non-specific nuclear and cytosolic profiles unlike Myc-DDK or M-255. No immunolabeling was observed in the absence of primary antibodies. These data support our ex vivo analysis confirming that 1G3 is able to detect rat FcRn but not mouse FcRn. Furthermore, M-255 can be used to detect both rat and mouse FcRn.

BCEC immunolabeling studies suggest non-endothelial FcRn & FcγRIIb expression

We further analyzed at BCECs (rBCECs) and mouse BCECs (mBCECs) for Fc receptor immunoreactivity via *in vitro* immunocytochemistry experiments. Here, all four antibodies (1G3, M-255, $CD32B_C$, $CD32B_N$) and their respective isotype controls (mIgG, rIgG) were tested for FcR expression relative to tight junction proteins (labeled by anti-zonula occludens, ZO-1, red). Positive 1G3 but negative M-255 immunoreactivity was detected in rBCECs (Fig. 18A, B). FcγRIIb immunoreactivity was either undetectable $CD32B_C$ (Fig. 18C) or non-specific $CD32B_N$ (Fig. 18D) in rBCECs. mBCECs were consistently negative for anti-FcR and control IgG (Fig. 19)

Glial cell culture immunolabeling supports astrocytic M-255 and macrophage CD32B$_N$ profiles

We further investigated *in vitro* FcR immunoreactivity in rat and mouse brain-derived glial cell cultures. Here, M-255 immunolabeling was detected in primary rat (Fig. 20A) and mouse (Fig. 21A) astrocytes while CD32B$_N$ labeled non-astrocytic glial cells in the rat glial cell culture (Fig. 20D). Extremely low levels of CD32B$_C$ immunolabeling was detected in GFAP-positive astrocytes (Fig. 20C, 21C). Similar to *ex vivo* findings, a slight 1G3 immunolabeling of rat glial cell cultures were observed (Fig. 20B) whereas no 1G3 immunolabeling was observed in the mouse glial cell culture (Fig. 21B).

Gene expression analysis for Fc receptors in endothelial cells and astrocytes cell cultures

Finally, we performed *in vitro* gene expression studies to investigated endothelial and astrocytic expression of various Fc receptor genes (*Fcgrt, β2m, Fcgr2b1, Fcgr2b2*). Gene expression values were calculated as fold-difference relative to corresponding expression values in astrocytes for the rat and mouse respectively (Fig. 22). Relative expression values for FcγRIIb genes (*Fcgr2b1, Fcgr2b2)* remained undetected in rBCECs and mBCECs as predicted by the immunocytochemical studies. Second, mBCECs had significantly higher *Fcgrt* expression values compared to murine astrocytes but rat *Fcgrt* were not significantly difference between rBCECs and primary rat astrocytes. Interestingly, rBCECs had non-significantly high *β2m* but low *Fcgrt* values suggesting that FcRn is more likely to be expressed by mouse endothelial cells and rat astrocytes based on gene expression values.

Discussion

Early efforts to characterize FcR distribution in the CNS utilized IgG uptake in the presence and absence of antigens as a measure to detect site with active FcR activity. These sites include the choroid plexus epithelial cells, leptomeninges, stromal cells in the arachnoid granulations, periventricular cell, perivascular cells around larger blood vessels, and pericytes around brain capillaries (Braathen *et al.*, 1979; Oehmichen *et al.*, 1976; Nyland & Matre, 1978; Peress *et al.*, 1981; Peress *et al.*, 1987, Siegelman *et al.*, 1987).

However, previously used detection methods (e.g. phagocytosis assessment using aggregated IgG-coated erythrocytes) have certain limitations. First, reproducibility of these findings is often not guaranteed (Schreiber & Perry, 1982; Vedeler *et al.*, 1994). Second, receptors such as FcγRIIb have non-phagocytotic isoforms that reversibly interacts with IgG at low-affinity and may remain undetected (Hunziker & Mellman, 1989; Miettnen *et al.*, 1992). Advances in receptor biology, monoclonal antibody development, and immunohistochemical methods studies have now made it feasible to detect non-phagocytic Fc receptors in the brain and validate these findings. We know from imaging-based studies that FcR activity is present in meningeal macrophages, subarachnoid space, ependymal cells, pericytes and ramified microglia in the brain parenchyma (Jordan & Thomas, 1988; Peress *et al.*, 1993). These findings have led to FcR-based isolation of brain microglial cells (Hayes *et al.*, 1988). However, these cells have not been mapped to specific FcR subtypes. In addition, studies involving multiple monoclonal antibodies against the same FcR epitope have detected different cellular profiles, indicating that FcR expression may exert heterogeneity in different extracellular environments (Vedeler *et al.*, 1994). Given these issues, the goal of our study was to map two FcR subtypes, FcRn and FcγRIIb, to cells at the brain-CSF interface as an attempt to address questions regarding their role in IgG distribution.

Results in this study suggest evident FcRn and FcγRIIb immunoreactivity at brain-CSF interfaces in the rat, i.e. the olfactory nerve layer, leptomeninges, glia limitans, subventricular astrocytes, perivascular macrophages and astrocytes, and choroid plexus cells as putative sites for IgG uptake. At the cellular level, immunoreactivity associated with meningeal cells, astrocytes, microglia and macrophages, suggesting the likelihood of IgG engagement by non-endothelial cells. We further observed different cellular immunoreactivity profiles for antibodies targeting the same receptor (e.g. $CD32B_C$ and $CD32B_N$). We presume these differences could be due to changes in receptor structure or conformation across cells and tissues (Antoun *et al.*, 1989) or overlapping epitopes across different FcγRs (Williams *et al.*, 2012). Indeed, other sources of commercially available anti-FcγRIIb antibodies suggest a percentage of cross-reactivity with activating FcγRs when the epitope involved alpha chain residues (e.g. Novus Biologicals; R&D

System, Cell Signaling Technology). There is a possibility that $CD32B_N$ with an extracellular alpha chain epitope detects activating and inhibitory FcγRIIb, whereas $CD32B_C$ targeting the ITIM region provides FcγRIIb distribution profiles. Cells immunoreactive for both FcγRs (e.g. meningeal cells, macrophages, neurons) may then offer a platform to manipulate their potential to engage and internalize IgG in the CNS. Subpopulations of cells immunoreactive for either epitope (e.g. astrocytes vs microglia) can provide a platform to investigate the role of a given FcγR at a brain-CSF interface. FcγRIIb immunolabeling of mouse brain sections revealed inter-species differences in FcR expression. FcγRIIb immunoreactivity was associated with neurons, astrocytes, microglia and macrophages compared to only neuronal expression in C57BL6 mice.

While murine FcRn immunoreactivity studies using anti-FcRn antibodies (mouse IgG1) did not reveal a lot of information, differences were clearly visible in terms of intense vascular immunoreactivity for endogenous mouse IgG in APPswe/PS1dE9 mice but lacking in C57BL/6 mice. Similar profiles have been reported for large (> 100μm) cerebral blood vessels and choroid plexus epithelium in the transgenic (Tg276 > Tg32) mice followed by wild-type mice (C57BL/6) mice and transgenic mice using an anti-FcRn antibody raised in rabbits as the host species (Latvala *et al.*, 2017). Differences in FcRn expression between wild-type and transgenic mice (Li & Balthasar, 2018; Whelan *et al.*, 1987) have also been documented in the peripheral nervous system. Altered Fc receptor immunoreactivity profiles could be putative compensatory mechanisms to prevent BBB disruption in animal models (Bien-Ly *et al.*, 2015). Studies have extensively investigated inter-species IgG immunoreactivity differences in the CNS (Hazama *et al.*, 2005; Niu *et al.* 2011; Pizzo, unpublished; Yoshimi *et al.*, 2002) but differences in FcR expression have not yet been explored in the CNS. Inter-strain (Balb/c mice versus C57BL/6 mice) differences in FcR expression are another unexplored territory that has not been investigated yet but may provide a better grasp on the efficiencies of non-related background strains to address a given mutation (Nimmerjahn & Ravetch, 2007).

Complementing *ex vivo* immunofluorescence results with *in vitro* immunocytochemical analysis answered several questions surrounding Fc receptor expression in the rodent CNS. Primary rat and mouse brain capillary endothelial cells (rBCECs and mBCECs) were ideal *in vivo* models for this study since they have been previously characterized for intact *in vivo* BBB properties such as the expression of tight junction protein complexes and high transendothelial electrical resistance (TEER) (Burkhardt *et al.*, 2015; Thomsen *et al.*, 2016). Sparse M-255 endothelial immunolabeling and non-specific 1G3 immunolabeling has not been highlighted in previous reports on endothelial FcRn expression (Deane *et al.*, 2001; Schlachetzki *et al.*, 2002). Similar *ex vivo* 1G3 and mIgG1 immunoreactivity profiles in the mouse brain tissue, together with lack of *in vitro* immunofluorescence for mouse FcRn-transfected bEnd.3 cells question the efficacy of 1G3 for detecting mouse FcRn as per our setup.

Immunohistochemical findings for endothelial FcRn protein expression have been sparsely reported in the past, with only one study highlighting glucose transporter-1 (GLUT-1)/1G3 colocalization in the rat brain capillaries (Schlachetzki *et al.*, 2002) but not the precise location (luminal/abluminal) or cellular origin (intravascular/perivascular) of FcRn. GLUT-1 has been demonstrated to have heterogeneous expression across the luminal/abluminal endothelial cell surfaces (Lippoldt *et al.*, 2002; Pardridge *et al.*, 1990; Simpson *et al.*, 2001), between adjacent cells (Releigh *et al.*, 2008), brain regions (Dobrogowska & Vorbrodt, 2011) and across species (Bolz *et al.*, 1996; Conrford *et al.*, 1993; Farrell & Pardridge, 2006; Gerhart *et al.*, 1989; Vorbrodt *et al.*, 1999) suggesting that 1G3/GLUT-1 colocalization may not be specific to the luminal endothelial cell surface at the least. The close proximity between astrocytes and endothelial cells (Kacem *et al.*, 1998) pose an argument for investigating astrocyte/endothelial cell interface for FcRn expression. Further, GLUT-1 has multiple isoforms expressed by non-endothelial cells at the BBB such as pericytes (Cornford & Hyman, 2005; Virgintino *et al.*, 1997) that have not been studied for FcRn expression using relevant cellular markers. Lower endogenous IgG sequestration due to pericytes loss provides a basis for investigating pericytes for FcRn levels (Villaseñor *et al.*, 2016).

We consulted existing murine single-cell mRNA sequencing databases (key findings summarized in Table 3 & 4) to guide our study design and correlate our findings. First, murine pericytes (Vanlandewijck *et al.*, 2018; Zeisel *et al.*, 2015; Zeisel *et al.*, 2018), vascular leptomeningeal cells (Marques *et al.*, 2016; Zeisel *et al.*, 2015; Zeisel *et al.*, 2018) and choroid plexus epithelial cells (Li *et al.*, 2019; Vanlandewijck *et al.*, 2018; Zeisel *et al.*, 2015; Zeisel *et al.*, 2018) had sufficiently high *Fcgrt* mRNA levels. Second, murine *Fcgr2b* mRNA expression in these databases (key findings summarized in table 4) suggested predominant expression associated with microglia/macrophages followed be neuronal cells compared to other cell types, correlating with *in vitro* and *ex vivo* $CD32B_N$ immunolabeling findings. Third, highest murine *Fcgrt* mRNA expression levels were found to be associated with endothelial cells followed by fibroblasts, microglia and perivascular macrophages (Clarke *et al.*, 2018; Bennett *et al.*, 2016; Li *et al.*, 2019; Vanlandewijck *et al.*, 2018; Zeisel *et al.*, 2015; Zhang *et al.*, 2003). We confirmed this trend through our gene expression for murine endothelial cells (mBCECs). but we did not see significant differences in gene expression between rBCECs and primary rat astrocytes.

Astrocytes were interesting cells to follow through as our protein-based immunoreactivity results did not completely correlate with murine mRNA expression studies for these cells. Murine astrocytes have been reported to have second to lowest average *Fcgrt* expression values (Vanlandewijck *et al.*, 2018). Astrocytic *Fcgrt* mRNA has been consistently reported to be lower than endothelial cells, microglia/macrophages, pericytes, leptomeningeal cells, choroid plexus cells across multiple studies (Clarke *et al.*, 2018, Zeisel *et al.*, 2015; Zhang *et al.*, 2014). However, immunolabeling findings in this study suggest Fcgrt protein expression in astrocytes compared to non-specific profiles in endothelial cells for rats and mice. Astrocytic Fcgrt immunoreactivity was further detected in the rat brain at the cortical surfaces (glia limitans, olfactory nerve layer), subependymal layers (subventricular astrocytes), and the parenchyma (white matter tracts, neocortex, perivascular spaces) in rats.

It remains uncertain why *Fcgrt* mRNA and protein expression profiles would not correlate for rat endothelial cells and astrocytes. Astrocytic FcR protein expression at the BBB and brain-CSF interfaces may be in place to prevent unneeded mRNA translation in endothelial cells. For instance, astrocytes upregulate FcγRs through changes in cellular, molecular, or functional properties (reactive astrogliosis) (Sofroniew & Vinters, 2010) in Alzheimer's disease (Fernandez-Vizarra *et al.*, 2012) and lysosomal storage disorders (Ogawa *et al.*, 2017), and FcγRIIb during brain infections (Sheng *et al.*, 2010) and metastatic melanomas (Cohen-Solal *et al.*, 2010). Astrocytic FcR expression has not been extensively investigated but may have a role in IgG sequestration to maintain IgG homeostasis at the BBB (Bernstein *et al.*, 1993). FcRn and FcγRIIb immunoreactivity associated with neuronal profiles may have a role in intraneuronal IgG uptake (Fabian & Petroff, 1987) and Purkinje cell IgG internalization (Fishman *et al.*, 1990; Gill *et al.*, 2006) in rats. Only recent evidence exists for *Fcgr2b* mRNA levels in neuronal and astrocytic subpopulations for the developing rat brain, and for *Fcgr2b* protein expression in primary astrocyte and neuronal cell cultures (Stamou *et al.*, 2018), indicating this could be an unexplored area of research.

Finally, previous pharmacokinetic reports have suggested no significant differences in brain IgG levels upon intravenous IgG injections in wild-type and Fc receptor knockout mice (Abuqayyas & Balthasar, 2013; Chen *et al.*, 2014; Garg & Balthasar, 2009). Investigating the role of Fc receptors following central IgG delivery may offer a different perspective due to multiple reasons. First, intravenous IgG administration leads to restricted endothelial extravasation into the brain parenchyma (Eigenmann *et al.*, 2017; Haqqani *et al.*, 2017; St-Amour *et al.*, 2013; Yu *et al.*, 2014). Second, these studies do not include CSF sampling which offers a true readout of IgG transfer when coupled with brain homogenization experiments (St-Amour *et al.*, 2013; Webster *et al.*, 2016). Third, basal levels of FcR expression can be altered in transgenic mice. Pharmacokinetic studies utilizing the central routes suggest that IgG-FcR interactions influence IgG distribution profiles in the brain (Bergman *et al.*, 1998; Cooper *et al.*, 2013; Pizzo *et al.*, 2018; Zhang & Pardridge, 2001). FcR expression in astrocytic and macrophages lining at the rodent brain-CSF interfaces

(olfactory nerve layer, glia limitans, leptomeninges, ependymal layers, perivascular spaces) may facilitate the understanding of central delivery mechanisms for IgG-based therapies in the CNS.

References

Abbott NJ (2013). Blood-brain barrier structure and function and the challenges for CNS drug delivery. *J Inherit Metab Dis* **36**, 437–449.

Abbott NJ, Patabendige AAK, Dolman DEM, Yusof SR & Begley DJ (2010). Structure and function of the blood-brain barrier. *Neurobiol Dis* **37**, 13–25.

Abulrob A, Guiseppin S, Andrade MF, McDermid A, Moreno M & Stanimirovic D (2004). Interactions of EGFR and caveolin-1 in human glioblastoma cells: evidence that tyrosine phosphorylation regulates EGFR association with caveolae. *Oncogene* **23**, 6967-6979.

Abuqayyas L & Balthasar JP (2013). Investigation of the role of FcgammaR and FcRn in mAb distribution to the brain. *Mol Pharm* **10**, 1505–1513.

Aihara N, Tanno H, Hall JJ, Pitts LH & Noble LJ (1994). Immunocytochemical localization of immunoglobulins in the rat brain: Relationship to the blood-brain barrier. *J Compar Neurol* **342**, 481-496.

Akilesh S, Petkova S, Sproule, TJ, Shaffer DJ, Christianson GJ & Roopenian D (2004). The MHC class I–like Fc receptor promotes humorally mediated autoimmune disease. *J Clin Investig* **113**, 1328–1333.

Anderson CL (2014). There's been a flaw in our thinking. *Front Immunol* **5**, 540.

Ganesan LP, Kim J, Wu Y, Mohanty S, Phillips GS, Birmingham DJ, Robinson JM & Anderson CL (2012). FcγRIIb on Liver Sinusoidal Endothelium Clears Small Immune Complexes. *J Immunol* **189**, 4981–4988.

Andoh T & Kuraishi Y (2004). Direct action of immunoglobulin G on primary sensory neurons through Fc gamma receptor I. *FASEB J* **18**, 182–184.

Antoun GR, Longenecker BM & Zipf TF (1989). Comparison of the 40kDA hematopoietic cell antigens bound by monoclonal antibodies IV3, 41H16 and KB61. *Mol Immunol* **26**, 333–338.

Bacskai BJ, Kajdasz ST, McLellan ME, Games D, Seubert P, Schenk D & Hyman BT (2002). Non-Fc-Mediated Mechanisms Are Involved in Clearance of Amyloid-Beta *in vivo* by Immunotherapy *J Neurosci* **22**, 7873–7878.

Banks WA, Terrell B, Farr SA, Robinson SM, Nonaka N & Morley JE (2003). Passage of amyloid-β protein antibody across the blood–brain barrier in a mouse model of Alzheimer's disease. *Peptides* **23**, 2223–2226.

Bayry J, Lacroix-Desmazes S, Kazatchkine MD & Kaveri SV (2007). Monoclonal antibody and intravenous immunoglobulin therapy for rheumatic diseases. *Nat Clin Pract Rheumatol* **3**, 262–2732.

Bennett ML, Bennett FC, Liddelow SA, Ajami B, Zamanian JL, Fernhoff NB, Mulinyawe SB, Bohlen CJ, Adil A, Tucker A, Weissman IL, Chang EL, Li, G, Grant GA, Hayden Gephart MG & Barres BA (2016). New tools for studying microglia in the mouse and human CNS. *Proc Natl Acad Sci* **113**, E1738-E1746.ta

Bergman I, Burckart GJ, Pohl CR, Venkataramanan R, Barmada MA, Griffin JA & Cheung NK (1998). Pharmacokinetics of IgG and IgM anti-ganglioside antibodies in rats and monkeys after intrathecal administration. *J Pharmacol Exp Ther* **284**, 111–115.

Bernstein JJ, Willingham LA & Goldberg WJ (1993). Sequestering of immunoglobulins by astrocytes after cortical lesion and homografting of fetal cortex. *Int J Dev Neurosci* **11**, 117–124.

Bien-ly N, Boswell CA, Jeet S, Beach TG, Hoyte K, Luk W, Shihadeh V, Ulufatu S, Foreman O, Lu Y, DeVoss J, van der Brug M & Watts RJ (2015). Lack of Widespread BBB Disruption in Alzheimer's Disease Models: Focus on Therapeutic Antibodies. *Neuron* **88**, 289–297.

Bolz S, Farrell CL, Dietz K & Wolburg H (1996). Subcellular distribution of glucose transporter (GLUT-1) during development of the blood-brain barrier in rats. *Cell Tissue Res* **284**, 355–365.

Booth BJ, Ramakrishnan B, Narayan K, Wollacott AM, Babcock GJ, Shriver Z & Vishwanathan K (2018). Extending human IgG half-life using structure-guided design. *mAbs*. **10**, 1098–1110.

Borrok MJ, Mody N, Lu X, Kuhn ML, Wu H, Dall'Acqua WF & Tsui P (2017). An "Fc-Silenced" IgG1 Format with Extended Half-Life Designed for Improved Stability. *J Pharm Sci* **106**, 1008–1017.

Borvak J, Richardson J, Medesan C, Antohe F, Radu C, Simionescu M, Ghetie V & Ward ES (1998). Functional expression of the MHC class I-related receptor, FcRn, in endothelial cells of mice. *Int Immunol* **10**, 1289–1298.

Braathen LR, Førre ØT, Husby G & Williams RC (1979). Evidence for Fc IgG receptors and complement factor C3b receptors in human choroid plexus. *Clin Immunol Immunopathol* **14**, 284–291.

Brambell FWR (1969). The transmission of immune globulins from the mother to the fetal and newborn young. *Proc Nutr Soc* **28**, 35–41.

Burkhart A, Thomsen LB, Thomsen MS, Lichota J, Fazakas C, Krizbai I & Moos T (2015). Transfection of brain capillary endothelial cells in primary culture with defined blood-brain barrier properties *Fluids Barriers CNS* **12**, 19.

Burmeister WP, Huber AH & Bjorkman PJ (1994). Crystal structure of the complex of rat neonatal Fc receptor with Fc *Nature* **372**, 379–383.

Camilleri-Broët S, Cassaed L, Broët P, Delmer A, Le Touneau A, Diebold J, Fridman WH, Molina TJ & Sautes-Fridman C (2004). FcgammaRIIB is differentially expressed during B cell maturation and in B-cell lymphomas. *Br J Haematol* **124**, 55–62.

Caram-Salas N, Boileau E, Farrington GK, Garber E, Brunette E, Abulrob A & Stanimirovic D (2011). *In vitro* and *in vivo* methods for assessing FcRn-mediated reverse transcytosis across the blood-brain barrier. *Methods Mol Biol* **763**, 383–401.

Chen N, Wang W, Fauty S, Fang Y, Hamuro L, Hussain A & Prueksaritanont T (2014). The effect of the neonatal Fc receptor on human IgG biodistribution in mice. *mAbs* **6**, 502–508.

Cianga P, Cianga C, Cozma, L, Ward ES & Carasevici E (2003). The MHC Class I Related Fc Receptor, FcRn, is Expressed in the Epithelial Cells of the Human Mammary Gland. *Hum Immunol* **64**, 1152–1159.

Clarke LE, Liddlelow SA, Chakraborty C, Munch AE, Heiman M & Barres BA (2018). Normal aging induces A1-like astrocyte reactivity. *Proc Natl Acad Sci* **115**, E1896–E1905.

Claypool SM, Dickinson BL, Wagner JS, Johansen FE, Venu N, Borawski JA, Lencer WI & Blumberg RS (2004). Bidirectional Transepithelial IgG Transport by a Strongly Polarized Basolateral Membrane Fc gamma Receptor *Mol Biol Cell* **15**, 1746–1759.

Cohen-Solal JF, Cassard L, Fournier EM, Loncar SM, Fridman WH & Sautes-Fridman C (2010). Metastatic melanomas express inhibitory low affinity Fc gamma receptor and escape humoral immunity. *Dermatol Res Pract* **2010**, 657406.

Congdon EE, Gu J, Sait HBR & Sigurdsson EM (2013). Antibody uptake into neurons occurs primarily via clathrin-dependent Fc gamma receptor endocytosis and is a prerequisite for acute tau protein clearance *J Biol Chem* **288**, 35452–35465.

Cooper PR, Ciambrone GJ, Kliwinski CM, Maze E, Johnson L, Li Q, Feng Y & Hornby RJ (2013). Efflux of monoclonal antibodies from rat brain by neonatal Fc receptor, FcRn. *Brain Res* **1534**, 13–21.

Cornford EM & Hyman S (2005) Localization of brain endothelial luminal and abluminal transporters with immunogold electron microscopy. *NeuroRx* **2**, 27–43.

Cornford M, Hyman S & Pardridge M (1993). An Electron Microscopic Immunogold Analysis of Developmental Up-Regulation of the Blood-Brain Barrier GLUT1 Glucose Transporter. *J Cereb Blood Flow Metab* **13**, 841–848.

Croll SD, Chesnutt CR, Rudge JS, Acheson A, Ryan TE, Siuciak JA, DiStefano PS, Wiegand SJ & Lindsay RM (1998). Co-infusion with a TrkB-Fc receptor body carrier enhances BDNF distribution in the adult rat brain. *Exp Neurol* **152(1)**: 20-33.

Das P, Howard V, Loosbrock N, Dickson D, Murphy MP & Golde TE *et al* (2018). Amyloid-*β* Immunization Effectively Reduces Amyloid Deposition in FcRγ -/- Knock-Out Mice *J Neurosci* **23**, 8532–8538.

Deane R, Sagare A, Hamm K, PArisi M, LaRue B, Guo H, Wu Z, Holtzman DM & Zlokovic BV (2005). IgG-Assisted Age-Dependent Clearance of Alzheimer's Amyloid Peptide by the Blood-Brain Barrier Neonatal Fc Receptor. *J Neurosci* **25**, 11495–11503.

Deissler HL, Lang GK & Lang GE (2017). Neonatal Fc receptor FcRn is involved in intracellular transport of the Fc fusion protein aflibercept and its transition through retinal endothelial cells. *Exp Eye Res* **154**, 39–46.

Dobrogowska DH & Vorbrodt AW (2011). Quantitative Immunocytochemical Study of Blood-Brain Barrier Glucose Transporter (GLUT-1) in Four Regions of Mouse Brain. *J Histochem Cytochem* **47**, 1021–1030.

Eigenmann MJ, Karlsen TV, Krippendorff BF, Tenstad O, Fronton L, Otteneder MB & Wiig H (2017). Interstitial IgG antibody pharmacokinetics assessed by combined *in vivo* and physiologically-based pharmacokinetic modelling approaches. *J Physiol* **595**, 7311–7330.

Engelhardt B & Sorokin L (2009). The blood-brain and the blood-cerebrospinal fluid barriers: Function and dysfunction. *Semin Immunopathol* **31**, 497–511.

Fabian RH & Petroff G (1987). Intraneuronal IgG in the central nervous system: uptake by retrograde axonal transport *Neurology* **37**, 1780–1784.

Farrell CL & Pardridge WM (2006). Blood-brain barrier glucose transporter is asymmetrically distributed on brain capillary endothelial lumenal and ablumenal membranes: an electron microscopic immunogold study. *Proc Natl Acad Sci* **88**, 5779–5783.

Fernandez-Vizarra P, Lopez-Franco O, Mallavia B, Higuera-Matas A, Lopez-Parra V, Ortiz-Munoz G, Ambrosio E, Egido J & Gomez-Guerrero C (2012). Immunoglobulin G Fc receptor deficiency prevents Alzheimer-like pathology and cognitive impairment in mice. *Brain* **135**, 2826–2837.

Firan M, Bowdon R, Radu C, Ober RJ, Eaken D, Antohe F, Ghetie V & Ward ES (2001). The MHC class I-related receptor, FcRn, plays an essential role in the maternofetal transfer of γ-globulin in humans. *Int Immunol* **13**, 993–1002.

Fishman PS, Farrand DA & Kristt DA (1990). Internalization of plasma proteins by cerebellar Purkinje cells. *J Neurol Sci* **100**, 43–49.

Garg A & Balthasar JP (2009). Investigation of the Influence of FcRn on the Distribution of IgG to the Brain. *AAPS J* **11**, 553–557.

Gerhart DZ, Levasseur RJ, Broderius MA & Drewes LR (1989). Glucose transporter localization in brain using light and electron immunocytochemistry. *J Neurosci Res* **22**, 464–472.

Gill R, Iversen L, Elliott P, Borges L & Iversen S (2006). Selective extraction of small and large molecules from the cerebrospinal fluid by Purkinje neurons. *Science* **228**, 346–348.

Goldsmith SK (2002). Haloperidol reduces IgG immunoreactivity in the rat brain. *Int J Neuropsychopharmacol* **5**, 309-313.

Gosk, S, Moos, T, Gottstein C & Bendas G (2008). VCAM-1 directed immunoliposomes selectively target tumor vasculature *in vivo*. *Biochimica et Biophys Acta* **1778**, 854–863.

Griffin DE & Giffels J (1982). Study of protein characteristics that influence entry into the cerebrospinal fluid of normal mice and mice with encephalitis. *J Clin Investig* **70**, 289–295.

Haqqani AS, Delaney CE, Brunette E, Baumann E, Farrington GK, Sisk W, Eldredge J, Ding W, Tremblay TL & Stanimirovic DB (2018). Endosomal trafficking regulates receptor-mediated transcytosis of antibodies across the blood brain barrier. *J Cereb Blood Flow & Metab* **0**, 1–14.

Hayes GM, Woodroofe MN & Cuzner ML (1988). Characterization of Microglia Isolated from Adult Human and Rat-Brain. *J Neuroimmunol* **19**, 177–189.

Hazama GI, Yasuhara O, Morita H, Aimi Y, Tooyama I & Kimura H (2005). Mouse Brain IgG-Like Immunoreactivity: Strain-Specific Occurrence in Microglia and Biochemical Identification of IgG. *J Comp Neurol* **492**, 234–249.

He W, Ladinsky MS, Huey-Tubman KE, Jensen GJ, McIntosh JR & Bjorkman PJ (2008). FcRn-mediated antibody transport across epithelial cells revealed by electron tomography. *Nature* **455**, 542–546.

Heidl S, Ellinger I, Niederberger V, Waltl EE & Fuchs R (2016). Localization of the human neonatal Fc receptor (FcRn) in human nasal epithelium. *Protoplasma* **253**, 1557–1564.

Hemmings WA & Brambell FWR (1961). Protein Transfer Across Fetal Membranes. *Br Med Bull* **17**, 96–101.

Hochwald GM (1970). Influx of serum proteins and their concentration in spinal fluid along the neuraxis. *J Neurol Sci* 10, 269–278.

Huang H, Hara A, Homma T, Yonekawa Y & Ohgaki H (2005). Altered expression of immune defense genes in pilocytic astrocytomas. *J Neuropathol Exp Neurol* **64**, 891–901.

Hunziker W & Mellman I (1989). Expression of macrophage-lymphocyte Fc receptors in Madin-Darby canine kidneys cells: Polarity and transcytosis differ for isoforms with or without coated pit localization domains. *J Cell Biol* **109**, 3291–3302.

Ishikawa T, Takizawa T, Iwaki J, Mishima T, Ui-Tei K, Takeshita T, Matsubara S, Takizawa T (2015). Fc gamma receptor IIb participates in maternal IgG trafficking of human placental endothelial cells. *Int J Mol Medicine* **35**, 1273–1289.

Jefferis R (2012). Isotype and glycoform selection for antibody therapeutics. *Arch Biochem Biophys* 526, 159–166.

Jordan FL & Thomas WE (1988). Brain macrophages: questions of origin and interrelationship. *Brain Res Rev* **13**, 165–178.

Junghans RP (1997). IgG biosynthesis: no 'immunoregulatory feedback'. *Blood* **90**, 3815–3818.

Kacem K, Lacombe P, Seylaz J & Bonvento G (1998). Structural organization of the perivascular astrocyte end feet and their relationship with the endothelial glucose transporter: A confocal microscopy study. *Glia* **23**, 1–10.

Kim H, Fariss RN, Zhang C, Robinson SB, Thill M & Csaky KG (2008). Mapping of the Neonatal Fc Receptor in the Rodent Eye. *Investig Ophthalmol Vis Sci* **49**, 2025–2029.

Kristoffersen EK & Matre R (1996). Co-localization of the neonatal Fcy receptor and IgG in human placental term syncytiotrophoblasts. *Eur J Immunol* **26**, 1668–1671.

Kumar NN, Gautam M, Lochhead JJ, Wolak DJ, Ithapu V, Singh V & Thorne RG (2016). Relative vascular permeability and vascularity across different regions of the rat nasal mucosa: Implications for nasal physiology and drug delivery. *Sci Rep* **6**, 1-14.

Kumar NN, Lochhead JJ, Pizzo ME, Nehra G, Boroumand S, Greene G & Thorne RG (2018). Delivery of immunoglobulin G antibodies to the rat nervous system following intranasal administration: Distribution, dose-response, and mechanisms of delivery. *J Control Release* **286**, 467–484.

Ladel S, Flamm J, Zadeh AS, Filzwieser D, Walter JC, Schlossbauer P, Kinscherf R, Lischka K, Luksch H & Schindowski K (2018). Allogenic Fc Domain-Facilitated Uptake of IgG in Nasal Lamina Propria: Friend or Foe for Intranasal CNS Delivery?

Latvala S, Jacobsen B, Otteneder MB, Herrmann A & Kronenberg S (2017). Distribution of FcRn Across Species and Tissues. *J Histochem Cytochem* **65**, 321–333.

Leach JL, Sedmak DD, Osborne JM, Rahill B, Lairmore MD & Anderson CL (1996). Isolation from human placenta of the IgG transporter, FcRn, and localization to the syncytiotrophoblast: implications for maternal-fetal antibody transport. *J Immunol* **157**, 3317–3322.

Lein ES, Hawrylycz MJ, Ao N, Ayres M, Bensinger A, Bernard A, Boe AF, Boguski MS, Brockway KS, Byrnes EJ, Chen L, Chen L, Chen TM, Chin MC, Chong J, Crook BE, Czaplinska A, Dang CN, Datta S, Dee NR, Desaki AL, Desta T, Diep E, Dolbeare TA, Donelan MJ, Dong HW, Dougherty JG, Duncan BJ, Ebbert AJ, Eichele G, Estin LK, Faber C, Facer BA, Fields R, Fischer SR, Fliss TP, Frensley C, Gates SN, Glattfelder KJ, Halverson KR, Hart MR, Hohmann JG, Howell MP, Jeung DP, Johnson RA, Karr PT, Kawal R, Kidney JM, Knapik RH, Kuan CL, Lake JH, Laramee AR, Larsen KD, Lau C, Lemon TA, Liang AJ, Liu Y, Luong LT, Michaels J, Morgan JJ, Morgan RJ, Mortrud MT, Mosqueda NF, Ng LL, Ng R, Orta GJ, Overly CC, Pak TH, Parry SE, Pathak SD, Pearson OC, Puchalski RB, Riley ZL, Rockett HR, Rowland SA, Royall JJ, Ruiz MJ, Sarno NR, Schaffnit K, Shapovalova NV, Sivisay T, Slaughterbeck CR, Smith SC, Smith KA, Smith BI, Sodt AJ, Stewart NN, Stumpf KR, Sunkin SM, Sutram M, Tam A, Teemer CD, Thaller C, Thompson CL, Varnam LR, Visel A, Whitlock RM, Wohnoutka PE, Wolkey CK, Wong VY, Wood M, Yaylaoglu MB, Young RC, Youngstrom BL, Yuan XF, Zhang B, Zwingman TA & Jones AR. (2006). Genome-wide atlas of gene expression in the adult mouse brain. *Nature* **445**, 168–176.

Li F, Smith P & Ravetch JV (2014). Inhibitory Fc Receptor Is Required for the Maintenance of Tolerance through Distinct Mechanisms. *J Immunol* **192**, 3021–3028.

Li Q, Cheng Z, Zhou L, Darmanis S, Neff NF, Okamoto J, Gulati G, Bennett ML, Sun LO, Clarke LE, Marschallinger J, Yu G, Quake SR, Wyss-Coray T & Barres BA (2019). Developmental Heterogeneity of Microglia and Brain Myeloid Cells Revealed by Deep Single-Cell RNA Sequencing. *Neuron* **101**, 207–223e10.

Li T & Balthasar JP (2018). FcRn Expression in Wildtype Mice, Transgenic Mice, and in Human Tissues. *Biomolecules* **8**, 115.

Linkert M, Rueden CT, Allan C, Burel J-M, Moore W, Patterson A, Loranger B, Moore J, Neves C, MacDonald D, Tarkowska A, Sticco C, Hill E, Rossner M, Eliceiri KW & Swedlow JR (2010). Metadata matters: access to image data in the real world. *J Cell Biol* **189**, 777–782.

Lippoldt A, Kniesel U, Liebner S, Kalbacher H, Kirsch T, Wolburg H & Haller H (2002). Structural alterations of tight junctions are associated with loss of polarity in stroke-prone spontaneously hypertensive rat blood–brain barrier endothelial cells. *Brain Res* **885**, 251–261.

Liu L (2018). Pharmacokinetics of monoclonal antibodies and Fc-fusion proteins. *Protein Cell* **9**, 15–32

Lochhead JJ, Wolak DJ, Pizzo ME & Thorne RG (2015). Rapid transport within cerebral perivascular spaces underlies widespread tracer distribution in the brain after intranasal administration. *J Cereb Blood Flow Metab* **35**, 371–381.

Marques S, Zeisel A, Codeluppi S, van Bruggen D, Mendanha Falcao A, Xiao L, Li H, Haring M, Hochgerner H Romanov RA, Gyllborg D, Munoz Manchado A, La Manno G, Lonnerberg P, Floriddia EM, Rezayee F, Ernfors P, Arenas E, Hjerling-Leffler J, Harkany T, Richardson WD, Linnarsson S & Castelo-Branco G (2016). Oligodendrocyte heterogeneity in the mouse juvenile and adult central nervous system. *Science* **352**, 1326–1329.

Miettinen HM, Matter K, Hunziker W, Rose JK & Mellman I (1992). Fc Receptor Endocytosis Is Controlled by a Cytoplasmic Domain Determinant That Actively Prevents Coated Pit Localization. *J Cell Biol* **116**, 857–888.

Mimura Y, Katoh T, Saldova R, O'Flaherty R, Izumi T, Mimura-Kimura Y, Utsunomiya T, Mizukami Y, Yamamoto K, Matsumoto T & Rudd PM (2018). Glycosylation engineering of therapeutic IgG antibodies: challenges for the safety, functionality and efficacy. *Protein Cell* **9**, 47–62.

Nakahara J & Aiso S (2006). Fc receptor-positive cells in remyelinating multiple sclerosis lesions. *J Neuropathol Exp Neurol* **65**, 582–591

Nakahara J, Tan-Takeuchi K, Seiwa C, Gotoh M, Kaifu T, Ujike A, Inui M, Yagi T, Ogawa M, Aiso S, Takai T & Asou H (2003). Signaling via immunoglobulin Fc receptors induces oligodendrocyte precursor cell differentiation. *Dev Cell* **4**, 841–852.

Nakamura K, Hirai H, Torashima T, Miyazaki T, Tsurui H, Xiu Y, Ohtsuji M, Lin QS, Tsukamoto K, Nishimura H, Ono M, Watanabe M & Hirose S (2007). CD3 and Immunoglobulin G Fc Receptor Regulate Cerebellar Functions. *Mol Cell Biol* **27**, 5128–5134.

Nimmerjahn F & Ravetch JV (2006). Fcγ receptors: Old Friends and New Family Members. *Immunity* **24**, 19–28.

Nimmerjahn F & Ravetch JV (2008). Anti-Inflammatory Actions of Intravenous Immunoglobulin. *Ann Rev Immunol* **26**, 513–533.

Nimmerjahn F & Ravetch JV (2008). Fcγ receptors as regulators of immune responses. *Nat Rev Immunol* **8**, 34–47.

Nitta T, Yagita H, Sato K & Okumura K (1992). Expression of Fcγ receptors on astroglial cell lines and their role in the central nervous system. *Neurosurgery* **31**, 83–88.

Niu N, Zhang J, Guo Y, Zhao Y, Korteweg C & Gu J (2011). Expression and distribution of immunoglobulin G and its receptors in the human nervous system. *Int J Biochem Cell Biol* **43**, 556–563.

Nyland H & Matre R (1978). Fcγ receptors in human choroid plexus. *Acta Pathol Microbiol Scand* 86, 141–143.

Oehmichen M (1976). Receptor activity on some mesenchymal cells in CNS of normal rabbits. *Acta Neuropathol* Berlin 205–218.

Ogawa Y, Sano T, Irisa M, Kodama T, Saito T, Furusawa E, Kaizu K, Yanagi Y, Tsukimura T, Togawa T, Yamanaka S, Itoh K, Sakuraba H & Oishi K (2017). FcRγ-dependent immune activation initiates astrogliosis during the asymptomatic phase of Sandhoff disease model mice. *Sci Rep* **7**, 40518.

Okun E, Mattson MP & Arumugam, TV (2010). Involvement of Fc Receptors in Disorders of the Central Nervous System. *Neuromolec Med* **12**, 164–178.

Pardridge WM & Boado R J (2012). Reengineering biopharmaceuticals for targeted delivery across the blood-brain barrier. *Methods Enzymol* **503**, 269-292.

Pardridge WM, Boado R J & Farrell CR (1990). Brain-type Glucose Transporter (GLUT-1) Is Selectively Localized to the Blood-Brain Barrier. *J Biol Chem* **265**, 18035–18040.

Peress NS, Fleit HB, Perillo E, Kuljis R & Pezzullo C (1993). Identification of Fc gamma RI, II & III on normal human brain ramified microglia & on microglia in senile plaques in Alzheimer's disease. *J Neuroimmunol* **48**, 71-79.

Peress NS, Roxburgh VA & Gelfand MC (1981). Binding Sites for Immune Components in Human Choroid Plexus. *Arthritis Rheum* **24**, 520–526.

Peress NS, Siegelman J & Fleit HB (1987). High avidity periventricular IgG-Fc receptor activity in human and rabbit brain. *Clin Immunol Immunopathol* **42**, 229–238.

Peress NS, Siegelman J, Fleit HB, Fanger MW & Perillo E (1989). Monoclonal antibodies identify three IgG Fc receptors in normal human central nervous system. *Clin Immunol Immunopathol* 53, 268–280.

Perry VH, Hume DA & Gordon S (1985). Immunohistochemical localization of macrophages and microglia in the adult and developing mouse brain. *Neuroscience* **15**, 313–326.

Pfaffl MW (2001). A new mathematical model for relative quantification in real-time RT-PCR. *Nucleic Acids Res* 29, e45

Pizzo ME, Wolak DJ, Kumar NN, Brunette E, Brunnquell CL, Hannocks MJ, Abbott NJ, Meyerand ME, Sorokin L, Stanimirovic DB & Thorne RG (2018). Intrathecal antibody distribution in the rat brain: surface diffusion, perivascular transport and osmotic enhancement of delivery. *J Physiol* **596**, 445–475.

Podulso JF & Curran GL (1994). Glycation increases the permeability of proteins across the blood-nerve and blood-brain barriers. *Brain Res Mol Brain Res* **23**, 157-162.

Popov S, Hubbard JG, Kim J, Ober B, Ghetie V & Ward ES (1996). The stoichiometry and affinity of the interactions of murine Fc fragments with the MHC class I-related receptor, FcRn. *Mol Immunol* **33**, 521–530.

Powner MB, McKenzie JAG, Christianson GJ, Roopenian DC & Fruttiger M (2014). Expression of Neonatal Fc Receptor in the Eye. *Investig Opthalmol Vis Sci* **55**, 1607.

Preterit HF & Rubbert-Roth A (2009). Rituximab levels in cerebrospinal fluid of patients with neurological autoimmune disorders. *Multiple Scler* 15, 189–192.

Pyzik M, Rath T, Lencer WI, Baker K & Blumberg RS (2015). FcRn: The Architect Behind the Immune and Nonimmune Functions of IgG and Albumin. *J Immunol* **194**, 4595–4603.

Radulescu L, Antohe F, Jinga V, Ghetie V & Simionescu M (2004). Neonatal Fc receptors discriminates and monitors the pathway of native and modified immunoglobulin G in placental endothelial cells. *Hum Immunol* **65**, 578–585.

Raghavan M, Chen MY, Gastinel LN & Bjorkman PJ (1994). Investigation of the interaction between the class I MHC-related Fc receptor and its immunoglobulin G ligand. *Immunity* **1**, 303–315.

Raleigh, MJ, Damian RT, Cornford ME, Hyman S & Cornford EMA (2008). Single Glucose Transporter Configuration in Normal Primate Brain Endothelium: Comparison with Resected Human Brain. *J Neuropathol Exp Neurol* **57**, 699–713.

Rapaport SI & Pettigrew KD (1979). A Heterogenous, Pore-Vesicle Membrane Model for Protein Transfer from Blood to Cerebrospinal Fluid at the Choroid Plexus. *Microvasc Res* **18**, 105–119.

Ravetch JV & Bolland S (2001). IgG Fc receptors. *Ann Rev Immunol* **19**, 275–290.

Roberts DM, Guenthert M & Rodewald R (1990). Isolation and characterization of the Fc receptor from the fetal yolk sac of the rat. *J Cell Biol* **111**, 1867–1876.

Rodewald R & Kraehenbuhl J-P (1984). Receptor-mediated transport of IgG. *J Cell Biol* **99**, 159s–164s.

Rojas, R & Apodaca (2002). G Immunoglobulin transport across polarized epithelial cells. *Nat Rev Mol Cell Biol* **3**, 944–955.

Roopenian D, Christianson GJ, Sproule TJ, Brown AC, Akilesh S, Jung N, Petkova S, Avanessian L, Choi EY, Shaffer DJ, Eden PA & Anderson CL (2003). The MHC Class I-Like IgG Receptor Controls Perinatal IgG Transport, IgG Homeostasis, and Fate of IgG-Fc-Coupled Drugs. *J Immunol* **170**, 3528–3533.

Roopenian DC & Akilesh S (2007). FcRn: The neonatal Fc receptor comes of age. *Nat Rev Immunol* **7**, 715–725.

Schindelin J, Arganda-Carreras I, Frise E, Kaynig V, Longair M, Pietzsch T, Preibisch S, Rueden C, Saalfeld S, Schmid B, Tinevez JY, White DJ, Hartenstein V, Eliceiri K, Tomancak P & Cardona A (2012). Fiji: an open-source platform for biological-image analysis. *Nat Methods* **9**, 676–682.

Schindelin J, Rueden CT, Hiner MC & Eliceiri KW (2015). The ImageJ ecosystem: An open platform for biomedical image analysis. *Mol Reproduction* Dev **82**, 518–529.

Schlachetzki F, Zhu C & Pardridge WM (2002). Expression of the neonatal Fc receptor (FcRn) at the blood-brain barrier. *J Neurochem* **81**, 203–206.

Schneider CA, Rasband WS & Eliceiri KW (2012). NIH Image to ImageJ: 25 years of image analysis. *Nat Methods* **9**, 2089.

Schrieber L & Penny R (1982). Tissue distribution of IgG Fc receptors. *Clin Exp Immunol* **47**, 535–540 (1982)

Shah U, Dickinson BL, Blumberg RS, Simister NE, Lencer WI & Walker WA (2003). Distribution of the IgG Fc receptor, FcRn, in the human fetal intestine. *Pediatr Res* **53**, 295–301.

Sheng WS, Lokensgard JR, Prasad S, Chauhan P & Hu S (2017). Modulation of Microglial Cell Fcγ Receptor Expression Following Viral Brain Infection. *Sci Reports* **7**, 41889.

Shrestha B, Paul D & Patcher JS (2014). Alterations in tight junction protein and IgG permeability accompany leukocyte extravasation across the choroid plexus during neuroinflammation. *J Neuropathol Exp Neurol* **3**, 1047-1061

Siegelman J, Fleit HB & Peress NS (1987). Characterization of immunoglobulin G-Fe receptor activity in the outflow system of the cerebrospinal fluid. *Cell Tissue Res* **248**, 599–605.

Simister NE & Mostov KE (1989). An Fc receptor structurally related to MHC class I antigens. *Nature* **337**, 184–187.

Simister NE, Story CM, Chen HL & Hunt JS (1996). An IgG-transporting Fc receptor expressed in the syncytiotrophoblast of human placenta. *Eur J Immunol* **26**, 1527–1531.

Simpson IA, Vannucci SJ, DeJoseph MR & Hawkins RA (2001). Glucose Transporter Asymmetries in the Bovine Blood-Brain Barrier. *J Biol Chem* **276**, 12725–12729.

Sofroniew MV & Vinters HV (2010). Astrocytes: Biology and pathology. *Acta Neuropathol* **119**, 7–35.

Spiegelberg HL & Fishkin BG (1972). The catabolism of human G immunoglobulins of different heavy chain subclasses. *Clin Exp Immunol* **10**, 599–607.

Spiekermann GM *et al* (2002). Receptor-mediated Immunoglobulin G Transport Across Mucosal Barriers in Adult Life: Functional Expression of FcRn in the Mammalian Lung. *J Exp Med* **196**, 303–310.

Stamou M, Grodzki AC, van Oostrum M, Wollscheid B & Lein PJ (2018). Fc gamma receptors are expressed in the developing rat brain and activate downstream signaling molecules upon cross-linking with immune complex. *J Neuroinflammation* **15**, 7.

St-Amour I, Paré I, Alata W, Coulombe K, Ringuette-Goulet C, Drouin-Ouellet J, Vandal M, Soulet D, Bazin R & Calon F. (2013). Brain bioavailability of human intravenous immunoglobulin and its transport through the murine blood-brain barrier. *J Cereb Blood Flow Metab* **33**, 1983–1992.

Stanimirovic DB, Kemmerich K, Haqqani AS & Farrington GK (2015). Engineering and pharmacology of blood-brain barrier-permeable bispecific antibodies. *Expert Opin Drug Discov* **10**, 141-155.

Stapleton NM, Armstrong-Fisher SS, Anderson JT, van der Schoot CE, Porter C, Page KR, Falconer D, de Haas M, Williamson LM, Clark MR, Vidarsson G & Armour KL (2018). Human IgG lacking effector functions demonstrate lower FcRn-binding and reduced transplacental transport. *Mol Immunol* **95**, 1–9.

Strazielle N & Ghersi-Egea JF (2013). Physiology of blood-brain interfaces in relation to brain disposition of small compounds and macromolecules. *Mol Pharm* **10**, 1473–1491.

Takai T (2002). Roles of Fc receptors in autoimmunity. *Nat Rev Immunol* **2**, 580–592.

Takizawa T, Anderson CL & Robinson JMA (2005). Novel Fc R-Defined, IgG-Containing Organelle in Placental Endothelium. *J Immunol* **175**, 2331–2339.

Thomsen MS, Birkelund S, Burkhart A, Stensballe A & Moos T (2016). Synthesis and deposition of basement membrane proteins by primary brain capillary endothelial cells in a murine model of the blood-brain barrier. *J Neurochem* **140**, 741–754.

Tian X, Nyerg S, S Sharp P, Madsen J, Daneshpur N, Armes SP, Berwick J, Azzouz M, Shaw P, Abbott NJ & Battaglia G (2015). LRP-1-mediated intracellular antibody delivery to the Central Nervous System. *Sci Rep* **5**, 11990.

Ulvestad E, Williams K, Matre R, Nyland H, Olivier A & Antel J (1994). Reactive microglia in multiple sclerosis lesions have an increased expression of receptors for the Fc part of IgG. *J Neurol Sci* **121**, 125–131.

Van Gog FB, Brakenhoff, RH, Snow GB & Van Dongen GAMS (1997). Rapid elimination of mouse/human chimeric monoclonal antibodies in nude mice. *Cancer Immunol Immunother* **44**, 103–111.

Vanlandewijck M, He L, Mae MA, Andrae J, Ando K, Del Gaudio F, Nahar K, Lebouvier T, Lavina B, Gouveia L, Sun Y Raschperger E, Rasanem M, Zarb Y, Mochizuki N, Keller A, Lendahl U & Betshotlz C (2018). A molecular atlas of cell types and zonation in the brain vasculature *Nature* **554**, 475-480.

Vedeler C, Ulvestad E, Grundt I, Conti G, Nyland H, Matre R, Pleasure D (1994). Fc receptor for IgG (FcR) on rat microglia. *J Neuroimmunol* **49**, 19–24.

Vedeler CA, Matre R, Kristoffersen, EK & Ulvestad, E (1991). IgG Fc receptor heterogeneity in human peripheral nerves. *Acta Neurol Scand* **84**, 177–180.

Vedeler CA, Nilsen R & Matre R (1989). Localization of Fc gamma receptors and complement receptors CR1 on human peripheral nerve fibers by immunoelectron microscopy. *J Neuroimmunol* **23**, 29–33.

Vieira P & Rajewsky K (1998). The half-lives of serum immunoglobulins in adult mice. *Eur J Immunol* **18**, 313-316.

Villaseñor R, Ozmen L, Messaddeq N, Gruninger F, Loetscher H, Keller A, Betsholtz C, Freskgard PO & Collin L (2016). Trafficking of Endogenous Immunoglobulins by Endothelial Cells at the Blood-Brain Barrier. *Sci Reports* **6**, 25658.

Virgintino D *et al* (1997). Glucose transporter GLUT1 in human brain microvessels revealed by ultrastructural immunocytochemistry. *J Submicrosc Cytol Pathol* **29**, 365–370.

Vogel DYS *et al* (2013). Macrophages in inflammatory multiple sclerosis lesions have an intermediate activation status. *J Neuroinflammation* **10**, 1–12.

Vorbrodt AW, Dobrogowska DH, Meeker HC & Carp RI (1999). Immunogold study of regional differences in the distribution of glucose transporter (GLUT-1) in mouse brain associated with physiological and accelerated aging and scrapie infection. *J Neurocytol* **28**, 711–719.

Waldmann TA & Jones EA (2008). The role of cell-surface receptors in the transport and catabolism of immunoglobulins. *Protein Turnover* **9**, 5–18.

Wallace KH & Rees AR (1980). Studies on the immunoglobulin-G Fc-fragment receptor from neonatal rat small intestine. *Biochem J* **188**, 9–16.

Wang Q, Delva L, Weinreb PH PEpinsky RB, Graham D, Veizai E, Cheung AE, Chen W, Nestorov I Rohde E, Caputo R, Kuersters GM, Bohnert & Gan LS (2018). Monoclonal antibody exposure in rat and cynomolgus monkey cerebrospinal fluid following systemic administration. *Fluids Barriers CNS* **15**, 10.

Wang X, Mathieu M & Brezski RJ (2018). IgG Fc engineering to modulate antibody effector functions. *Protein Cell* **9**, 63–73

Ward SE & Ober RJ (2015). Trafficking analyses of FcRn and IgG ligand in the post-Brambell era. *Front Immunol* **6**, 351

Webster CI, Caram-Salas N, Haqqani AS, Thorn G, Brown L, Rennie K, Yogi A, Costain W, Brunette E & Stanimirovic DB (2016). Brain penetration, target engagement, and disposition of the blood-brain barrier-crossing bispecific antibody antagonist of metabotropic glutamate receptor type 1. *FASEB J* **30**, 1927-1940.

Whelan JP, Eriksson U & Lampson LA (1986). Expression of mouse beta 2-microglobulin in frozen and formaldehyde-fixed central nervous tissues: comparison of tissue behind the blood-brain barrier and tissue in a barrier-free region. *J Immunol* **137**, 2561–2566.

Williams EL, Tutt AL, French RR, Chan HT, Lau B, Penfold CA, Mockridge CI, Roghanian A, Cox KL, Verbeek JS, Glennie MJ & Cragg MS (2012). Development and characterisation of monoclonal antibodies specific for the murine inhibitory FcγRIIB (CD32B). *Eur J Immunol* **42**, 2109–2120.

Wolak DJ, Pizzo ME & Thorne RG (2015). Probing the extracellular diffusion of antibodies in brain using *in vivo* integrative optical imaging and *ex vivo* fluorescence imaging. *J Control Release* **197**, 78–86.

Woof JM & Burton DR (2004). Human antibody–Fc receptor interactions illuminated by crystal structures. *Nat Rev Immunol* **4**, 89–99.

Wurster U & Haas J (1994). Passage of intravenous immunoglobulin and interaction with the CNS *J Neurol Neurosurg Psych* **57**, 21–25.

Ye L, Zeng R, Bai Y, Roopenian DC & Zhu X (2011). Efficient mucosal vaccination mediated by the neonatal Fc receptor *Nat Biotechnol* **29**, 158–165.

Yoshimi K, Woo M, Son Y, Baudry M & Thompson RF (2002). IgG-immunostaining in the intact rabbit brain: Variable but significant staining of hippocampal and cerebellar neurons with anti-IgG. *Brain Res* **956**, 53–66.

Yu YJ, Atwal JK, Zhang Y, Tong RK, Wildsmith KR, Tan C, Bien-Ly N, Hersom M, Maloney JA, Meilandt WJ, Bumbaca D, Gadkar K, Hoyte K, Luk W, Lu Y, Ernst JA, Scearce-Levie K, Couch JA, Dennis M S & Watts RJ (2014). Therapeutic bispecific antibodies cross the blood-brain barrier in nonhuman primates. *Sci Transl Med* **6**, 261ra154.

Yu, Y J & Watts RJ (2013). Developing Therapeutic Antibodies for Neurodegenerative Disease. *Neurotherapeutics* **10**, 459–472.

Zeisel A, Hochgerner H, Lonnerberg P, Johnsson A, Memic F, va der Zwan J, Haring M, Braun E, Borm LE, LA Manno G, Codeluppi S, Furlan A, Lee K, Skene N, Harriz KD, Hjerling-Leffler J, Arenas E, Ernfors P, Marklund U & Linnarsson S (2018). Molecular architecture of the mouse nervous system. *Cell* **174**, 999-1014.

Zeisel A, Munoz-Manchando AB, Codeluppi S, Lonnerberg P, La Manno G, Jureus A, Marques S, Munguba H, He L, Betsoltz C, Rolny C, Castelo-Branco G, Hjerling-Leffler J & Linnarsson S (2015). Brain Structure: Cell types in the mouse cortex and hippocampus revealed by single-cell RNA-seq. *Science* **347**, 1138–1142.

Zhang J, Niu N, Li B & McNutt MA (2013). Neuron-derived IgG Protects Neurons from Complement-dependent Cytotoxicity. *J Histochem Cytochem* **61**, 869–879.

Zhang Y & Pardridge WM (2001). Mediated efflux of IgG molecules from brain to blood across the blood-brain barrier. *J Neuroimmunol* **114**, 168–172.

Zhang Y, Chen K, Sloan SA, Bennett ML, Scholze AR, O'Keeffe S, Phatnani HP, Guarnieri P, Caneda C, Ruderisch N, Deng S, Liddelow SA, Zhang C & Daneman R (2014). An RNA-sequencing transcriptome and splicing database of glia, neurons, and vascular cells of the cerebral cortex. *J Neurosci* **34**, 11929–11947.

Zhu X, Meng G, Dickinson BL, Li X, Mizoguchi E, Miao L, Wang Y, Robert C, Wu B, Smith PD, Lencer WI & Blumberg RS (2001). MHC class I-related neonatal Fc receptor for IgG is functionally expressed in monocytes, intestinal macrophages, and dendritic cells. *J Immunol* **166**, 3266–76 (2001)

Zhu X, Meng GY, Dickinson BT, Li X, Mizoguchi E, Miao L, Wang Y, Chapman P, Wu B, Smith PD, Lencer WI & Blumberg RS (2008). A Major Histocompatibility Complex Class I-related Fc Receptor for IgG on Rat Hepatocytes. *J Clin Investig* **95**, 2397–2402.

Table 1. *Ex vivo* FcRn immunolabeling summary

Cell type	Sprague-Dawley rat	C57BL/6 mouse	APP/PS1 mouse
Astrocytes (parenchymal)	M-255/H-4, 1G3	H-4, 1G3*	H-4, 1G3*
Astrocytes (perivascular)	M-255/H-4, 1G3	H-4, 1G3*	H-4, 1G3*
Astrocytes (subventricular)	M-255/H-4, 1G3	H-4, 1G3*	H-4, 1G3*
Choroid plexus epithelial cells	M-255, 1G3	H-4, 1G3*	H-4, 1G3*
Choroid plexus macrophages	M-255, 1G3	H-4, 1G3*	H-4, 1G3*
Dural cells	M-255, 1G3	Not Tested	Not Tested
Endothelial cells	M-255, 1G3		
Ependymal cells	M-255, 1G3	H-4, 1G3*	H-4, 1G3*
Leptomeningeal cells	M-255/H-4, 1G3	H-4, 1G3*	H-4, 1G3*
Perivascular macrophages	M-255/H-4, 1G3	H-4, 1G3*	H-4, 1G3*
Microglia	Absent	-	-
Neurons (cortical)	H-4, 1G3	-	-
Purkinje Cells	M-255, 1G3	-	-

n = 4; M-255 and H-4 are rabbit IgG & mouse IgG1 raised against mouse Fcgrt extracellular N-terminal residues (aa 22-276); 1G3 is mouse IgG1 raised against purified soluble FcRn (Fcgrt-β2m heterodimer, unknown epitope, Raghavan *et al.*, 1994); *similar results with mouse IgG1 immunolabeling, non-mouse anti-FcRn IgG recommended for future studies

Table 2. *Ex vivo* FcγRIIb immunolabeling summary

Cell type	Sprague-Dawley rat	C57BL/6 mouse	APP/PS1 mouse
Astrocytes (parenchymal)	$CD32B_C$	-	-
Astrocytes (perivascular)	$CD32B_C$	-	-
Astrocytes (subventricular)	$CD32B_C$	$CD32B_C$, $CD32B_N$	$CD32B_C$, $CD32B_N$
Choroid plexus epithelial cells	$CD32B_C$	Not Tested	Not Tested
Choroid plexus macrophages	$CD32B_C$, $CD32B_N$	Not Tested	Not Tested
Dural cells	$CD32B_C$, $CD32B_N$	Not Tested	Not Tested
Endothelial cells	-	-	-
Ependymal cells	$CD32B_C$, $CD32B_N$	$CD32B_C$	$CD32B_C$
Leptomeningeal cells	$CD32B_C$, $CD32B_N$	$CD32B_C$	-
Perivascular macrophages	$CD32B_C$, $CD32B_N$	-	$CD32B_C$
Microglia	$CD32B_N$	-	$CD32B_C$
Neurons (cortical)	$CD32B_C$, $CD32B_N$	$CD32B_C$, $CD32B_N$	$CD32B_C$
Purkinje Cells	$CD32B_C$	$CD32B_C$	Not Tested

n = 4; $CD32B_C$ and $CD32B_N$ are rabbit IgG polyclonal antibodies raised against of intracellular C-terminal residues (aa 270-310) and extracellular N-terminal residues (aa 1-212) of Fcgr2b alpha chain: $CD32B_C$ and $CD32B_N$ may label different subpopulation of cells

Table 3. *Fcgrt* mRNA expression reported in murine single-cell transcriptomics studies

Cell type	References
Astrocytes	Zhang *et al.* 2014; Clarke *et al.* 2018; Zeisel *et al.* 2015; Vanlandewijck *et al.*, 2018
Choroid plexus epithelial cells	Zeisel *et al.* 2015; Zeisel *et al.* 2018; Li & Balthasar, 2018
Endothelial cells	Zhang *et al.* 2014; Zeisel *et al.* 2015; Vanlandewijck *et al.*, 2018; Zeisel *et al.* 2018
Ependymal cells	Zeisel *et al.* 2015
Leptomeningeal cells	Vanlandewijck *et al.*, 2018; Zeisel *et al.* 2018; Marques *et al.*, 2016
Macrophages	Zhang *et al.* 2014; Zeisel *et al.* 2018
Microglia	Zhang *et al.* 2014; Zeisel *et al.* 2015; Vanlandewijck *et al.*, 2018; Li & Balthasar, 2018
Neurons	Zeisel *et al.* 2018
Oligodendrocytes	Zhang *et al.* 2014; Zeisel *et al.* 2015; Marques *et al.*, 2016
Pericytes / Smooth muscle cells	Zeisel *et al.* 2015; Vanlandewijck *et al.*, 2018; Zeisel *et al.* 2018

Table 4. *Fcgr2b* mRNA expression reported in murine single-cell transcriptomics studies

Cell type	References
Astrocytes	Clarke *et al.* 2018; Zeisel *et al.* 2015
Choroid plexus epithelial cells	Li & Balthasar, 2018
Endothelial cells	Vanlandewijck *et al.*, 2018
Leptomeningeal cells	Zhang *et al.* 2014; Zeisel *et al.* 2018
Macrophages	Zhang *et al.* 2014; Zeisel *et al.* 2015; Vanlandewijck *et al.*, 2018; Li & Balthasar, 2018
Microglia	Zhang *et al.* 2014; Zeisel *et al.* 2015; Vanlandewijck *et al.*, 2018; Li & Balthasar, 2018
Neurons	Zeisel *et al.* 2015
Oligodendrocytes	Zhang *et al.* 2014; Zeisel *et al.* 2015; Marques *et al.*, 2016
Pericytes / Smooth muscle cells	Zeisel *et al.* 2015

Table 5. List of primary antibodies used in this study

Antibody (alias, target species, clonality)	Vendor	Catalog #	Dilution
Rabbit anti-CD32B (CD32B$_C$, 270-310 aa, r/m, pc)	Bioss	bs-6031R	1:250, 1:500
Rabbit anti-CD32B (CD32B$_N$, 1-212 aa, r, pc)	Sino Biological	80018-RP02	1 μg/mL
Mouse anti-FcRn (1G3, unknown, r, mc)	Bio-X-Cell	BE0222	1:250, 1:500
Rabbit anti-FcRn (M-255, 22-276 aa, r/m, pc)	Santa Cruz BT	sc-66893	1:10
Mouse anti-FcRn (H-4, 22-276 aa, r/m, mc)	Santa Cruz BT	sc-166413	1:500
Mouse anti-ZO-1 (ZO-1, r/m, mc)	Invitrogen	ZO1-1A12	1:200
Mouse anti-RECA-1 (RECA-1, r, mc)	Abcam	ab9774	1:500
Mouse anti-aquaporin-4 (AQP4, r/m, mc)	Abcam	ab9512	1:100
Rabbit anti-NeuN or Fox3 (NeuN, r/m, mc)	Abcam	ab177487	1:500
Goat anti-PECAM-1 (CD31, r/m, pc)	Novus	AF3628	10 μg/mL
Chicken anti-GFAP (GFAP, r/m, pc)	Novus Biologicals	NBP1-05198	1:1000
Mouse anti-UCHL1 (UCHL-1, r/m, mc)	Novus Biologicals	NB100-1160	1:250
Goat anti-IbA1 (Iba1, r/m, pc)	Novus Biologicals	NB100-1028	1:100
Sheep anti-LYVE-1 (LYVE-1, r, pc)	R&D Systems	AF7939	1:1000
Mouse anti-Podoplanin (Podoplanin, r, mc)	AngioBio	11-033	1:200
*Mouse anti-αSMA (αSMA, N-terminus r/m, mc)	Millipore-Sigma	C6198	1:500

RECA-1, rat endothelial cell antigen 1; PECAM-1, platelet derived cell adhesion molecule 1; αSMA, alpha smooth muscle actin; GFAP, glial fibrillary acidic protein; NeuN, neuronal nuclei; UCHL-1, ubiquitin C-terminal hydrolase L1; Iba1, ionized calcium binding adapter molecule 1; LYVE-1, lymphatic vessel endothelial hyaluronic acid receptor 1; r, rat; m, mouse; pc, polyclonal; mc, monoclonal; *Cy3® labeled

Table 6. List of secondary antibodies used in this study

Antibody (alias, target species, clonality)	Vendor	Catalog #	Dilution
AF405 goat anti-mouse IgG	Life Technologies	A-31553	1:500
AF546 donkey anti-goat IgG	Life Technologies	A-11056	1:500
AF594 donkey anti-sheep IgG	Life Technologies	A-11016	1:500
AF647 donkey anti-rabbit IgG	Life Technologies	A-31573	1:500
AF594 goat anti-mouse IgG	Abcam	ab150172	1:500
AF647 donkey anti-goat IgG	Abcam	ab150107	1:500
CF488A donkey anti-goat IgG	Biotium	20016	1:500
CF488A donkey anti-mouse IgG	Biotium	20014	1:500
CF488A donkey anti-mouse IgG	Biotium	20014	1:500

AF, Alexa Fluor®; CF, Cyanine-based fluorescence®

Table 7. List of mRNA reference sequences used for RT-qPCR in this study

mRNA	Accession ID
Rat *Fcgrt*	NM_033351.2
Mouse *Fcgrt*	NM_010189.3
Rat *β2m*	NM_012512.2
Mouse *β2m*	NM_009735.3
Rat *Fcgr2b1*	NM_175756.1
Mouse *Fcgr2b1*	NM_001077189.1
Rat *Fcgr2b2*	XM_017598710.1
Mouse *Fcgr2b2*	NM_010187.2
Rat *β*-actin	NM_031144.3

Fcgrt: FcRn large p51 subunit or alpha chain transporter; *β2m*: FcRn beta-2 microglobulin subunit; *Fcgr2b1*: FcγRIIb receptor isoform 1; *Fcgr2b2*: FcγRIIb receptor isoform 2

Table 8. List of primer sequences used for RT-qPCR in this study

Target	Primer Type	Primer Sequence
Rat *Fcgrt*	Forward	GCCAGGAAGGAGAGCGAGTTC
	Reverse	GGAGCCAGAGTTGCCAGGAC
Mouse *Fcgrt*	Forward	GTCAAACGTGGAGATGAGCACCATT
	Reverse	ACCACCAGCAATAAACCAAGAACGA
Rat *β2m*	Forward	ACGATGGCTCGCTCGGTGA
	Reverse	TCCGGTGGATGGCGAGAGTA
Mouse *β2m*	Forward	CACTGACCGGCCTGTATGCT
	Reverse	GAGGCGGGTGGAACTGTGTT
Rat *Fcgr2b1*	Forward	ATTGTAGCTGCTGTCGCTGGAA
	Reverse	GGCTTCTCCCATTTCCCTGTGA
Mouse *Fcgr2b1*	Forward	GTGGCTGCTGTCACTGGGATT
	Reverse	TCCTCTGGAAGGGTTTCTCCCA
Rat *Fcgr2b2*	Forward	CAGCAGTTCGTTGCCGGT
	Reverse	CCAGAAGGAGTGTCTGGAACCT
Mouse *Fcgr2b2*	Forward	GCAGGTTCCAGACAATCCTCCT
	Reverse	TGTGGTTCTGGTAATCATGCTCTGT

Fcgrt: FcRn large p51 subunit or alpha chain transporter; *β2m*: FcRn beta-2 microglobulin subunit; *Fcgr2b1*: FcγRIIb receptor isoform 1; *Fcgr2b2*: FcγRIIb receptor isoform 2

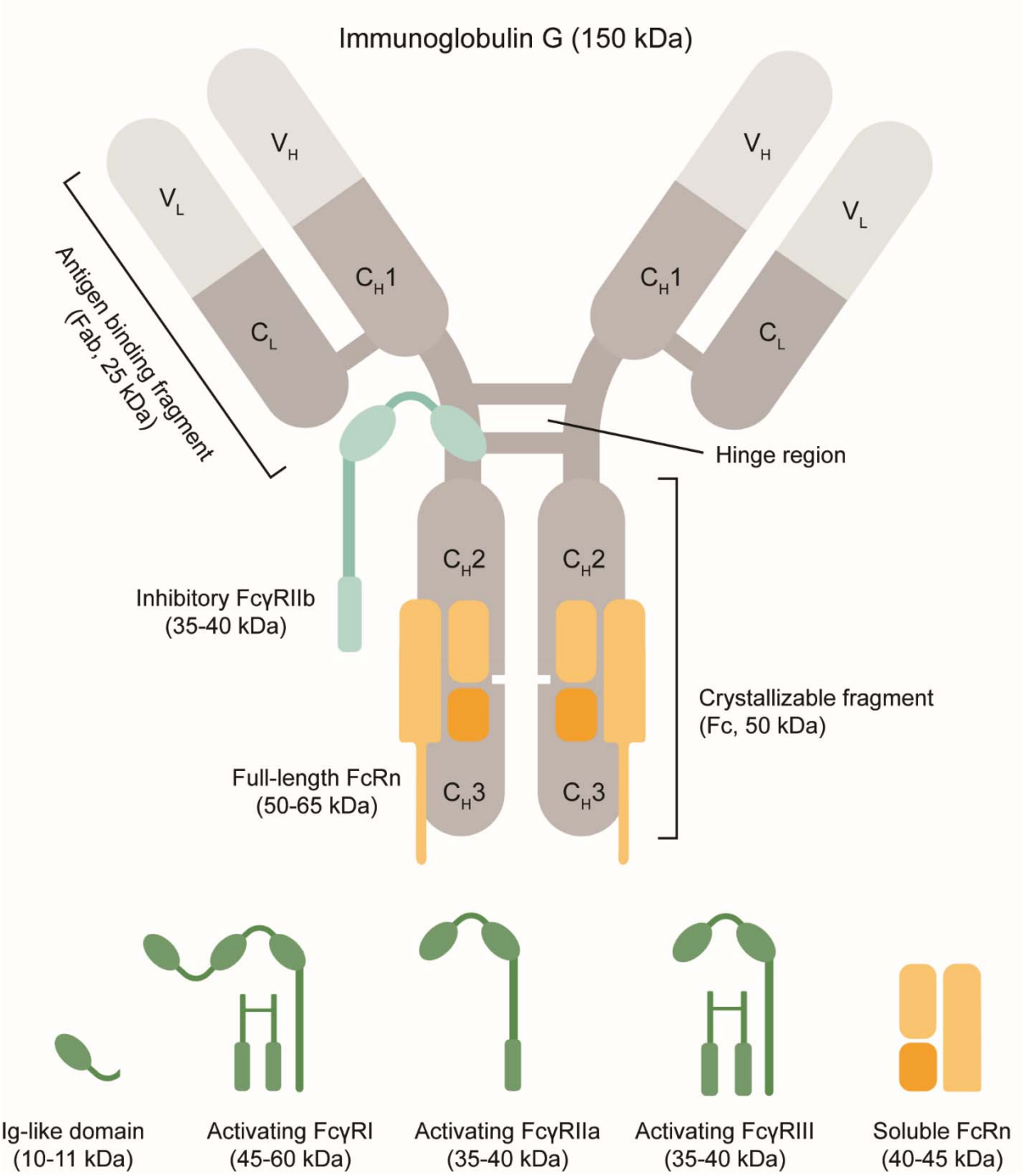

Figure 1. Schematic representation of IgG-Fc receptor interactions (adapted from multiple sources). IgG (~150 kDa) comprises of two antigen-binding fragments (Fab regions, 25 kDa in size) for target engagement and one crystallizable fragment (Fc region, 50 kDa in size) responsible for immune effector

functions. Each fragment consists of a heavy chain (H) and a light chain (C) that can be further classified into domains of ~110 amino acid sequences with variable (V) or constant (C) sequences. This way, IgG consists of V_H, V_L, C_H, and C_L subunits that form the Fab or Fc region. Fc receptors that interact with IgG molecules are smaller transmembrane proteins (roughly one-third the size of an IgG molecule). Neonatal Fc receptor (FcRn) consists of an alpha chain subunit (or p51 subunit) covalently linked to a beta-2 microglobulin subunit. These units interact with each other and collectively bind to one IgG molecule (binding site indicated in the figure). In this manner, two FcRn molecules can bind to one IgG molecule simultaneously at the C_H2-C_H3 domain intersection. Fc gamma receptors (FcγRs), on the other hand, consist of multiple immunoglobulin-like domains (or Ig-like domains) connected to a transmembrane region for signal transduction. Each Ig-like domain is approximately 70-80 amino acids, connected to the next Ig-like domain by a linker chain (~15-20 amino acids). Two or more of these Ig-like domains interact with an IgG molecule between the hinge region and C_H2 domain. Antibodies tested in this study bind to different Fc receptor regions - 1G3 identifies an unknown epitope sequence associated with the soluble FcRn molecule; M-255 and H-4 antibodies bind to the extracellular region of Fcgrt chain in full-length FcRn protein; $CD32B_N$ epitope comprises of two Ig-like domains in the extracellular FcγRIIb region; and $CD32B_C$ epitope resides in the intracellular region, in the vicinity of the phosphorylation site at the ITIM motif (blue rectangle).

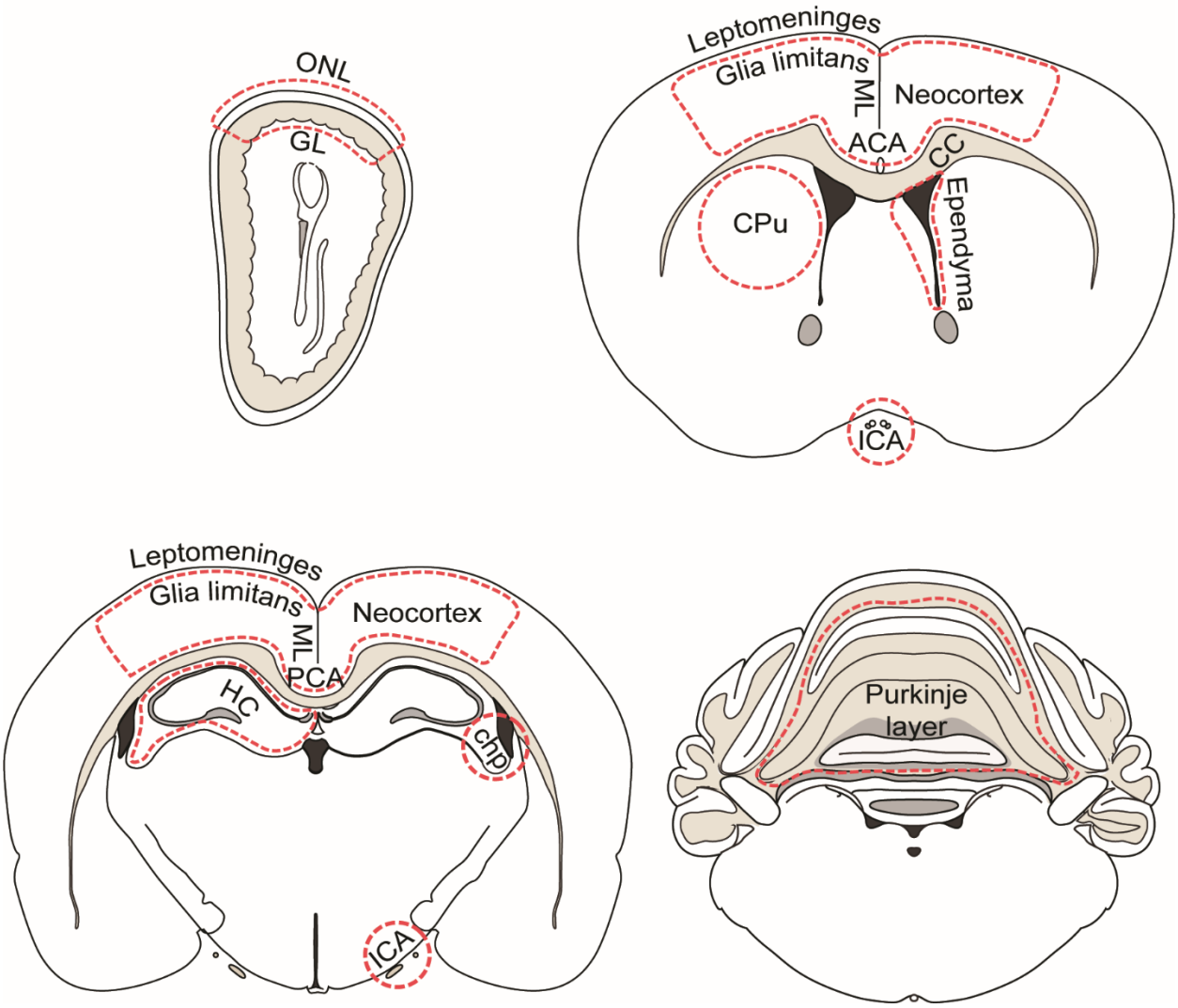

Figure 2. Representative rodent brain sections with approximate regions of interest (red) imaged for Fc receptor immunoreactivity (adapted from Paxinos & Watson, 2007; Franklin & Paxinos, 2008). ACA: Anterior cerebral artery; CC: Corpus callosum; chp: Choroid plexus; CPu: Caudoputamen; GL: Glomerular layer; HC: Hippocampus; ICA: Internal carotid artery; ML: Midline; ONL: Olfactory nerve layer; PCA: Posterior communicating artery

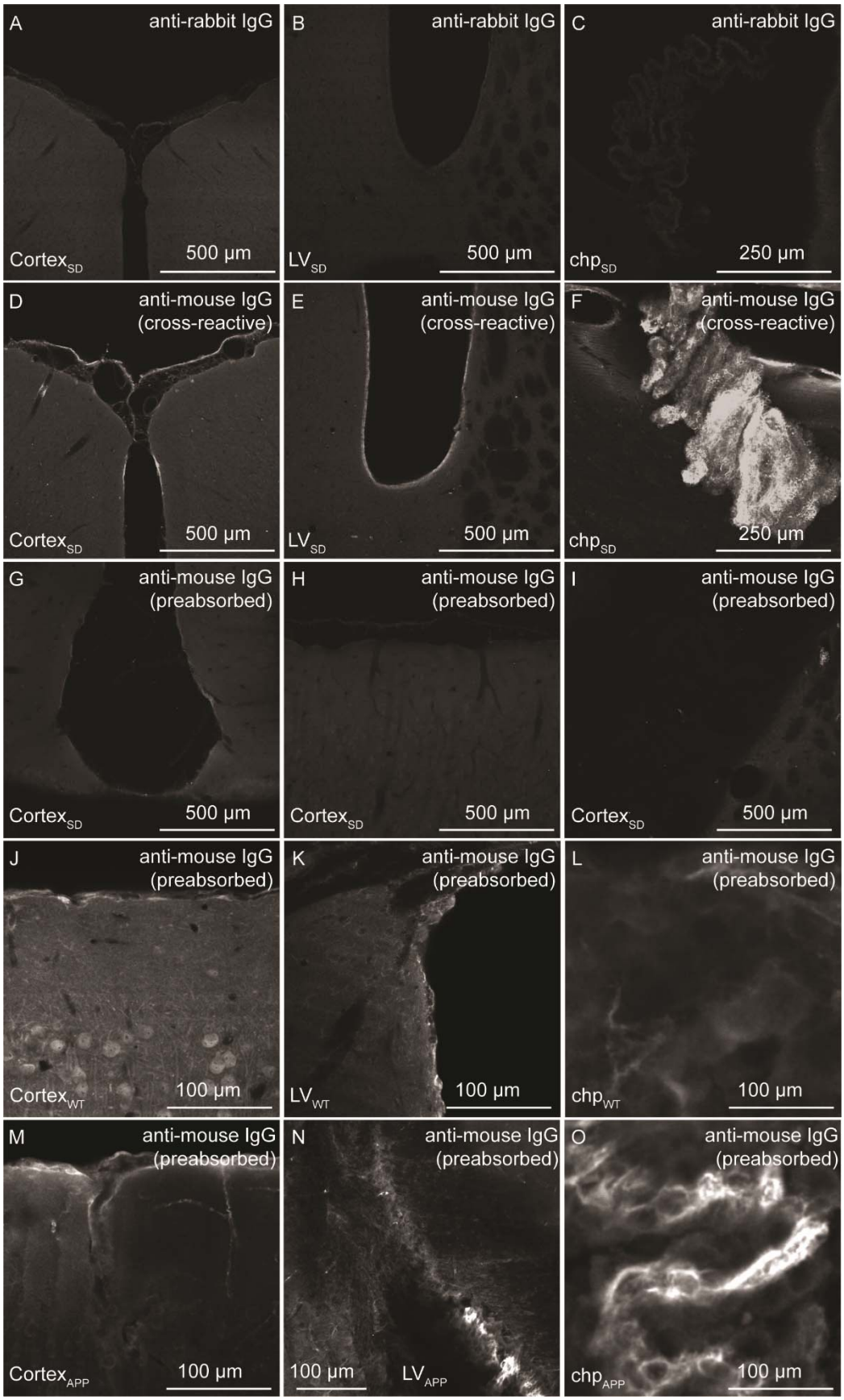
A
anti-rabbit IgG
Cortex$_{SD}$
500 µm
B
anti-rabbit IgG
LV$_{SD}$
500 µm
C
anti-rabbit IgG
chp$_{SD}$
250 µm
D
anti-mouse IgG
(cross-reactive)
Cortex$_{SD}$
500 µm
E
anti-mouse IgG
(cross-reactive)
LV$_{SD}$
500 µm
F
anti-mouse IgG
(cross-reactive)
chp$_{SD}$
250 µm
G
anti-mouse IgG
(preabsorbed)
Cortex$_{SD}$
500 µm
H
anti-mouse IgG
(preabsorbed)
Cortex$_{SD}$
500 µm
I
anti-mouse IgG
(preabsorbed)
Cortex$_{SD}$
500 µm
J
anti-mouse IgG
(preabsorbed)
Cortex$_{WT}$
100 µm
K
anti-mouse IgG
(preabsorbed)
LV$_{WT}$
100 µm
L
anti-mouse IgG
(preabsorbed)
chp$_{WT}$
100 µm
M
anti-mouse IgG
(preabsorbed)
Cortex$_{APP}$
100 µm
N
anti-mouse IgG
(preabsorbed)
100 µm
LV$_{APP}$
O
anti-mouse IgG
(preabsorbed)
chp$_{APP}$
100 µm

Figure 3. **Immunoreactivity of isotype controls at brain-cerebrospinal fluid interfaces.** Minimal surface immunoreactivity was detected with polyclonal rabbit IgG in the rat (A-I) brain sections. Mouse IgG1 immunolabeling was associated with the cortical surface and associated blood vessels (D), ependyma (E), and choroid plexus (F) in the rat brain. These profiles were likely due to anti-mouse IgG secondary antibodies cross-reacting with endogenous rat IgG. These profiles were not detected with preabsorbed anti-mouse IgG secondary antibodies (G-I). Mouse IgG1 immunolabeling using the same preabsorbed antibodies was not sufficient to block endogenous mouse IgG interactions at the cortical surface (J, M), ependymal layer (K, N), and within choroid plexus macrophages (L, O). Endogenous mouse IgG levels were relatively high at these site in APswe/PS1dE9 mouse brain sections (M-O) but not for C57BL6 mice (J-L). SD: Sprague-Dawley rats; WT: C57BL/6N mice; APP: APPswe/PS1dE9 mice.

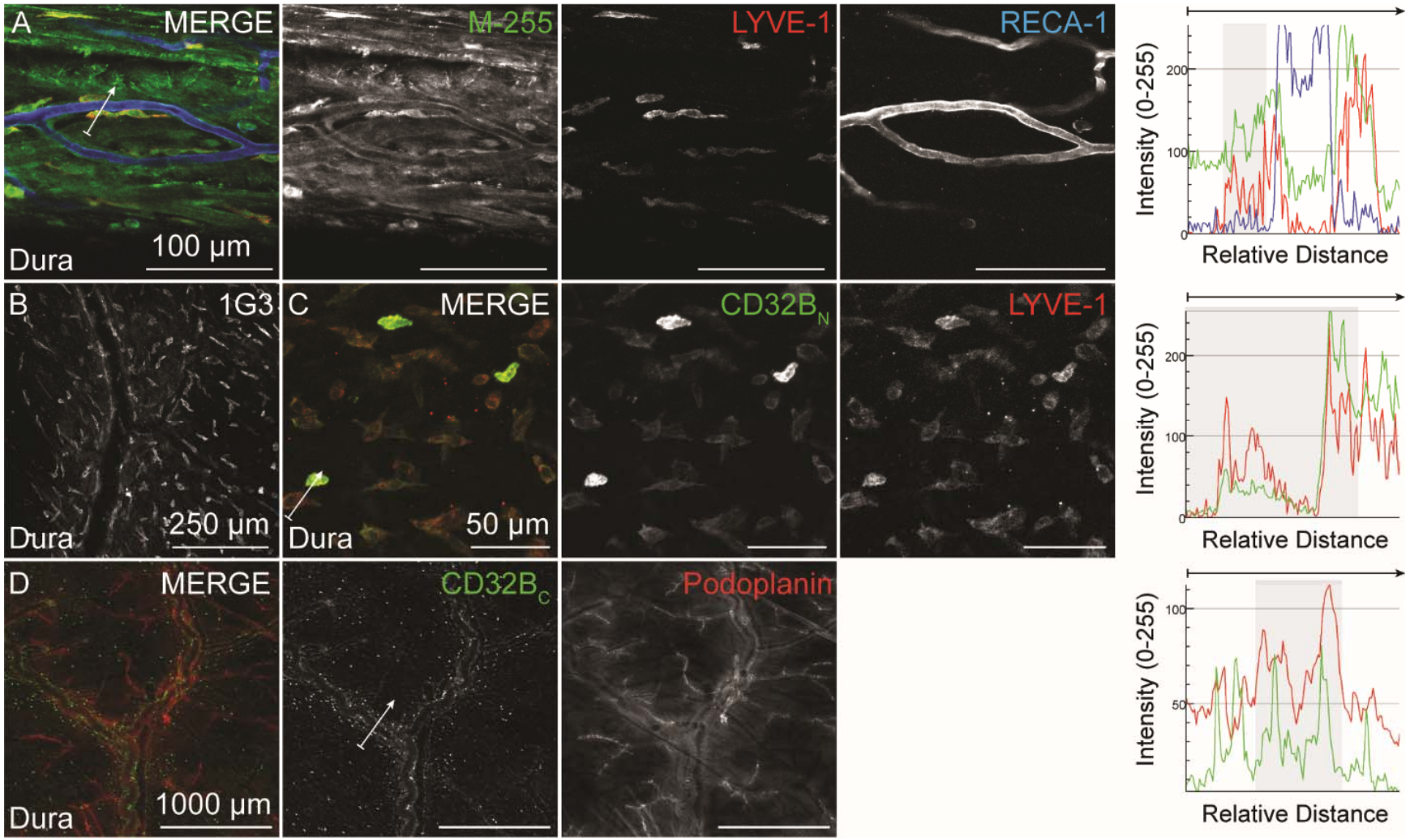

Figure 4. Fc receptor immunoreactivity in the rat dura. M-255. (A), 1G3 (B), $CD32B_N$ (C), and $CD32B_C$ (D) profiles are shown in green. Lymphatic vessel endothelial hyaluronan receptor 1 (LYVE-1, red) and podoplanin (red) are glycoproteins specific to lymphatic vessels and

macrophages. All Fc receptors are present in dural cells based on occasional immunolabeling next to vascular (A) or non-lymphatic (D) endothelial cells detected in the dura. Grey regions in the intensity-vs-position plots highlight instances of perfect/imperfect colocalization and arrows indicate regions selected for colocalization analysis.

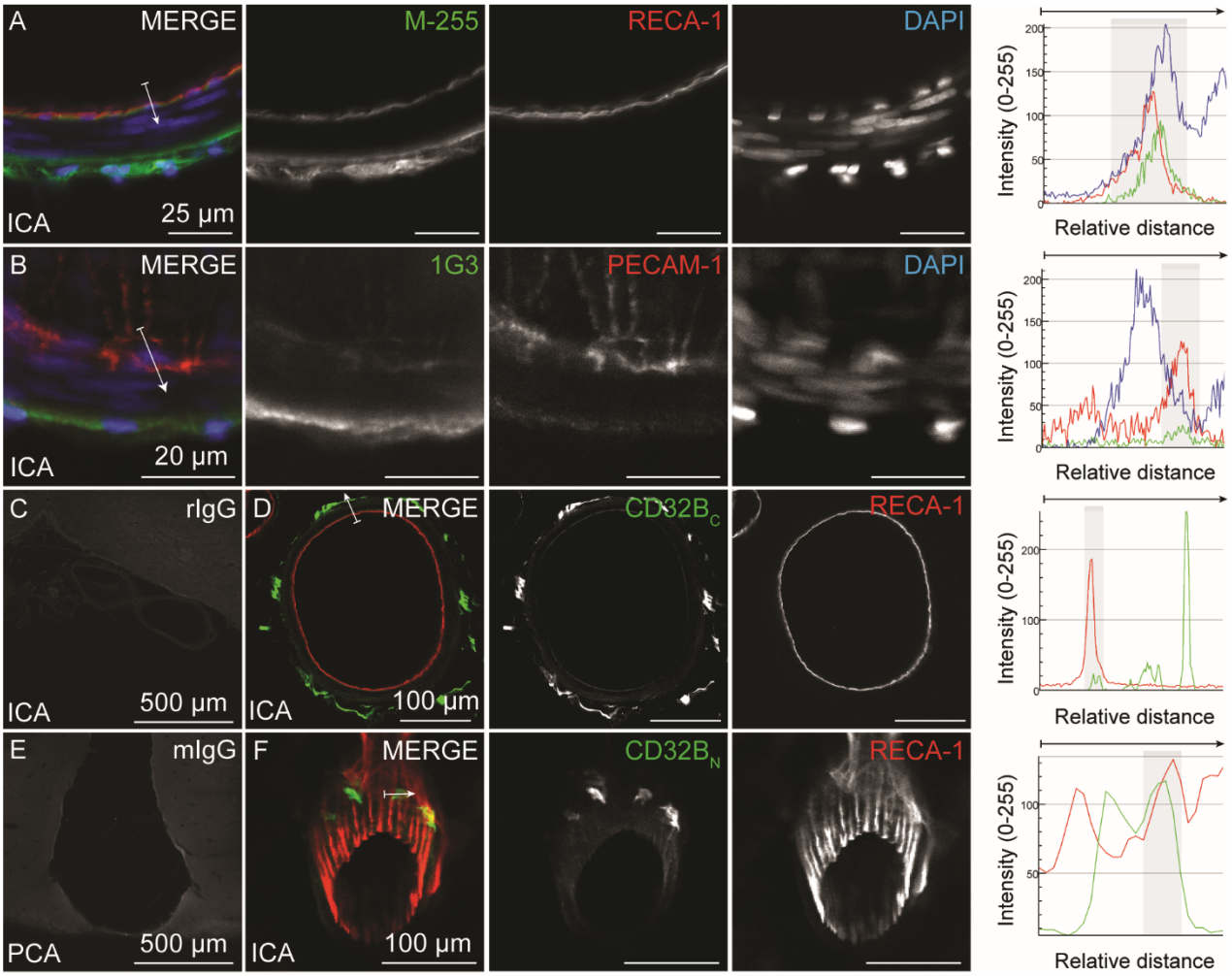

Figure 5. Fc receptor immunoreactivity around leptomeningeal blood vessels in the rat brain. M-255 (A), 1G3 (B), $CD32B_C$ (D), and $CD32B_N$ (F) profiles are shown in green. Rat endothelial cell antigen (RECA-1, red) and platelet-endothelial cell adhesion molecule-1 (PECAM-1, red) are endothelial cell-specific molecule and membrane protein respectively. Minimal immunoreactivity was associated with the abluminal endothelial cell surface with anti-FcRn antibodies (A, B). Non-endothelial leptomeningeal cells (putative macrophages and fibroblasts) surrounding the branches of the internal carotid artery (ICA) were consistently immunopositive for all four antibodies. Note the continuous FcRn immunoreactivity profiles but discreet FcγRIIb immunoreactivity in these cells. Non-specific immunolabeling with non-specific rabbit and mouse IgG1 controls was minimal (C, E). Cell nuclei are labeled with DAPI (blue; A, B). ICA: internal carotid artery; PCA: posterior communicating artery; rIgG: rabbit IgG; mIgG: mouse IgG1. Grey regions

in the intensity-vs-position plots highlight instances of perfect/imperfect colocalization and arrows indicate regions selected for colocalization analysis.

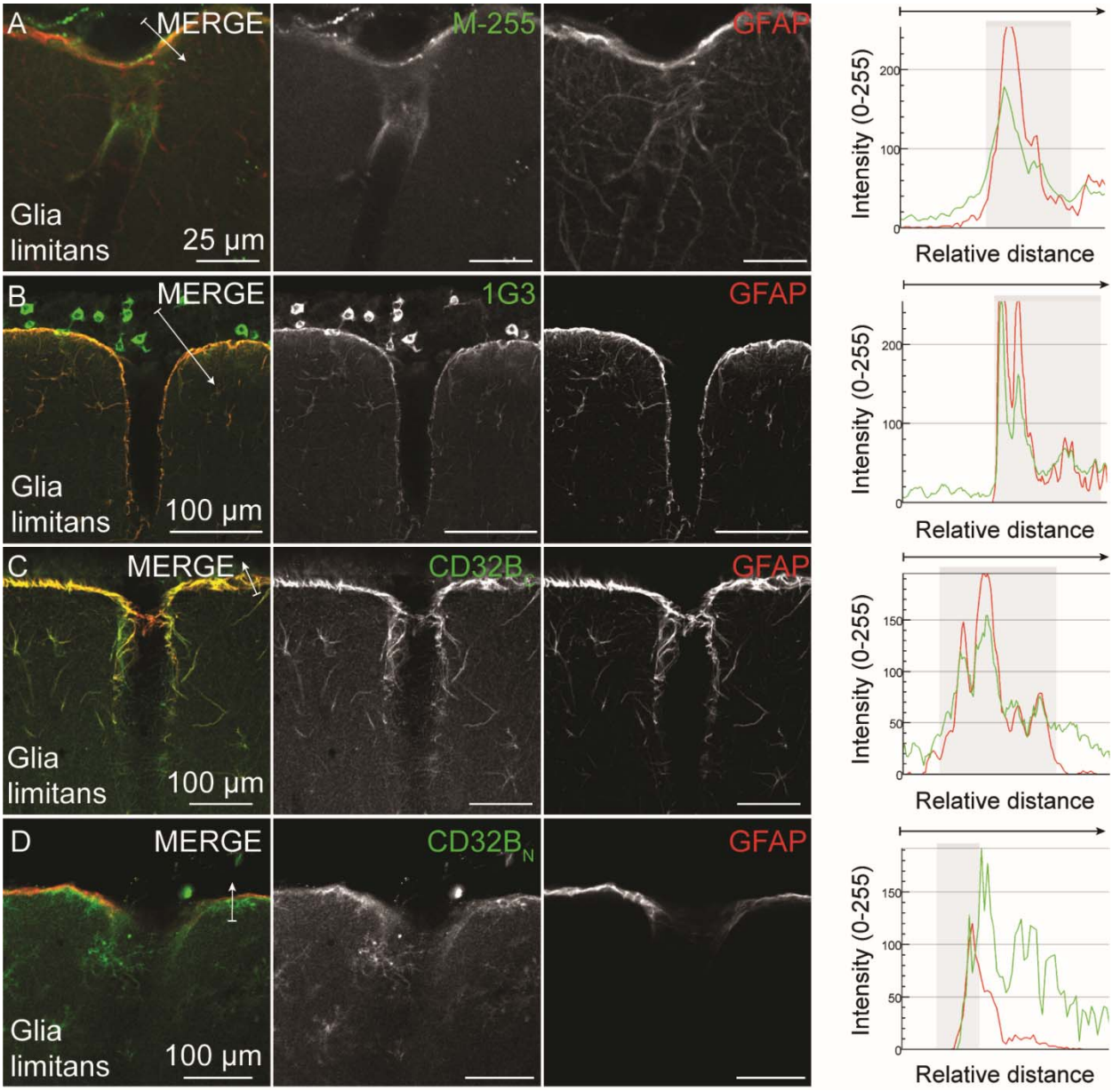

Figure 6. Astrocytic Fc receptor immunoreactivity at the glia limitans in the rat brain. M-255 (A), 1G3 (B), $CD32B_C$ (C), and $CD32B_N$ (D) profiles are shown in green. Glial fibrillary acidic protein (GFAP, red) is an intermediate filament cytoskeletal protein within astrocytic foot processes. Glia limitans were consistently immunoreactive for all anti-FcR antibodies. 1G3 labeled astrocytes and putative meningeal macrophages (B; see Fig. 10B for Iba1/1G3 colocalization). GFAP colocalization was strictly limited with $CD32B_N$ (D), rather GFAP-negative microglia (see arrow) at the cortical surface were immunoreactive for

$CD32B_N$. Grey regions in the intensity-vs-position plots highlight instances of perfect/imperfect colocalization and arrows indicate regions selected for colocalization analysis.

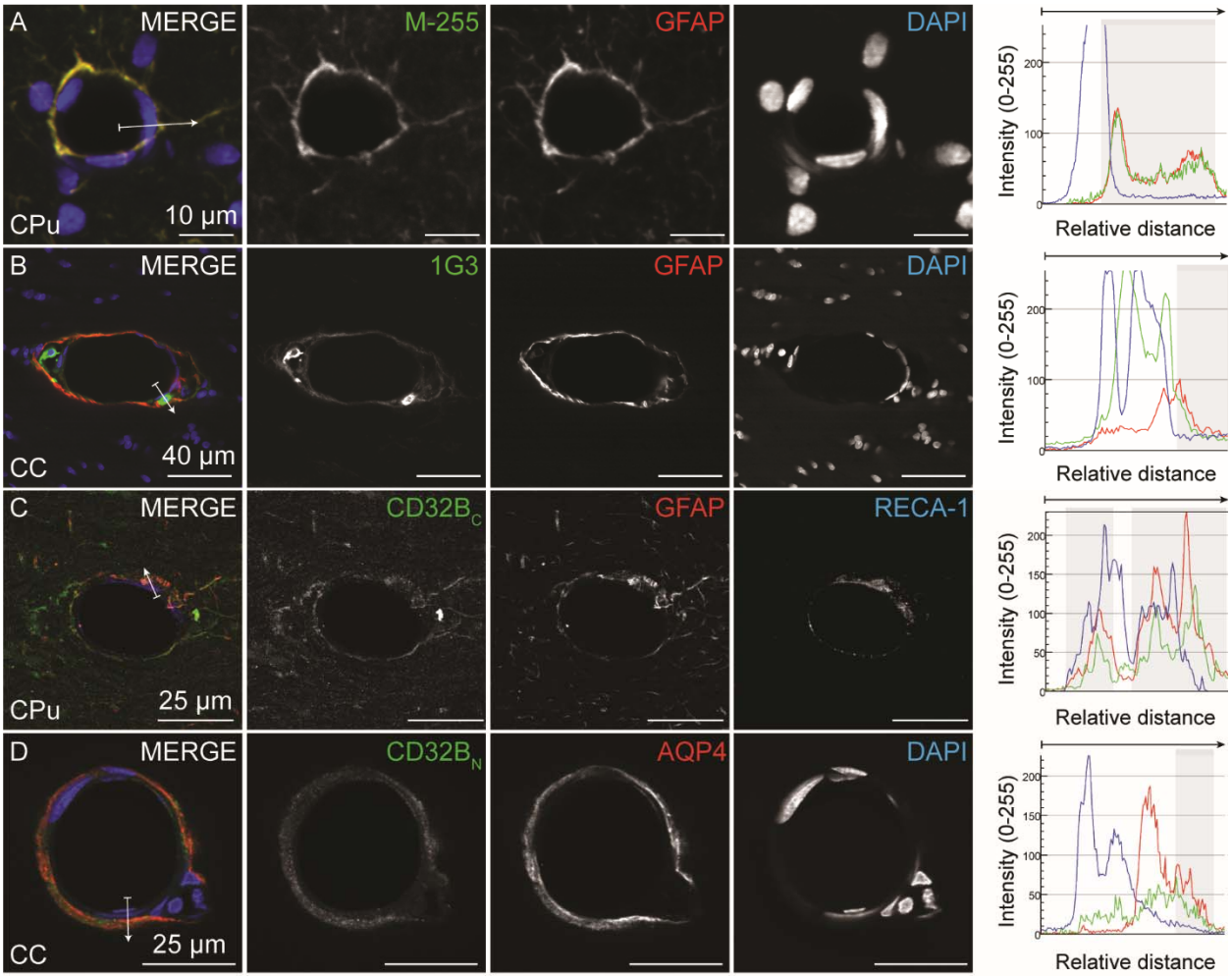

Figure 7. Perivascular Fc receptor immunoreactivity in the rat brain. M-255 (A), 1G3 (B), $CD32B_C$ (C), and $CD32B_N$ (D) profiles are shown in green. Glial fibrillary acidic protein (GFAP, red) is an intermediate filament cytoskeletal protein within astrocytic foot processes; aquaporin-4 (AQP4, red) is a soluble water channel protein highly enriched at the astrocyte endfeet. Perivascular astrocytes were immunopositive for M-255, 1G3, $CD32B_C$ but not $CD32B_N$. Minimal $CD32B_N$ signal was associated with astrocytic foot processes or endfeet labeled with AQP4 (D; red). M-255 and 1G3 positive cells in the perivascular spaces indicated putative macrophages (see Fig. 10B for Iba1/1G3 colocalization within macrophages). $CD32B_C$ immunoreactivity was also consistent with these cells (shown in Fig. 6). Cell nuclei

are labeled with DAPI (blue; A, C, D). CC: Corpus callosum; CPu: Caudoputamen. Grey regions in the intensity-vs-position plots highlight instances of perfect/imperfect colocalization and arrows indicate regions selected for colocalization analysis.

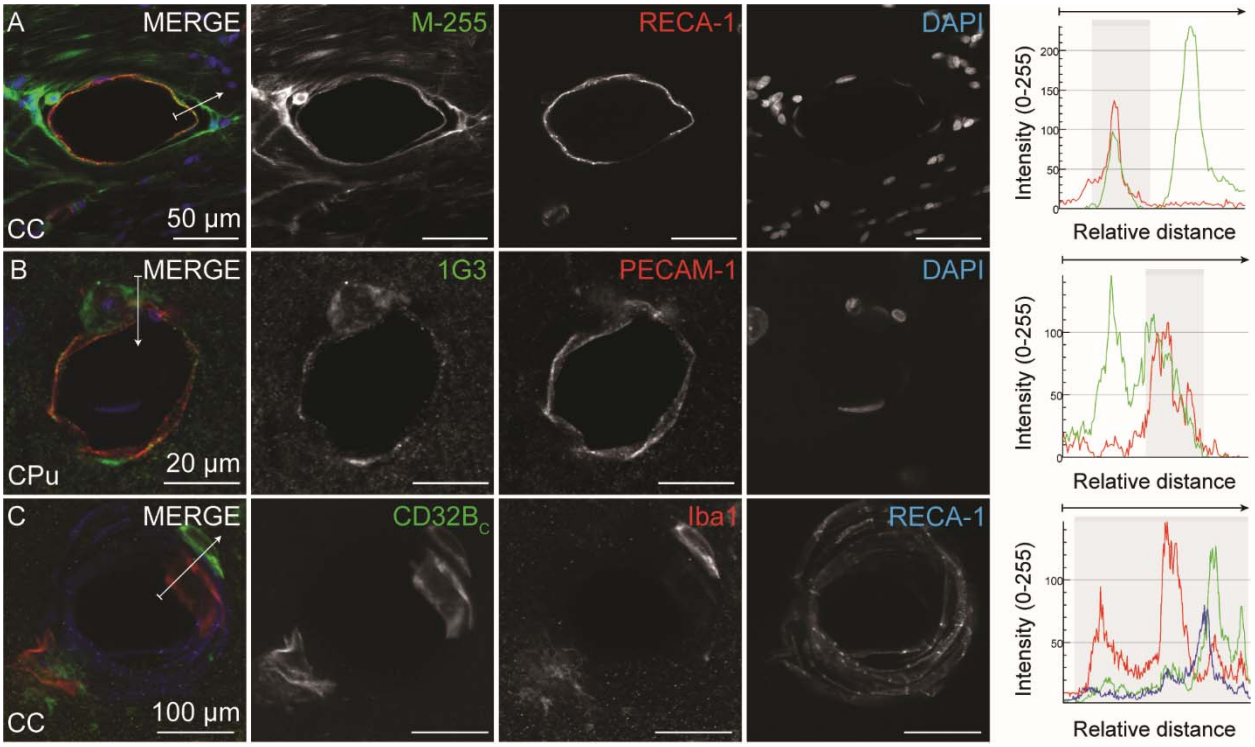

Figure 8. Abluminal Fc receptor immunoreactivity in the rat brain perivascular spaces. M-255 (A), 1G3 (B), and CD32B$_C$ (C) profiles are shown in green. Glial fibrillary acidic protein (GFAP, red) is an intermediate filament cytoskeletal protein within astrocytic foot processes; ionized calcium binding adaptor molecule 1 (Iba1, red) is a phagocytosis-specific cytoskeletal protein present in microglia and macrophages. M-255 and 1G3 immunoreactivity were associated with endothelial cells (A, B), albeit at relatively lower levels compared to astrocytic and/or macrophageal profiles (shown in in Fig.5). CD32B$_C$ immunoreactivity colocalized with putative perivascular macrophages, but not microglia or endothelial cells (C). CD32B$_N$ profiles were rarely visible in perivascular astrocytes or endothelial cells (data not shown). Cell nuclei are labeled with DAPI (blue; A, B). CC: Corpus callosum; CPu: Caudoputamen. Grey regions in the intensity-vs-position plots highlight instances of perfect/imperfect colocalization and arrows indicate regions selected for colocalization analysis.

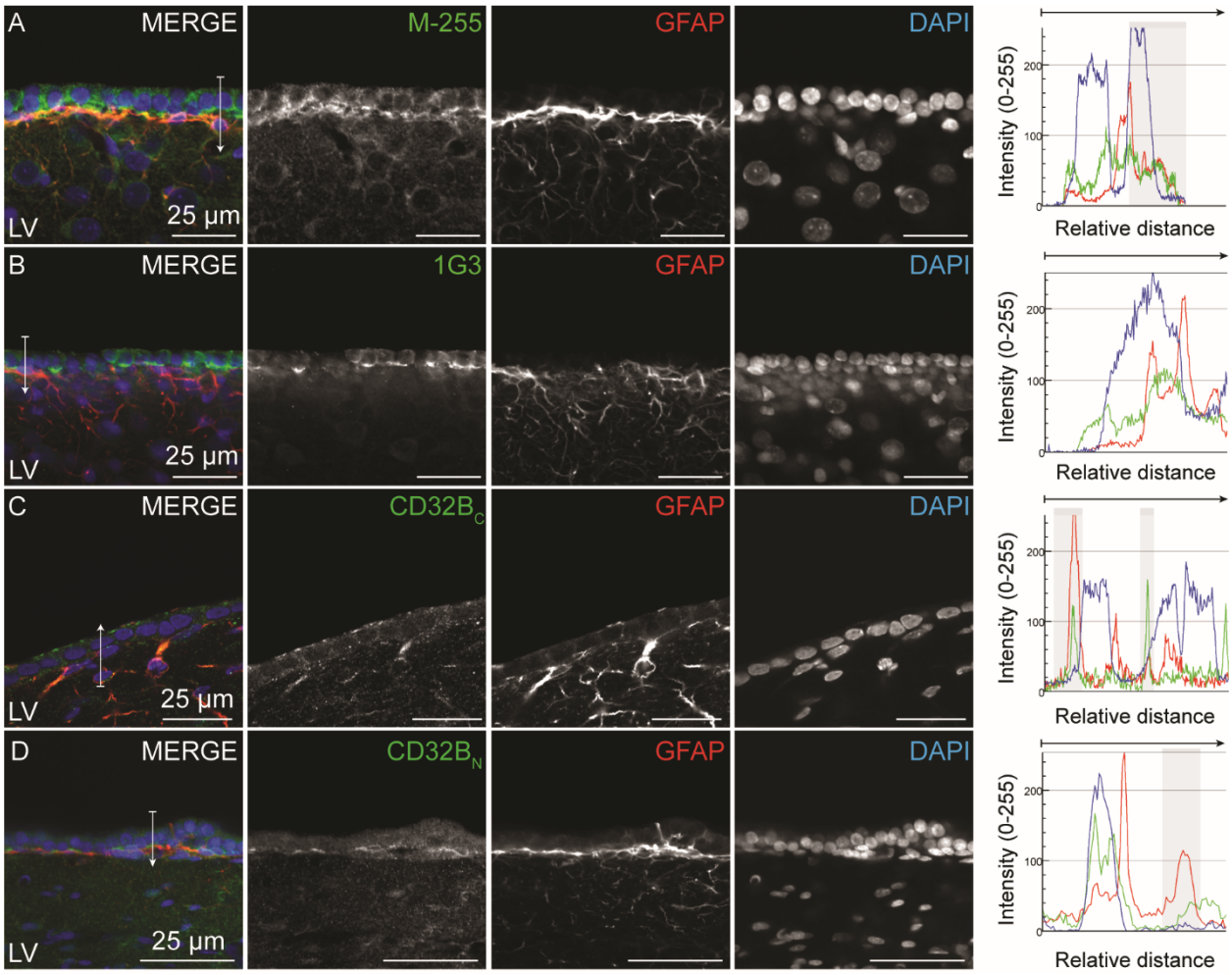

Figure 9. Fc receptor immunoreactivity associated with subventricular astrocytes and ependymal cells in the rat brain. M-255 (A), 1G3 (B), $CD32B_C$ (C), and $CD32B_N$ (D) profiles are shown in green. Glial fibrillary acidic protein (GFAP, red) is an intermediate filament cytoskeletal protein within astrocytic foot processes. Basal surface of ependymal cells was consistently immunoreactive for all anti-FcR antibodies. M-255 and $CD32B_C$ immunolabeling perfectly colocalized with GFAP profiles for subventricular astrocytes; 1G3 signal was relatively low in these cells, $CD32B_N$ immunolabeling was completely absent. Cell nuclei are labeled with DAPI (blue; A-D). LV: Lateral ventricle. Grey regions in the intensity-vs-position plots highlight instances of perfect/imperfect colocalization and arrows indicate regions selected for colocalization analysis.

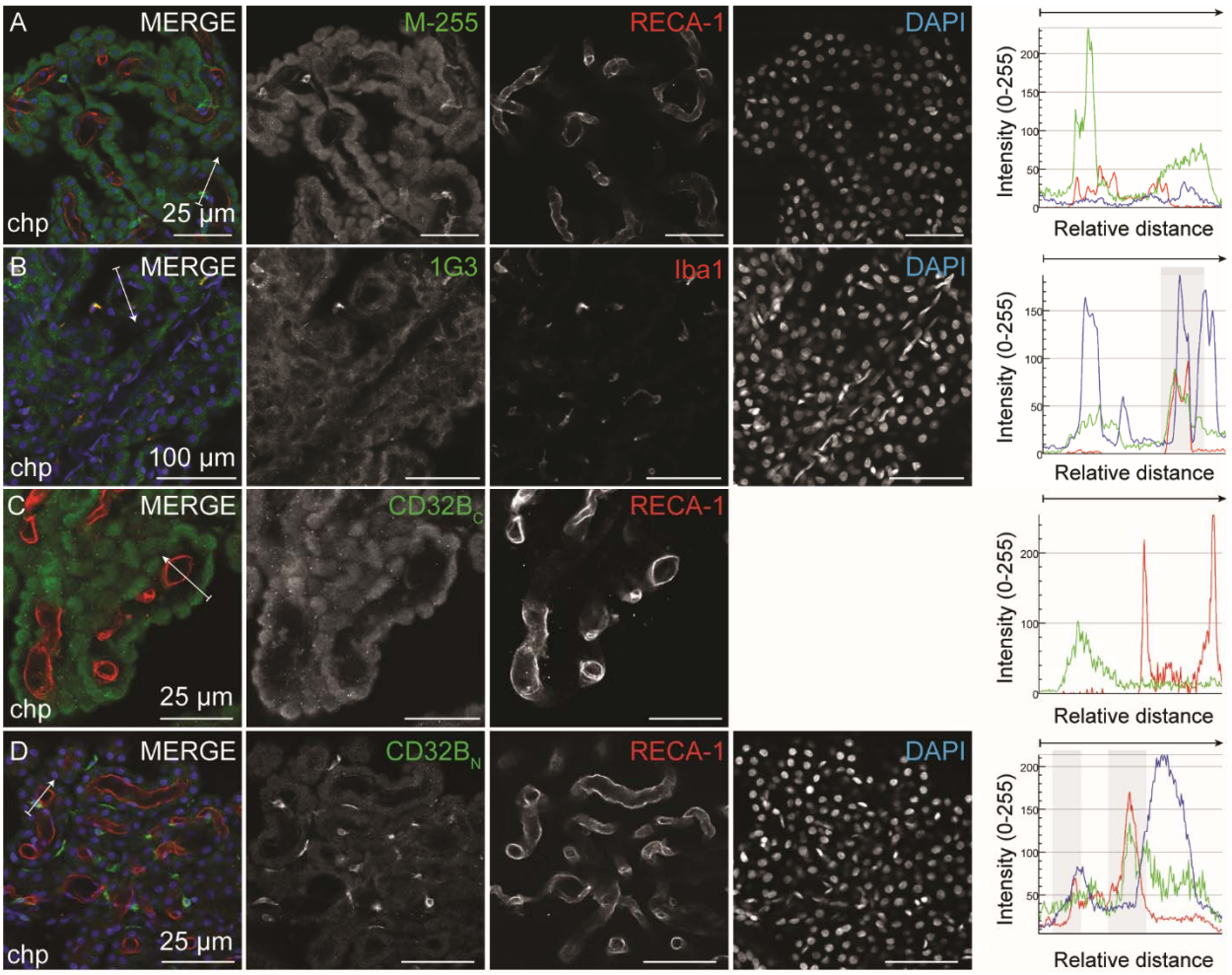

Figure 10. Fc receptor immunoreactivity for epithelial cells and macrophages in the rat chp. M-255 (A), 1G3 (B), $CD32B_C$ (C), and $CD32B_N$ (D) profiles are shown in green. Rat endothelial cell antigen (RECA-1, red) is an endothelial cell surface-specific molecule; ionized calcium binding adaptor molecule 1 (Iba1, red) is a phagocytosis-specific cytoskeletal protein in microglia and macrophages. Epithelial cells were immunoreactive for M-255, 1G3, and $CD32B_C$ but not $CD32B_N$. Putative macrophages in the choroid plexus stroma were consistently immunolabeled by M-255, 1G3, and $CD32B_N$. Iba1 immunostaining was later performed to confirm their cellular origin (B). Macrophages were labeled by $CD32B_C$ in the stroma. Endothelial FcR expression was not detected. Cell nuclei are labeled with DAPI (blue; A, B, D). Grey regions in the intensity-vs-position plots highlight instances of perfect/imperfect colocalization and arrows indicate regions selected for colocalization analysis. chp: Choroid plexus.

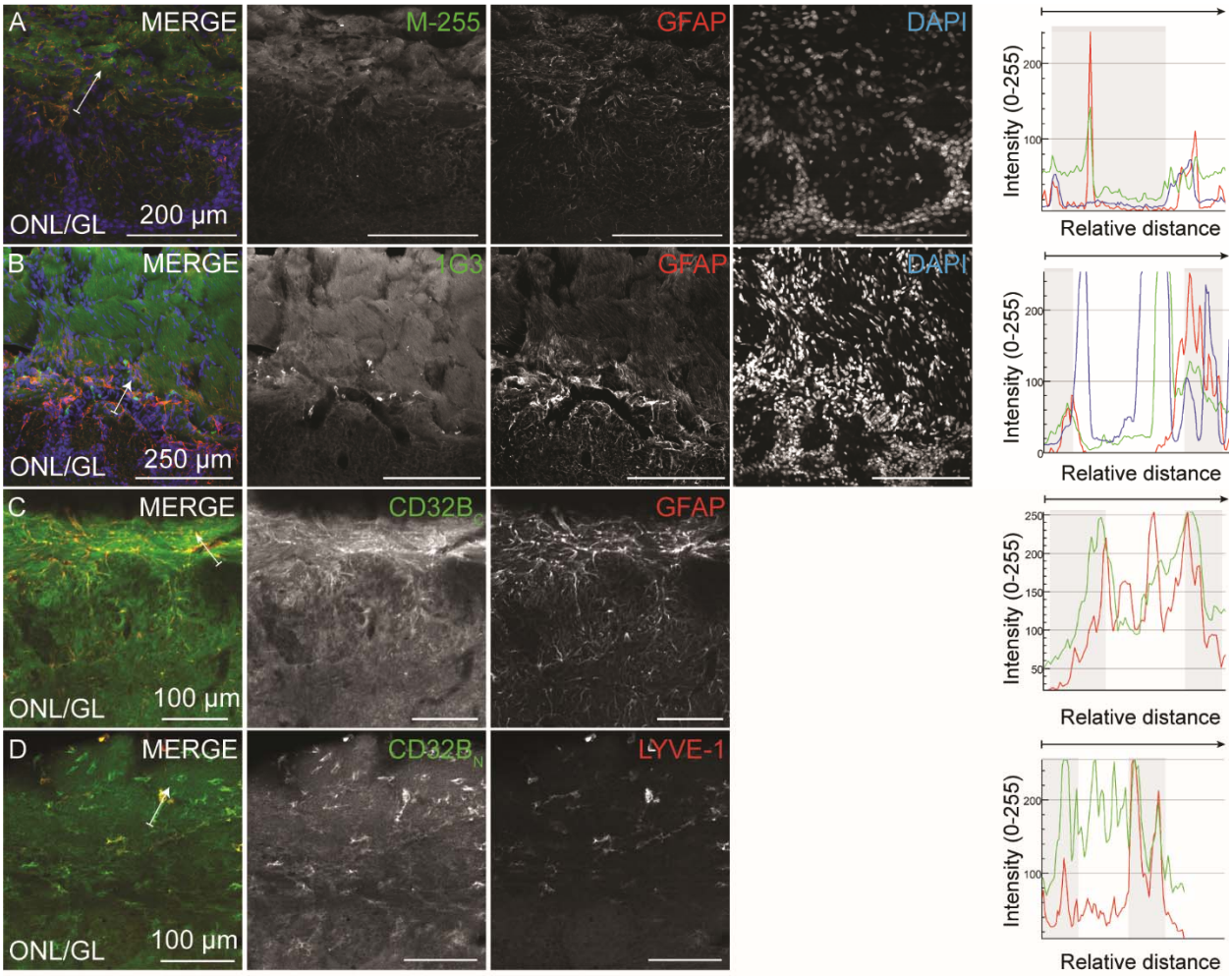

Figure 11. **Fc receptor immunoreactivity at the rat olfactory bulbs.** M-255 (A), 1G3 (B), CD32B$_C$ (C), and CD32B$_N$ (D) profiles are shown in green. Glial fibrillary acidic protein (GFAP, red) is an intermediate filament cytoskeletal protein within astrocytic foot processes; lymphatic endothelial hyaluronan receptor 1 (LYVE-1, red) is a glycoprotein specific to macrophages and myeloid cells. Relatively high immunofluorescence at the olfactory nerve layer was detected for M-255, 1G3, and CD32B$_C$. M-255 (A) and CD32B$_C$ (C) was also associated with astrocytic foot processes above the glomerular layer. 1G3 (B) was associated with putative perivascular macrophages. CD32B$_N$ immunolabeling was localized within LYVE-1-positive macrophages and microglial cells. Cell nuclei are labeled with DAPI (blue; A, B). ONL: Olfactory nerve layer; GL: Glomerular layer. Grey regions in the intensity-vs-position plots highlight

instances of perfect/imperfect colocalization and arrows indicate regions selected for colocalization analysis.

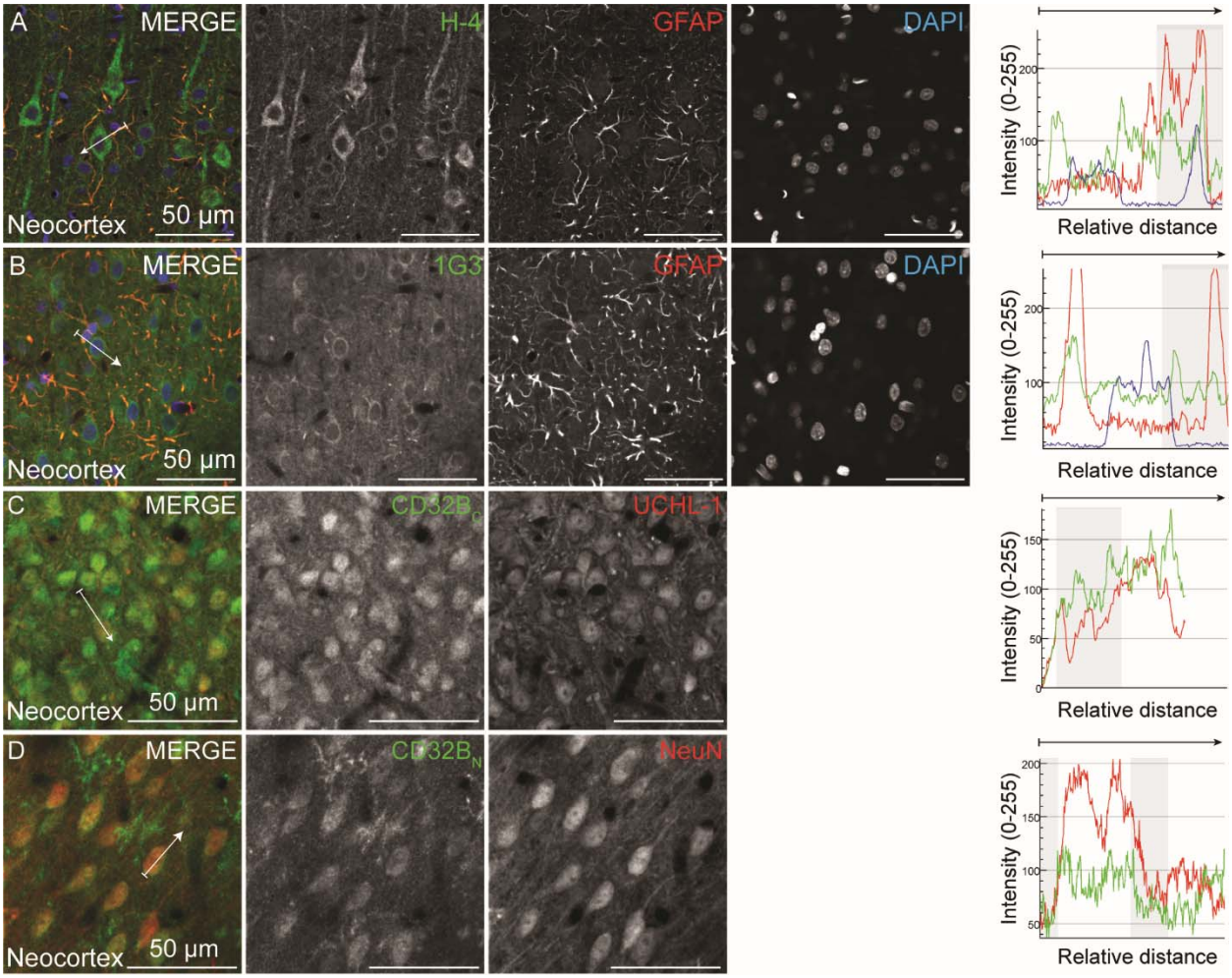

Figure 12. **Fc receptor immunoreactivity in the rat brain parenchyma (neocortex).** H-4 (A), 1G3 (B), $CD32B_C$ (C), and $CD32B_N$ (D) profiles are shown in green. Glial fibrillary acidic protein (GFAP, red) is an intermediate filament cytoskeletal protein within astrocytic foot processes; ubiquitin carboxy-terminal hydrolase L1 (UCHL-1, red) label neuronal cytoplasmic space; neuronal nuclei (NeuN, red) labels forkhead box P3 (FoxP3) proteins specific to neuronal cells (nuclei and cytosol). H-4 immunoreactivity (A) was relatively high for neuronal cells compared to astrocytes at the neocortex; 1G3 profiles (B) were similar across both cell types (GFAP, red). $CD32B_C$ (C) and $CD32B_N$ (D) immunoreactivities were associated with neurons based on colocalization with neuronal markers (UCHL1, NeuN). Cell nuclei are labeled with DAPI (blue; A, B) or NeuN (red; C, D). Grey regions in the intensity-vs-position plots highlight instances of perfect/imperfect colocalization and arrows indicate regions selected for colocalization analysis.

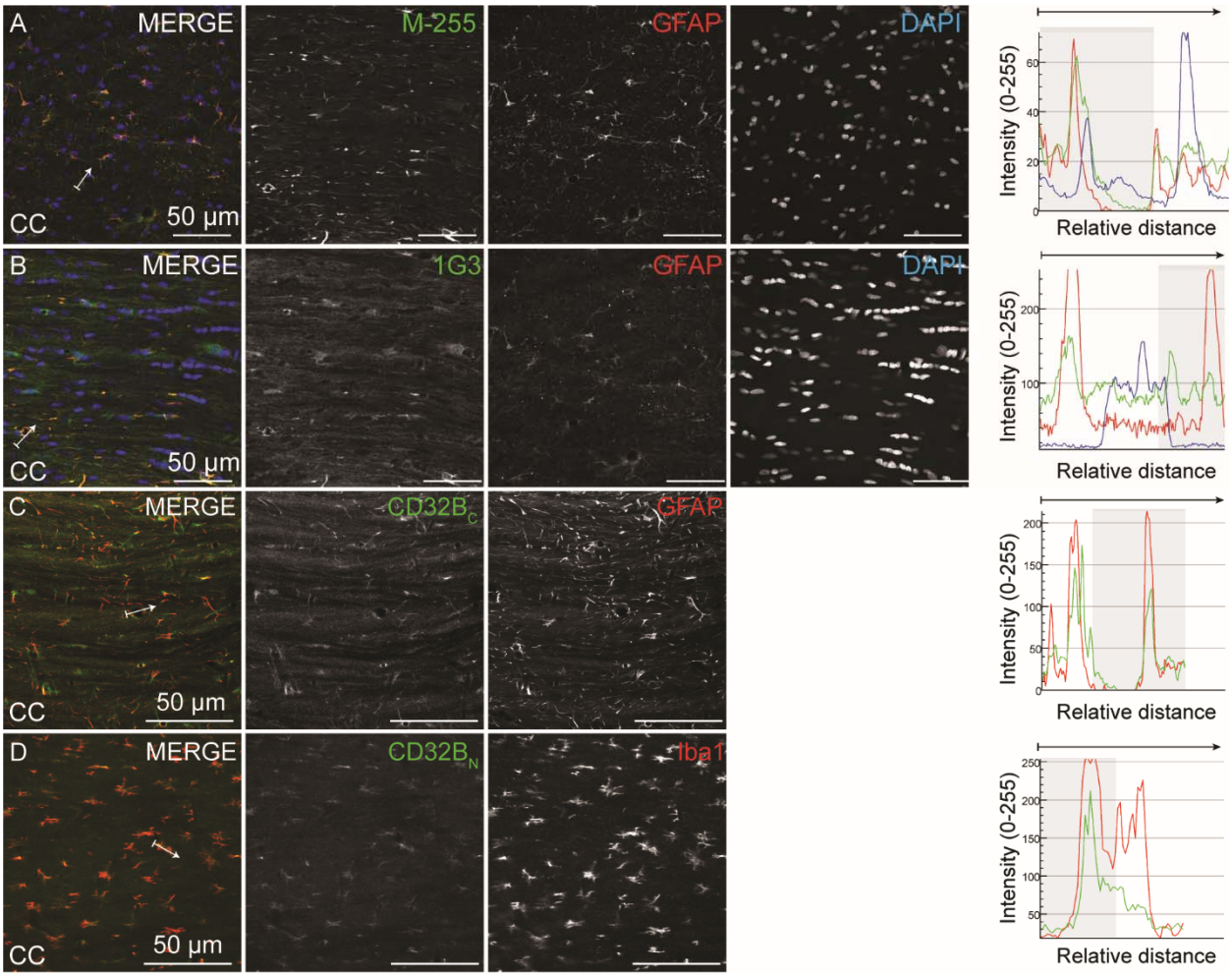

Figure 13. **Fc receptor immunoreactivity in the rat brain parenchyma (white matter tracts).** Fc receptors are labeled in green. M-255 (A), 1G3 (B), $CD32B_C$ (C), and $CD32B_N$ (D) profiles are shown in green. Glial fibrillary acidic protein (GFAP, red) is an intermediate filament cytoskeletal protein within astrocytic foot processes; ionized calcium binding adaptor molecule 1 (Iba1, red) is a phagocytosis-specific cytoskeletal protein in microglia and macrophages. M-255 and $CD32B_C$ were specifically associated with GFAP-positive astrocytes (C). 1G3 (C) detected other cells in addition to astrocytes. $CD32B_N$ (D) immunoreactivity was associated with Iba1-positive microglial cells. Cell nuclei are labeled with DAPI (blue; A, B). Grey regions in the intensity-vs-position plots highlight instances of perfect/imperfect colocalization and arrows indicate regions selected for colocalization analysis.

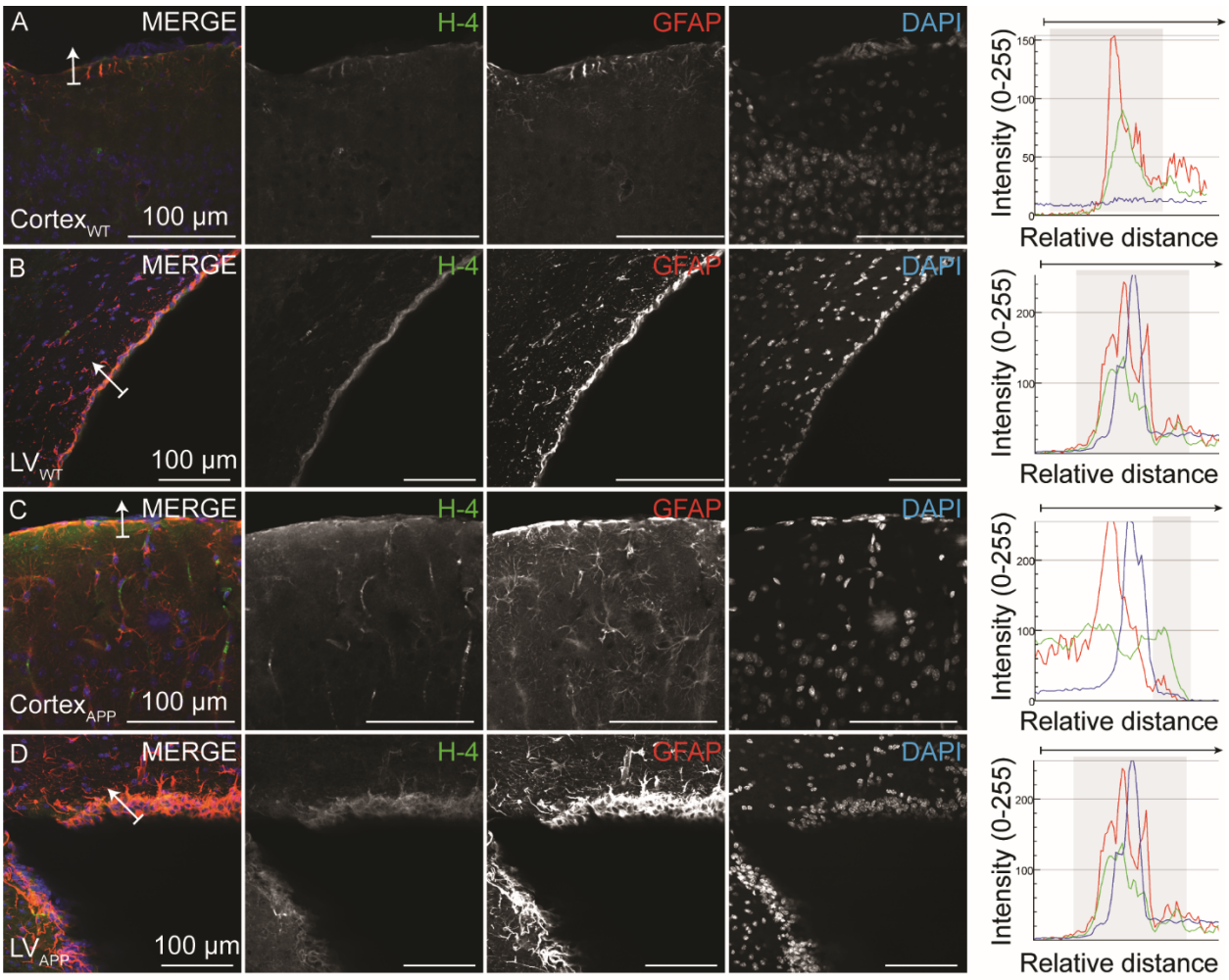

Figure 14. **FcRn immunoreactivity at the mouse brain-cerebrospinal fluid interfaces using H-4 (mouse IgG1 alias of M-255).** Glial fibrillary acidic protein (GFAP, red) is an intermediate filament cytoskeletal protein within astrocytic foot processes. H-4 immunoreactivity profiles were associated with astrocytes but similar profiles were also observed with mIgG1 isotype controls (Fig. 3). Cell nuclei are labeled with DAPI (blue; A-D). WT: C57BL/6N mice; APP: APPswe/PS1dE9 mice. Grey regions in the intensity-vs-position plots highlight instances of perfect/imperfect colocalization and arrows indicate regions selected for colocalization analysis.

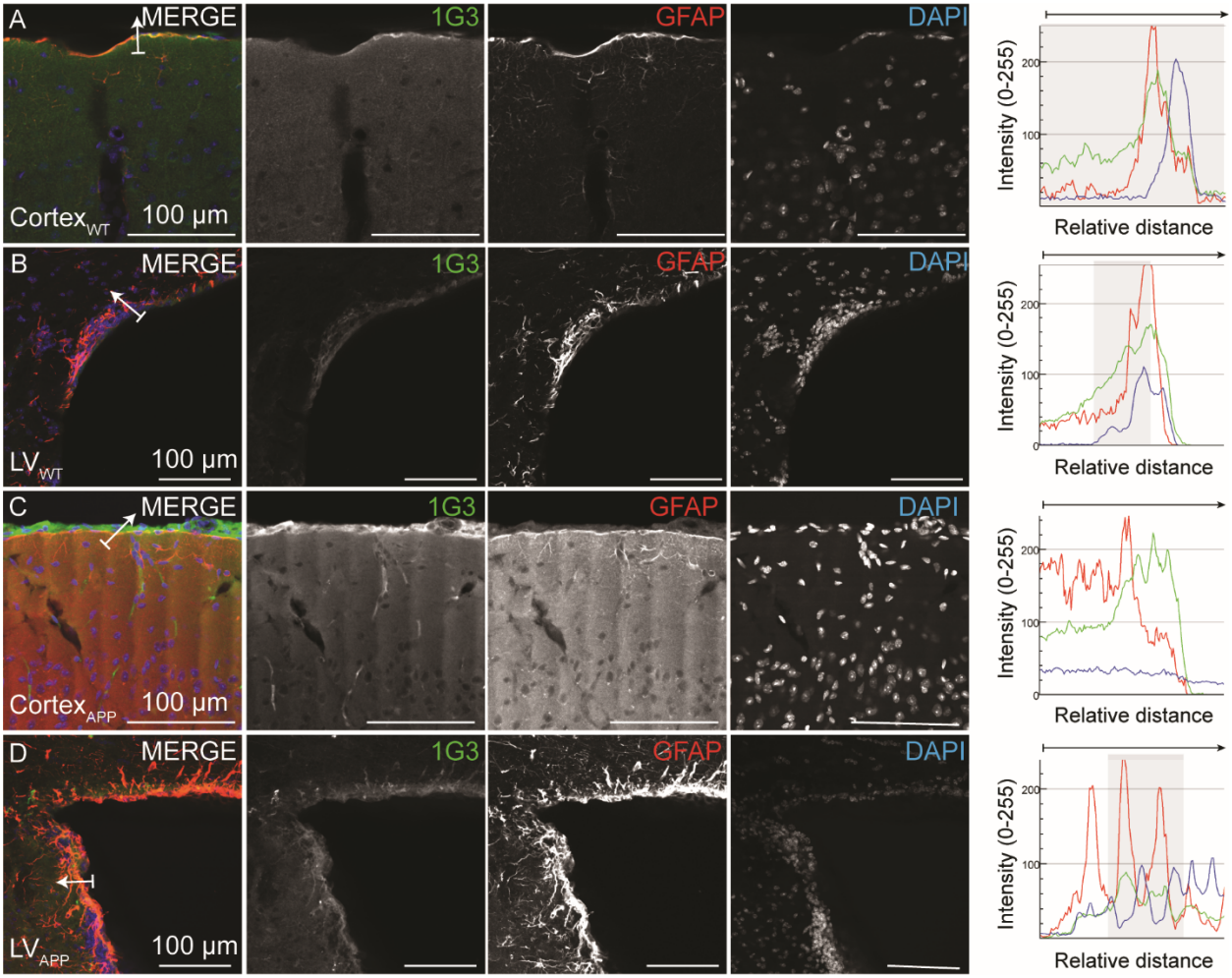

Figure 15. **FcRn immunoreactivity at the mouse brain-cerebrospinal fluid interfaces using 1G3.** Glial fibrillary acidic protein (GFAP, red) is an intermediate filament cytoskeletal protein within astrocytic foot processes; 1G3 immunoreactivity profiles were similar to mIgG1 isotype control (Fig. 3). Cell nuclei are labeled with DAPI (blue; A-D). WT: C57BL/6N mice; APP: APPswe/PS1dE9 mice. Grey regions in the intensity-vs-position plots highlight instances of perfect/imperfect colocalization and arrows indicate regions selected for colocalization analysis.

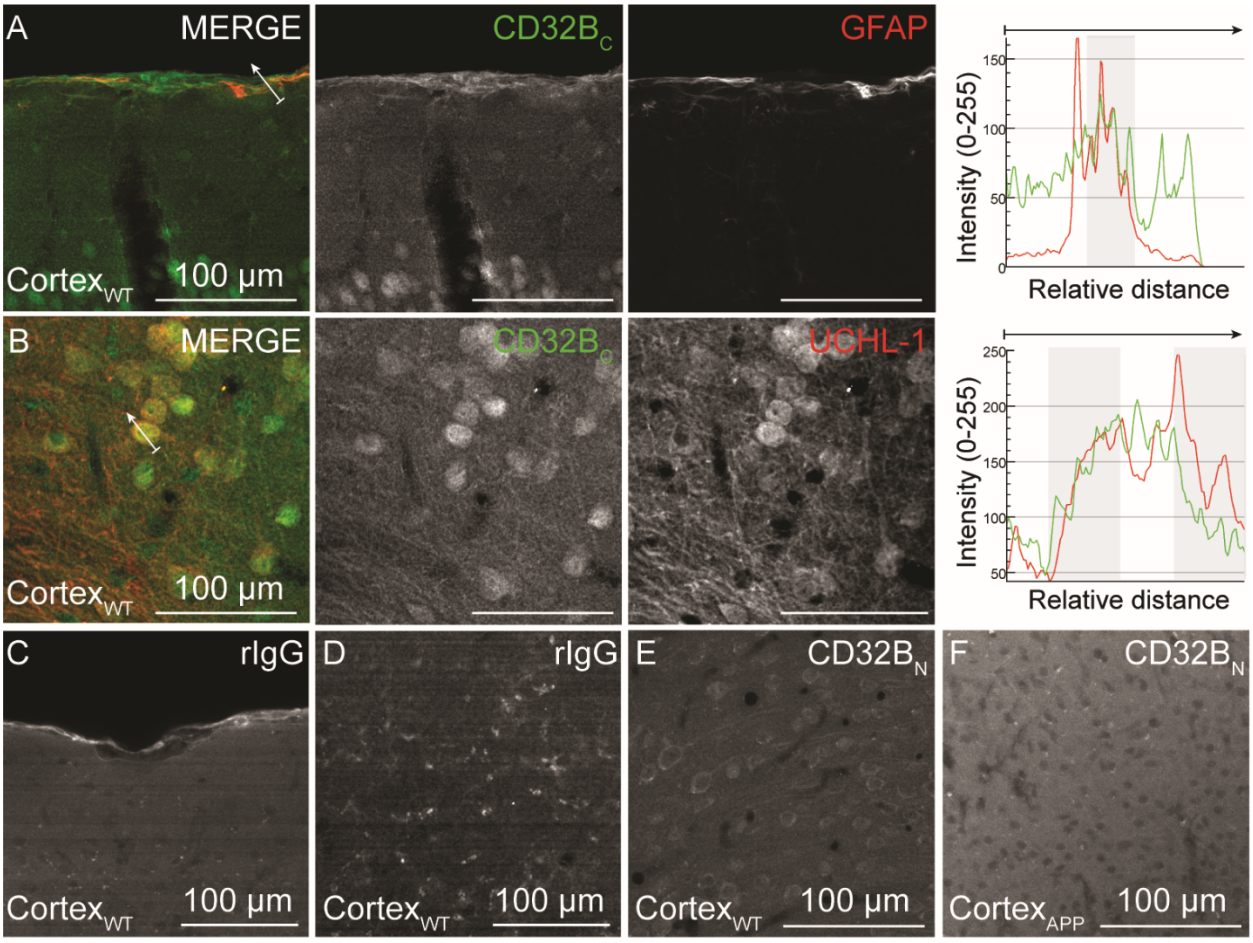

Figure 16. **FcγRIIb immunoreactivity at the mouse brain-cerebrospinal fluid interfaces.** CD32B$_C$ and CD32B$_N$ is shown in green (A-D) and white (E, F) respectively. Glial fibrillary acidic protein (GFAP, red) is an intermediate filament cytoskeletal protein within astrocytic foot processes; ubiquitin carboxy-terminal hydrolase L1 (UCHL-1, red) are ubiquitin-cleaving enzymes in the neuronal cytoplasmic space. CD32B$_C$ (A), CD32B$_N$ (not shown) and non-specific rabbit IgG (E) immunoreactivity were high at the cortical surface in WT mouse. UCHL-1-positive neuronal cells were detected by CD32B$_C$ (B) and CD32B$_N$ (E). CD32B$_N$ was not detected in APP mice (F). Astrocytic immunolabeling was minimal in both cases. WT: C57BL/6N mice; APP: APPswe/PS1dE9 mice. Grey regions in the intensity-vs-position plots highlight instances of perfect/imperfect colocalization and arrows indicate regions selected for colocalization analysis.

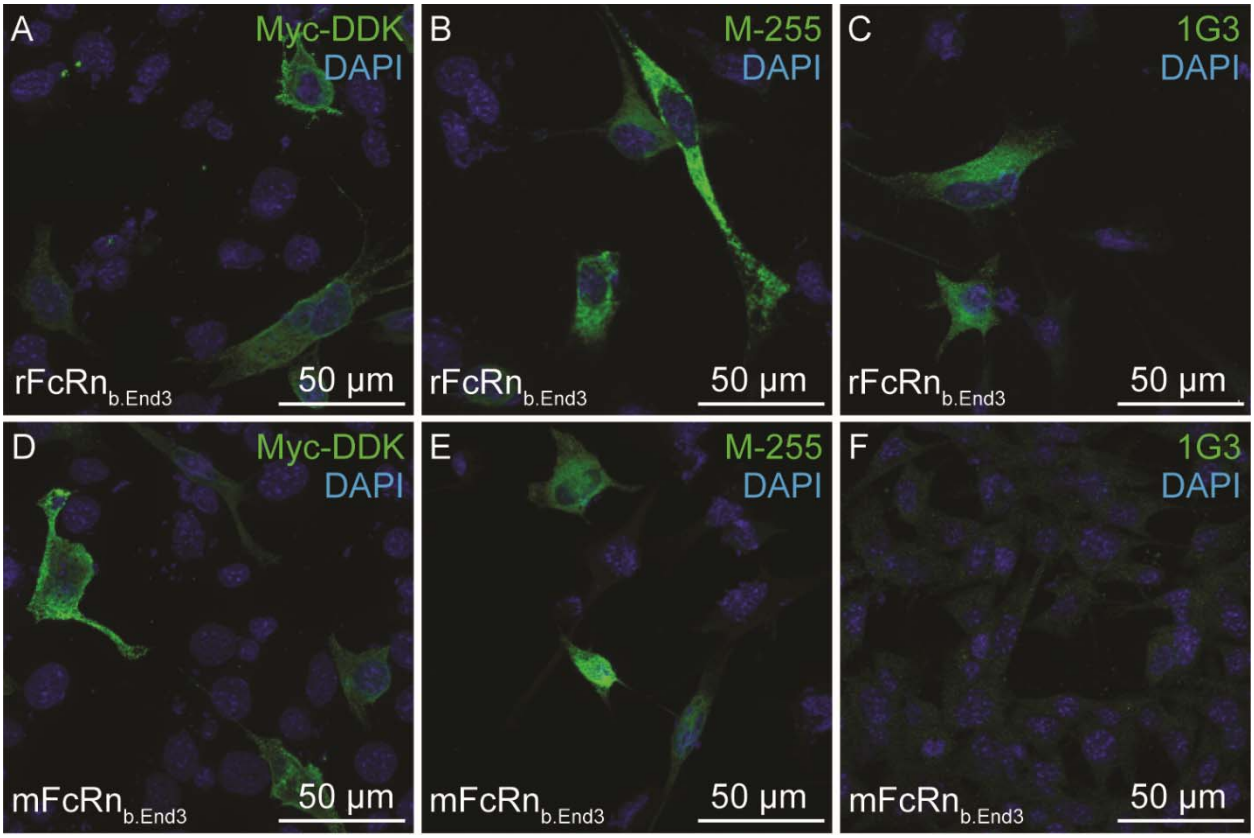

Figure 17. **Validating specificity of anti-FcRn antibodies in FcRn-transfected b. End3 cells.** Transfected cells with Myc-DDK-tagged rat FcRn and mouse FcRn are shown in green. (A, D) Positive control for transfection success of rat *Fcgrt* (A) and mouse *Fcgrt* (D) are indicated by anti-Myc-DDK immunofluorescence. M-255 immunolabeling in bEnd.3 transfected with r*Fcgrt* (B) and m*Fcgrt* (E). detected both Fcgrt proteins. 1G3 immunolabeling detected rFcgrt (E) but not mFcgrt (F). Cell nuclei are labeled with DAPI (blue, A-F). r*Fcgrt*: rat FcRn large subunit p51; m*Fcgrt*: mouse FcRn large subunit p51; b.End3: mouse brain endothelial cells.

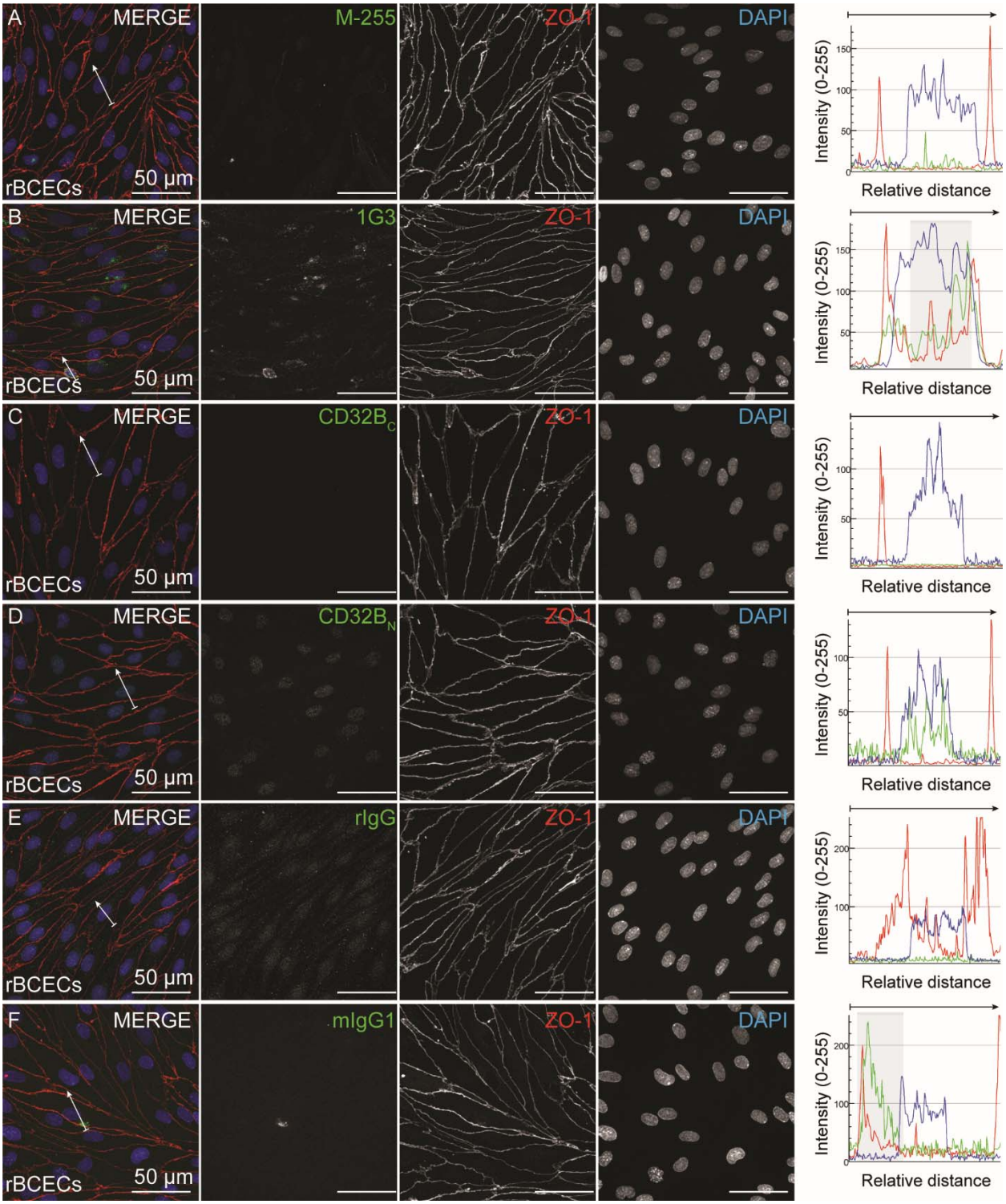

Figure 18. ***In vitro*** **Fc receptor immunoreactivity in rat brain capillary endothelial cells (rBCECs).** Zonula occludens (ZO-1, red) are tight-junction protein complexes between endothelial cells. Fc receptors are labeled in green. Minimal M-255 (A) immunolabeling in rBCECs was detected, compared to non-

specific rabbit IgG immunolabeling (E). 1G3 (B) was sparsely detected in a fraction of rBCECs. $CD32B_N$ immunolabeling (D) was nuclear and non-specific; $CD32B_C$ and non-specific mIgG1 immunolabeling (C, F) were absent. Cell nuclei are labeled with DAPI (blue; A-F). Grey regions in the intensity-vs-position plots highlight instances of perfect/imperfect colocalization and arrows indicate regions selected for colocalization analysis.

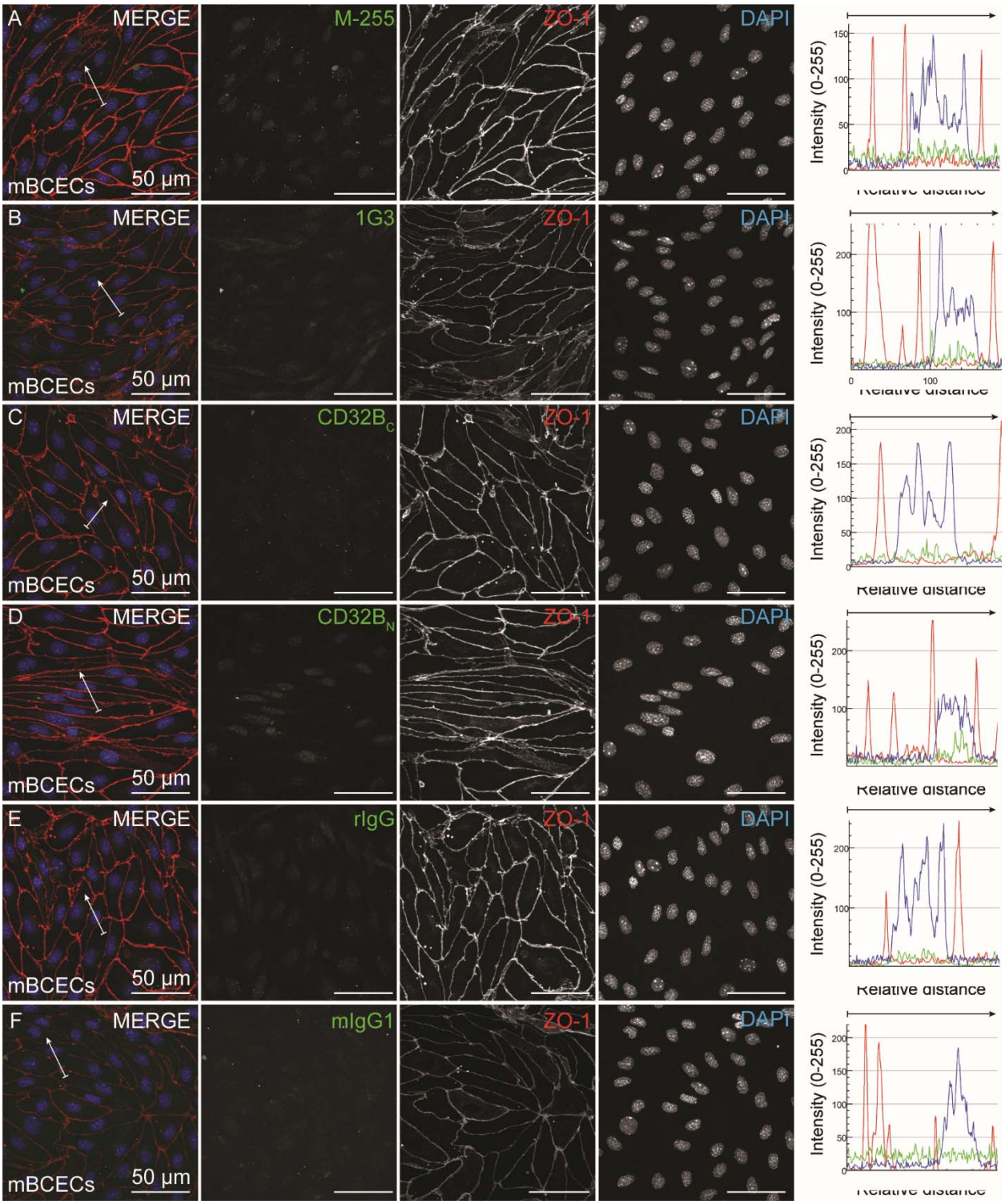

Figure 19. *In vitro* Fc receptor immunoreactivity in mouse brain capillary endothelial cells (mBCECs). Zonula occludens (ZO-1, red) are tight-junction protein complexes between endothelial cells. Fc receptors are labeled in green. Fc receptors are not expressed by mBCECs based on non-specific nuclear

staining. Nuclear immunolabeling profiles (A-D) were comparable to non-specific rabbit and mouse IgG1 antibody controls (E, F). Cell nuclei are labeled with DAPI (blue; A-F). Grey regions in the intensity-vs-position plots highlight instances of perfect/imperfect colocalization and arrows indicate regions selected for colocalization analysis.

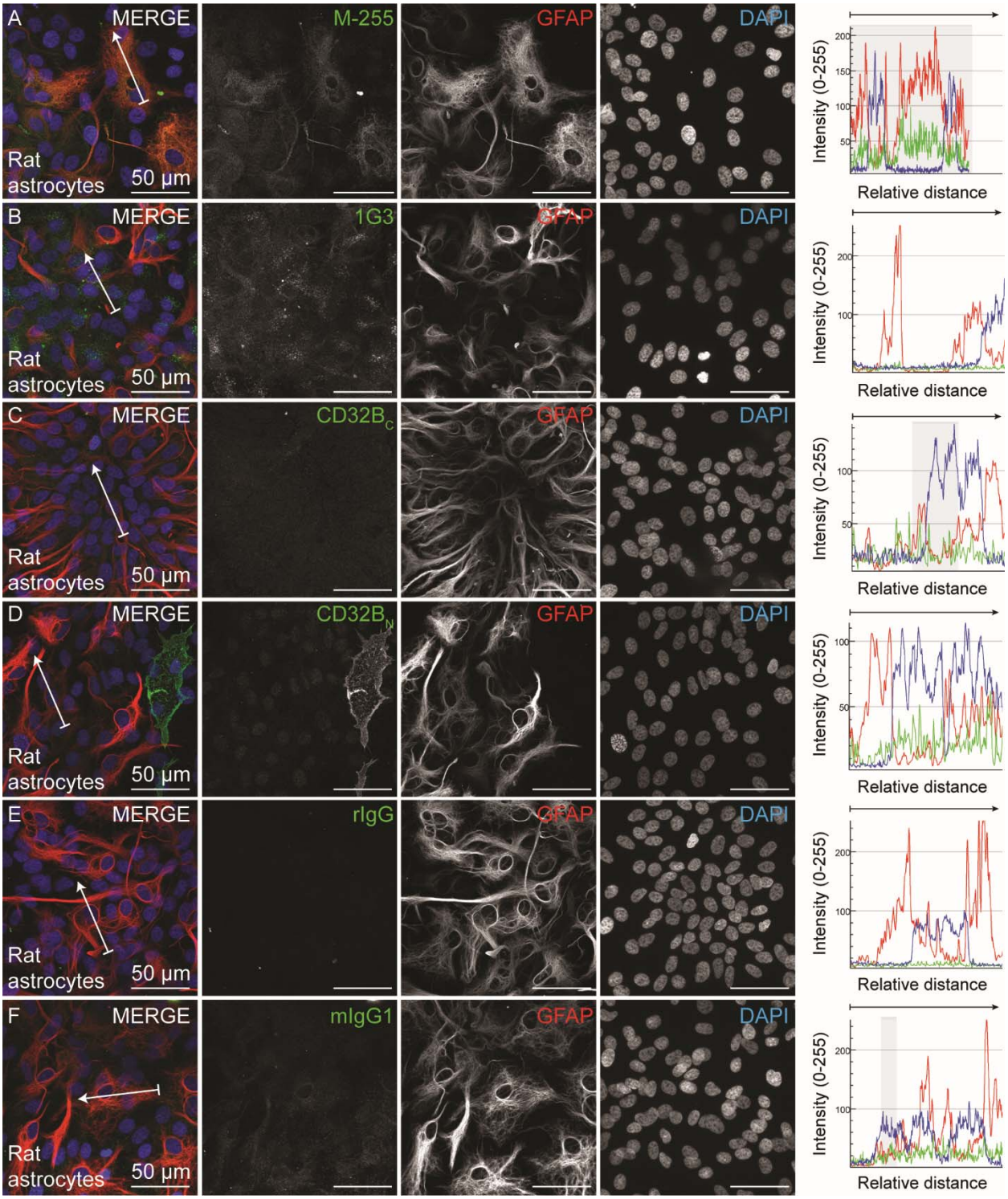

Figure 20. ***In vitro*** **Fc receptor immunoreactivity in primary rat astrocytes.** Fc receptors are shown in green. Glial fibrillary acidic protein (GFAP, red) is an intermediate filament cytoskeletal protein within astrocytic foot processes. Cytoplasmic M-255 (A) immunolabeling was associated with GFAP-positive

cells. Basal levels of 1G3 immunolabeling (B) were detected in GFAP-positive cells that was similar to non-specific mouse IgG1 immunolabeling (F). $CD32B_C$ (C) and rabbit IgG (F) immunolabeling was absent in primary rat astrocytes. $CD32B_N$ levels were relatively low and perinuclear in in GFAP-positive cells but high in non-GFAP-positive cells. These cells could be putative microglial derived from mixed glial cell culture preparations. Cells are labeled with DAPI (blue; A-F). Grey regions in the intensity-vs-position plots highlight instances of perfect/imperfect colocalization and arrows indicate regions selected for colocalization analysis.

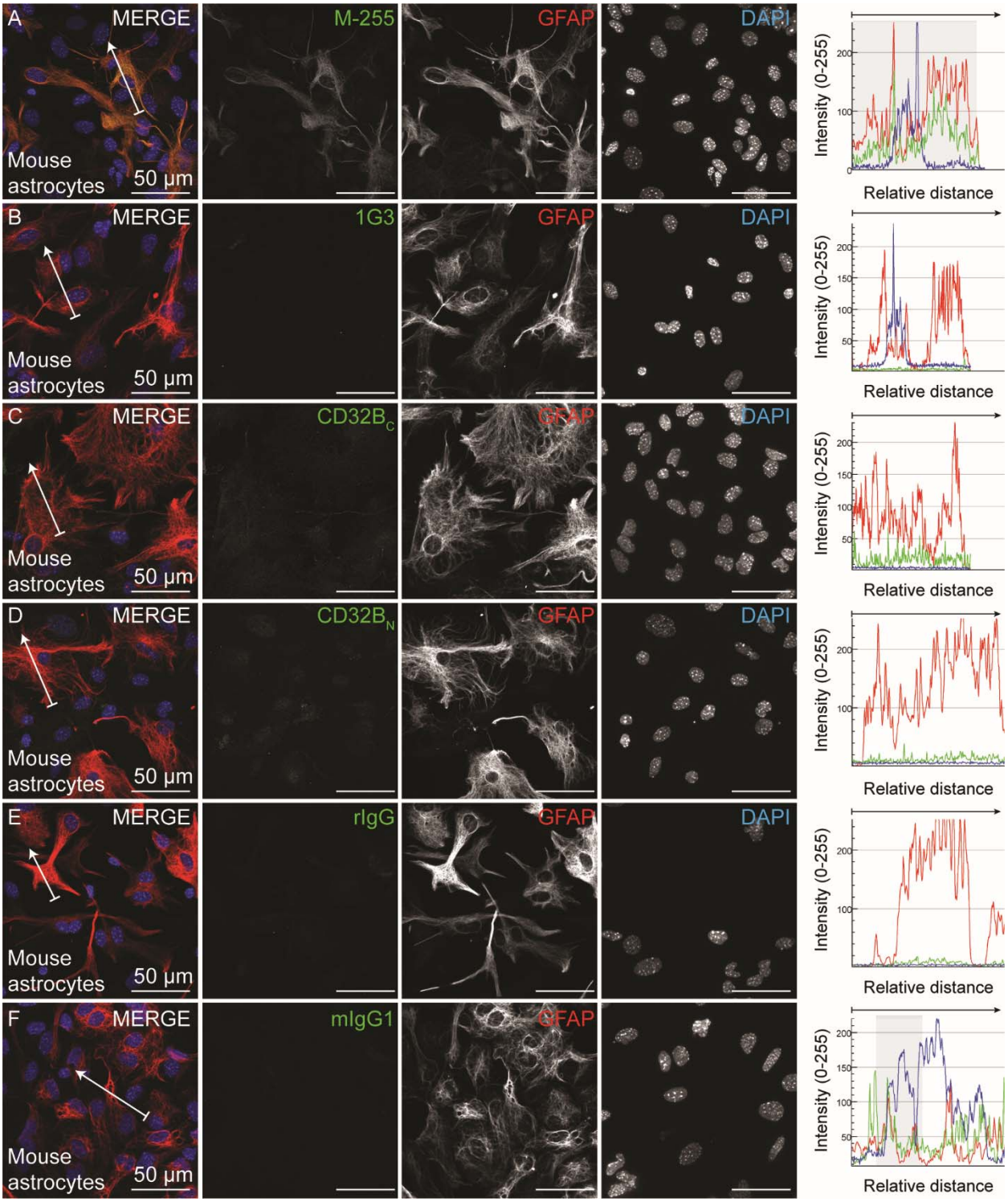

Figure 21. *In vitro* Fc receptor immunoreactivity in primary mouse astrocytes. Fc receptors are shown in green. Glial fibrillary acidic protein (GFAP, red) is an intermediate filament cytoskeletal protein within astrocytic foot processes. M-255 (A) immunolabeling was detected in GFAP-positive cells.

Immunolabeling remained below detection limits for all other antibodies (B-F). Cell nuclei were labeled with DAPI (blue; A-F). Grey regions in the intensity-vs-position plots highlight instances of perfect/imperfect colocalization and arrows indicate regions selected for colocalization analysis.

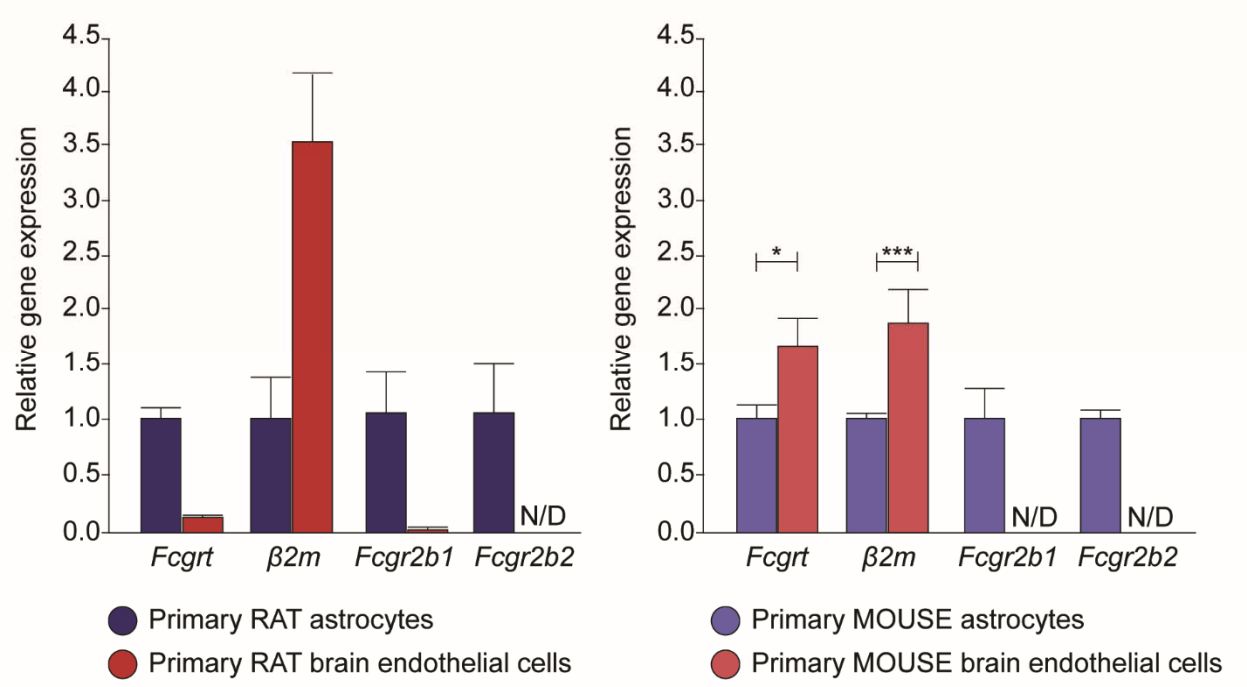

Figure 22. Gene expression analyses for Fc receptors in primary astrocytes and brain endothelial cell cultures. (A) Relative gene expression values are indicated for Fc receptor genes (*Fcgrt, β2m*, *Fcgr2b1*, *Fcgr2b2*) in rat astrocytes (n = 4), rBCECs (n = 4), mouse astrocytes (n = 4), and mBCECs (n = 4). (A) *β2m* gene expression is substantially high in rBCECs but no statistically significance was observed; *FCGRT* levels were relatively lower in rBCECs than primary rat astrocytes; *Fcgr2b1* and *Fcgr2b2* levels were minimal or undetected. (B) *Fcgrt* and *β2m* levels were higher in mBCECs compared to astrocytes, with statistically significant values for *Fcgrt* gene expression in mBCECs. Values are normalized to housekeeping genes (actin and hypoxanthine phosphoribosyltransferase-1). *$p < 0.05$ & *** $p < 0.001$, Student's t-test; N/D: not detectable; *FCGRT*: FcRn p51 subunit; *β2m*: FcRn beta-2 microglobulin subunit, *FCGR2B1*: FcγRIIb isotype 1; *FCGR2B2*: FcγRIIb isotype 2; rBCECs: rat brain capillary endothelial cells; mBCECs: mouse brain capillary endothelial cells.

EPILOGUE

Key findings from this thesis can be summarized as follows: (a) intranasal delivery of a tracer dose of perillyl alcohol (POH) led to ~10-fold higher CSF levels than an equal-dose intravascular POH injection; (b) acute intranasal and intraperitoneal [^{125}I]-IgG administration in mice at equal-dose resulted in similar blood [^{125}I]-IgG levels but ~5-10-fold higher brain [^{125}I]-IgG concentrations at the olfactory bulbs with intranasal delivery; (c) MMP-9 enhances intranasal [^{125}I]-IgG delivery to the murine CNS, although the extent of enhancement (~1-2-fold) is lower than previously reported values for rats (~5-fold increase at the olfactory bulbs; Kumar *et al.*, 2018); (d) olfactory nerve-associated pathways may be more relevant than trigeminal nerve pathways for intranasal targeting to the CNS in mice, based on non-significant changes in trigeminal nerve [^{125}I]-IgG levels following intranasal [^{125}I]-IgG administration and intraperitoneal [^{125}I]-IgG administration; (e) subtle physiological differences in transgenic APPswe/PS1dE9 and wild-type C57BL/6J mice may be responsible for improved [^{125}I]-IgG distribution in the CNS with and without intranasal MMP-9 pretreatment; (f) APPswe/PS1dE9 mice may experience significant changes in olfactory sensitivity (reduced sniff time) due to chronic MMP-9 exposure as well as chronic intraperitoneal injections, (g) chronic intranasal administration of an Aβ N-terminus-targeting antibody in APPswe/PS1dE9 mice may lead to dose-dependent resolution of fibrillar plaques into higher-order soluble oligomers, and (h) astrocytes and macrophages lining key brain-CSF interfaces (i.e. the olfactory nerve layer, leptomeninges, glia limitans, subventricular regions, perivascular spaces, and choroid plexus) could be active sites for molecular interaction between intranasally administered substances, endogenous receptors, and biotransformation enzymes. Taken together, these results offer some new perspectives on target engagement and uptake in the CNS and CSF following intranasal delivery of small and large molecules across different species, models and cell-types.

Nevertheless, a number of questions still remain unanswered by the work presented in this thesis. Although this thesis describes much new data for POH and IgG distribution from the external environment of the nasal passages to various different central fluid compartments (cerebrospinal fluid, perivascular fluid, and

the interstitial fluid within the brain extracellular spaces), a better appreciation of the precise mechanisms governing the exchange of these and other molecules *between* these central compartments awaits further study (Abbott *et al.*, 2018).

In **Chapter 1**, we demonstrated that intranasal delivery of POH led to enhanced CSF exposure for POH (parent compound) but not for its metabolite (perillic acid, PA). We hypothesize that solute carrier proteins like MCT-1 may have a role in bidirectional transport of perillic acid across the CNS barriers based on high MCT-1 expression at the BBB and BCSFBs (Pierre *et al.*, 2000). To our knowledge, POH or PA have not yet been evaluated for MCT-1 substrate activity so further studies investigating PA – MCT-1 interactions may provide useful information to understand the full nature of PA transport across the BBB and BCSFB. We have also demonstrated that intranasal delivery potentially allows for both free and albumin-bound POH to directly access the CSF via olfactory and trigeminal associated pathways in rats; we suggest that dehydrogenases expressed on astrocytes and microglial cells (Barrera-Sandoval *et al.*, 2019) may have a role in POH-PA biotransformation along these pathways. Distribution studies using fluorescently-labeled or radiolabeled POH would provide useful information about the rates of POH-PA conversion at the nasal epithelial layer, lamina propria, and the cortical surface. It is now well recognized that CSF sampling often has limited value in accurately predicting brain concentrations (Abbott *et al.*, 2018), so it will obviously be important for future studies to examine intranasal biodistribution of POH to brain tissue in addition to CSF. In addition, it is important to consider that tumor-bearing and wild-type Sprague-Dawley rats will obviously present physiological differences that may greatly impact POH biodistribution, cell uptake, and metabolism; hence, future distribution studies utilizing rat models of glioblastoma may prove highly informative. Additional studies making use of different animal brain cancer models may well reveal new insights into altered distribution and pharmacodynamic efficacy of POH not fully appreciated from our present work.

Chapter 2 highlights the biodistribution and pharmacodynamic efficacy profiles for full-length IgG

following acute and chronic intranasal IgG delivery in mice. Comparisons were made against equal-dose intraperitoneal experiments to inform us about the maximum IgG levels following systemic delivery. In our acute studies, we observed maximal [^{125}I]-IgG exposure at the olfactory bulb following [^{125}I]-IgG intranasal delivery. While this finding was consistent across animal models, treatment strategies, and autoradiography studies, it also perfectly aligned with previously reported values for rats and macaques (Kumar *et al.* 2018; Lochhead *et al.*, 2015; Thorne *et al.*, 2004; Thorne *et al.*, 2008). Further, [^{125}I]-IgG concentrations in the olfactory bulbs were similar to values reported for intranasally applied IgG at a 2-fold higher dose in rats; these values suggest that higher exposure is a likely consequence of shorter olfactory nerve-associated pathways in mice. One interesting finding in this study was non-significant differences in [^{125}I]-IgG associated with the trigeminal nerves. One possible explanation for this finding could be the reduced thickness of dura mater in mice since cranial surgical preparations have been reported to be less labor-intensive in mice compared to rats (Shih *et al.*, 2012). Branches of the trigeminal nerve innervate the dura so it is possible that reduced dural thickness may affect the extent of IgG exposure or clearance from the trigeminal pathways in some as yet unappreciated way; such questions were beyond the scope of this thesis but may be important areas of further investigation.

We also characterized MMP-9 induced nasal permeation enhancement in two different mouse models – while intranasal MMP-9 pre-treatment did result in brain exposure increases in these mice, it did so at levels (~2-fold enhancement) less than previously reported in rats (Kumar *et al.*, 2018). One conclusion from these observations that merits further study is the possibility that there are important differences in MMP-9 substrate activity in the nasal mucosa between rats, mice, and possibly other species. Early morphometric estimates suggest that the surface area of the respiratory and olfactory nasal mucosae increase by 60-70% between 7 and 16 weeks of age in rats, while no changes in nasal volume or surface area occur beyond 7 weeks of age in mice (Gross *et al.*, 1982). It may therefore be possible that the re-epithelialization rates (i.e. turnover and production of new epithelium) in adult rats and mice may be quite different over these time frames such that other related mechanistic differences (e.g. the expression of tissue inhibitors of

metalloproteinases) may significantly affect nasal tissue responses to exogenous MMP-9. Studies investigating endogenous MMP-9 expression and tissue inhibitor levels in the nasal mucosae of mice have not yet been reported; such studies may provide a further physiological basis to our findings.

Interestingly, we observed subtle differences in [^{125}I]-IgG brain levels following intranasal [^{125}I]-IgG delivery to C57BL/6J mice versus APPswe/PS1dE9 mice irrespective of pretreatment strategy (saline or MMP-9). Intranasally applied [^{125}I]-IgG had similar distribution profiles in C57BL/6J mice with MMP-9 pretreatment (i.e. the enhanced brain delivery paradigm) compared to that observed for APPswe/PS1dE9 mice with saline pretreatment (i.e. the non-enhanced delivery paradigm), suggesting that the wild-type mice had a poorer / more highly variable IgG distribution that needed nasal permeation enhancement just to reach the baseline IgG distribution observed in APPswe/PS1dE9 mice. The reasons underlying these differences are unknown but they may be due in part to abnormalities in the olfactory epithelium (reduced thickness, cell counts, neuronal density) following amyloid deposition in AD-model animals (Yao *et al.*, 2017). Such epithelial abnormalities might have resulted in a higher extent of transport (e.g. enhanced diffusion through the nasal mucosa, higher transcytosis rates across the nasal mucosa, increased access to the lamina propria, and/or a higher degree of perivascular entry with a subsequently higher flux into the brain as the end result) in our 7-to-10-month old APPswe/PS1dE9 mice (pathology initiating at 3 months of age). Indeed, IgG levels measured within the major cerebral arteries (and their associated perivascular spaces) were greater than ~2-fold higher for transgenic mice when compared to wild-type saline-treated mice. High resolution confocal microscopy suggested perivascular IgG access based on abluminal & vascular AF594-IgG profiles overlapping PECAM-1 positive endothelial cells. The cellular origin of this signal (perivascular space/pericyte/smooth muscle/endothelial cells) needs further investigation.

In our chronic study paradigm (Chapter 2), we observed that repeated intranasal MMP-9 + IgG administrations led to similar endpoints as repeated intraperitoneal IgG injections. While this similar outcome for the two treatment groups may at first glance seem to argue against the intranasal route, it is

important to realize that the intraperitoneal dose administered to mice was excessively high compared to typical systemic antibody dosing in mice. Allometric scaling of such high systemic doses would likely not be feasible in human beings while scaling from mice to human beings of the intranasal dose volumes used in our study would in fact likely be feasible (more below). Additional pharmacokinetic information for IgG entry and distribution in the mouse brain from pilot autoradiography work in our laboratory also suggests a biodistribution advantage for the intranasal route at longer times (6 h; Fig. 1). Similar studies in APPswe/PS1dE9 mice may yet provide further important information on differences in brain biodistribution by each route. Additionally, more fully exploring the nature of the [^{125}I]-IgG signal observed in our autoradiography data over different brain regions and compartments may yet reveal differences in IgG stability and functionality (e.g. metabolized IgG fragments versus intact IgG) for the different routes.

A key endpoint of our chronic efficacy/survival study was our quantification of Thioflavin-S fluorescence intensity as a surrogate for fibrillar amyloid burden in transgenic mice. The specific quantification procedure we used has previously been employed to assess distribution profiles for different intrathecally infused molecules in the brain in other work from our laboratory (Pizzo *et al.* 2018; Wilken-Resman, unpublished). Applying this technique to estimate the number of immunohistochemical profiles in brain sections could in theory provide information about the degree of CNS inflammation following a certain treatment strategy. For example, Iba1-positive microglial profiles might be quantified at a given brain region (Fig. 2) but such a strategy was felt to be too challenging due to low signal-to-noise. As a first pass, we selected Thioflavin-S for quantitation of fibrillar Aβ in this study due to high fluorescence above white matter background levels, ease of image acquisition using low resolution stereotaxic microscopy, and the ability to image and interpret findings for fibrillar aggregate species specifically. Future quantification of other forms of Aβ aggregates (e.g. using anti-Aβ antibodies such as 4G8, 6E10, or A11), astrogliosis (e.g. using GFAP staining), or other markers may highlight additional pathological outcomes and be a next step to this study. Further, studies in PD/APP mice indicate that IgG2a isotypes targeting the Aβ N-terminus may offer better outcomes in terms of fibrillar plaque resolution (Bussière *et al.*, 2004); hence, testing

isotype effects could be another logical question to pursue next.

Our olfactory sensitivity tests in the chronic study suggested altered sensitivity for MMP-9 treated and intraperitoneal 6E10 treatment groups over time, although significant differences across treatment groups at any given time were not evident. Additionally, latency readouts were not significantly different across treatment groups. Incorporating two scents (one attractant, one repulsive) in future studies might aid interpretations of these tests based on shifts in inclination towards a given scent. These would further aid in correlating cognitive impairment with changes in olfaction for future intranasal studies.

Lastly, as already alluded to above, chronic antibody exposure following intranasal or systemic administration at equal doses may not scale in the same manner across species. Allometric scaling of intranasal administration dosing for direct brain delivery is thought to be primarily a function of nasal cavity volume [(Thorne. PhD Thesis. 2002; Thorne *et al.*, 2008) and this volume is expected to increase by about ~20-30 times between mice and humans. Intraperitoneal injections scale allometrically based on body weight with a much higher fold-increase expected (~3500-fold increase for a 70 kg human being compared to an adult mouse). While conducting intranasal studies in human subjects utilizing a ~20-30-fold higher dose (0.5 – 0.6 mg) of intranasally applied antibody might be considered a realistic treatment strategy in terms of cost and inventory management, sustaining a chronic study at a ~3500-fold higher dose (70 g) intraperitoneal antibody injection is not only out of feasibility but may lead to amyloid-related imaging abnormalities (ARIA) such as edema and higher incidences of hemorrhages (Thakker *et al.*, 2009; Sperling *et al.*, 2011). The possibility to achieve a realistic, non-invasive dosing regimen using the intranasal route of administration will further help in achieving desired efficacy endpoints in clinical studies, if properly validated.

Chapter 4 describes an exploration of the distribution of different Fc receptors in the brains of rodents. This work grew out of our laboratory's increasing focus on IgG antibodies in our drug delivery work

coupled with frustrations over a lack of reliable guiding information in the literature about where in the brain the binding sites and transport proteins for these antibodies are located in our species of choice (rats and mice). We ultimately found that staining with anti-Fc receptor antibodies against different epitopes led to different immunoreactivity profiles, making conclusions difficult (but not impossible). The specific causes behind these differences were not closely investigated in this thesis. However, heterogeneity in cellular immunoreactivity profiles could be due to changes in receptor conformation across cells and tissues (Antoun *et al.*, 1989) or cross-reactivity with activating FcγRs (French *et al.*, 2012). Indeed, other sources of commercially available anti-FcγRIIb antibodies provide a percentage of cross-reactivity with activating FcγRs when the epitope involved alpha chain residues (e.g. antibodies from Novus Biologicals; R&D System, and Cell Signaling Technology). There is a possibility that one of the antibodies we utilized, $CD32B_N$ with an extracellular alpha chain epitope, could be collectively detecting both activating and inhibitory FcγRs since extracellular Ig domains are reported to be similar across FcγRs (Nimmerjahn & Ravetch, 2008). These challenges aside, we believe that cells consistently immunoreactive for both FcγRIIb and FcRn (e.g. meningeal cells, macrophages, neurons) might be investigated as a platform to study the effects of manipulating activation/inhibitory potential in order to shortlist cells that may have a higher likelihood for internalizing IgG in the CNS. Anti-FcγRIIb antibodies applied to mouse brain sections and cell cultures were not immunoreactive for mouse astrocytes as they were in rats; hence, future experiments with antibodies specific to mouse-FcR epitopes in wild-type and FcR-knockout mice would be helpful to confirm inter-species differences in FcR expression. Consideration of emerging transcriptomics data for rodents contained in publications and databases (Vanlandewijck *et al.*, 2018; Betsholtz et al. Personal communication) may ultimately aid in this exercise.

Our murine FcRn immunoreactivity studies using anti-FcRn antibodies (mouse IgG1) highlighted differences in APPswe/PS1dE9 mice that was not observed in C57BL/6 mice, particularly with respect to an intense vascular immunoreactivity. Similar differences have been reported for large (> 100μm) cerebral blood vessels and choroid plexus epithelial cells in other transgenic mice (Tg276 > Tg32) compared to

wild-type mice (C57BL/6) using an anti-FcRn antibody raised in rabbits (Latvala *et al.*, 2017). Differences in FcRn expression between wild-type and transgenic mice have also been documented for the peripheral nervous system (Li & Balthasar, 2018; Whelan *et al.*, 1987). Indeed, the active investigation of murine FcRn immunoreactivity has accelerated in the past decade as these differences have become increasingly apparent across mouse models (Avery *et al.*, 2016; Fan *et al.*, 2016; Roopenian *et al.*, 2010; Tam *et al.*, 2013). It has been suggested that altered Fc receptor immunoreactivity profiles could be a putative compensatory mechanism that prevents BBB disruption in animal models (Bien-Ly *et al.*, 2015). Inter-strain (Balb/c mice versus C57BL/6 mice) differences in FcR expression are yet another poorly explored subject that deserves further study (Nimmerjahn & Ravetch, 2006). Inter-species IgG immunoreactivity differences in the CNS (Hazama *et al.*, 2005; Niu *et al.* 2011; Pizzo, unpublished; Yoshimi *et al.*, 2002) have been reported more often than differences in FcR expression profiles in the CNS. Our results in Chapter 4 may stimulate further work in this area. Finally, correlations between protein expression and mRNA expression from murine single-cell mRNA sequencing databases have also been discussed briefly. Mouse astrocytes have been consistently reported to express low levels of FcR mRNA across multiple studies (Clarke *et al.*, 2018, Zeisel *et al.*, 2015; Zhang *et al.*, 2014). Our findings suggest astrocyte FcR expression may differ between rats and mice for unknown reasons. Unfortunately, the current lack of open-access rat mRNA sequencing databases prevents any further inferences. The anticipated development of rat transcriptomics resources will allow better considerations of species differences in the future.

This thesis has carefully contrasted results obtained from equal-dose systemic and intranasal dosing experiments using a variety of tracer molecules, multiple species and different durations of treatment with the aim of better characterizing various aspects of intranasal delivery in preclinical animal models. The intranasal route of administration is well recognized for both merits (rapid delivery, bypassing first-pass hepatic elimination, direct brain access) and challenges (inter-subject variability, mucociliary clearance, species-differences). It is our hope that the in-depth analyses of different research models, molecules, kinetics and dose-response relationships provided within this thesis moves the field closer to a better and

more complete understanding of the mechanisms that govern CNS drug disposition in animal models following intranasal delivery.

References

Abbott NJ, Pizzo ME, Preston JE, Janigro D & Thorne RG (2018). The role of brain barriers in fluid movement in the CNS: is there a 'glymphatic' system? *Acta Neuropathol* **135(3)**: 387-407.

Antoun GR, Longenecker BM & Zipf TF (1989). Comparison of the 40kDA hematopoietic cell antigens bound by monoclonal antibodies IV3, 41H16 and KB61. *Mol Immunol* **26**, 333–338.

Avery LB, Wang M, Kavosi MS, Joyce A, Kurz JC, Fan YY, Dowty ME, Zhang M, Zhang Y, Cheng A, Hua F, Jones HM, Neubert H, Pelzer RJ & O'Hara DM (2016). Utility of a human FcRn transgenic mouse model in drug discovery for early assessment and prediction of human pharmacokinetics of monoclonal antibodies. *MAbs* **8(6)**: 1064-1078.

Bien-ly N, Boswell CA, Jeet S, Beach TG, Hoyte K, Luk W, Shihadeh V, Ulufatu S, Foreman O, Lu Y, DeVoss J, van der Brug M & Watts RJ (2015). Lack of Widespread BBB Disruption in Alzheimer's Disease Models: Focus on Therapeutic Antibodies. *Neuron* **88**, 289–297.

Bussière T, Bard F, Barbour R, Grajeda H, Guido T, Khan K, Schenk D, Games D, Seubert P & Buttini M (2004). Morphological characterization of Thioflavin-S-positive amyloid plaques in transgenic Alzheimer mice and effect of passive Abeta immunotherapy on their clearance. *Am J Pathol* **165(3)**: 987-995.

Clarke LE, Liddlelow SA, Chakraborty C, Munch AE, Heiman M & Barres BA (2018). Normal aging induces A1-like astrocyte reactivity. *Proc Natl Acad Sci* **115**, E1896–E1905.

Fan YY, Avery LB, Wang M, O'Hara DM, Leung S & Neubert H (2016). Tissue expression profile of human neonatal Fc receptor (FcRn) in Tg32 transgenic mice. *MAbs* **8(5):** 848-853.

Gross EA, Swenberg JA, Fields S & Popp JA (1982). Comparative morphometry of the nasal cavity in rats and mice. *J Anat* **135(Pt 1):** 83-88.

Hazama GI, Yasuhara O, Morita H, Aimi Y, Tooyama I & Kimura H (2005). Mouse Brain IgG-Like Immunoreactivity: Strain-Specific Occurrence in Microglia and Biochemical Identification of IgG. *J Comp Neurol* **492**, 234–249.

Kumar NN, Lochhead JJ, Pizzo ME, Nehra G, Boroumand S, Greene G & Thorne RG (2018). Delivery of immunoglobulin G antibodies to the rat nervous system following intranasal administration: Distribution, dose-response, and mechanisms of delivery. *J Control Release* **286**, 467–484.

Latvala S, Jacobsen B, Otteneder MB, Herrmann A & Kronenberg S (2017). Distribution of FcRn Across Species and Tissues. *J Histochem Cytochem* **65**, 321–333.

Li T & Balthasar JP (2018). FcRn Expression in Wildtype Mice, Transgenic Mice, and in Human Tissues. *Biomolecules* **8**, 115.

Lochhead JJ, Wolak DJ, Pizzo ME & Thorne RG (2015). Rapid transport within cerebral perivascular spaces underlies widespread tracer distribution in the brain after intranasal administration. *J Cereb Blood Flow Metab* **35**, 371–381.

Nimmerjahn F & Ravetch JV (2007). Fc-receptors as regulators of immunity. *Adv Immunol* **96**, 179-204.

Nimmerjahn F & Ravetch JV (2008). Fcγ receptors as regulators of immune responses. *Nat Rev Immunol* **8**, 34–47.

Niu N, Zhang J, Guo Y, Zhao Y, Korteweg C & Gu J (2011). Expression and distribution of immunoglobulin G and its receptors in the human nervous system. *Int J Biochem Cell Biol* **43**, 556–563.

Pierre K, Pellerin L, Debernardi R, Riederer BM & Magistretti PJ (2000). Cell-specific localization of monocarboxylate transporters, MCT1 and MCT2, in the adult mouse brain revealed by double immunohistochemical labeling and confocal microscopy. *Neuroscience* **100(3)**: 617-627.

Pizzo ME, Wolak DJ, Kumar NN, Brunette E, Brunnquell CL, Hannocks MJ, Abbott NJ, Meyerand ME, Sorokin L, Stanimirovic DB & Thorne RG (2018). Intrathecal antibody distribution in the rat brain: surface diffusion, perivascular transport and osmotic enhancement of delivery. *J Physiol* **596(3)**: 445-475.

Roopenian DC, Christianson GJ & Sproule TJ (2010). Human FcRn transgenic mice for pharmacokinetic evaluation of therapeutic antibodies. *Methods Mol Biol* **602**: 93-104.

Shih AY, Driscoll JD, Drew PJ, Nishimura N, Schaffer CB & Kleinfeld D (2012). Two-photon microscopy as a tool to study blood flow and neurovascular coupling in the rodent brain. *J Cereb Blood Flow Metab* **32(7)**: 1277-1309.

Sperling RA, Jack CR Jr, Black SE, Frosch MP, Greenberg SM, Hyman BT, Scheltens P, Carrillo MC, Thies W, Bednar MM, Black RS, Brashear HR, Grundman M, Siemers ER, Feldman HH & Schindler RJ (2011). Amyloid-related imaging abnormalities in amyloid-modifying therapeutic trials: recommendations from the Alzheimer's Association Research Roundtable Workgroup. *Alzheimers Dement* **7(4)**: 367-385.

Tam SH, McCarthy SG, Brosnan K, Goldberg KM & Scallon BJ (2013). Correlations between pharmacokinetics of IgG antibodies in primates vs. FcRn-transgenic mice reveal a rodent model with predictive capabilities. *MAbs* **5(3)**: 397-405.

Thakker DR, Weatherspoon MR, Harrison J, Keene TE, Lane DS, Kaemmerer WF, Stewart GR & Shafer LL (2009). Intracerebroventricular amyloid-beta antibodies reduce cerebral amyloid angiopathy and associated micro-hemorrhages in aged Tg2576 mice. *Proc Natl Acad Sci U S A*. **106(11)**: 4501-4506.

Thorne RG, Hanson LR, Ross TM, Tung D & Frey WH 2nd (2008). Delivery of interferon-beta to the monkey nervous system following intranasal administration. *Neuroscience* **152(3)**: 785-797.

Thorne RG, Pronk GJ, Padmanabhan V & Frey WH 2nd (2004). Delivery of insulin-like growth factor-I to the rat brain and spinal cord along olfactory and trigeminal pathways following intranasal administration. *Neuroscience* **127(2)**: 481-496.

Whelan JP, Eriksson U & Lampson LA (1986). Expression of mouse beta 2-microglobulin in frozen and formaldehyde-fixed central nervous tissues: comparison of tissue behind the blood-brain barrier and tissue in a barrier-free region. *J Immunol* **137**, 2561–2566.

Williams EL, Tutt AL, French RR, Chan HT, Lau B, Penfold CA, Mockridge CI, Roghanian A, Cox KL, Verbeek JS, Glennie MJ & Cragg MS (2012). Development and characterisation of monoclonal antibodies specific for the murine inhibitory FcγRIIB (CD32B). *Eur J Immunol* **42**, 2109–2120.

Yao ZG, Hua F, Zhang HZ, Li YY & Qin YJ (2017). Olfactory dysfunction in the APP/PS1 transgenic mouse model of Alzheimer's disease: Morphological evaluations from the nose to the brain. *Neuropathology* **37(6)**: 485-494.

Yoshimi K, Woo M, Son Y, Baudry M & Thompson RF (2002). IgG-immunostaining in the intact rabbit brain: Variable but significant staining of hippocampal and cerebellar neurons with anti-IgG. *Brain Res* **956**, 53–66.

Zeisel A, Munoz-Manchando AB, Codeluppi S, Lonnerberg P, La Manno G, Jureus A, Marques S, Munguba H, He L, Betsoltz C, Rolny C, Castelo-Branco G, Hjerling-Leffler J & Linnarsson S (2015). Brain Structure: Cell types in the mouse cortex and hippocampus revealed by single-cell RNA-seq. *Science* **347**, 1138–1142.

Zhang Y, Chen K, Sloan SA, Bennett ML, Scholze AR, O'Keeffe S, Phatnani HP, Guarnieri P, Caneda C, Ruderisch N, Deng S, Liddelow SA, Zhang C & Daneman R (2014). An RNA-sequencing transcriptome and splicing database of glia, neurons, and vascular cells of the cerebral cortex. *J Neurosci* **34**, 11929–11947.

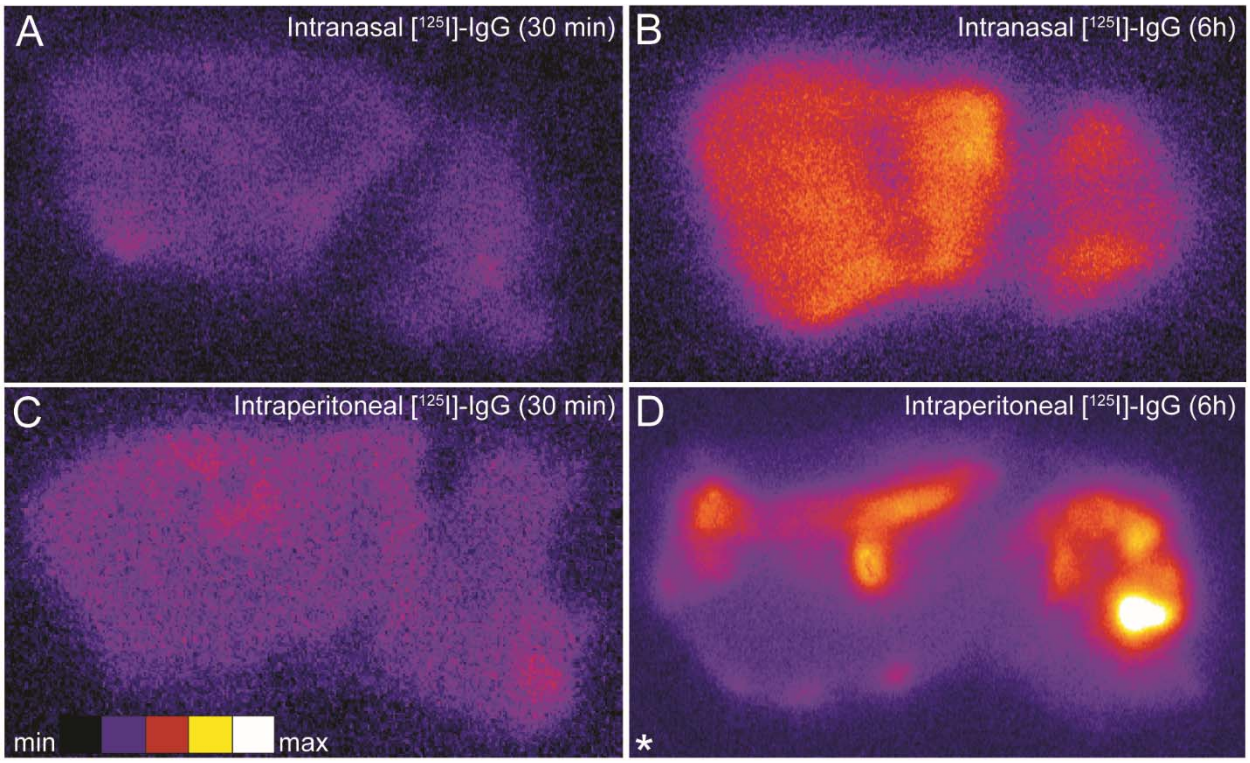

Figure 1. **Autoradiography images of [^{125}I]-IgG distribution in sagittal brain sections of C57BL/6J mouse.** (A) [^{125}I]-IgG exposure at the ventral cortical regions 30 min following intranasal [^{125}I]-IgG delivery. (B) [^{125}I]-IgG distribution and intensity increased in the brain 6 h following intranasal [^{125}I]-IgG delivery. (C) Equal-dose intraperitoneal [^{125}I]-IgG delivery demonstrated [^{125}I]-IgG profiles at the ventricular region and brainstem, indicating putative access through the choroid plexus (CP) and circumventricular organs (CVOs). (D) [^{125}I]-IgG distribution profile did not change substantially at 6 h post intraperitoneal [^{125}I]-IgG administration, suggesting diffusion through the CVO and CP regions at 6 h.

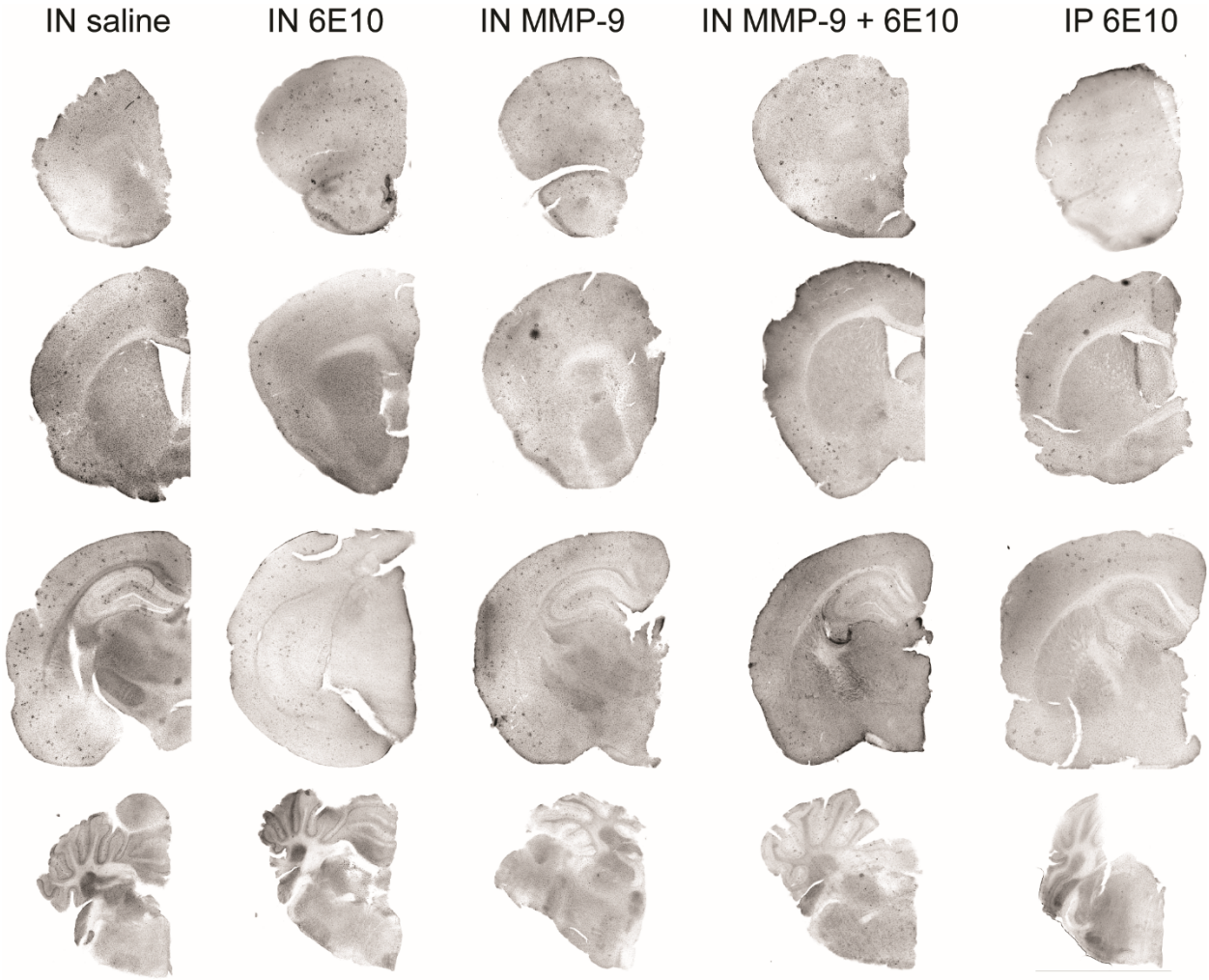

Figure 2. **Immunohistochemical analysis of ionized calcium binding adapter molecule-1 (Iba1) in the coronal section of hemibrains from the chronic efficacy/survival study.** Brain sections highlight the distribution of Iba-1, a phagocytosis-specific protein highly enriched in microglia and macrophages within the central nervous system. Visual differences across treatment groups can be observed from these representative sections. Estimation of these profiles would require selection threshold values above background autofluorescence that may have inter-animal variability and differences between sections at the same distance from bregma (0 mm) or among section at different distances from bregma (0 mm).